JOURNAL OF THE AERONAUTICAL SCIENCES

VOLUME 23 SEPTEMBER, 1956 NUMBER 9

ST LOUIS SEP 1956

CONTENTS

Stiffness and Deflection Analysis of Complex Structures
M. J. TURNER, R. W. CLOUGH, H. C. MARTIN, AND L. J. TOPP 805

Forced Responses of Two Elastic Beams Interconnected by Spring-Damper Systems
MICHAEL DUBLIN AND HANS R. FRIEDRICH 824

The Rotational Field Behind a Curved Shock Wave Calculated by the Method of Flux Analysis
SHIGEO UCHIDA AND MICHIRU YASUHARA 830

On Equations of Motion for a Compressible Viscous Gas
E. V. LAITONE 846

An Investigation of the Noise Produced by a Subsonic Air Jet
J. H. GERRARD 855

Inelastic Column Buckling
L. HANNES LARSSON 867

Aspect Ratio Influence at High Subsonic Speeds
GORDON F. ANDERSON 874

A Creep Buckling Hypothesis
GEORGE GERARD 879

Creep Deflection of Viscoelastic Plate Under Uniform Edge Compression
T. H. LIN 883

Readers' Forum 888–900

Published by
INSTITUTE OF THE AERONAUTICAL SCIENCES, INC.

JOURNAL OF THE AERONAUTICAL SCIENCES

Editor: W. R. SEARS
Director, Graduate School of Aeronautical Engineering, Cornell University

Associate Editor: ROBERT R. DEXTER *Managing Editor:* RITA J. TURINO
Editorial Assistant: CAROLINE TAYLOR

Editorial Committee

Aerodynamics and Fluid Mechanics
Holt Ashley
H. Julian Allen
Dean R. Chapman
Francis H. Clauser
Hugh L. Dryden
John C. Evvard
Antonio Ferri
Alexander Flax
Wallace D. Hayes
R. T. Jones
Carl Kaplan
H. W. Liepmann
C. C. Lin
H. F. Ludloff
Harold Luskin
Clark B. Millikan
C. D. Perkins
H. J. E. Reid
George S. Schairer
G. B. Schubauer
John Stack
Theodore Theodorsen
Arthur N. Tifford
Th. von Kármán

Flight Testing
R. R. Gilruth
Melvin N. Gough
W. L. Howland
W. F. Milliken, Jr.

Rotating Wing Aircraft
F. B. Gustafson
K. H. Hohenemser
Bartram Kelley
R. B. Maloy
Ralph McClarren
R. H. Miller
R. H. Prewitt
Igor I. Sikorsky

Structures
John E. Duberg
N. J. Hoff
Samuel Levy
J. F. McBrearty
W. Ramberg
E. E. Sechler
F. R. Shanley
C. R. Strang
S. Timoshenko

Meteorology
C. F. Brooks
D. M. Little
F. W. Reichelderfer
K. C. Spengler

Vibration and Flutter
Lee Arnold
M. A. Biot
R. L. Bisplinghoff
Harold A. Cheilek
I. E. Garrick
Martin Goland

Aircraft Design
W. E. Beall
E. H. Heinemann
Hall L. Hibbard
Richard Hutton
C. L. Johnson
A. A. Kartveli
E. G. Stout
F. K. Teichmann
Robert J. Woods

Electronics
Welcome W. Bender
K. C. Black
M. V. Kiebert, Jr.
David S. Little
S. B. Rogers
Paul Rosenberg
L. M. Sherer

Physiologic Problems
H. G. Armstrong
Louis H. Bauer
Robert J. Benford
W. Randolph Lovelace, II
Ross A. MacFarland

Flight Propulsion
William Bollay
George W. Brady
R. P. Kroon
Frank E. Marble
Abe Silverstein
Martin Summerfield
E. S. Taylor

Instruments
Alan G. Binnie
Charles H. Colvin
Frank R. Cook
C. S. Draper
S. G. Eskin
C. F. Savage
R. C. Sylvander

SUBSCRIPTION RATES

JOURNAL OF THE AERONAUTICAL SCIENCES, Published Monthly.—United States and Possessions: 1 Year, $15.00; Single Copies, $1.50. Foreign Countries Including Canada (American Currency Rates): 1 Year, $16.00; Single Copies, $1.50.

AERONAUTICAL ENGINEERING REVIEW, Published Monthly.—United States and Possessions: 1 Year, $3.00; Single Copies, $0.50. Foreign Countries Including Canada (American Currency Rates): 1 Year, $3.50; Single Copies, $0.50.

Notices of change of address should be sent to the Institute at least 30 days prior to actual change of address.

Manuscripts for publication, proofs, and all correspondence should be addressed to the Editorial Office of the JOURNAL.

Correspondence regarding subscriptions may be addressed to the Editorial Office of the JOURNAL OF THE AERONAUTICAL SCIENCES, 2 East 64th Street, New York 21, N.Y., or to the Publication Office, 20th and Northampton Sts., Easton, Pa.

© *Copyright, 1956, by the Institute of the Aeronautical Sciences, Inc.*

Entered as Second Class Matter at the Post Office, Easton, Pa., May 1, 1937. Acceptance for mailing at a special rate of Postage provided for in the Act of August 24, 1912. Authorized April 29, 1937.

JOURNAL OF THE AERONAUTICAL SCIENCES

VOLUME 23 SEPTEMBER, 1956 NUMBER 9

Stiffness and Deflection Analysis of Complex Structures

M. J. TURNER,* R. W. CLOUGH,† H. C. MARTIN,‡ AND L. J. TOPP**

ABSTRACT

A method is developed for calculating stiffness influence coefficients of complex shell-type structures. The object is to provide a method that will yield structural data of sufficient accuracy to be adequate for subsequent dynamic and aeroelastic analyses.

Stiffness of the complete structure is obtained by summing stiffnesses of individual units. Stiffnesses of typical structural components are derived in the paper. Basic conditions of continuity and equilibrium are established at selected points (nodes) in the structure. Increasing the number of nodes increases the accuracy of results. Any physically possible support conditions can be taken into account. Details in setting up the analysis can be performed by nonengineering trained personnel; calculations are conveniently carried out on automatic digital computing equipment.

Method is illustrated by application to a simple truss, a flat plate, and a box beam. Due to shear lag and spar web deflection, the box beam has a 25 per cent greater deflection than predicted from beam theory. It is shown that the proposed method correctly accounts for these effects.

Considerable extension of the material presented in the paper is possible.

(I) INTRODUCTION

PRESENT CONFIGURATION TRENDS in the design of high-speed aircraft have created a number of difficult, fundamental structural problems for the worker in aeroelasticity and structural dynamics. The chief problem in this category is to predict, for a given elastic structure, a comprehensive set of load-deflection relations which can serve as structural basis for dynamic load calculations, theoretical vibration and flutter analyses, estimation of the effects of structural deflection on static air loads, and theoretical analysis of aeroelastic effects on stability and control. This is a problem of exceptional difficulty when thin wings and tail surfaces of low aspect ratio, either swept or unswept, are involved.

It is recognized that camber bending (or rib bending) is a significant feature of the vibration modes of the newer configurations, even of the low-order modes; in order to encompass these characteristics it seems likely that the load-deflection relations of a practical structure must be expressed in the form of either deflection or stiffness influence coefficients. One approach is to employ structural models and to determine the influence coefficients experimentally; it is anticipated that the experimental method will be employed extensively in the future, either in lieu of or as a final check on the result of analysis. However, elaborate models are expensive, they take a long time to build, and tend to become obsolete because of design changes; for these reasons it is considered essential that a continuing research effort should be applied to the development of analytical methods. It is to be expected that modern developments in high-speed digital computing machines will make possible a more fundamental approach to the problems of structural analysis; we shall expect to base our analysis on a more realistic and detailed conceptual model of the real structure than has been used in the past. As indicated by the title, the present paper is exclusively concerned with methods of theoretical analysis; also it is our object to outline the development of a method that is well adapted to the use of high-speed digital computing machinery.

(II) REVIEW OF EXISTING METHODS OF STRUCTURAL ANALYSIS

(1) *Elementary Theories of Flexure and Torsion*

The limitations of these venerable theories are too well known to justify extensive comment. They are

Received June 29, 1955. This paper is based on a paper presented at the Aeroelasticity Session, Twenty-Second Annual Meeting, IAS, New York, January 25–29, 1954.

* Structural Dynamics Unit Chief, Boeing Airplane Company, Seattle Division.

† Associate Professor of Civil Engineering, University of California, Berkeley.

‡ Professor of Aeronautical Engineering, University of Washington, Seattle.

** Structures Engineer, Structural Dynamics Unit, Boeing Airplane Company, Wichita Division.

adequate only for low-order modes of elongated structures. When the loading is complex (as in the case of inertia loading associated with a mode of high order) refinements are required to account for secondary effects such as shear lag and torsion-bending.

(2) *Wide Beam Theory: Schuerch*[1]

Schuerch has devised a generalized theory of combined flexure and torsion which is applicable to multispar wide beams having essentially rigid ribs. Torsion-bending effects are included but not shear lag. It is expected that wide beam theory will be used extensively in the solution of static aeroelastic problems (effect of air-frame flexibility on steady air loads, stability, etc.). However, the rigid rib assumption appears to limit its utility rather severely for vibration and flutter analysis of thin low aspect ratio wings.

(3) *Method of Redundant Forces: Levy, Bisplinghoff and Lang, Langefors, Rand, Wehle and Lansing*[2-6]

These writers have contributed the basic papers leading to the present widespread use of energy principles, matrix algebra, and influence coefficients in the solution of structural deflection problems. Redundant internal loads are determined by the principle of least work, and deflections are obtained by application of Castigliano's theorem. The method is, of course, perfectly general. However, the computational difficulties become severe if the structure is highly redundant, and the method is not particularly well adapted to the use of high-speed computing machines. Rand has suggested a method of solution for stresses in highly redundant structures which might also be used for calculating deflections. Instead of using member loads as redundants, he proposes to employ systems of self-equilibrating internal stresses. These redundant stresses may be regarded as perturbations of a primary stress distribution that is in equilibrium with the external loads (but does not generally satisfy compatibility conditions). The number of properly chosen redundants required to obtain a satisfactory solution may be considerably less than the "degree of redundancy." Successful application of this method requires a high degree of engineering judgment, and the accuracy of the results is very difficult to evaluate.

(4) *Plate Methods: Fung, Reissner, Benscoter, and MacNeal*[7-9]

As the trend toward thinner sections approaches the ultimate limit, we enter first a regime of very thick walled hollow structures, such that the flexural and torsional rigidities of the individual walls make a significant contribution to the overall stiffness of the entire wing. Finally we come to the solid plate of variable thickness. During the past few years a substantial research effort has been devoted to the development of methods of deflection analysis for these structural types, and important contributions have been made by all of the aforementioned authors.

(5) *Direct Stiffness Calculation: Levy, Schuerch*[10, 11]

In a recent paper Levy has presented a method of analysis for highly redundant structures which is particularly suited to the use of high-speed digital computing machines. The structure is regarded as an assemblage of beams (ribs and spars) and interspar torque cells. The stiffness matrix for the entire structure is computed by simple summation of the stiffness matrices of the elements of the structure. Finally, the matrix of deflection influence coefficients is obtained by inversion of the stiffness matrix. Schuerch has also presented a discussion of the problem from the point of view of determining the stiffness coefficients.

(III) Some Unsolved Problems

At the present time, it is believed that the greatest need is to derive a numerical method of analysis for a class of structures intermediate between the thin stiffened shell and the solid plate. These are hollow structures having a rather large share of the bending material located in the skin, which is relatively thick but still thin enough so that we may safely neglect its plate bending stiffness. In order to cope with this class of structures successfully, we must base our analysis upon a structural idealization that is sufficiently realistic to encompass a fairly general two-dimensional stress distribution in the cover plates; and our method of analysis must yield the load-deflection relations associated with such stresses. It is characteristic of these problems that the directions of principal stresses in certain critical parts of the structure cannot be determined by inspection. Hence, the familiar methods of structural analysis based upon the concepts of axial load carrying members, joined by membranes carrying pure shear, are not satisfactory, even if we employ effective width concepts to account for the bending resistance of the skin. We should like to include shear lag, torsion-bending, and Poisson's ratio effects to a sufficient approximation for reliable prediction of vibration modes and natural frequencies of moderate order. Also, we should like to avoid any assumptions of closely spaced rigid diaphragms or of orthotropic cover plates, which have been introduced in many papers on advanced structural analysis. The actual rib spacing and finite rib stiffnesses should be accounted for in a realistic fashion. In summary, what is required is an approximate numerical method of analysis which avoids drastic modification of the geometry of the structure or artificial constraints of its elastic elements. This is indeed a very large order. However, modern developments in high-speed digital computing machines offer considerable hope that these objectives can be attained.

(IV) Method of Direct Stiffness Calculation

For a given idealized structure, the analysis of stresses and deflections due to a given system of loads is a purely mathematical problem. Two conditions

must be satisfied in the analysis: (1) the forces developed in the members must be in equilibrium and (2) the deformations of the members must be compatible—i.e., consistent with each other and with the boundary conditions. In addition, the forces and deflections in each member must be related in accordance with the stress-strain relationship assumed for the material.

The analysis may be approached from two different points of view. In one case, the forces acting in the members of the structure are considered as unknown quantities. In a statically indeterminate structure, an infinite number of such force systems exist which will satisfy the equations of equilibrium. The correct force system is then selected by satisfying the conditions of compatible deformations in the members. This approach has been widely used for the analysis of all types of indeterminate structures but is, as already noted, particularly advantageous for structures that are not highly redundant.

In the other approach, the displacements of the joints in the structure are considered as unknown quantities. An infinite number of systems of mutually compatible deformations in the members are possible; the correct pattern of displacements is the one for which the equations of equilibrium are satisfied. The concept of static determinateness or indeterminateness is irrelevant when the analysis is considered from this viewpoint. This approach is the basis for many relaxation type analyses (such as moment distribution) and has been applied to the analysis of complex aircraft structures by Levy in the aforementioned paper. This will be called the method of direct stiffness calculation hereafter.

After reviewing the various methods available to the dynamics engineer for computing load-deflection relations of elastic structures, it is concluded that the most promising approach to our present difficulties is to extend further the method of direct stiffness calculation. The remainder of this paper is concerned with methods by which that extension may be accomplished.

(V) Simple Examples of Stiffness Influence Coefficients

(1) *Elastic Spring*

If an elastic spring deflects an amount δ under axial load F, Hooke's Law applies and

$$F = k\delta \tag{1}$$

Here k can be regarded as the force required to produce a unit deflection; hence it can be considered to be a stiffness influence coefficient.

Eq. (1) can also be written as

$$\delta = (1/k)F = cF \tag{2}$$

where c is the deflection due to a unit force (deflection influence coefficient).

(2) *Two-Dimensional Elastic Body*

Extending the above relations to the two-dimensional body is most conveniently accomplished by introducing matrix notation. Eqs. (1) and (2) become, respectively,

$$\{F\} = [K]\{\delta\} \tag{3}$$

$$\{\delta\} = [K]^{-1}\{F\} = [C]\{F\} \tag{4}$$

Here $[K]$ is the matrix of stiffness influence coefficients. A typical element of $[K]$ is $k_{ij}^{\xi\eta}$ = force required at i in the ξ-direction, to support a unit displacement at j in the η-direction. If ξ and η always refer to the same direction, we can use the simpler form k_{ij}. In either case an element of $[K]$, and also of $[C]$, must obey the well-known reciprocal relations. In other words, the $[K]$ and $[C]$ matrices are symmetric, provided they are referred to orthogonal coordinate systems. As will be seen later, the symmetry condition does not apply if oblique coordinates are used.

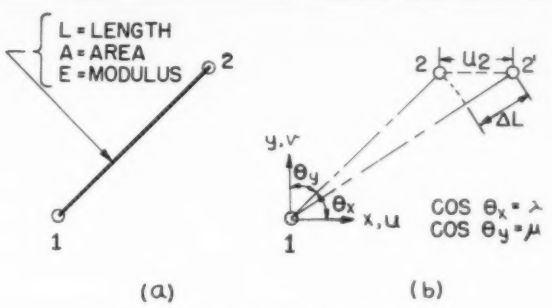

Fig. 1. Typical pin-ended truss member.

(3) *Truss Member*

Fig. 1(a) shows a typical pin ended truss member. We wish to determine its matrix of stiffness influence coefficients. Loads may be applied at points (nodes) 1 and 2. Each node can experience two components of displacement. Therefore, prior to introducing boundary conditions (supports), $[K]$ for this member will be of order 4×4.

To develop one column of $[K]$, subject the member to $u_2 \neq 0$, $u_1 = v_1 = v_2 = 0$. Then

$$\Delta L = u_2 \cos\theta_x = u_2\lambda$$

The axial force needed to produce ΔL is

$$P = (AE/L)\Delta L = (AE/L)\lambda\, u_2$$

The components of P at node 2 are

$$F_{x_2} = P\cos\theta_x = (AE/L)\,\lambda^2\, u_2$$

$$F_{y_2} = P\cos\theta_y = (AE/L)\,\lambda\mu\, u_2$$

Equilibrium gives the forces at node 1 as

$$F_{x_1} = -F_{x_2}$$

$$F_{y_1} = -F_{y_2}$$

Eq. (3) for this member then takes the form

$$\begin{Bmatrix} F_{x_1} \\ F_{x_2} \\ F_{y_1} \\ F_{y_2} \end{Bmatrix} = \frac{AE}{L}\begin{bmatrix} . & -\lambda^2 & . & . \\ . & \lambda^2 & . & . \\ . & -\lambda\mu & . & . \\ . & \lambda\mu & . & . \end{bmatrix}\begin{Bmatrix} u_1 \\ u_2 \\ v_1 \\ v_2 \end{Bmatrix} \tag{5}$$

The other elements in $[K]$ are found in a similar manner. We get

$$[K]_{\substack{\text{truss}\\ \text{member}}} = \frac{AE}{L}\begin{bmatrix} & u_1 & u_2 & v_1 & v_2 \\ & \lambda^2 & & & \\ & -\lambda^2 & \lambda^2 & & \\ & \lambda\mu & -\lambda\mu & \mu^2 & \\ & -\lambda\mu & \lambda\mu & -\mu^2 & \mu^2 \end{bmatrix} \tag{6}$$

As given in Eq. (6), $[K]$ is singular—that is, its determinant vanishes and its inverse does not exist. This is overcome by supplying boundary conditions or supports for the bar sufficient to prevent it from moving as a rigid body. For example, we may choose $u_1 = v_1 = u_2 = 0$, $v_2 \neq 0$. Node 1 is then fixed, while node 2 is provided with a roller in the y-direction. The only force component now capable of straining the bar is F_{y_2}. The force in the bar and the reactions are given by Eqs. (5) and (6).

Any other physically correct boundary conditions can be imposed. In other words, once $[K]$ has been determined, a solution can be found for any set of support conditions. The only requirement is that the structure be fixed against rigid body displacement.

(VI) Stiffness Analysis of Simple Truss

Once stiffness matrices for the various component units of a structure have been determined, the next step of finding the stiffness of the composite structure may be taken. The procedure for doing this is essentially independent of the complexity of the structure. As a result, it will be illustrated for a simple truss as shown in Fig. 2.

The stiffness of any one member of the truss is given by Eq. (6). Since length varies for the truss members, this term should be brought inside the matrix. It is then convenient to call the elements of the stiffness matrix $\bar{\lambda}^2 = \lambda^2/\text{length}$, etc. Then $\bar{\lambda}^2$, $\bar{\mu}^2$, and $\bar{\lambda}\bar{\mu}$ represent the essential terms defining the stiffness of the separate truss members. These are conveniently calculated by setting up Table 1.

From the last three columns of Table 1 the truss stiffness matrix can be written directly. This is best seen by forming the truss equation [Eq. (7a)] analogous to Eq. (5) for the single member.

The formation of all columns in Eq. (7a) can be explained by considering any one of them as an example. The second column will be chosen. It represents the case for which $v_1 \neq 0$, all other node displacements = 0.

$$\begin{Bmatrix} F_{x_1} \\ F_{y_1} \\ F_{x_2} \\ F_{y_2} \\ F_{x_3} \\ F_{y_3} \end{Bmatrix} = AE \begin{bmatrix} \frac{1}{2\sqrt{2}L} & -\frac{1}{2\sqrt{2}L} & 0 & 0 & -\frac{1}{2\sqrt{2}L} & \frac{1}{2\sqrt{2}L} \\ -\frac{1}{2\sqrt{2}L} & \frac{1}{L}+\frac{1}{2\sqrt{2}L} & 0 & -\frac{1}{L} & \frac{1}{2\sqrt{2}L} & -\frac{1}{2\sqrt{2}L} \\ 0 & 0 & \frac{1}{L} & 0 & -\frac{1}{L} & 0 \\ 0 & -\frac{1}{L} & 0 & \frac{1}{L} & 0 & 0 \\ -\frac{1}{2\sqrt{2}L} & \frac{1}{2\sqrt{2}L} & -\frac{1}{L} & 0 & \frac{1}{L}+\frac{1}{2\sqrt{2}L} & -\frac{1}{2\sqrt{2}L} \\ \frac{1}{2\sqrt{2}L} & -\frac{1}{2\sqrt{2}L} & 0 & 0 & -\frac{1}{2\sqrt{2}L} & \frac{1}{2\sqrt{2}L} \end{bmatrix} \begin{Bmatrix} u_1 \\ v_1 \\ u_2 \\ v_2 \\ u_3 \\ v_3 \end{Bmatrix} \tag{7a}$$

or

$$\{F\} = [K]\{\delta\} \tag{7b}$$

In this second column the y-components of force are given by the $\bar{\mu}^2$ terms in Table 1; the x-components of force are given by the $\bar{\lambda}\bar{\mu}$ terms. Thus F_{y_1} is the sum of $\bar{\mu}^2$ for members 1–2 and 1–3 since these are strained due to displacement v_1. Also F_{y_2} is $-\bar{\mu}^2$ for member 1–2, and F_{y_3} is $-\bar{\mu}^2$ for member 1–3. The signs follow from the basic stiffness matrix given in Eq. (6). Since equilibrium must hold, the sum of these y-components of force must vanish.

Similarly, F_{x_1} is the sum of the $\bar{\lambda}\bar{\mu}$ terms for members 1–2 and 1–3. Likewise, F_{x_2} is the negative value of $\bar{\lambda}\bar{\mu}$ for member 1–2. Finally F_{x_3} is $-\bar{\lambda}\bar{\mu}$ for member 1–3. These forces must also sum to zero if equilibrium is to hold.

Table 1

Member	x	y	Length	λ	μ	λ^2	μ^2	$\lambda\mu$	$\bar{\lambda}^2$	$\bar{\mu}^2$	$\bar{\lambda}\bar{\mu}$
1-2	0	$-L$	L	0	-1	0	1	0	0	$\frac{1}{L}$	0
1-3	L	$-L$	$\sqrt{2}L$	$\frac{1}{\sqrt{2}}$	$-\frac{1}{\sqrt{2}}$	$\frac{1}{2}$	$\frac{1}{2}$	$-\frac{1}{2}$	$\frac{1}{2\sqrt{2}L}$	$\frac{1}{2\sqrt{2}L}$	$-\frac{1}{2\sqrt{2}L}$
2-3	L	0	L	1	0	1	0	0	$\frac{1}{L}$	0	0

This process is repeated for all columns. In this way all possible node displacement components are taken into account. In each case the displacements are compatible ones for all members of the truss.

A structure having various kinds of structural components—beams as well as axially loaded members, for example—would be treated in the same manner. However, the basic stiffness matrix for each type of member would have to be known. Deriving these for units of interest in aircraft design represents a major part of this paper.

The matrix of Eq. (7a) is singular. This is altered by providing supports for the truss sufficient to prevent it from displacing as a rigid body when loads are applied. Any sufficient set of supports may be imposed; here we choose to put

$$u_1 = v_1 = u_2 = v_2 = 0$$

In other words, nodes 1 and 2 are fixed, while 3 is left free.

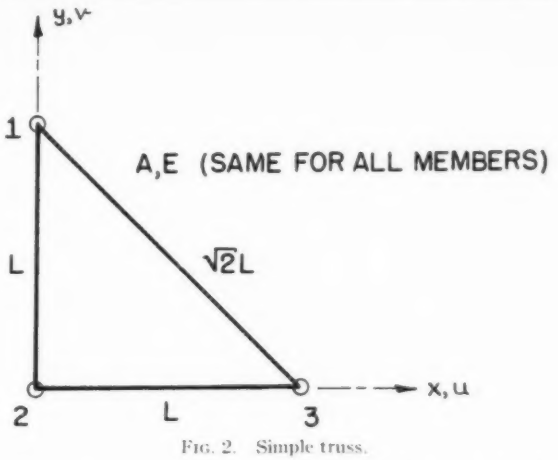

FIG. 2. Simple truss.

It is now convenient to rewrite Eq. (7a) and simultaneously partition it as shown by the broken lines in Eq. (7c).

$$\begin{Bmatrix} F_{x_3} \\ F_{y_3} \\ F_{x_1} \\ F_{y_1} \\ F_{x_2} \\ F_{y_2} \end{Bmatrix} = \frac{AE}{L} \left[\begin{array}{cccc|cc} 1+\frac{1}{2\sqrt{2}} & -\frac{1}{2\sqrt{2}} & -\frac{1}{2\sqrt{2}} & \frac{1}{2\sqrt{2}} & -1 & 0 \\ -\frac{1}{2\sqrt{2}} & \frac{1}{2\sqrt{2}} & \frac{1}{2\sqrt{2}} & -\frac{1}{2\sqrt{2}} & 0 & 0 \\ -\frac{1}{2\sqrt{2}} & \frac{1}{2\sqrt{2}} & \frac{1}{2\sqrt{2}} & -\frac{1}{2\sqrt{2}} & 0 & 0 \\ \frac{1}{2\sqrt{2}} & -\frac{1}{2\sqrt{2}} & -\frac{1}{2\sqrt{2}} & 1+\frac{1}{2\sqrt{2}} & 0 & -1 \\ -1 & 0 & 0 & 0 & 1 & 0 \\ 0 & 0 & 0 & -1 & 0 & 1 \end{array}\right] \begin{Bmatrix} u_3 \\ v_3 \\ u_1 = 0 \\ v_1 = 0 \\ u_2 = 0 \\ v_2 = 0 \end{Bmatrix} \tag{7c}$$

If the partitioned square (stiffness) matrix is designated by

$$\begin{bmatrix} A_{2\times 2} & B_{2\times 4} \\ B'_{4\times 2} & D_{4\times 4} \end{bmatrix}$$

expanding Eq. (7c) leads to the following two sets of equations:

$$\begin{Bmatrix} F_{x_3} \\ F_{y_3} \end{Bmatrix} = [A] \begin{Bmatrix} u_3 \\ v_3 \end{Bmatrix} \tag{8a}$$

and

$$\begin{Bmatrix} F_{x_1} \\ F_{y_1} \\ F_{x_2} \\ F_{y_2} \end{Bmatrix} = [B]' \begin{Bmatrix} u_3 \\ v_3 \end{Bmatrix} \tag{8b}$$

Eq. (8a) gives unknown node displacements in terms of applied forces,

$$\begin{Bmatrix} u_3 \\ v_3 \end{Bmatrix} = [A]^{-1} \begin{Bmatrix} F_{x_3} \\ F_{y_3} \end{Bmatrix} \tag{9a}$$

while Eq. (8b), together with Eq. (9a), gives unknown reactions in terms of applied forces,

$$\begin{Bmatrix} F_{x_1} \\ F_{y_1} \\ F_{x_2} \\ F_{y_2} \end{Bmatrix} = [B]' [A]^{-1} \begin{Bmatrix} F_{x_3} \\ F_{y_3} \end{Bmatrix} \tag{9b}$$

In dynamic analyses of aircraft structures it is ordinarily sufficient to determine $[A]^{-1}$. This is the flexibility matrix. It is interesting to note that $[A]$ can be found from the complete $[K]$ matrix by merely striking out columns and rows corresponding to zero displacements as prescribed by the support conditions.

A complete stress analysis leading to the truss member forces can also be carried out. It is merely necessary to know the force-deflection relations for the individual members, or components, of the structure. This is a straightforward problem for the truss and, therefore, will not be discussed further in this paper.

It is worth while to notice that once the stiffness matrix has been written, the solution follows by a series of routine matrix calculations. These are rapidly carried out on automatic digital computing equipment. Changes in design are taken care of by properly modifying the stiffness matrix. This cuts

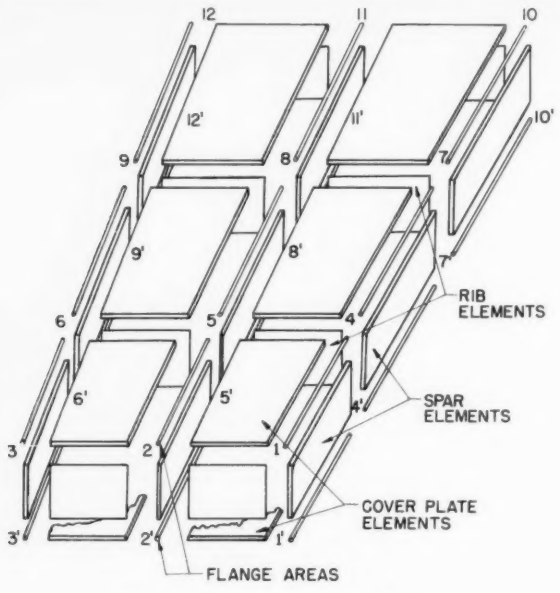

FIG. 3. Wing structure breakdown.

analysis time to a minimum, since development of the stiffness matrix is also a routine procedure. In fact, it may also be programmed for the digital computing machine.

(VII) SUMMARY—METHOD OF DIRECT STIFFNESS CALCULATION

(1) A complex structure must first be replaced by an equivalent idealized structure consisting of basic structural parts that are connected to each other at selected node points.

(2) Stiffness matrices must be either known or determined for each basic structural unit appearing in the idealized structure.

(3) While all other nodes are held fixed, a given node is displaced in one of the chosen coordinate directions. The forces required to do this and the reactions set up at neighboring nodes are then known from the various individual member stiffness matrices. These forces and reactions determine one column in the overall stiffness matrix. When all components of displacement at all nodes have been considered in this manner, the complete stiffness matrix will have been developed. In the general case, this matrix will be of order $3n \times 3n$, where n equals the number of nodes. The stiffness matrix so developed will be singular.

(4) Desired support conditions can be imposed by striking out columns and corresponding rows, in the stiffness matrix, for which zero displacements have been specified. This reduces the order of the stiffness matrix and renders it nonsingular.

(5) For any given set of external forces at the nodes, matrix calculations applied to the stiffness matrix then yield all components of node displacement plus the external reactions.

(6) Forces in the internal members can be found by applying the appropriate force-deflection relations.

The primary functions of the engineer will be to provide the information required in steps (1) and (2) above and to provide the individual member force-deflection relations if a stress analysis is to be carried out. Steps (3) through (6) can be performed by non-engineering trained personnel. Changes in design can be taken into account by correcting local stiffness contributions to K. Node densities can be increased in regions of maximum complexity and importance. If vertical deflections only are required, as in the case of the aircraft wing problem, the $3n \times 3n$ matrix for K can be reduced to order $n \times n$ by a sequence of matrix calculations. Physically, continuity of displacements in three directions at each node will still be maintained.

(VIII) STIFFENED SHELL STRUCTURES

In carrying the above procedure over to stiffened shell structures, it is first necessary to perform steps (1) and (2) of the previous outline.

For a wing structure the idealization will be made by replacing the actual structure by an assemblage of spar segments, rib segments, stiffeners, and cover plate elements, joined together at selected nodes. Fig. 3 shows the proposed idealized structure. The decomposition of the structure can be carried further with some increase in accuracy (for example, by decomposing spar segments into spar caps and shear webs), or it can be simplified by treating the structure as an assemblage of spars and torque boxes. The degree of breakdown should be consistent with the complexity of structural deformations required by the problem at hand. (In a vibration analysis the order of the highest mode is a determining factor.) In light of the proposed idealization, it is necessary that stiffness matrices be developed for the following components: beam segments consisting of flanges joined by thin webs, and plate elements of arbitrary shape. In addition, provision must be made for taking stiffeners into account and possibly for including the effect of sandwich type skin panels.

In the general case, spars will be swept, nonparallel, and not necessarily orthogonal to ribs. It will generally be convenient to transfer stiffness values for any given member to a fixed set of reference axes. These reference axes will be chosen as rectangular Cartesian (x, y, z) in order to preserve symmetry in the total K-matrix.

An outline of the determination of member stiffness for simple structural elements is given in the paper. Further details are presented in Appendixes. Derivation of stiffness matrices for more complex elements can be accomplished in a straightforward manner. However, in the analysis of an actual structure, it will be necessary to weigh the relative advantages of employing a small number of large complex elements against the advantages of using a larger number of small elements for which simple stiffness coefficients

may be employed. The main criterion to be observed in resolving this issue is that the problem must be programmed so that as much as possible of the data processing is performed automatically by the computer and not by human operators substituting in complex formulas.

(IX) Spars and Ribs

First we consider the untapered beam segment of uniform cross section shown in Fig. 4. Its stiffness matrix will be determined by application of beam theory, which is extended, however, to include shear web flexibility.

Nodes, 1, 1′, 2, and 2′ are established as shown in Fig. 4. The following notation is used:

I = moment of inertia of beam section about neutral (y) axis
$t_w = t$ = thickness of shear web
E = modulus of elasticity of flange material
G = modulus of rigidity of shear web material
ν = Poisson ratio

Displacements are assumed such as to be compatible with elementary beam theory. In other words,

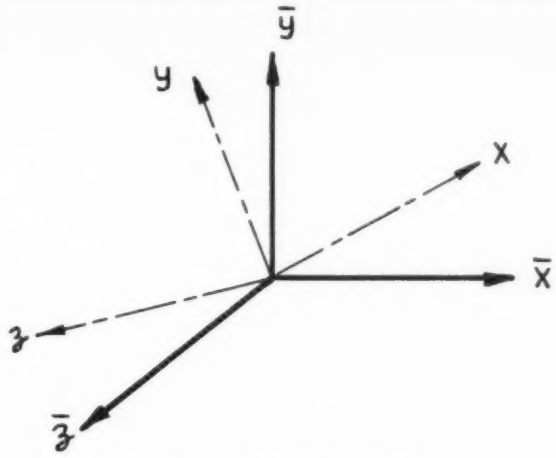

Fig. 5. Rectangular Cartesian axes systems.

$$\left.\begin{aligned} w_1 &= w_{1'}, & w_2 &= w_{2'} \\ u_1 &= -u_{1'}, & u_2 &= -u_{2'} \end{aligned}\right\} \tag{10}$$

Stiffness in the y-direction is assumed negligible.

An outline of the derivation of the stiffness matrix for the above beam segment is given in Appendix (A). It is shown to be of the form

$$[K] = \frac{6EI}{Lh^2(1+4n)} \begin{bmatrix} & u_1 & v_1 & w_1 & u_2 & v_2 & w_2 \\ & (4/3)\,(1+n) & & & & & \\ & 0 & 0 & & & & \\ & -(h/L) & 0 & h^2/L^2 & & & \\ & (2/3)\,(1-2n) & 0 & -(h/L) & (4/3)\,(1+n) & & \\ & 0 & 0 & 0 & 0 & 0 & \\ & h/L & 0 & -(h^2/L^2) & h/L & 0 & h^2/L^2 \end{bmatrix} \tag{11a}$$

where $$n = 3(E/G)\,[I/(htL^2)] \tag{11b}$$

Contribution of shear web deformation to the above stiffness matrix is indicated by values of $n > 0$; for a rigid shear web $n = 0$.

As a simple example of the use of the beam stiffness matrix, we consider a cantilever of length L and loaded by force P at the free end (nodes 1 and 1′). Putting $n = 0$ and applying Eq. (11a) gives:

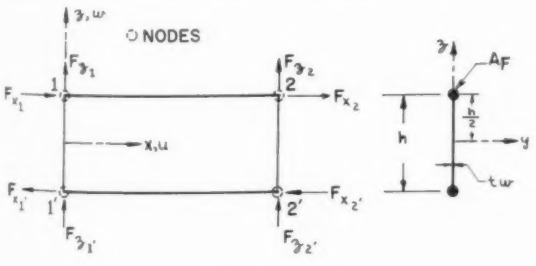

Fig. 4. Beam (spar or rib) segment.

$$\begin{Bmatrix} F_{z_1} \\ F_{z_2} \end{Bmatrix} = \frac{6EI}{L^3} \begin{bmatrix} 4 & L^2 & L \\ \frac{4}{3} & h^2 & \frac{L}{h} \\ \frac{L}{h} & & 1 \end{bmatrix} \begin{Bmatrix} u_2 \\ w_2 \end{Bmatrix} \tag{12}$$

Eq. (12) may be inverted to yield tip displacements u_1 and w_1 in terms of applied load P ($F_{x_1} = 0$, $F_{z_1} = P/2$). The results are

$$u_2 = -(PL^2/2EI)\,(h/2), \qquad w_2 = PL^3/3EI$$

which agree with known results.

In an actual wing structure, spar and rib segments will be more or less randomly oriented with respect to a set of standard reference axes. As a result, transformation of stiffness matrices for these members to the standard set of axes will generally be necessary. The basis for such transformations is given below.

Let the direction cosines of x, y, z-axes with respect to standard $\bar{x}$, $\bar{y}$, $\bar{z}$-axes, Fig. 5, be

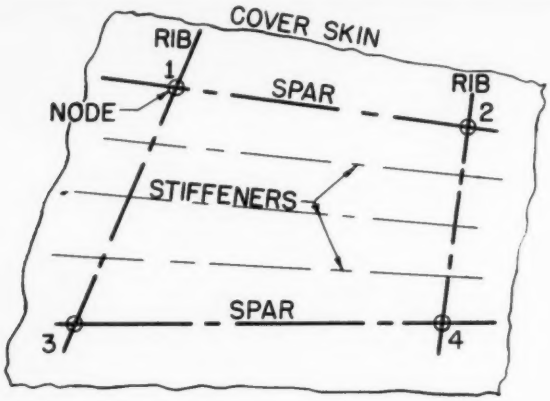

FIG. 6. Stiffened cover skin element.

	x	y	z
$\bar{x}$	λ_x	λ_y	λ_z
$\bar{y}$	μ_x	μ_y	μ_z
$\bar{z}$	ν_x	ν_y	ν_z

Simple geometrical considerations then give the following equation for relating forces in the x, y, z system to forces in the $\bar{x}$, $\bar{y}$, $\bar{z}$ system:

$$\begin{Bmatrix} F_{x_1} \\ F_{y_1} \\ F_{z_1} \\ F_{x_2} \\ F_{y_2} \\ F_{z_2} \end{Bmatrix} = \begin{bmatrix} \lambda_x & \lambda_y & \lambda_z & 0 & 0 & 0 \\ \mu_x & \mu_y & \mu_z & 0 & 0 & 0 \\ \nu_x & \nu_y & \nu_z & 0 & 0 & 0 \\ 0 & 0 & 0 & \lambda_x & \lambda_y & \lambda_z \\ 0 & 0 & 0 & \mu_x & \mu_y & \mu_z \\ 0 & 0 & 0 & \nu_x & \nu_y & \nu_z \end{bmatrix} \begin{Bmatrix} \bar{F}_{x_1} \\ \bar{F}_{y_1} \\ \bar{F}_{z_1} \\ \bar{F}_{x_2} \\ \bar{F}_{y_2} \\ \bar{F}_{z_2} \end{Bmatrix} \tag{13a}$$

or,

$$\{F\} = [\Phi] \{\bar{F}\} \tag{13b}$$

Displacements are vectors similarly related to the coordinate systems as forces and hence transform under a rotation of axes in the same manner. Consequently,

$$\{\delta\} = [\Phi] \{\bar{\delta}\} \tag{14}$$

where

$$\{\bar{\delta}\} = \begin{Bmatrix} \bar{u}_1 \\ \bar{v}_1 \\ \cdot \\ \cdot \\ \cdot \\ \bar{w}_2 \end{Bmatrix} \text{ etc.}$$

From the above and Eq. (3) it follows that,

$$[\bar{K}] = [\Phi] [K] [\Phi]^{-1} = [\Phi] [K] [\Phi]' \tag{15}$$

where $[\bar{K}]$ is the stiffness matrix referred to the standard $\bar{x}$, $\bar{y}$, $\bar{z}$ set of axes. Beam segments encountered in the analysis of real structures will be tapered in depth, and flange areas will be variable; generally the segments will be taken short enough so that the variation in depth may be assumed linear. Derivation of stiffness matrices for elements of this kind is straightforward, and details will not be included in the present paper.

(X) Stiffened Plates

(1) *Stiffeners*

A plan view of a typical portion of stiffened cover skin structure is shown in Fig. 6. Nodes are initially established at points 1, 2, 3, and 4. The included structure then consists of spar segments (1–2 and 3–4), rib segments (1–3 and 2–4), and stiffened plate element 1–2–3–4. Stiffeners may be conveniently lumped with spar caps and, if desired, into one or more equivalent stiffeners located between spars. In this latter event additional nodes must be established, as at the intersections of these equivalent stiffeners with the ribs. The stiffness matrix for a lumped stiffener of constant area A, length L, and modulus E is

$$[K]_{\text{stiffener}} = \frac{AE}{L} \begin{bmatrix} 1 & -1 \\ -1 & 1 \end{bmatrix} \tag{16}$$

Derivation of a similar matrix for a tapered member is straightforward; the area A is replaced by a suitable mean value. The influence of shear lag effects on load-deflection relations for the panel and stiffeners can only be included if nodes are established at intermediate points on the ribs, between spars.

(2) *Plate Stiffness*

The quadrilateral plate element 1–2–3–4 of Fig. 6 is assumed to possess in-plane stiffness only. Since two independent displacement components can occur at each node, the order of the K-matrix for this plate element will be 8×8. The problem of calculating K is not an easy one, and the solution offered here is felt to have potential usefulness for finding approximate solutions to many two-dimensional problems in elasticity.

Before proceeding with the method developed for calculating K of the plate element, it is pointed out that a so-called framework analogy[12] exists, which permits one to replace the elastic plate with a lattice of elastic bars. Under certain conditions the framework then deforms as does the plate and hence can be used to calculate the plate stiffness. The determination of a lattice representation for a rectangular plate is relatively straightforward; however, plate elements of nonrectangular form present basic difficulties. For example, if one attempts to apply the rectangular gridwork to a nonrectangular plate, difficulties arise in attempting to satisfy boundary conditions. On the other hand, if one goes to nonrectangular lattice forms, difficulties arise when attempting to satisfy the stress-strain relations in the interior of the plate. Considerations such as these led to eventual abandonment of this approach.

The concept finally employed for determining plate stiffness is based on approximating actual plate strains by a restricted strain representation. In other words, no matter what the actual strains in the plate may be, these will be approximated by a superposition of several simple strain states. The method for doing

this and the accuracy of results based on such a representation form an important portion of this paper.

To give an initial illustration, the actual strain distribution in a rectangular plate element can be approximated by superimposing the strains that correspond to each of the simple external load states shown in Fig. 7. These load states are seen to represent uniform and linearly varying stresses plus constant shear, along the plate edges. Later it will be seen that the number of load states must be $2n - 3$, where n = number of nodes.

Before commenting further on the scheme suggested here for analyzing plate elements, the method will be applied to the triangular plate of Fig. 8. The triangle is not only simpler to handle than the rectangle but later it will be used as the basic "building block" for calculating stiffness matrices for plates of arbitrary shape.

We start by assuming constant strains, or

$$\left.\begin{aligned} \epsilon_x &= a = (1/E)(\sigma_x - \nu\sigma_y) = \partial u/\partial x \\ \epsilon_y &= b = (1/E)(\sigma_y - \nu\sigma_x) = \partial v/\partial y \\ \gamma_{xy} &= c = (1/G)\tau_{xy} = (\partial u/\partial y) + (\partial v/\partial x) \end{aligned}\right\} \quad (17a)$$

Later it will be pointed out why we are restricted in the choice of strain expressions. Integrating we find the displacements to be

$$\left.\begin{aligned} u &= ax + Ay + B \\ v &= by + (c - A)x + C \end{aligned}\right\} \quad (17b)$$

where, A, B, and C are constants of integration which define rigid body translation and rotation of the triangle. Hence the triangle can displace as a rigid body in its own plane and undergo uniform straining according to Eq. (17a).

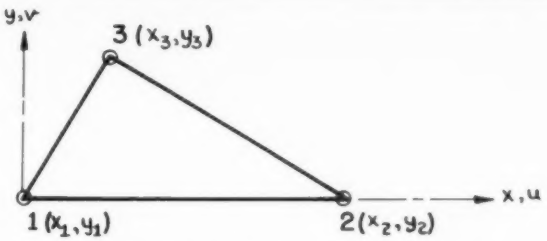

FIG. 8. Node designation for triangular plate element.

Displacements at the nodes can be determined by inserting applicable node coordinates into Eq. (17b). In this way six equations occur which are just sufficient for uniquely determining the six constants of Eq. (17b). As a result the constants become known in terms of node displacements and coordinates. It is this part of the solution which determines the number of terms which must be chosen in the strain expressions or alternatively the number of applied edge stress states which must be used. The number is always twice the number of nodes minus three. Hence, for the triangle we require three terms and five for the rectangle (or quadrilateral).

To proceed with the solution, we solve directly for stresses in terms of node displacements u_1, v_1, u_2, etc. If $x_{ij} = x_i - x_j$ and $\lambda_1 = (1 - \nu)/2$, this gives

$$\begin{Bmatrix} \sigma_x \\ \sigma_y \\ \tau_{xy} \end{Bmatrix} = \frac{E}{1-\nu^2} \begin{bmatrix} -\frac{1}{x_2} & \frac{\nu x_{32}}{x_2 y_3} & \frac{1}{x_2} & -\frac{\nu x_3}{x_2 y_3} & 0 & \frac{\nu}{y_3} \\ -\frac{\nu}{x_2} & \frac{x_{32}}{x_2 y_3} & \frac{\nu}{x_2} & -\frac{x_3}{x_2 y_3} & 0 & \frac{1}{y_3} \\ \frac{\lambda_1 x_{32}}{x_2 y_3} & -\frac{\lambda_1}{x_2} & -\frac{\lambda_1 x_3}{x_2 y_3} & \frac{\lambda_1}{x_2} & \frac{\lambda_1}{y_3} & 0 \end{bmatrix} \begin{Bmatrix} u_1 \\ v_1 \\ u_2 \\ v_2 \\ u_3 \\ v_3 \end{Bmatrix} \quad (18a)$$

or

$$\{\sigma\} = [S]\{\delta\} \quad (18b)$$

The next step is to obtain the concentrated forces at the nodes which are statically equivalent to the applied constant edge stresses. The procedure for doing this will be briefly illustrated for the case of the shear stress.

Fig. 9(a) shows the shear stresses on the circumscribed rectangular element, and Fig. 9(b) shows the corresponding edge shear forces on the triangle. As before x_i, y_i refer to coordinates of node points.

Forces on any edge are equally distributed between nodes lying on that edge. For the forces as given in Fig. 9(b), this leads to

$$\left.\begin{aligned} F_{x_1}^{(3)} &= -(x_2 - x_3)(t/2)\tau_{xy} \\ F_{y_1}^{(3)} &= -y_3(t/2)\tau_{xy} \\ F_{x_2}^{(3)} &= -x_3(t/2)\tau_{xy} \\ F_{y_2}^{(3)} &= +y_3(t/2)\tau_{xy} \\ F_{x_3}^{(3)} &= +x_2(t/2)\tau_{xy} \\ F_{y_3}^{(3)} &= 0 \end{aligned}\right\} \quad (19)$$

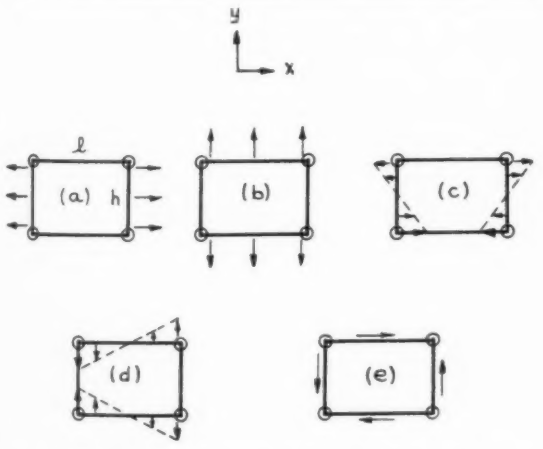

FIG. 7. Applied loads on edges of rectangular plate element.

where the superscript refers to case 3 (that of shear stress). This procedure is repeated for the two normal stresses. Superimposing results for these three cases then leads to the following system of equations for node forces in terms of applied edge stresses:

$$\begin{Bmatrix} F_{x_1} \\ F_{y_1} \\ F_{x_2} \\ F_{y_2} \\ F_{x_3} \\ F_{y_3} \end{Bmatrix} = \frac{t}{2} \begin{bmatrix} -y_3 & 0 & -(x_2 - x_3) \\ 0 & -(x_2 - x_3) & -y_3 \\ y_3 & 0 & -x_3 \\ 0 & -x_3 & y_3 \\ 0 & 0 & x_2 \\ 0 & x_2 & 0 \end{bmatrix} \begin{Bmatrix} \sigma_x \\ \sigma_y \\ \tau_{xy} \end{Bmatrix} \tag{20a}$$

or

$$\{F\} = [T]\{\sigma\} \tag{20b}$$

Substituting Eq. (18b) into Eq. (20b),

$$\{F\} = [T][S]\{\delta\} \tag{20c}$$

Comparing this last equation with Eq. (3) shows that

$$[K] = [T][S] \tag{21}$$

Carrying out the indicated matrix multiplication and putting $\lambda_2 = (1 + \nu)/2$ gives

$$[K]_{\substack{\text{Plate} \\ \text{(triangle)}}} = \frac{Et}{2(1 - \nu^2)} \begin{bmatrix} \frac{y_3}{x_2} + \frac{\lambda_1 x_{23}^2}{x_2 y_3} & & & & & \\ -\frac{\lambda_2 x_{32}}{x_2} & \frac{x_{23}^2}{x_2 y_3} + \frac{\lambda_1 y_3}{x_2} & & & & \\ -\frac{y_3}{x_2} + \frac{\lambda_1 x_3 x_{23}}{x_2 y_3} & \frac{\nu x_{32}}{x_2} + \frac{\lambda_1 x_3}{x_2} & \frac{y_3}{x_2} + \frac{\lambda_1 x_3^2}{x_2 y_3} & & & \\ \frac{\nu x_3}{x_2} + \frac{\lambda_1 x_{32}}{x_2} & \frac{x_3 x_{23}}{x_2 y_3} - \frac{\lambda_1 y_3}{x_2} & -\frac{\lambda_2 x_3}{x_2} & \frac{x_3^2}{x_2 y_3} + \frac{\lambda_1 y_3}{x_2} & & \\ -\frac{\lambda_1 x_{23}}{y_3} & -\lambda_1 & -\frac{\lambda_1 x_3}{y_3} & \lambda_1 & \frac{\lambda_1 x_2}{y_3} & \\ -\nu & -\frac{x_{23}}{y_3} & \nu & -\frac{x_3}{y_3} & 0 & \frac{x_2}{y_3} \end{bmatrix} \tag{22}$$

An alternative approach to the above method for calculating the plate stiffness matrix is to calculate the strain energy in the plate due to the assumed strain distribution and to then apply Castigliano's Theorem for finding the node forces. This procedure can also be conveniently carried out in terms of matrix operations; details will not be included here, however, since the result is the same as that already obtained.

Stiffness matrices for plates having four and more nodes have been derived and studied. The advantage in introducing additional nodes lies in the fact that a more general strain expression may then be employed—or equivalently additional load states as illustrated by Fig. 7 may be used for the plate. As a result a choice between two points of view may be adopted; first, the simplest or triangular plate stiffness matrix may be used and the desired accuracy obtained by using a sufficient number of subelements, or second, a more general plate stiffness matrix may be used with fewer subelements. Experience to date indicates that satisfactory results can be obtained using the triangular plate stiffness matrix.

Some additional plate stiffness matrices are given in Appendix (B).

To summarize briefly the meaning and significance of the plate stiffness matrix, it is first pointed out that this matrix relates node forces to node displacements. As a result the plate stiffness can be immediately added to spar, rib, etc., stiffnesses which are also given for specified nodal points. However, the plate node forces are statically equivalent to certain plate edge stresses. Furthermore, these edge stresses will tend to approach actual edge stresses, even of a complex nature, if sufficient subelements are used. A result of these equivalent edge stresses is that continuity will tend to be approximately maintained along common edges of subelements, between nodes. In other words, we are assuming that a plate under complex strains will deform in a manner that can be approximated by relatively simple strains acting on subelements into which the larger plate has been divided. The accuracy of this representation should increase as the number of subelements increases.

(3) *Quadrilateral Plates*

In the analysis of wings and tail surfaces it is generally convenient to employ a subdivision of cover plates such that most elements are of quadrilateral shape. The stiffness matrix for such elements can then be derived in one of two ways: (a) the previous solution demonstrated for the triangle can be extended to include the quadrilateral and (b) the quadrilateral can be subdivided into triangles and its stiffness matrix determined by superposition of the stiffnesses of the individual triangles. In this section the latter procedure will be adopted.

Two simple subdivisions of the quadrilateral into triangles are shown in Figs. 10(a) and 10(*b*). These lead to different stiffness matrices for the quadrilateral. A unique result is obtained by using the subelements shown in Fig. 10(c). The interior node will be located at the centroid, although any other choice could be used.

For the general quadrilateral plate it has proved to be preferable to program the calculation of the stiffness matrix for high-speed computing equipment. In the case of the rectangle, however, an explicit derivation can be readily carried out. The necessary calculations, included below, are given here, since the end result is useful and since these calculations serve to illustrate a step of some importance in carrying out the analysis of a more complete structure—for example, a wing or tail surface.

The rectangle and its four triangular subelements, with interior node number 5 at the centroid, is shown in Fig. 11. Stiffness matrices for the triangles can be calculated from Eq. (22), or more conveniently from Eq. (B-3) of Appendix (B). In determining K of the rectangle, superposition in the following form is used:

$$K_{\text{rectangle}} = K_{\text{I}} + K_{\text{II}} + K_{\text{III}} + K_{\text{IV}}$$

Since five nodes have been established, K for the rectangle will initially be of order 10×10. This will later be reduced to order 8×8 to give a result consistent with the choice of four external nodes; only at these external nodes is contact implied with adjoining structure. The immediate point is, however, that K for each triangle must be increased to order 10×10 before superposition is carried out. This is accomplished in the usual way—that is, by introducing appropriate rows and columns of zero elements.

In order to simplify the expressions for elements appearing in the stiffness matrices the derivation of K for the rectangle will be restricted to $\nu = 1/3$.

On superimposing stiffnesses for the component triangles of Fig. 11 it becomes possible to express Eq. (3) in the form

$$\begin{Bmatrix} F_{x_1} \\ F_{x_2} \\ F_{x_3} \\ F_{x_4} \\ F_{y_1} \\ F_{y_2} \\ F_{y_3} \\ F_{y_4} \\ \hline F_{x_5} \\ F_{y_5} \end{Bmatrix} = \left[\begin{array}{c|c} A_{8\times 8} & B_{8\times 2} \\ \hline B'_{2\times 8} & C_{2\times 2} \end{array}\right] \begin{Bmatrix} u_1 \\ u_2 \\ u_3 \\ u_4 \\ v_1 \\ v_2 \\ v_3 \\ v_4 \\ \hline u_5 \\ v_5 \end{Bmatrix} \tag{23}$$

Since forces are to be applied to the rectangle by stresses equivalent to forces acting at nodes 1, 2, 3, and 4, the condition

$$F_{x_5} = F_{y_5} = 0$$

can be applied to Eq. (23). Doing this results in the two sets of equations written below:

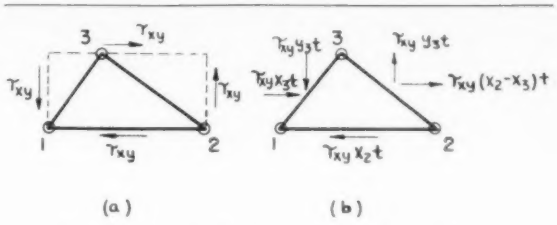

FIG. 9. Shear loading on triangular plate element.

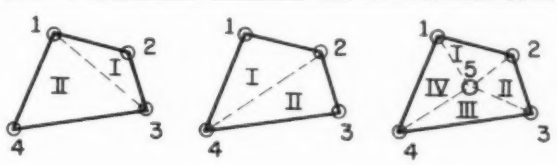

FIG. 10. Decomposition of quadrilateral plate into triangular subelements.

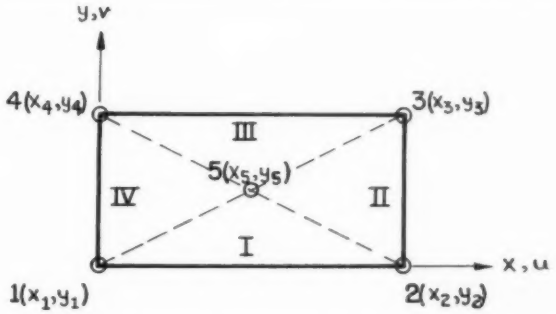

FIG. 11. Triangular subelements for rectangular plate.

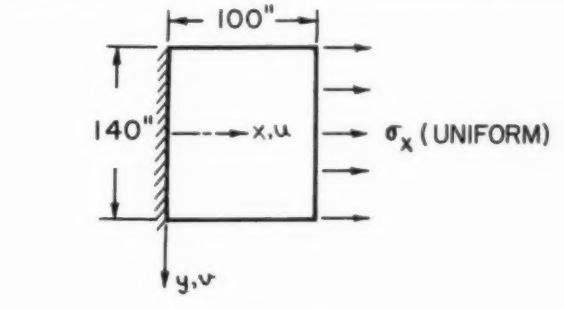

$t = 0.050$ IN.
$E = 10.5 \times 10^6$ PSI
$\nu = 1/3$
TOTAL LOAD = 2 LBS.

FIG. 12. Clamped rectangular plate subjected to uniform tensile loading.

$$\begin{Bmatrix} F_{x_1} \\ F_{x_2} \\ F_{x_3} \\ F_{x_4} \\ F_{y_1} \\ F_{y_2} \\ F_{y_3} \\ F_{y_4} \end{Bmatrix} = [A] \begin{Bmatrix} u_1 \\ u_2 \\ u_3 \\ u_4 \\ v_1 \\ v_2 \\ v_3 \\ v_4 \end{Bmatrix} + [B] \begin{Bmatrix} u_5 \\ v_5 \end{Bmatrix} \tag{24a}$$

$$\begin{Bmatrix} 0 \\ 0 \end{Bmatrix} = [B]' \begin{Bmatrix} u_1 \\ u_2 \\ u_3 \\ u_4 \\ v_1 \\ v_2 \\ v_3 \\ v_4 \end{Bmatrix} + [C] \begin{Bmatrix} u_5 \\ v_5 \end{Bmatrix} \tag{24b}$$

Solving Eq. (24b) for displacements at node 5 and substituting the result into Eq. (24a),

$$\begin{Bmatrix} F_{x_i} \\ F_{y_i} \end{Bmatrix} = ([A] - [B]\,[C]^{-1}\,[B]') \begin{Bmatrix} u_i \\ v_i \end{Bmatrix} \tag{25}$$

where $i = 1, 2, 3, 4$. Comparing Eq. (25) with Eq. (3) gives

$$[K]_{\text{rectangle}} = [A] - [B]\,[C]^{-1}\,[B]' \tag{26}$$

Carrying out the calculations required by Eq. (26) results in the following rectangular plate stiffness matrix:

$$[K]_{\text{rectangle}} = \frac{3Et}{16} \begin{bmatrix} K_{11} & K_{12} \\ K_{21} & K_{22} \end{bmatrix} \tag{27a}$$

where, when $m = (x_2 - x_1)/(y_4 - y_1)$,

$$K_{11} = \frac{1}{4} \begin{array}{c} \begin{matrix} u_1 & u_2 & u_3 & u_4 \end{matrix} \\ \begin{bmatrix} 3m + \frac{9}{m} & & & \\ m - \frac{9}{m} & 3m + \frac{9}{m} & & \\ -m - \frac{3}{m} & -3m + \frac{3}{m} & 3m + \frac{9}{m} & \\ -3m + \frac{3}{m} & -m - \frac{3}{m} & m - \frac{9}{m} & 3m + \frac{9}{m} \end{bmatrix} \end{array} + \frac{1}{3m + \frac{1}{m}} \begin{array}{c} \begin{matrix} u_1 & u_2 & u_3 & u_4 \end{matrix} \\ \begin{bmatrix} -1 & & & \\ 1 & -1 & & \\ -1 & 1 & -1 & \\ 1 & -1 & 1 & -1 \end{bmatrix} \end{array} \tag{27b}$$

$$K_{22} = \frac{1}{4} \begin{array}{c} \begin{matrix} v_1 & v_2 & v_3 & v_4 \end{matrix} \\ \begin{bmatrix} 9m + \frac{3}{m} & & & \\ 3m - \frac{3}{m} & 9m + \frac{3}{m} & & \\ -3m - \frac{1}{m} & -9m + \frac{1}{m} & 9m + \frac{3}{m} & \\ -9m + \frac{1}{m} & -3m - \frac{1}{m} & 3m - \frac{3}{m} & 9m + \frac{3}{m} \end{bmatrix} \end{array} + \frac{1}{m + \frac{3}{m}} \begin{array}{c} \begin{matrix} v_1 & v_2 & v_3 & v_4 \end{matrix} \\ \begin{bmatrix} -1 & & & \\ 1 & -1 & & \\ -1 & 1 & +1 & \\ 1 & -1 & 1 & -1 \end{bmatrix} \end{array} \tag{27c}$$

$$K_{12} = \begin{array}{c} \begin{matrix} v_1 & v_2 & v_3 & v_4 \end{matrix} \\ \begin{bmatrix} 1 & & & \\ 0 & -1 & & \\ -1 & 0 & 1 & \\ 0 & 1 & 0 & -1 \end{bmatrix} \end{array} \tag{27d}$$

$$K_{21} = K_{12}' \tag{27e}$$

If the order of v-terms in the above equations are rearranged from v_1, v_2, v_3, v_4 to v_1, v_4, v_3, v_2, it will be discovered that K_{22} equals K_{11} provided we replace m in K_{11} everywhere by $1/m$. The corresponding form for K_{12} may be written without difficulty. It is again pointed out that the above plate stiffness matrix is based on $\nu = 1/3$.

The process of eliminating displacements at node 5 is similar to the situation that arises when only w displacements are to be retained in a wing analysis. In this latter problem it then becomes necessary to eliminate all u and v components of displacement. The procedure for doing this is the same as that used in eliminating u_5 and v_5 from the above problem of the rectangular plate.

(4) *Example*

It is of interest to carry out calculations on a simple example and compare results obtained by applying the plate stiffness matrix with values that can be regarded as correct.

For this purpose the plate of Fig. 12 is analyzed using several different methods. Deflections at several points due to the indicated loading will be calculated. Since an exact solution is not available, correct displacements

TABLE 2

Solution No.	Method	Fig.	u_1	u_2	u_3	u_4	u_5	v_1	v_2	v_4
			Multiply all values by 10^{-6}							
1	Relaxation	13	2.703	2.607	2.703	1.391	1.248	0.686	−0.685	0.562
2	Simple theory	13	2.721	2.721	2.721	1.360	1.360	0.635	−0.635	
3	Plate K-matrix	13a	2.595		2.595			0.740	−0.740	
4	Plate K-matrix	13b	2.692	2.578	2.692	1.355	1.199	0.680	−0.680	0.568
5	Plate K-matrix	13c	2.718		2.697			0.686	−0.717	
6	Plate K-matrix	13d	2.714		2.712			0.688	−0.691	

will be taken as those calculated by applying the relaxation method to the fundamental equations governing this problem. Although details of these calculations are not presented, results are listed in Table 2.

The problem is interesting for at least two reasons. First, the accuracy obtainable using various numbers of subelements can be observed, and second, the effect of using random orientation of subelements—with respect to the plate edges—can be observed.

Results of all calculations are summarized in Table 2. Node locations and subelements are illustrated in Fig. 13.

In Table 2 the solution based on simple theory was obtained from $u = PL/AE$ and $\epsilon_y = -\nu\,\epsilon_x$. It is observed that on this basis both u_1 and v_1 agree quite well with the relaxation solution.

The crudest plate matrix solution is listed in Table 2 as Solution No. 3. It was obtained by considering the plate as a single element whose stiffness is given by Eq. (27). The results for u_1 and v_1 are seen to be reasonably good. Solution No. 4 considers the plate as consisting of four rectangular subelements as shown in Fig. 13(b). Again the stiffness matrix was obtained by using Eq. (27), this time for each subelement. Agreement with relaxation results is seen to be satisfactory, particularly in regard to u_1. Also the differences between u_1 and u_2 are approximated accurately by this solution. It is to be remembered that the actual strain distribution in the plate is complex in nature.

Solutions 5 and 6 in Table 2 were carried out in a matter of minutes on a high-speed digital computer. Each subquadrilateral was considered as consisting of four triangles in a manner analogous to the treatment described previously for the rectangle of Fig. 11. In Solution No. 5 we note that u_1 and u_3 are not equal, a consequence of the random nature of orientation of the subelements. By increasing the number of random subelements as in Solution No. 6, this lack of symmetry in results is virtually removed. Comparison with relaxation values is seen to be very good for both Solutions 5 and 6.

A more comprehensive example is given in the next section of the paper.

(XI) Analysis of Box Beam

As a final example, the box beam of Fig. 14 will be analyzed for deflections, using the stiffness matrices previously derived.

The box is uniform in section, unswept, and contains a rib at the unsupported end. The following dimensions apply: $a/b = \pi$, $2b/h = 10$, $t_c = t_w = t = 0.05$ in., $A_F = bt/2$, $a = 400$ in.

As the simplest possible breakdown, we consider the box to consist of two spars, one rib, and two cover skins. The nodes are then as shown in Fig. 15. Forces may be applied at the nodes at the free end. Two cases will be investigated: (1) up loads at each spar (bending) and (2) up load on one spar and a down load at the other spar (twisting).

The spar matrix is given by Eq. (11a). Calculation shows it to be

$$[K]_{\text{spar}} = \frac{Et}{2}\begin{array}{c} \\ u_1 \text{ or } u_2 \\ w_1 \text{ or } w_2 \\ u_3 \text{ or } u_4 \\ w_3 \text{ or } w_4 \end{array}\begin{array}{c} \begin{array}{cccc} u_1 \text{ or } u_2 & w_1 \text{ or } w_2 & u_3 \text{ or } u_4 & w_3 \text{ or } w_4 \end{array} \\ \begin{bmatrix} 1.13903 & & & \\ 0.05227 & 0.00333 & & \\ 0.50303 & 0.05227 & 1.13903 & \\ -0.05227 & -0.00333 & -0.05227 & 0.00333 \end{bmatrix} \end{array} \tag{28}$$

Cover plate stiffness is given by Eq. (27a) and for this case becomes

$$[K]_{\substack{\text{cover}\\ \text{plate}}} = \frac{Et}{2}\begin{array}{c} \\ u_1 \\ v_1 \\ u_2 \\ v_2 \\ u_3 \\ v_3 \\ u_4 \\ v_4 \end{array}\begin{array}{c} \begin{array}{cccccccc} u_1 & v_1 & u_2 & v_2 & u_3 & v_3 & u_4 & v_4 \end{array} \\ \begin{bmatrix} 0.90878 & & & & & & & \\ -0.37500 & 1.39778 & & & & & & \\ -0.19329 & 0 & 0.90879 & & & & & \\ 0 & -1.15928 & 0.37500 & 1.39778 & & & & \\ -0.31916 & 0 & -0.39634 & -0.37500 & 0.90879 & & & \\ 0 & 0.37109 & -0.37500 & -0.60959 & 0.37500 & 1.39778 & & \\ -0.39634 & 0.37500 & -0.31916 & 0 & -0.19329 & 0 & 0.90879 & \\ 0.37500 & -0.60959 & 0 & 0.37109 & 0 & -1.15928 & -0.37500 & 1.39778 \end{bmatrix} \end{array} \tag{29}$$

The rib has not been defined as yet. Two possible rib configurations will be analyzed in this paper. In the first case, the rib is considered as a beam identical in section to the spar. This leads to the following stiffness matrix for the rib:

$$[K]_{\text{rib}} = \frac{Et}{2}\begin{array}{c} \\ v_1 \\ w_1 \\ v_2 \\ w_2 \end{array}\begin{array}{c} \begin{array}{cccc} v_1 & w_1 & v_2 & w_2 \end{array} \\ \begin{bmatrix} 0.13086 & & & \\ -0.00976 & 0.00098 & & \\ 0.06413 & -0.00976 & 0.13086 & \\ 0.00976 & -0.00098 & 0.00976 & 0.00098 \end{bmatrix} \end{array} \tag{30a}$$

In the second case, the rib is treated as a flat plate. The general stiffness matrix which has been derived for a rectangular flat plate is of order 8×8. However, in the present instance, the following conditions must be introduced to insure compatibility with the other portions of the structure (see Fig. 15 for subscript locations):

$$w_1 = w_{1'} \qquad v_1 = -v_{1'}$$
$$\text{and}$$
$$w_2 = w_{2'} \qquad v_2 = -v_{2'}$$

and, likewise, for the forces

$$F_{z_1} = F_{z_{1'}} \qquad F_{y_1} = -F_{y_{1'}}$$
$$\text{and}$$
$$F_{z_2} = F_{z_{2'}} \qquad F_{y_2} = -F_{y_{2'}}$$

Treating the rib as a flat plate ($t = 0.050$ in.) and applying the above conditions leads to the following rib stiffness matrix:

$$[K]_{\text{rib}} = \frac{Et}{2}\begin{array}{c} \\ v_1 \\ w_1 \\ v_2 \\ w_2 \end{array}\begin{array}{c} \begin{array}{cccc} v_1 & w_1 & v_2 & w_2 \end{array} \\ \begin{bmatrix} 5.65088 & & & \\ -0.37500 & 0.03754 & & \\ 1.84181 & -0.37500 & 5.65088 & \\ 0.37500 & -0.03754 & 0.37500 & 0.03754 \end{bmatrix} \end{array} \tag{30b}$$

It is anticipated that the choice of rib will have little effect on deflections due to the bending-type loading and a more pronounced effect on the twisting-type loading.

Using the same technique as described for the simple truss, it is now a straightforward matter to form the stiffness matrix for the complete box. Advantage can be taken of the following: (1) structural symmetry that exists for the box with respect to the xy-midplane and (2) restriction in this problem to loads that act normal to this plane. Under these conditions each pair of upper and lower surface nodes will experience, in addition to equal vertical deflections, equal but opposite displacements with respect to the xy-midplane. In other words, the box will deflect in the sense of a conventional beam. The spar and rib stiffness matrices already provide for such elastic behavior. The plate stiffness matrices make no distinction, other than in the sign of the node forces, for a reversal in direction of node displacement. Consequently, if the normal loading is carried equally by upper and lower nodes, only the upper set will need be considered when forming the box stiffness matrix. Due to the division of loading, correct deflections will result. In this manner the stiffness matrix for the box is found to be [Eq. (30a) used for rib stiffness]

$$[K]_{\text{box}} = \frac{Et}{2}\begin{array}{c} \\ u_1 \\ v_1 \\ w_1 \\ u_2 \\ v_2 \\ w_2 \end{array}\begin{array}{c} \begin{array}{cccccc} u_1 & v_1 & w_1 & u_2 & v_2 & w_2 \end{array} \\ \begin{bmatrix} 2.04782 & & & & & \\ -0.37500 & 1.52864 & & & & \\ -0.05227 & -0.00976 & 0.00430 & & & \\ -0.19329 & 0 & 0 & 2.04782 & & \\ 0 & -1.09515 & -0.00976 & 0.37500 & 1.52864 & \\ 0 & 0.00976 & -0.00098 & -0.05227 & 0.00976 & 0.00430 \end{bmatrix} \end{array} \tag{31}$$

The inverse of this matrix is the flexibility matrix.

$$[K]^{-1}_{\text{box}} = [C] = \frac{2}{Et}\begin{array}{c} \\ F_{x_1} \\ F_{y_1} \\ F_{z_1} \\ F_{x_2} \\ F_{y_2} \\ F_{z_2} \end{array}\begin{array}{c} \begin{array}{cccccc} F_{x_1} & F_{y_1} & F_{z_1} & F_{x_2} & F_{y_2} & F_{z_2} \end{array} \\ \begin{bmatrix} 0.81646 & & & & & \\ 0.22705 & 1.66224 & & & & \\ -10.47344 & 2.72965 & 409.39998 & & & \\ 0.20384 & -0.08123 & -5.55027 & 0.81646 & & \\ 0.08123 & 1.26026 & 5.01982 & -0.22705 & 1.66224 & \\ -5.55027 & -5.01982 & 142.67751 & -10.47344 & -2.72965 & 409.39998 \end{bmatrix} \end{array} \tag{32}$$

From the flexibility matrix, deflections due to applied loads can be found at once. For the two cases of applied loadings we find the following (rib treated as beam).

Case 1 (bending):

Forces of 1 lb. acting upward at each spar (nodes 1 and 2).

$$w_1 = 11{,}041.55/E \qquad u_1 = -320.47/E \qquad v_1 = -45.80/E$$
$$w_2 = 11{,}041.55/E \qquad u_2 = -320.47/E \qquad v_2 = 45.80/E$$

Case 2 (twisting):

Force of 1 lb. upward at node 1 and 1 lb. downward at node 2.

$$w_1 = 5{,}334.45/E \qquad u_1 = -98.46/E \qquad v_1 = 154.99/E$$
$$w_2 = -5{,}334.45/E \qquad u_2 = 98.46/E \qquad v_2 = 154.99/E$$

Similar results may be calculated for the case when the rib is assumed as a plate. Complete details are not given. In bending we get $w_1 = 10{,}888.12/E$, $u_1 = -310.56/E$, and $v_1 = -18.25/E$. Twisting results are $w_1 = 3615.72/E$, $u_1 = -25.84/E$, and $v_1 = 349.52/E$.

It is now advisable to select additional nodes and recalculate the previous deflection data. When added nodes have little effect on results, the process can be considered to have converged. Whether convergence be to the correct values requires additional information. These questions are now examined.

First, solutions are found for the node patterns shown in Fig. 16. Vertical deflections at node 1 for bending-type loading are as follows:

Fig. 16(a) $w_1 = 8558.0/E$

Fig. 16(b) $w_1 = 8591.2/E$

Fig. 16(c) $w_1 = 8548.4/E$

It is seen that the change in w_1 in going from the node pattern of Fig. 16(b) to 16(c) is about 1/2 per cent. Consequently convergence can be assumed to have been attained with the solution found from Fig. 16(b).

Obviously the first solution, based on Fig. 15, is in considerable error. This is due to the poor tie between spars and cover plate. Fig. 16(a) introduces an additional tie between these two components. The decreased value of w_1 for this case therefore reflects the added stiffness due to including the two nodes at the mid-span location.

An unexpected result is the close agreement between the solutions based on Figs. 16(a) and 16(b). In fact it would seem reasonable to expect Fig. 16(b) to lead to a smaller value for w_1 than that given by Fig. 16(a). Careful scrutiny, however, indicates that these results are quite reasonable. Whereas the node pattern of Fig. 16(b) accounts for shear lag in the cover plate, this is not the case with Fig. 16(a). As a result, the added stiffness in Fig. 16(b), due to the additional nodes connecting spars and cover skins, is offset by the added flexibility introduced by shear lag in cover skins. The results indicate these factors to be nearly equal; hence the reason for the nearly correct values given by Fig. 16(a).

Fig. 16(c) allows for shear lag and, at the same time, provides for adequate tie between spars and cover plates. It can therefore be felt that this node pattern will give final results which represent convergence of the method. As mentioned previously, this is substantiated by comparison with values obtained from Fig. 16(b).

There remains the question as to what is the correct value for w_1 for this problem. Elementary beam theory gives $w_1 = 6{,}900/E$, and, if extended to include shear distortion of spar webs, gives $w_1 = 7{,}740/E$. Using Reissner's shear lag theory,[13] the tip deflection is obtained as $w_1 = 7{,}900/E$. Finally if Reissner's shear lag theory is modified to include spar shear web deformation, the result is $w_1 = 8{,}740/E$. This is the most accurate theory available. It agrees to approximately 2 per cent with the numerical solution based on stiffness matrices.

The pronounced shear lag effect in this problem and its marked influence on the vertical tip deflection are significant. It is precisely this effect that produces a very complex stress distribution in the cover skins. Nevertheless the plate stiffness matrix developed in Eq. (27a) and based on triangular subelements represents this stress pattern with gratifying effectiveness.

The solution for the node pattern of Fig. 16(c) was obtained in a few minutes by utilizing a program for a high-speed digital computer that computed individual plate and spar stiffnesses and then combined these into the stiffness matrix for the complete box.

(XII) Reduction in Order of Stiffness Matrix

(1) *Eliminating Components of Node Displacement*

In an actual problem—as a wing analysis—the number of nodes to be used can become quite large. If, for purposes of discussion, 50 nodes are assumed, the stiffness matrix becomes of order 150 × 150. By eliminating u and v components of displacement at each node, the stiffness matrix can be reduced to order 50 × 50. However, this reduction process [see treatment of Eq. (23), for example] can require the calculation of the inverse of a 100 × 100 matrix. Such calculations are best avoided at present.

The problem that arises in eliminating the u and v components can be handled satisfactorily in any one of several ways. First, the calculation of the inverse of a large-order matrix can be avoided by eliminating a single component at a time. This is a practical expedient when automatic digital computing equipment

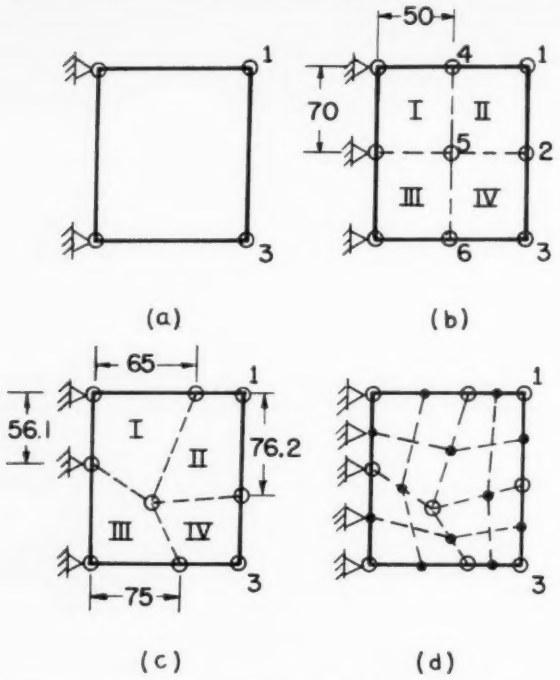

FIG. 13. Nodes and supports for clamped rectangular plate.

is available. Second, in some cases it may be feasible to eliminate "blocks" of u and v components at a time, thereby reducing the order of matrices to be inverted at any one time to a reasonable size (say 20×20). Third, the analysis can be carried out for sections of the structure, taken one by one. For each section, as a spanwise portion of the wing, the complete stiffness matrix can be determined. Elimination of u and v components can then be carried out at any selected nodes, except those common to two distinct sections of the structure. Each section can be treated in this manner. By properly adding the individual section stiffness matrices, the total stiffness matrix can be obtained. Finally u and v displacements at nodes where the sections join together can be eliminated. The stiffness matrix that remains will apply to w deflections only.

From a practical standpoint, the method just described has several worth-while features. For example all components of displacement at a given node may be eliminated. This can be useful when additional nodes are felt to be necessary in order to account properly for regions of maximum structural complexity. Even though eventually eliminated, these nodes will have contributed to the elements retained in the stiffness matrix.

(2) *Inversion of Stiffness Matrix*

Ordinarily, only the first few low-order vibration nodes and frequencies are required for the purpose of carrying out subsequent dynamic analyses. Using the stiffness matrix directly in the matrix iteration method leads to the highest frequency and corresponding mode. If the order of the stiffness matrix is high (say, 50×50), it becomes impractical to eliminate successively the higher modes and so eventually obtain the lowest modes.

Inversion of the stiffness matrix leads to the flexibility matrix. This matrix used in the matrix iteration procedure yields results for the lowest mode. Therefore, it is ordinarily preferable to know the flexibility matrix.

If the stiffness matrix is of high order (say, 50×50), inverting it becomes a major problem in itself. This can be overcome to some extent by employing the capabilities of present-day digital computing equipment. However, in many instances an alternative procedure may either be useful or necessary. Consequently, a possible approach to overcoming this difficulty will be outlined here.

The proposed method consists of converting the original stiffness matrix K into a lower order stiffness matrix K^*. This is accomplished by introducing a set of generalized coordinates which are related to the original displacements (on which K is based) through a set of appropriately chosen functions. The accuracy inherent in K will have a direct influence on K^*.

Suppose K is known for the cantilever beam of Fig. 17. The order of K is 10×10. Now assume a set of polynomials of the form

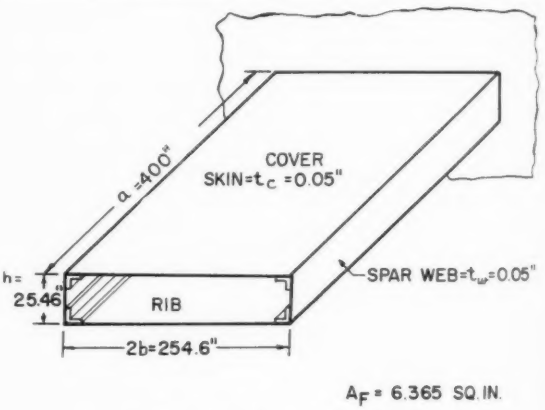

FIG. 14. Cantilevered box beam.

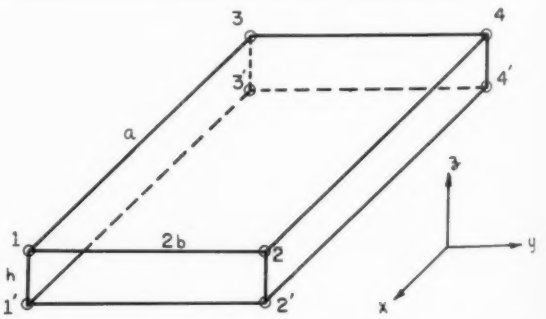

FIG. 15. Simplest node pattern for box beam.

$$\begin{aligned} P_1(x) &= a_1x^2 + b_1x^3 + c_1x^4 \\ P_2(x) &= a_2x^2 + b_2x^3 + c_2x^4 \\ &\cdot \\ &\cdot \\ P_5(x) &= a_5x^2 + b_5x^3 + c_5x^4 \end{aligned} \tag{33}$$

Each of these will be made to satisfy the boundary conditions of the cantilever which are,

$$P_i(0) = P_i'(0) = P_i''(L) = P_i'''(L) = 0$$

Applying these conditions results in

$$\begin{aligned} P_1(x) &= 6(x/L)^2 - 4(x/L)^3 + (x/L)^4 \\ P_2(x) &= 20(x/L)^2 - 10(x/L)^3 + (x/L)^5 \\ &\cdot \\ &\cdot \\ P_5(x) &= 140(x/L)^2 - 56(x/L)^3 + (x/L)^8 \end{aligned} \tag{34}$$

We now introduce generalized coordinates q_i which are related to the displacements y_i through the above polynomials. This relationship is established through the equations

$$\begin{Bmatrix} y_1 \\ y_2 \\ \cdot \\ \cdot \\ \cdot \\ \cdot \\ \cdot \\ \cdot \\ y_{10} \end{Bmatrix} = \begin{bmatrix} P_1(x_1) & P_2(x_1) & \cdot & \cdot & P_5(x_1) \\ P_1(x_2) & P_2(x_2) & \cdot & \cdot & P_5(x_2) \\ & & \cdot & & \\ & & \cdot & & \\ & & \cdot & & \\ & & \cdot & & \\ & & \cdot & & \\ & & \cdot & & \\ P_1(x_{10}) & P_2(x_{10}) & \cdot & \cdot & P_5(x_{10}) \end{bmatrix} \begin{Bmatrix} q_1 \\ q_2 \\ q_3 \\ q_4 \\ q_5 \end{Bmatrix} \tag{35}$$

It is seen that the ten displacements $y_1, y_2, \ldots, y_{10}$ are to be replaced by the five coordinates $q_1, q_2, \ldots, q_5$.

The free vibration problem for the cantilever can be set up in terms of kinetic and potential energies. In terms of original displacements $y_1, y_2, \ldots, y_{10}$, these energies are, respectively,

$$\left.\begin{aligned} T &= (1/2)\,\{\dot{y}\}'\,[M]\,\{\dot{y}\} \quad \text{and} \\ V &= (1/2)\,\{y\}'\,[K]\,\{y\} \end{aligned}\right\} \tag{36}$$

where $[M]$ is the inertia (mass) matrix and $[K]$ the original 10×10 stiffness matrix.

Writing Eq. (35) as

$$\{y\} = [P]\,\{q\}$$

and substituting into Eqs. (36),

$$\begin{aligned} T &= (1/2)\,\{\dot{q}\}'\,[P]'\,[M]\,[P]\,\{\dot{q}\} \\ V &= (1/2)\,\{q\}'\,[P]'\,[K]\,[P]\,\{q\} \end{aligned}$$

from which we define

$$\left.\begin{aligned} [K^*] &= [P]'\,[K]\,[P] \\ [M^*] &= [P]'\,[M]\,[P] \end{aligned}\right\} \tag{37}$$

If K is of order 10×10 and P of order 10×5, K^* will be of order 5×5. The vibration analysis is now performed using K^* and M^*. By inverting K^* the lower modes can be calculated directly. Or alternatively, K^* can be used and all modes and frequencies determined, starting with the highest. This is feasible if K^* is of sufficiently low order (say, 10×10).

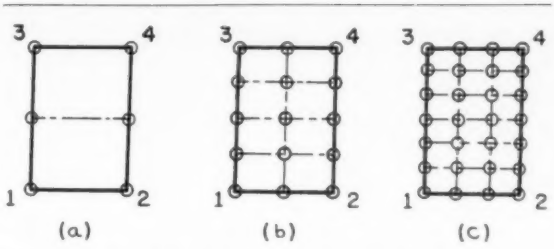

FIG. 16. Additional node patterns for box beam.

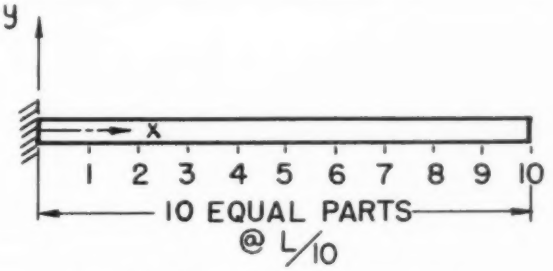

FIG. 17. Station selections on cantilever beam.

This process can be modified in several respects, and the purpose here is not to give an exhaustive treatment but rather to simply point out a possible approach to the problem. Preliminary calculations indicate that the idea may possess practical value. Extension to a two-dimensional grid can be made by generalizing the procedure suggested above.

APPENDIX (A)

Derivation of Spar Stiffness Matrix

The structure and notation are described in Section (IX) and Fig. 4.

Flanges are assumed to carry axial stresses, while the web carries shear stresses. Cover plate material is not included as part of spar flanges. Derivation below is based on conventional beam theory.

Case 1

$u_1 = -u_1' \neq 0$; all other components of node displacement for the beam = 0.

The deflected beam and necessary forces and reactions are shown in Fig. A-1. Due to forces F_x at the left end, the beam deflects upward. The F_z forces cause a downward deflection. Beam theory, including effects of uniformly distributed shear in web, gives

$$w = \frac{F_{x_1}hL^2}{2EI} + \frac{2F_{z_1}L^3}{3EI}(1 + n) \tag{A-1}$$

$$\theta = \frac{F_{x_1}hL}{(EI)} + \frac{F_{z_1}L^2}{(EI)} \tag{A-2}$$

where w and θ are deflection and slope at the left end of

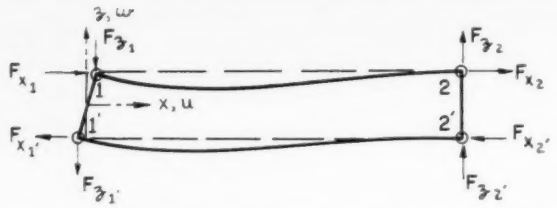

FIG. A-1. First beam displacement required in developing beam stiffness matrix.

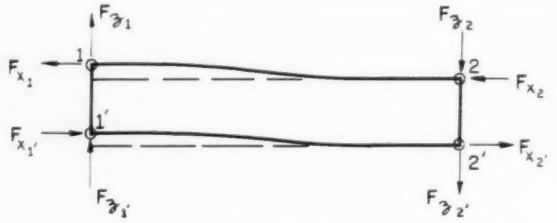

FIG. A-2. Second beam displacement required in developing beam stiffness matrix.

the beam, respectively, and n is given by Eq. (11b). Due to boundary conditions, $w = 0$; also, from the geometry of the deflected beam, $\theta = 2u_1/h$. Using these relations in Eqs. (A-1) and (A-2) and solving for forces gives

$$F_{x_1} = \frac{8EI}{h^2L}\frac{1+n}{1+4n}u_1 = \frac{6EI}{Lh^2(1+4n)}\frac{4}{3}(1+n)\,u_1 \tag{A-3}$$

$$F_{z_1} = -\frac{6EI}{hL^2}\frac{1}{1+4n}u_1 = -\frac{6EI}{Lh^2(1+4n)}\frac{h}{L}u_1 \tag{A-4}$$

Forces at node 2 follow from equilibrium considerations. They are

$$F_{x_2} = \frac{4EI}{h^2L}\frac{1-2n}{1+4n}u_1 = \frac{6EI}{Lh^2(1+4n)}\frac{2}{3}(1-2n)\,u_1 \tag{A-5}$$

$$F_{z_2} = -F_{z_1} \tag{A-6}$$

The above forces represent the first column of the required stiffness matrix. The other columns are found in a similar manner. When $w_1 = w_{1'} \neq 0$, while all other nodes are held fixed, the forces of Fig. A-2 apply.

Forces due to displacements imposed on the right-hand end of the beam may be written from the above results by analogy. The final spar stiffness matrix is given as Eq. (11a).

APPENDIX (B)

PLATE STIFFNESS MATRICES

Several plate stiffness matrices are given here without derivation.

(1) *Triangle—Arbitrary Node Locations*

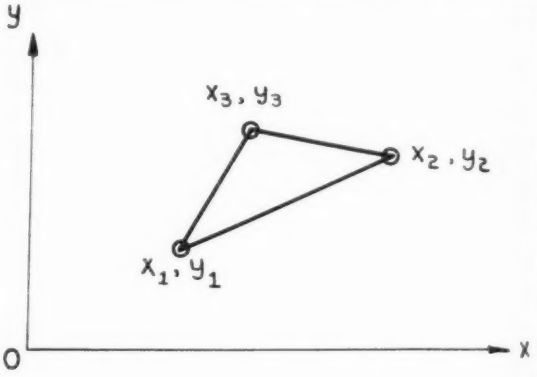

FIG. B-1. Triangular plate element with arbitrary node locations.

The stiffness matrix will be defined with respect to the equation

$$\begin{Bmatrix} F_{x_1} \\ F_{y_1} \\ F_{x_2} \\ F_{y_2} \\ F_{x_3} \\ F_{y_3} \end{Bmatrix} = [K] \begin{Bmatrix} u_1 \\ v_1 \\ u_2 \\ v_2 \\ u_3 \\ v_3 \end{Bmatrix} \tag{B-1}$$

Again adopting the notation

$$x_{ij} = x_i - x_j, \quad \lambda_1 = (1-\nu)/2, \quad \lambda_2 = (1+\nu)/2 \tag{B-2}$$

we get

$$[K] = \frac{Et}{2}\phi \begin{bmatrix} \lambda_1 x_{23}^2 + y_{23}^2 & & & & & \\ \lambda_2 x_{32}y_{23} & x_{23}^2 + \lambda_1 y_{23}^2 & & & & \\ \lambda_1 x_{23}x_{31} + y_{23}y_{31} & \lambda_1 x_{13}y_{23} + \nu x_{32}y_{31} & \lambda_1 x_{31}^2 + y_{31}^2 & & & \\ \lambda_1 x_{32}y_{31} + \nu x_{13}y_{23} & x_{23}x_{31} + \lambda_1 y_{23}y_{31} & \lambda_2 x_{13}y_{31} & x_{31}^2 + \lambda_1 y_{31}^2 & & \\ \lambda_1 x_{12}x_{23} + y_{12}y_{23} & \lambda_1 x_{21}y_{23} + \nu x_{32}y_{12} & \lambda_1 x_{12}x_{31} + y_{12}y_{31} & \lambda_1 x_{21}y_{31} + \nu x_{13}y_{12} & \lambda_1 x_{12}^2 + y_{12}^2 & \\ \lambda_1 x_{32}y_{12} + \nu x_{21}y_{23} & x_{12}x_{23} + \lambda_1 y_{12}y_{23} & \lambda_1 x_{13}y_{12} + \nu x_{21}y_{31} & x_{12}x_{31} + \lambda_1 y_{12}y_{31} & \lambda_2 x_{21}y_{12} & x_{12}^2 + \lambda_1 y_{12}^2 \end{bmatrix} \tag{B-3}$$

where

$$\phi = \frac{1/(1-\nu^2)}{x_{21}y_3 + x_{13}y_2 + x_{32}y_1}$$

(2) ***Rectangle***

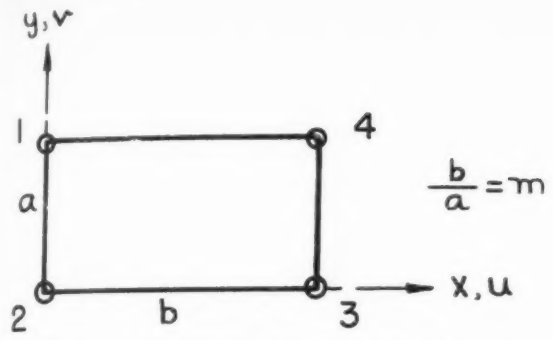

FIG. B-2. Node locations for rectangular plate element.

The stiffness matrix given below for the rectangle is based on the load states shown in Fig. 7. As a result this matrix is more general than that given in Eq. (27) due to the inclusion of linear terms in the strain expressions.

Again the stiffness matrix is arranged to agree with the equation

$$\begin{Bmatrix} F_{x_1} \\ F_{y_1} \\ F_{x_2} \\ F_{y_2} \\ F_{x_3} \\ F_{y_3} \\ F_{x_4} \\ F_{y_4} \end{Bmatrix} = [K] \begin{Bmatrix} u_1 \\ v_1 \\ u_2 \\ v_2 \\ u_3 \\ v_3 \\ u_4 \\ v_4 \end{Bmatrix} \tag{B-4}$$

in which $[K]$ is given by

$$[K] = \frac{Et}{8(1-\nu^2)} \begin{array}{c} \begin{matrix} u_1 & v_1 & u_2 & v_2 & u_3 & v_3 & u_4 & v_4 \end{matrix} \\ \begin{bmatrix} a_1+b_1 & & & & & & & \\ 1+\nu & a_2+b_2 & & & & & & \\ a_1-b_1 & 1-3\nu & a_1+b_1 & & & & & \\ 3\nu-1 & c_2-a_2 & -1-\nu & a_2+b_2 & & & & \\ -a_1-c_1 & -1-\nu & c_1-a_1 & 1-3\nu & a_1+b_1 & & & \\ -1-\nu & -a_2-c_2 & 3\nu-1 & a_2-b_2 & 1+\nu & a_2+b_2 & & \\ c_1-a_1 & 3\nu-1 & -a_1-c_1 & 1+\nu & a_1-b_1 & 1-3\nu & a_1+b_1 & \\ 1-3\nu & a_2-b_2 & 1+\nu & -a_2-c_2 & 3\nu-1 & c_2-a_2 & -1-\nu & a_2+b_2 \end{bmatrix} \end{array} \tag{B-5}$$

where, in the above matrix,

$$\begin{aligned} a_1 &= m(1-\nu), & b_1 &= (2/3m)(4-\nu^2), & c_1 &= (2/3m)(2+\nu^2) \\ a_2 &= (1-\nu)/m, & b_2 &= (2m/3)(4-\nu^2), & c_2 &= (2m/3)(2+\nu^2) \end{aligned} \tag{B-6}$$

$$m = l/h \qquad \text{(see Fig. 7)} \tag{B-7}$$

Eq. (B-5) simplifies to the following if $\nu = 1/3$:

$$[K] = \frac{Et}{96} \begin{array}{c} \begin{matrix} u_1 & v_1 & u_2 & v_2 & u_3 & v_3 & u_4 & v_4 \end{matrix} \\ \begin{bmatrix} \varphi_1(m) & & & & & & & \\ 18 & \varphi_1(1/m) & & & & & & \\ \varphi_2(m) & 0 & \varphi_1(m) & & & & & \\ 0 & \varphi_2(1/m) & -18 & \varphi_1(1/m) & & & & \\ \varphi_4(m) & -18 & \varphi_3(m) & 0 & \varphi_1(m) & & & \\ -18 & \varphi_4(1/m) & 0 & \varphi_2(1/m) & 18 & \varphi_1(1/m) & & \\ \varphi_3(m) & 0 & \varphi_4(m) & 18 & \varphi_2(m) & 0 & \varphi_1(m) & \\ 0 & \varphi_2(1/m) & 18 & \varphi_4(1/m) & 0 & \varphi_3(1/m) & -18 & \varphi_1(m) \end{bmatrix} \end{array} \tag{B-8}$$

where

$$\begin{aligned} \varphi_1(m) &= 9m + (35/m), & \varphi_1(1/m) &= (9/m) + 35m \\ \varphi_2(m) &= 9m - (35/m), & \varphi_2(1/m) &= (9/m) - 35m \\ \varphi_3(m) &= -9m + (19/m), & \varphi_3(1/m) &= (-9/m) + 19m \\ \varphi_4(m) &= -9m - (19/m), & \varphi_4(1/m) &= (-9/m) - 19m \end{aligned}$$

(3) ***Other Shapes***

Although the parallelogram and arbitrary quadrilateral can be treated in a manner similar to that used for the rectangle, the individual elements in $[K]$ tend to become unwieldy. For that reason use of automatic digital computing equipment is considered to offer the practical means for obtaining stiffnesses of such plates. Programs for carrying out such calculations can be determined by following the basic ideas developed in this paper.

REFERENCES

[1] Schuerch, H. U., *Structural Analysis of Swept, Low Aspect Ratio, Multispar Aircraft Wings*, Aeronautical Engineering Review, Vol. 11, No. 11, p. 34, November, 1952.

(*Continued on page 854*)

Forced Responses of Two Elastic Beams Interconnected by Spring-Damper Systems

MICHAEL DUBLIN* AND HANS R. FRIEDRICH†

Convair, A Division of General Dynamics Corporation

SUMMARY

This paper presents a method of obtaining the forced responses due to a sinusoidal input of two elastic beams interconnected by spring-damper systems (see Fig. 1). The elastic beams are assumed to have variable mass, variable stiffness, and variable structural damping distributions.

The theory developed has practical application in the investigation of forced responses during rough water taxiing of a seaplane equipped with hydroskis. It can also be used in other forced vibration problems where the elasticity of the beams is important.

Numerical results are presented to show application of the theory for a simplified configuration (see Fig. 2). These results clearly bring out the importance of the elasticity of the beam in such forced response investigations.

Finally, remarks are made on how to utilize the results of this paper to obtain the responses due to an arbitrary force input.

(1) SYMBOLS

Referring to Fig. 1 the following nomenclature is used:

y_n = vertical displacement of lower beam (in.) at any station "n" (positive down)

α_n = angular displacement of lower beam (rad.) at any station "n" (positive counterclockwise)

m_n = mass of lower beam at any station "n" (lb. sec.^{2}/in.)

S_n = shear on lower beam in pounds at any station "n" (positive due to down load at left end of beam)

B_n = bending moment on lower beam (in. lbs.) at any station "n" (positive due to a down load at left end of beam)

ω = frequency of exciting force on lower beam (rad./sec.)

$P_1 = P_c e^{i\omega t}$ = sinusoidal exciting force on lower beam (lbs.)

k_c, k_d, k_e = linear spring constants (lbs./in.) as shown in Fig. 1

c_c, c_d, c_e = linear damping coefficients (lb. sec./in.) as shown in Fig. 1

x_n = horizontal coordinate of lower beam at any station "n" (in.)

$i = \sqrt{-1}$ = (only when not used as a subscript)

$\bar{v}_{Fn}, \bar{d}_{Fn}$ = complex elastic coefficients (lb.$^{-1}$ and in./lb., respectively) of lower beam at any station "n" due to a unit force F. These are as defined in reference (1)

$\bar{v}_{Mn}, \bar{d}_{Mn}$ = complex elastic coefficients (lb.$^{-1}$ in.$^{-1}$ and lb.$^{-1}$, respectively) of lower beam at any station "n" due to a unit moment M. These are as defined in reference (1).

r_n = distance between any two stations on the lower beam (in.)

R_c = reaction force (lbs.) between upper and lower beams at station "c" in Fig. 1

R_d = reaction force (lbs.) between upper and lower beams at station "d" in Fig. 1

ξ = arbitrary vertical displacement of lower beam at station "f" in Fig. 1 (in.)

φ = arbitrary angular displacement of lower beam at station "f" in Fig. 1 (rad.)

z_p = vertical displacement of upper beam (in.) at any station "p" (positive down)

β_p = angular displacement of upper beam in radians at any station "p" (positive counterclockwise)

q_p = mass of upper beam at any station "p" (lb. sec.^{2}/in.)

U_p = shear on upper beam (lbs.) at any station "p" (positive due to down load at left end of beam)

W_p = bending moment on upper beam (in. lbs.) at any station "p" (positive due to down load at left end of beam)

s_p = horizontal coordinate of upper beam at any station "p" (in.)

$\bar{u}_{Fp}, \bar{v}_{Fp}$ = complex elastic coefficients of upper beam at any station "p" (analogous respectively to $\bar{v}_{Fn}$ and $\bar{d}_{Fn}$)

$\bar{u}_{Mp}, \bar{v}_{Mp}$ = complex elastic coefficients of upper beam at any station "p" (analogous respectively to $\bar{v}_{Mn}$ and $\bar{d}_{Mn}$)

t_p = distance between any two stations on the upper beam (in.)

δ = arbitrary vertical displacement of upper beam at station "g" in Fig. 1 (in.)

γ = arbitrary angular displacement of upper beam at station "g" in Fig. 1 (in.)

Subscripts a, b, c, d, e, f, and g refer to stations shown in Fig. 1 for either upper or lower beams.

(2) INTRODUCTION

IN CERTAIN FORCED VIBRATION problems where beams are interconnected by spring-damper systems it is necessary to consider the elasticity of the beams in order to obtain realistic values of the forced responses—i.e., either the deflection shape or the force transmitted from one beam to another. A practical problem of this type is the forced response of a seaplane equipped with hydroskis when taxiing in rough water. Fig. 1 shows the idealized system configuration for this problem. In this figure the upper beam represents the wing and hull, the lower beam represents the ski, k_c and c_c represent the forward shock strut, k_d and c_d represent the aft shock strut, k_e and c_e represent the water spring constant and damping coefficient, and P_1 represents a sinusoidal input force. Although in practice the input force is not sinusoidal, if the response is known for a sinusoidal input then it can be utilized to obtain the response for an arbitrary input.

Received July 12, 1955.

* Chief of Dynamics, San Diego.

† Chief Flight Mechanics Engineer, San Diego. Also, Lecturer in Engineering, University of California, Los Angeles.

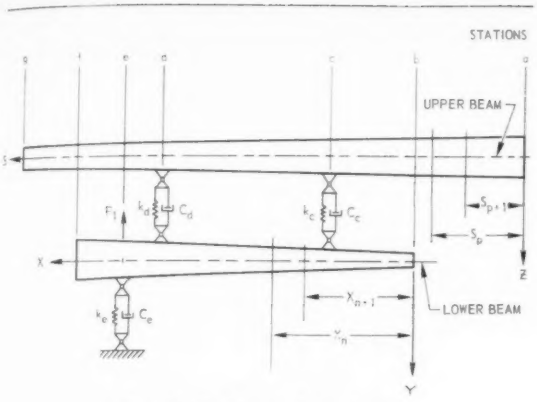

FIG. 1. System configuration.

Basically this paper presents a method of obtaining the forced responses due to a sinusoidal input on the system configuration shown in Fig. 1. It is assumed that the beams can be represented by discrete masses, so that, in effect, the beams are assumed to have variable mass, variable stiffness, and variable structural damping distributions. The method used herein is essentially an extension of Myklestad's method described in reference 1.

This paper also presents some numerical results to show application of the theory presented here.

(3) Response Equations for Two Elastic Beams

Referring to Fig. 1 and assuming harmonic motion, the shear and bending moment at any station "n" on the lower beam are, respectively,

$$S_n = \sum_{i=f}^{n} m_i y_i \omega^2 - P - (k_c + ic_c\omega)y_c - (k_d + ic_d\omega)(y_d - z_d) - (k_c + ic_c\omega)(y_c - z_c) \quad (1)$$

$$B_n = \sum_{i=f}^{n-1} m_i y_i \omega^2 (x_i - x_n) - P(x_c - x_n) - (k_c + ic_c\omega)(x_c - x_n)y_c - (k_d + ic_d\omega)(x_d - x_n) \times (y_d - z_d) - (k_c + ic_c\omega)(x_c - x_n)(y_c - z_c) \quad (2)$$

Analogously, the shear and bending moment at any station "p" on the upper beam are, respectively,

$$U_p = \sum_{j=g}^{p} q_j z_j \omega^2 + (k_d + ic_d\omega)(y_d - z_d) + (k_c + ic_c\omega)(y_c - z_c) \quad (3)$$

$$W_p = \sum_{j=g}^{p-1} q_j z_j \omega^2 (s_j - s_p) + (k_d + ic_d\omega)(s_d - s_p) \times (y_d - z_d) + (k_c + ic_c\omega)(s_c - s_p)(y_c - z_c) \quad (4)$$

Eqs. (1)-(4) apply to the right of station "c" in Fig. 1; at any station to the left of station "c" appropriate terms in the above equations are taken equal to zero.

The reaction forces between the upper and lower beams at stations "c" and "d" are, respectively,

$$R_c = (k_c + ic_c\omega)(y_c - z_c) \quad (5)$$

$$R_d = (k_d + ic_d\omega)(y_d - z_d) \quad (6)$$

For the lower beam the vertical and angular displacements at any station "n" and "n + 1" are, respectively,

$$y_n = -g_{\varphi_n}\varphi + g_{\xi_n}\xi - g_{\gamma_n}\gamma + g_{\delta_n}\delta - g_{P_n}P \quad (7)$$

$$\alpha_n = f_{\varphi_n}\varphi - f_{\xi_n}\xi + f_{\gamma_n}\gamma - f_{\delta_n}\delta - f_{P_n}P \quad (8)$$

$$y_{n+1} = y_n - r_n\alpha_{n+1} - S_n\bar{d}_{F_n} - B_n\bar{d}_{M_n} \quad (9)$$

$$\alpha_{n+1} = \alpha_n - S_n\bar{v}_{F_n} - B_n\bar{v}_{M_n} \quad (10)$$

where g_{φ_n}, g_{ξ_n}, etc., are linear amplitude coefficients, f_{φ_n}, f_{ξ_n}, etc., are angular amplitude coefficients, and the arbitrary displacements of the lower beam at station "f" in Fig. 1 are

$$y_f = \xi \quad (11)$$

$$\alpha_f = \varphi \quad (12)$$

The initial values of the linear and angular amplitude coefficients of the lower beam at station "f" are

$$\left.\begin{aligned} g_{\varphi_f} &= 0,\ g_{\xi_f} = 1,\ g_{\gamma_f} = 0,\ g_{\delta_f} = 0,\ g_{P_f} = 0 \\ f_{\varphi_f} &= 1,\ f_{\xi} = 0,\ f_{\gamma_f} = 0,\ f_{\delta_f} = 0,\ f_{P_f} = 0 \end{aligned}\right\} \quad (13)$$

For the upper beam the vertical and angular displacements at any station "p" and "p + 1" are, respectively,

$$z_p = -h_{\varphi_p}\varphi + h_{\xi_p}\xi - h_{\gamma_p}\gamma + h_{\delta_p}\delta - h_{P_p}P \quad (14)$$

$$\beta_p = k_{\varphi_p}\varphi - k_{\xi_p}\xi + k_{\gamma_p}\gamma - k_{\delta_p}\delta - k_{P_p}P \quad (15)$$

$$z_{p+1} = z_p - t_p\beta_{p+1} - U_p\bar{w}_{F_p} - W_p\bar{w}_{M_p} \quad (16)$$

$$\beta_{p+1} = \beta_p - U_p\bar{u}_{F_p} - W_p\bar{u}_{M_p} \quad (17)$$

where h_{φ_p}, h_{ξ_p}, etc. are linear amplitude coefficients, k_{φ_p}, k_{ξ_p}, etc., are angular amplitude coefficients, and the arbitrary displacements of the upper beam at station "g" in Fig. 1 are

$$z_g = \delta \quad (18)$$

$$\beta_g = \gamma \quad (19)$$

The initial values of the linear and angular amplitude coefficients of the upper beam at station "g" are:

$$\left.\begin{aligned} h_{\varphi_g} &= 0,\ h_{\xi_g} = 0,\ h_{\gamma_g} = 0,\ h_{\delta_g} = 1,\ h_{P_g} = 0 \\ k_{\varphi_g} &= 0,\ k_{\xi_g} = 0,\ k_{\gamma_g} = 1,\ k_{\delta_g} = 0,\ k_{P_g} = 0 \end{aligned}\right\} \quad (20)$$

Now, by substituting Eqs. (1), (2), (7), (8), (14), and (15) into Eqs. (9) and (10), and by substituting Eqs. (3), (4), (7), (8), (14), and (15) into Eqs. (16) and (17), there result, after considerable algebraic manipulation, the following equations for the linear and angular amplitude coefficients at stations "n + 1" and "p + 1":

$$g_{\varphi_{n+1}} = g_{\varphi_n} + r_n f_{\varphi_{n+1}} - \bar{d}_{F_n}(G_{\varphi_n} - H_{\varphi_n} + I_{\varphi_n} + N_{\varphi_n} - K_{\varphi_n} + R_{\varphi_n}) - \bar{d}_{M_n}(G_{\varphi_n}' - H_{\varphi_n}' - I_{\varphi_n}' + N_{\varphi_n}' - K_{\varphi_n}' + R_{\varphi_n}') \quad (21)$$

$$g_{\xi_{n+1}} = g_{\xi_n} + r_n f_{\xi_{n+1}} - d_{F_n}(G_{\xi_n} - H_{\xi_n} - I_{\xi_n} + N_{\xi_n} - K_{\xi_n} + R_{\xi_n}) - d_{M_n}(G_{\xi_n}' - H_{\xi_n}' - I_{\xi_n}' + N_{\xi_n}' - K_{\xi_n}' + R_{\xi_n}') \quad (22)$$

$$g_{\gamma_{n+1}} = g_{\gamma_n} + r_n f_{\gamma_{n+1}} - d_{F_n}(G_{\gamma_n} - H_{\gamma_n} - I_{\gamma_n} + N_{\gamma_n} - K_{\gamma_n} + R_{\gamma_n}) - d_{M_n}(G_{\gamma_n}' - H_{\gamma_n}' - I_{\gamma_n}' + N_{\gamma_n}' - K_{\gamma_n}' + R_{\gamma_n}') \quad (23)$$

$$g_{\delta_{n+1}} = g_{\delta_n} + r_n f_{\delta_{n+1}} - d_{F_n}(G_{\delta_n} - H_{\delta_n} - I_{\delta_n} + N_{\delta_n} - K_{\delta_n} + R_{\delta_n}) - d_{M_n}(G_{\delta_n}' - H_{\delta_n}' - I_{\delta_n}' + N_{\delta_n}' - K_{\delta_n}' + R_{\delta_n}') \quad (24)$$

$$g_{P_{n+1}} = g_{P_n} - r_n f_{P_{n+1}} - d_{F_n}(1 + G_{P_n} - H_{P_n} - I_{P_n} + N_{P_n} - K_{P_n} + R_{P_n}) - d_{M_n}(\{x_e - x_n\} + G_{P_n}' - H_{P_n}' - I_{P_n}' + N_{P_n}' - K_{P_n}' + R_{P_n}') \quad (25)$$

$$f_{\xi_{n+1}} = f_{\xi_n} + \bar{v}_{F_n}(G_{\xi_n} - H_{\xi_n} - I_{\xi_n} + N_{\xi_n} - K_{\xi_n} + R_{\xi_n}) + \bar{v}_{M_n}(G_{\xi_n}' - H_{\xi_n}' - I_{\xi_n}' + N_{\xi_n}' - K_{\xi_n}' + R_{\xi_n}') \quad (26)$$

$$f_{\varphi_{n+1}} = f_{\varphi_n} + \bar{v}_{F_n}(G_{\varphi_n} - H_{\varphi_n} - I_{\varphi_n} + N_{\varphi_n} - K_{\varphi_n} + R_{\varphi_n}) + \bar{v}_{M_n}(G_{\varphi_n}' - H_{\varphi_n}' - I_{\varphi_n}' + N_{\varphi_n}' - K_{\varphi_n}' + R_{\varphi_n}') \quad (27)$$

$$f_{\delta_{n+1}} = f_{\delta_n} + \bar{v}_{F_n}(G_{\delta_n} - H_{\delta_n} - I_{\delta_n} + N_{\delta_n} - K_{\delta_n} + R_{\delta_n}) + \bar{v}_{M_n}(G_{\delta_n}' - H_{\delta_n}' - I_{\delta_n}' + N_{\delta_n}' - K_{\delta_n}' + R_{\delta_n}') \quad (28)$$

$$f_{\gamma_{n+1}} = f_{\gamma_n} + \bar{v}_{F_n}(G_{\gamma_n} - H_{\gamma_n} - I_{\gamma_n} + N_{\gamma_n} - K_{\gamma_n} + R_{\gamma_n}) + \bar{v}_{N_n}(G_{\gamma_n}' - H_{\gamma_n}' - I_{\gamma_n}' + N_{\gamma_n}' - K_{\gamma_n}' + R_{\gamma_n}') \quad (29)$$

$$f_{P_{n+1}} = f_{P_n} - \bar{v}_{F_n}(1 + G_{P_n} - H_{P_n} - I_{P_n} + N_{P_n} - K_{P_n} + R_{P_n}) - \bar{v}_{M_n}(\{x_e - x_n\} + G_{P_n}' - H_{P_n}' - I_{P_n}' + N_{P_n}' - K_{P_n}' + R_{P_n}') \quad (30)$$

$$h_{\varphi_{p+1}} = h_{\varphi_p} + t_p k_{\varphi_{p+1}} - \bar{w}_{F_p}(M_{\varphi_p} + J_{\varphi_p} - Q_{\varphi_p} + L_{\varphi_p} - S_{\varphi_p}) - \bar{w}_{M_p}(M_{\varphi_p}' + J_{\varphi_p}' - Q_{\varphi_p}' + L_{\varphi_p}' - S_{\varphi_p}') \quad (31)$$

$$h_{\xi_{p+1}} = h_{\xi_p} + t_p k_{\xi_{p+1}} - \bar{w}_{F_p}(M_{\xi_p} + J_{\xi_p} - Q_{\xi_p} + L_{\xi_p} - S_{\xi_p}) - \bar{w}_{M_p}(M_{\xi_p}' + J_{\xi_p}' - Q_{\xi_p}' + L_{\xi_p}' - S_{\xi_p}') \quad (32)$$

$$h_{\gamma_{p+1}} = h_{\gamma_p} + t_p k_{\gamma_{p+1}} - \bar{w}_{F_p}(M_{\gamma_p} + J_{\gamma_p} - Q_{\gamma_p} + L_{\gamma_p} - S_{\gamma_p}) - \bar{w}_{M_p}(M_{\gamma_p}' + J_{\gamma_p}' - Q_{\gamma_p}' + L_{\gamma_p}' - S_{\gamma_p}') \quad (33)$$

$$h_{\delta_{p+1}} = h_{\delta_p} + t_p k_{\delta_{p+1}} - \bar{w}_{F_p}(M_{\delta_p} + J_{\delta_p} - Q_{\delta_p} + L_{\delta_p} - S_{\delta_p}) - \bar{w}_{M_p}(M_{\delta_p}' + J_{\delta_p}' - Q_{\delta_p}' + L_{\delta_p}' - S_{\delta_p}') \quad (34)$$

$$h_{P_{p+1}} = h_{P_p} - t_p k_{P_{p+1}} - \bar{w}_{F_p}(M_{P_p} + J_{P_p} - Q_{P_p} + L_{P_p} - S_{P_p}) - \bar{w}_{M_p}(M_{P_p}' + J_{P_p}' - Q_{P_p}' + L_{P_p}' - S_{P_p}') \quad (35)$$

$$k_{\varphi_{p+1}} = k_{\varphi_p} + \bar{u}_{F_p}(M_{\varphi_p} + J_{\varphi_p} - Q_{\varphi_p} + L_{\varphi_p} - S_{\varphi_p}) + \bar{u}_{M_p}(M_{\varphi_p}' + J_{\varphi_p}' - Q_{\varphi_p}' + L_{\varphi_p}' - S_{\varphi_p}') \quad (36)$$

$$k_{\xi_{p+1}} = k_{\xi_p} + \bar{u}_{F_p}(M_{\xi_p} + J_{\xi_p} - Q_{\xi_p} + L_{\xi_p} - S_{\xi_p}) + \bar{u}_{M_p}(M_{\xi_p}' + J_{\xi_p}' - Q_{\xi_p}' + L_{\xi_p}' - S_{\xi_p}') \quad (37)$$

$$k_{\gamma_{p+1}} = k_{\gamma_p} + \bar{u}_{F_p}(M_{\gamma_p} + J_{\gamma_p} - Q_{\gamma_p} + L_{\gamma_p} - S_{\gamma_p}) + \bar{u}_{M_p}(M_{\gamma_p}' + J_{\gamma_p}' - Q_{\gamma_p}' + L_{\gamma_p}' - S_{\gamma_p}') \quad (38)$$

$$k_{\delta_{p+1}} = k_{\delta_p} + \bar{u}_{F_p}(M_{\delta_p} + J_{\delta_p} - Q_{\delta_p} + L_{\delta_p} - S_{\delta_p}) + \bar{u}_{M_p}(M_{\delta_p}' + J_{\delta_p}' - Q_{\delta_p}' + L_{\delta_p}' - S_{\delta_p}') \quad (39)$$

$$k_{P_{p+1}} = k_{P_p} - \bar{u}_{F_p}(M_{P_p} + J_{P_p} - Q_{P_p} + L_{P_p} - S_{P_p}) - \bar{u}_{M_p}(M_{P_p}' + J_{P_p}' - Q_{P_p}' + L_{P_p}' - S_{P_p}') \quad (40)$$

where the abbreviated nomenclature shown in Table 1 is used.

By writing the equations for the shear and bending moment on the lower and upper beams at stations "b" and "a," respectively, the following equations are obtained, which, when solved simultaneously, give the arbitrary amplitudes φ, ξ, γ, and δ:

$$S_b = (-G_{\varphi_b} + H_{\varphi_b} + I_{\varphi_b} - N_{\varphi_b} + K_{\varphi_b} - R_{\varphi_b})\varphi + (G_{\xi_b} - H_{\xi_b} - I_{\xi_b} + N_{\xi_b} - K_{\xi_b} + R_{\xi_b})\xi + (-G_{\gamma_b} + H_{\gamma_b} + I_{\gamma_b} - N_{\gamma_b} + K_{\gamma_b} - R_{\gamma_b})\gamma + (G_{\delta_b} - H_{\delta_b} - I_{\delta_b} + N_{\delta_b} - K_{\delta_b} + R_{\delta_b})\delta + (-1 - G_{P_b} + H_{P_b} + I_{P_b} - N_{P_b} + K_{P_b} - R_{P_b})P = 0 \quad (41)$$

$$B_b = (-G_{\varphi_b}' + H_{\varphi_b}' + I_{\varphi_b}' - N_{\varphi_b}' + K_{\varphi_b}' - R_{\varphi_b}')\varphi + (G_{\xi_b}' - H_{\xi_b}' - I_{\xi_b}' + N_{\xi_b}' - K_{\xi_b}' + R_{\xi_b}')\xi + (-G_{\gamma_b}' + H_{\gamma_b}' + I_{\gamma_b}' - N_{\gamma_b}' + K_{\gamma_b}' - R_{\gamma_b}')\gamma + (G_{\delta_b}' - H_{\delta_b}' - I_{\delta_b}' + N_{\delta_b}' - K_{\delta_b}' + R_{\delta_b}')\delta + (-\{x_e - x_b\} - G_{P_b}' + H_{P_b}' + I_{P_b}' - N_{P_b}' + K_{P_b}' - R_{P_b}')P = 0 \quad (42)$$

$$U_a = (-M_{\varphi_a} - J_{\varphi_a} + Q_{\varphi_a} - L_{\varphi_a} + S_{\varphi_a})\varphi + (M_{\xi_a} + J_{\xi_a} - Q_{\xi_a} + L_{\xi_a} - S_{\xi_a})\xi + (-M_{\gamma_a} - J_{\gamma_a} + Q_{\gamma_a} - L_{\gamma_a} + S_{\gamma_a})\gamma + (M_{\delta_a} + J_{\delta_a} - Q_{\delta_a} + L_{\delta_a} - S_{\delta_a})\delta + (-M_{P_a} - J_{P_a} + Q_{P_a} - L_{P_a} + S_{P_a})P = 0 \quad (43)$$

$$W_a = (-M_{\varphi_a}' - J_{\varphi_a}' + Q_{\varphi_a}' - L_{\varphi_a}' + S_{\varphi_a}')\varphi + (M_{\xi_a}' + J_{\xi_a}' - Q_{\xi_a}' + L_{\xi_a}' - S_{\xi_a}')\xi + (-M_{\gamma_a}' - J_{\gamma_a}' + Q_{\gamma_a}' - L_{\gamma_a}' + S_{\gamma_a}')\gamma + (M_{\delta_a}' + J_{\delta_a}' - Q_{\delta_a}' + L_{\delta_a}' - S_{\delta_a}')\delta + (-M_{P_a}' - J_{P_a}' + Q_{P_a}' - L_{P_a}' + S_{P_a}')P = 0 \quad (44)$$

TABLE 1
Abbreviated Nomenclature for Eqs. (21)–(40)

$\sum_{i=f}^{n} m_i\omega^2 g_{\varphi i} = G_{\varphi n}$	$\sum_{i=f}^{n} m_i\omega^2 g_{\xi i} = G_{\xi n}$	$\sum_{i=f}^{n} m_i\omega^2 g_{\gamma i} = G_{\gamma n}$	$\sum_{i=f}^{n} m_i\omega^2 g_{\delta i} = G_{\delta n}$	$\sum_{i=f}^{n} m_i\omega^2 g_{P_i} = G_{P_n}$
$\sum_{i=f}^{n-1} m_i\omega^2 (x_i - x_n) g_{\varphi i} = G'_{\varphi n}$	$\sum_{i=f}^{n-1} m_i\omega^2 (x_i - x_n) g_{\xi i} = G'_{\xi n}$	$\sum_{i=f}^{n-1} m_i\omega^2 (x_i - x_n) g_{\gamma i} = G'_{\gamma n}$	$\sum_{i=f}^{n-1} m_i\omega^2 (x_i - x_n) g_{\delta i} = G'_{\delta n}$	$\sum_{i=f}^{n-1} m_i\omega^2 (x_i - x_n) g_{P_i} = G'_{P_n}$
$(k_e + ic_e\omega) g_{\varphi e} = H_{\varphi n}$	$(k_e + ic_e\omega) g_{\xi e} = H_{\xi n}$	$(k_e + ic_e\omega) g_{\gamma e} = H_{\gamma n}$	$(k_e + ic_e\omega) g_{\delta e} = H_{\delta n}$	$(k_e + ic_e\omega) g_{P_e} = H_{P_n}$
$(k_e + ic_e\omega)(x_e - x_n) g_{\varphi e} = H'_{\varphi n}$	$(k_e + ic_e\omega)(x_e - x_n) g_{\xi e} = H'_{\xi n}$	$(k_e + ic_e\omega)(x_e - x_n) g_{\gamma e} = H'_{\gamma n}$	$(k_e + ic_e\omega)(x_e - x_n) g_{\delta e} = H'_{\delta n}$	$(k_e + ic_e\omega)(x_e - x_n) g_{P_e} = H'_{P_n}$
$(k_d + ic_d\omega) g_{\varphi d} = I_{\varphi n} = J_{\varphi p}$	$(k_d + ic_d\omega) g_{\xi d} = I_{\xi n} = J_{\xi p}$	$(k_d + ic_d\omega) g_{\gamma d} = I_{\gamma n} = J_{\gamma p}$	$(k_d + ic_d\omega) g_{\delta d} = I_{\delta n} = J_{\delta p}$	$(k_d + ic_d\omega) g_{P_d} = I_{P_n} = J_{P_p}$
$(k_d + ic_d\omega)(x_d - x_n) g_{\varphi d} = I'_{\varphi n}$	$(k_d + ic_d\omega)(x_d - x_n) g_{\xi d} = I'_{\xi n}$	$(k_d + ic_d\omega)(x_d - x_n) g_{\gamma d} = I'_{\gamma n}$	$(k_d + ic_d\omega)(x_d - x_n) g_{\delta d} = I'_{\delta n}$	$(k_d + ic_d\omega)(x_d - x_n) g_{P_d} = I'_{P_n}$
$(k_d + ic_d\omega)(s_d - s_p) g_{\varphi d} = J'_{\varphi p}$	$(k_d + ic_d\omega)(s_d - s_p) g_{\xi d} = J'_{\xi p}$	$(k_d + ic_d\omega)(s_d - s_p) g_{\gamma d} = J'_{\gamma p}$	$(k_d + ic_d\omega)(s_d - s_p) g_{\delta d} = J'_{\delta p}$	$(k_d + ic_d\omega)(s_d - s_p) g_{P_d} = J'_{P_p}$
$(k_c + ic_c\omega) g_{\varphi c} = K_{\varphi n} = L_{\varphi p}$	$(k_c + ic_c\omega) g_{\xi c} = K_{\xi n} = L_{\xi p}$	$(k_c + ic_c\omega) g_{\gamma c} = K_{\gamma n} = L_{\gamma p}$	$(k_c + ic_c\omega) g_{\delta c} = K_{\delta n} = L_{\delta p}$	$(k_c + ic_c\omega) g_{P_c} = K_{P_n} = L_{P_p}$
$(k_c + ic_c\omega)(x_c - x_n) g_{\varphi c} = K'_{\varphi n}$	$(k_c + ic_c\omega)(x_c - x_n) g_{\xi c} = K'_{\xi n}$	$(k_c + ic_c\omega)(x_c - x_n) g_{\gamma c} = K'_{\gamma n}$	$(k_c + ic_c\omega)(x_c - x_n) g_{\delta c} = K'_{\delta n}$	$(k_c + ic_c\omega)(x_c - x_n) g_{P_c} = K'_{P_n}$
$(k_c + ic_c\omega)(s_c - s_p) g_{\varphi c} = L'_{\varphi p}$	$(k_c + ic_c\omega)(s_c - s_p) g_{\xi c} = L'_{\xi p}$	$(k_c + ic_c\omega)(s_c - s_p) g_{\gamma c} = L'_{\gamma p}$	$(k_c + ic_c\omega)(s_c - s_p) g_{\delta c} = L'_{\delta p}$	$(k_c + ic_c\omega)(s_c - s_p) g_{P_c} = L'_{P_p}$
$\sum_{j=g}^{p} q_j\omega^2 h_{\varphi j} = M_{\varphi p}$	$\sum_{j=g}^{p} q_j\omega^2 h_{\xi j} = M_{\xi p}$	$\sum_{j=g}^{p} q_j\omega^2 h_{\gamma j} = M_{\gamma p}$	$\sum_{j=g}^{p} q_j\omega^2 h_{\delta j} = M_{\delta p}$	$\sum_{j=g}^{p} q_j\omega^2 h_{P_j} = M_{P_p}$
$(k_d + ic_d\omega) h_{\varphi d} = N_{\varphi n} = Q_{\varphi p}$	$(k_d + ic_d\omega) h_{\xi d} = N_{\xi n} = Q_{\xi p}$	$(k_d + ic_d\omega) h_{\gamma d} = N_{\gamma n} = Q_{\gamma p}$	$(k_d + ic_d\omega) h_{\delta d} = N_{\delta n} = Q_{\delta p}$	$(k_d + ic_d\omega) h_{P_d} = N_{P_n} = Q_{P_p}$
$\sum_{j=g}^{p-1} q_j\omega^2 (s_j - s_p) h_{\varphi j} = M'_{\varphi p}$	$\sum_{j=g}^{p-1} q_j\omega^2 (s_j - s_p) h_{\xi j} = M'_{\xi p}$	$\sum_{j=g}^{p-1} q_j\omega^2 (s_j - s_p) h_{\gamma j} = M'_{\gamma p}$	$\sum_{j=g}^{p-1} q_j\omega^2 (s_j - s_p) h_{\delta j} = M'_{\delta p}$	$\sum_{j=g}^{p-1} q_j\omega^2 (s_j - s_p) h_{P_j} = M'_{P_p}$
$(k_d + ic_d\omega)(x_d - x_n) h_{\varphi d} = N'_{\varphi n}$	$(k_d + ic_d\omega)(x_d - x_n) h_{\xi d} = N'_{\xi n}$	$(k_d + ic_d\omega)(x_d - x_n) h_{\gamma d} = N'_{\gamma n}$	$(k_d + ic_d\omega)(x_d - x_n) h_{\delta d} = N'_{\delta n}$	$(k_d + ic_d\omega)(x_d - x_n) h_{P_d} = N'_{P_n}$
$(k_d + ic_d\omega)(s_d - s_p) h_{\varphi d} = Q'_{\varphi p}$	$(k_d + ic_d\omega)(s_d - s_p) h_{\xi d} = Q'_{\xi p}$	$(k_d + ic_d\omega)(s_d - s_p) h_{\gamma d} = Q'_{\gamma p}$	$(k_d + ic_d\omega)(s_d - s_p) h_{\delta d} = Q'_{\delta p}$	$(k_d + ic_d\omega)(s_d - s_p) h_{P_d} = Q'_{P_p}$
$(k_c + ic_c\omega) h_{\varphi c} = R_{\varphi n} = S_{\varphi p}$	$(k_c + ic_c\omega) h_{\xi c} = R_{\xi n} = S_{\xi p}$	$(k_c + ic_c\omega) h_{\gamma c} = R_{\gamma n} = S_{\gamma p}$	$(k_c + ic_c\omega) h_{\delta c} = R_{\delta n} = S_{\delta p}$	$(k_c + ic_c\omega) h_{P_c} = R_{P_n} = S_{P_p}$
$(k_c + ic_c\omega)(x_c - x_n) h_{\varphi c} = R'_{\varphi n}$	$(k_c + ic_c\omega)(x_c - x_n) h_{\xi c} = R'_{\xi n}$	$(k_c + ic_c\omega)(x_c - x_n) h_{\gamma c} = R'_{\gamma n}$	$(k_c + ic_c\omega)(x_c - x_n) h_{\delta c} = R'_{\delta n}$	$(k_c + ic_c\omega)(x_c - x_n) h_{P_c} = R'_{P_p}$
$(k_c + ic_c\omega)(s_c - s_p) h_{\varphi c} = S'_{\varphi p}$	$(k_c + ic_c\omega)(s_c - s_p) h_{\xi c} = S'_{\xi p}$	$(k_c + ic_c\omega)(s_c - s_p) h_{\gamma c} = S'_{\gamma p}$	$(k_c + ic_c\omega)(s_c - s_p) h_{\delta c} = S'_{\delta p}$	$(k_c + ic_c\omega)(s_c - s_p) h_{P_c} = S'_{P_p}$

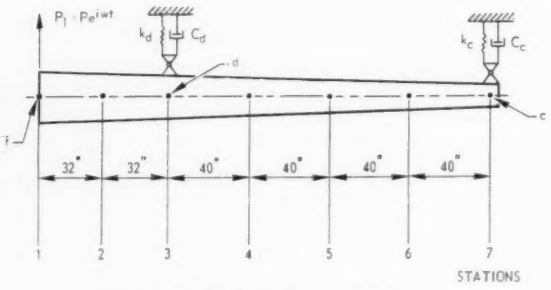

FIG. 2. Single elastic beam configuration.

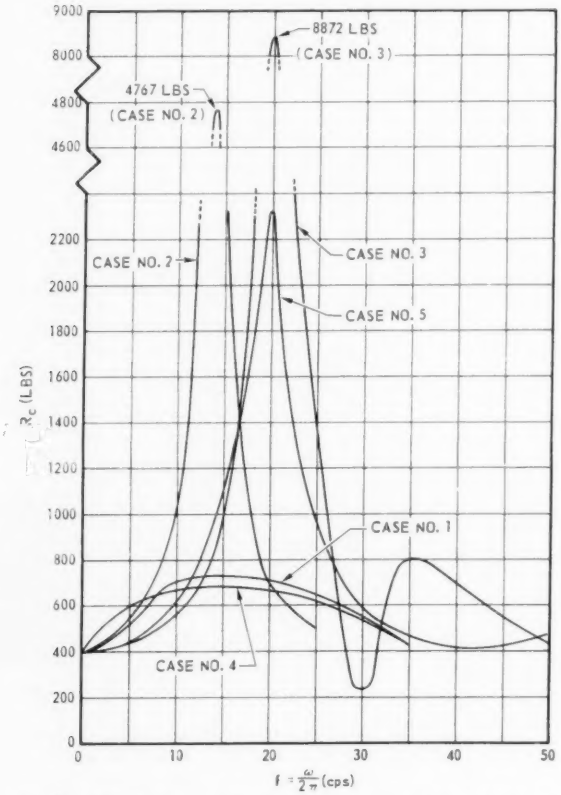

FIG. 3. Reaction force R_c vs. frequency. Case numbers are defined in Table 3.

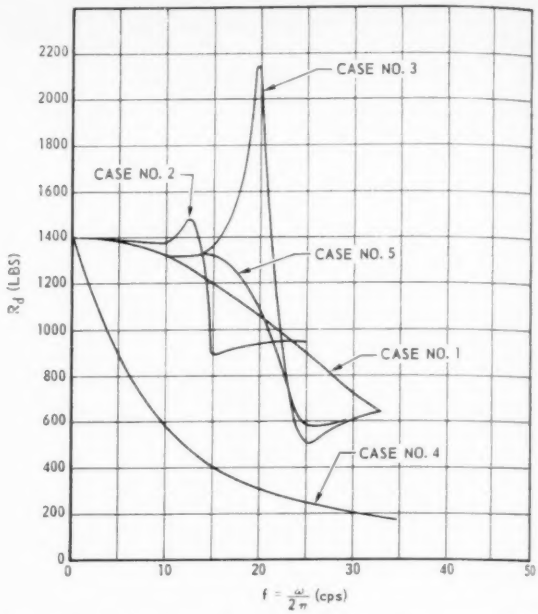

FIG. 4. Reaction force R_d vs. frequency. Case numbers are defined in Table 3.

TABLE 2
Mass and Elastic Coefficients

Sta. n	$\bar{m}_n$ (lb.sec.^{2}/in.)	$v_{F_n} \times 10^6 = d_{M_n} \times 10^6$ (lb.$^{-1}$)	$v_{M_n} \times 10^6$ (lb.$^{-1}$in.$^{-1}$)	$d_{F_n} \times 10^6$ (in./lb.)
1	.1088	.94003	.096226	16.602
2	.1813	.33257	.023568	6.6868
3	.2642	.51579	.024514	14.122
4	.2021	.78810	.036431	21.985
5	.1736	1.6538	.071866	47.509
6	.1192	7.6018	.28533	237.95
7	.06995	—	—	—

$\bar{v}_{F_n} = v_{F_n}(1 - jg)$ $\bar{d}_{F_n} = d_{F_n}(1 - jg)$ $g = +.03$ Structural damping coefficient

$\bar{v}_{M_n} = v_{M_n}(1 - jg)$ $\bar{d}_{M_n} = d_{M_n}(1 - jg)$

TABLE 3
Parameter Variations for Fig. 2 Configuration

Case	Beam Data	k_d (lbs./in.)	c_d (lb.sec./in.)	k_c (lbs./in.)	c_c (lb.sec./in.)	F (lbs.)
1	See Table II	350	83.3	833.3	20	1,000
2	See Table II	350	83.3	2,500	5	1,000
3	See Table II	350	83.3	5,000,000	0	1,000
4	See Table II	350	20	833.3	20	1,000
5	See Table II	350	83.3	833.3	83.3	1,000

In summary, for any ω and P, the equations derived permit the calculation of the elastic displacements by means of Eqs. (7) and (14), and the reaction forces between the upper and lower beams by means of Eqs. (5) and (6).

(4) Application of Theory

To show the application of the theory, consider the simplified single elastic beam configuration shown in Fig. 2. The necessary response equations can be readily obtained from those in the preceding section by putting appropriate terms equal to zero. When the point x_c for applying force P is replaced by point x_f, the following results are obtained from Eqs. (1) and (2).

$$S_n = \sum_{i=f}^{n} m_i y_i \omega^2 - P - (k_d + ic_d\omega)y_d - (k_c + ic_c\omega)y_c \quad (45)$$

$$B_n = \sum_{i=f}^{n-1} m_i y_i \omega^2 (x_i - x_n) - P(x_f - x_n) - (k_d + ic_d\omega)(x_d - x_n)y_d - (k_c + ic_c\omega)(x_c - x_n)y_c \quad (46)$$

From Eqs. (5) through (8) follows:

$$R_c = (k_c + ic_c\omega)y_c \quad (47)$$

$$R_d = (k_d + ic_d\omega)y_d \quad (48)$$

$$y_n = -g_{\varphi_n}\varphi + g_{\xi_n}\xi - g_{P_n}P \quad (49)$$

$$\alpha_n = f_{\varphi_n}\varphi - f_{\xi_n}\xi - f_{P_n}P \quad (50)$$

When the point x_c for applying force P is replaced by the point x_f the following results are obtained by Eqs. (21), (22), (25), (26), (27), and (30):

$$g_{\varphi_{n+1}} = g_{\varphi_n} + r_n f_{\varphi_{n+1}} - d_{F_n}(G_{\varphi_n} - I_{\varphi_n} - K_{\varphi_n}) - d_{M_n}(G_{\varphi_n}' - I_{\varphi_n}' - K_{\varphi_n}') \quad (51)$$

$$g_{\xi_{n+1}} = g_{\xi_n} + r_n f_{\xi_{n+1}} - d_{F_n}(G_{\xi_n} - I_{\xi_n} - K_{\xi_n}) - d_{M_n}(G_{\xi_n}' - I_{\xi_n}' - K_{\xi_n}') \quad (52)$$

$$g_{P_{n+1}} = g_{P_n} - r_n f_{P_{n+1}} - d_{F_n}(1 + G_{P_n} - I_{P_n} - K_{P_n}) - d_{M_n}(\tfrac{1}{2}x_f - x_n\tfrac{1}{2} + G_{P_n}' - I_{P_n}' - K_{P_n}') \quad (53)$$

$$f_{\varphi_{n+1}} = f_{\varphi_n} + \bar{v}_{F_n}(G_{\varphi_n} - I_{\varphi_n} - K_{\varphi_n}) + \bar{v}_{M_n}(G_{\varphi_n}' - I_{\varphi_n}' - K_{\varphi_n}') \quad (54)$$

$$f_{\xi_{n+1}} = f_{\xi_n} + \bar{v}_{F_n}(G_{\xi_n} - I_{\xi_n} - K_{\xi_n}) + \bar{v}_{M_n}(G_{\xi_n}' - I_{\xi_n}' - K_{\xi_n}') \quad (55)$$

$$f_{P_{n+1}} = f_{P_n} - \bar{v}_{F_n}(1 + G_{P_n} - I_{P_n} - K_{P_n}) - \bar{v}_{M_n}(\tfrac{1}{2}x_f - x_n\tfrac{1}{2} + G_{P_n}' - I_{P_n}' - K_{P_n}') \quad (56)$$

When the end point b is replaced by a new end point c and the point x_c for applying force P is replaced by the point x_f the following results are obtained by Eqs. (41) and (42):

$$S_c = (-G_{\varphi_c} + I_{\varphi_c} + K_{\varphi_c})\varphi + (G_{\xi_c} - I_{\xi_c} - K_{\xi_c})\xi + (-1 - G_{P_c} + I_{P_c} + K_{P_c})P = 0 \quad (57)$$

$$B_c = (-G_{\varphi_c}' + I_{\varphi_c}' + K_{\varphi_c}')\varphi + (G_{\xi_c}' - I_{\xi_c}' - K_{\xi_c}')\xi + (-\tfrac{1}{2}x_f - x_c\tfrac{1}{2} - G_{P_c}' + I_{P_c}' + K_{P_c}')P = 0 \quad (58)$$

If the beam is assumed rigid then Eqs. (45) through (58) are applicable by putting $d_{F_n} = d_{M_n} = \bar{v}_{F_n} = \bar{v}_{M_n} = 0$. If, in addition, it is assumed that the frequency is taken equal to zero, then the trivial static solution is obtained under Eqs. (13)—i.e.,

$$y_n = -g_{\varphi_n}\varphi + \xi \quad (59)$$

$$\alpha_n = \varphi \quad (60)$$

$$g_{\varphi_{n-1}} = g_{\varphi_n} + r_n \quad (61)$$

$$\varphi = \frac{P}{(g_{\varphi_c} - g_{\varphi_d})^2}\left(\frac{-k_c g_{\varphi_c} - k_d g_{\varphi_d}}{k_c k_d}\right) \quad (62)$$

$$\xi = \frac{P}{(g_{\varphi_c} - g_{\varphi_d})^2}\left(\frac{-k_c g_{\varphi_c}^2 - k_d g_{\varphi_d}^2}{k_c k_d}\right) \quad (63)$$

$$R_c = P\left(\frac{g_{\varphi_d}}{g_{\varphi_c} - g_{\varphi_d}}\right) \quad (64)$$

$$R_d = P\left(\frac{g_{\varphi_c}}{g_{\varphi_c} - g_{\varphi_d}}\right) \quad (65)$$

Now assume that the beam shown in Fig. 2 is idealized by 7 mass stations, and assume that the masses and complex elastic coefficients are as shown in Table 2. The reactions R_c and R_d were computed for the five cases of parameter variations listed in Table 3, and the results are plotted in Figs. 3 and 4.

A close examination of these figures shows the importance of the theory developed herein in designing a configuration such as shown in Fig. 2. It is seen that improper choice of parameters can result in loads transmitted to the foundation which are very much greater than the loads transmitted due to static loads. For one set of parameters considered—i.e., Case 3 in Table 3—it is seen that the load transmitted to the foundation at the forward support is 22 times greater than the load transmitted due to a static force. Further, from results of calculations not shown herein, it can be said that in general the elasticity of the beam cannot be ignored in such response calculations because the resulting loads transmitted to the foundation for a rigid beam would be considerably less than for an elastic beam.

To optimize a configuration such as shown in Fig. 2 in order to achieve minimum loads transmitted to the foundation requires a thorough study of parameter variations.

(5) Responses Due to Arbitrary Force Input

The theory presented above pertained to the responses of two elastic beams or a single elastic beam excited by a sinusoidal force. In practice, generally

(Continued on page 887)

The Rotational Field Behind a Curved Shock Wave Calculated by the Method of Flux Analysis*

SHIGEO UCHIDA† AND MICHIRU YASUHARA‡

Institute of Science and Technology, University of Tokyo

SUMMARY

Isoenergetic rotational flow behind a curved shock wave is studied by flux analysis using the streamline coordinates. The vorticity equation can be integrated along the curvilinear coordinate perpendicular to the streamlines and gives a relation between velocity and flow patterns under the known distribution of entropy in the following form:

$$q^2 h_\alpha{}^2 e^{-S/c_p} = q_b{}^2 h_{\alpha b}{}^2 e^{-S_b/c_p} + \frac{2a_0{}^2}{\gamma - 1} \int_{\psi_b}^{\psi} h_\alpha{}^2 \frac{de^{-S/c_p}}{d\psi} d\psi$$

Integrating the formula by the first assumed pattern of flow and entropy, the stream function can be calculated and flow patterns corrected. The flow field behind a curved shock wave will be determined by successive procedures. A calculated example of supersonic flow around a circular cylinder with a detached bow shock wave is shown to be in fairly good agreement with experiment. An asymptotic approximate solution of nonviscous supersonic or hypersonic flow along a flat plate is also presented.

SYMBOLS

x, y, z	=	Cartesian coordinates, where xy plane is chosen as reference or meridian plane
α, β, γ	=	orthogonal curvilinear coordinates
s, n, t	=	arc length of α, β, and γ axes, respectively
$h_\alpha, h_\beta, h_\gamma$	=	parameters in curvilinear coordinates
p	=	pressure
ρ	=	density
T	=	temperature (absolute)
S	=	entropy
i	=	enthalpy
R	=	gas constant
c_p, c_v	=	specific heat in constant pressure and volume, respectively
γ	=	c_p/c_v = ratio of specific heat
$\boldsymbol{q}, q$	=	velocity vector and its magnitude
$q_\alpha, q_\beta, q_\gamma$	=	α, β, and γ components of $\boldsymbol{q}$, respectively
u, v, w	=	x, y, and z components of $\boldsymbol{q}$, respectively
q_n, q_t	=	normal and tangential velocity component on a curved shock wave, respectively
a	=	velocity of sound
E	=	total energy
ψ	=	stream function
ζ	=	γ component of rot $\boldsymbol{q}$
ϵ	=	constant ($\epsilon = 0$ in two-dimensional flow and $\epsilon = 1$ in axisymmetric flow)
ω	=	angle between velocity vector and tangent to shock wave
δ	=	deflection angle of streamline through shock wave
θ	=	angle of flow direction
σ	=	angle between streamline and sonic line
φ	=	angle of station along surface of circular cylinder
K	=	connection factor for boundary condition at shock wave
l	=	reference length
d	=	diameter of circular cylinder
b	=	detachment distance of bow shock wave from nose of body
e	=	distance of end of cylinder from tunnel wall
C_p	=	$(p - p_1)/(\rho_1 U_1{}^2/2)$ = pressure coefficient
p_{01}	=	total pressure in uniform upstream
p_{02}	=	impact pressure indicated by pitot tube inserted in field behind curved bow shock wave (see Fig. 29)

Subscripts

0	=	quantities in state at rest of undisturbed flow
*	=	quantities at state of locally sonic
b	=	value along a certain boundary, which will be replaced by s in the present calculation
a	=	quantities along the fixed surface
s	=	quantities immediately behind the shock wave
1, 2	=	quantities before and behind the shock wave, respectively
m	=	grade of approximation

Received July 13, 1955.

* The basic part of this work was prepared for presentation at the Annual Meeting of the Institute of Science and Technology, October 3, 1953, by the senior author. The experimental investigation was made by the junior author.

The authors wish to acknowledge their indebtedness to Prof. S. Kawada, who gave them encouragement to promote this research, and to Dr. J. Hashimoto and C. S. Kim, who kindly offered their data to the present study before their publication.

† Associate Professor.

‡ Research Associate.

INTRODUCTION

THE ROTATIONAL FLOW behind a curved shock wave was first studied by Crocco,[1] who showed the possibility of getting local solutions immediately behind the shock wave. Analysis of the whole field, however, was not attempted for many years and, excepting several examples, it will not be sufficient even today.

The difficulty of the analysis of flow with a detached shock wave, especially in front of a blunt-nosed body, seems to be caused by the difficulty of finding proper means of linearization. By the wide range of velocities containing both stagnation and sonic state in the single field and by the remarkable deformation of flow patterns, neither Janzen-Rayleigh's M^2-expansion method nor the ordinary linearization respecting the small thickness of body can be applied.

In this connection, the method of series expansion with respect to coordinate variables was studied by Lin and Rubinov[2] and others[3–7] in rigorous forms, and

many of them gave a relation between shock location and the radius of curvature of the body nose under the known upstream conditions. As Busemann[8] pointed out, the shock location will not always be determined by the nose radius only, and the validity of cited results will be limited to the case where the shock wave is situated sufficiently close to the nose of the body as compared with its radius. Busemann also suggested that the configuration of the free streamline near the sonic line plays a significant part in the present problem. The same conception was developed by Moeckel,[9] who introduced rough assumptions into the form of the shock wave and the sonic line and produced a practical method for determining the location of the shock wave.

Another rigorous solution was given by Vincenti and Wagoner,[10] who solved the transonic small disturbance equation in the hodograph plane for the case of flow past a wedge profile, where the boundary conditions are completely given in the hodograph plane. The theory of small perturbation can be applied to the wedge of a small apex angle as a special case, and the effects of rotation can reasonably be neglected.

An analytical method for the hodograph plane will be unsuitable for the general case, not only because of its difficulty in prescribing the boundary condition along the body surface, but also because of its complexity in transforming the vortex flow into the hodograph plane, as was indicated by Goldstein and Lighthill,[11] while the effect of vorticity cannot be negligible in the general case of detached curved shock wave.[12]

In order to hold the nonlinearity of the flow pattern as well as the effects of rotationality, numerical calculations were studied by several authors.[13–16] Many of them treated the present problems by the relaxation method starting with the observed form of shock waves.

Another way of approximation was tried by Laitone[17] and Tamada,[18] who calculated the location of the shock wave by assuming the same configuration of flow as that of incompressible flow. The latter and similar calculations[19, 20] gave fairly good results for the flow around a sphere, but they were not sufficient for flow around a circular cylinder.

In the present paper, the method of flux analysis introduced by the senior author is applied to solve the whole field of rotational flow behind the curved shock wave. The general principle of the method was previously reported, and its application was made to the isentropic flow through a Laval nozzle with circular walls[21] and to compressible cascade flow through turbine blades.[22]

The principle of this method is to reduce the partial differential equation into the form of an ordinary one by taking suitably chosen curvilinear coordinates—that is, streamline coordinates, in this case. The equation of vorticity in the present isoenergetic rotational flow is given by Eq. (39), where only derivatives respecting a single variable are involved. Therefore, it can be integrated as shown in Eq. (41) and gives a relation among magnitude of velocity, flow pattern, and entropy gradient. This relation may be equivalent to the characteristics in a broad sense.

In this connection, Meyer[23] has also introduced the equation of motion in the rotational flow referred to the streamline coordinate and has indicated by general consideration that the streamline will have a property of characteristics because equations of motion do not determine the rate of change of velocity q and entropy S in the direction perpendicular to the streamlines. Hence, discontinuities of normal derivatives of these quantities to the streamlines are allowable.

A similar but slightly different principle from the present method has been reported independently by Fox and Southwell,[24] whose method differs in making correction of the coordinate factor—i.e., Eq. (15)—referring to the fixed curvilinear coordinates. Another principle of the method of fixed curvilinear coordinates and calculating the correction term in the differential equation, which is omitted in the first approximation, has also been found and studied independently by Green and Southwell[25] and the present senior author.[21] The latter principle of the method is more analytical but is not convenient for numerical calculation as it contains differential procedure in the way of successive calculations.

In the present paper, therefore, the former method—flux analysis—is employed. Computations are started by assuming the flow patterns and the form of the bow shock wave, which gives the distribution of entropy. Substituting these quantities into Eq. (42), velocities in the field are obtained, and, by further integration with the aid of the continuity and energy equations, the first approximation of the stream function can be calculated and permits the correction of the first assumed streamlines. The procedures are repeated, and successive calculations will give the final convergent solution. It is not difficult to satisfy the boundary conditions on the bow shock wave for the flow with the attached shock wave, where its original point is fixed. If the shock wave is detached, relaxed boundary conditions are satisfied in the first steps regarding the shock location as a parameter. A factor indicating the incompleteness of the boundary condition is found as a function of the parameter of the shock location, and the correct location can be determined by interpolating the value of completeness of the factor.

In this method, the property of nonlinearity of the flow pattern can be considered to a fairly great extent, but, since the processes are so complicated that the calculation must be performed by numerical or graphical procedures, very high accuracy cannot be expected.

Illustrations are given for the supersonic flow around a wing of semiconvex section with an attached shock wave and for the flow of Mach Number 2 around a circular cylinder as the simplest form of body with finite thickness. Experiments were also made for the case of the circular cylinder and compared with the analysis.

In the present method, if the flow pattern is known, the calculation is much simplified. As an example

of such a case, uniform parallel motion of nonviscous fluid as an asymptotic solution of the hypersonic flow along a flat plate is studied, where velocities can be determined by entropy distribution only. Assuming the form of the bow shock wave, velocity and pressure distributions are calculated for the flow of $M = 2$, 5, and 10.

Fundamental Equations

(a) *Fundamental Equations for Steady Rotational Flows*

The steady rotational flow of a nonviscous and non-heat-conductive compressible fluid is governed by the following relations—i.e.,

equation of state for the ideal gas:

$$p/\rho = RT \tag{1}$$

or its deformation with the aid of the first and second law of thermodynamics:

$$p = e^{S/c_v}\rho^{\gamma} \tag{2}$$

equation of continuity:

$$\text{div } (\rho \boldsymbol{q}) = 0 \tag{3}$$

equation of motion:

$$D\boldsymbol{q}/Dt \equiv \text{grad } [(1/2)q^2] - \boldsymbol{q} \times \text{rot } \boldsymbol{q} = -(1/\rho) \text{ grad } p \tag{4}$$

and equation of energy in steady flow without dissipation and heat conduction:

$$T(DS/Dt) \equiv \boldsymbol{q} \cdot \text{grad } S = 0 \tag{5}$$

The last equation means that entropy holds constant values along streamlines and, therefore, is given by the only function of the stream function, which is denoted by ψ.

$$S = f(\psi) \tag{6}$$

If Eq. (5) is substituted into the first law of thermodynamics expressed by

$$di = TdS + dp/\rho \tag{7}$$

the equation of energy on enthalpy is reduced as follows:

$$(Di/Dt) = (1/\rho)\,(Dp/Dt) \tag{8}$$

Introducing total energy defined by

$$E = \frac{1}{2}q^2 + i = \frac{1}{2}q^2 + \frac{\gamma}{\gamma - 1}\frac{p}{\rho} \tag{9}$$

another expression of the equation of energy is obtained with the aid of Eqs. (4) and (8).

$$DE/Dt = \boldsymbol{q} \cdot (\boldsymbol{q} \times \text{rot } \boldsymbol{q}) = 0 \tag{10}$$

For steady motion, Eq. (10) shows that the total energy carried by the unit mass of gas does not vary along the streamlines, and, similarly to entropy, it can be expressed by

$$E = g(\psi) \tag{11}$$

Thus, distributions of entropy and total energy are determined by the upstream boundary conditions as functions of ψ only.

Eliminating i and p from Eq. (4), Eq. (7), and the gradient of Eq. (9), a fundamental relation for vorticity is obtained.[1, 26]

$$\boldsymbol{q} \times \text{rot } \boldsymbol{q} + T \text{ grad } S = \text{grad } E = 0 \tag{12}$$

where the term on the right-hand side vanishes in this case.

(b) *Fundamental Equations Referred to the Orthogonal Curvilinear Coordinates*

In order to get a characterized relation, fundamental equations are expressed in the form referred to the orthogonal curvilinear coordinates as shown in Fig. 1. Introducing the parameters of curvilinear coordinates, h_α, h_β, and h_γ, the equation of continuity is

$$\text{div } (\rho \boldsymbol{q}) \equiv \frac{1}{h_\alpha h_\beta h_\gamma}\left[\frac{\partial(\rho q_\alpha h_\beta h_\gamma)}{\partial\alpha} + \frac{\partial(\rho q_\beta h_\gamma h_\alpha)}{\partial\beta} + \frac{\partial(\rho q_\gamma h_\alpha h_\beta)}{\partial\gamma}\right] = 0 \tag{13}$$

In the present paper, two-dimensional flow with the reference plane x, y and axially symmetric flow with the meridian plane x, y, where the x axis is identified with the axis of symmetry, are considered. If the γ axis is chosen to be perpendicular to the x, y plane, the equation of continuity will be expressed by using the ϵ-convention as follows:

$$\frac{1}{h_\alpha h_\beta y^\epsilon}\left[\frac{\partial(\rho q_\alpha h_\beta y^\epsilon)}{\partial\alpha} + \frac{\partial(\rho q_\beta h_\alpha y^\epsilon)}{\partial\beta}\right] = 0 \tag{14}$$

where $\epsilon = 0$ in two-dimensional and $\epsilon = 1$ in axially symmetric flow. Parameters of coordinates are defined by

$$\left.\begin{aligned} h_\alpha &= \lim_{\delta\alpha\to 0}\frac{\delta s}{\delta\alpha} = \sqrt{\left(\frac{\partial x}{\partial\alpha}\right)^2 + \left(\frac{\partial y}{\partial\alpha}\right)^2} \\ h_\beta &= \lim_{\delta\beta\to 0}\frac{\delta n}{\delta\beta} = \sqrt{\left(\frac{\partial x}{\partial\beta}\right)^2 + \left(\frac{\partial y}{\partial\beta}\right)^2} \end{aligned}\right\} \tag{15}$$

From the equation of continuity, the stream function can be introduced as an arbitrary function which identically satisfies Eq. (14), defining

$$q_\alpha = \frac{1}{\rho h_\beta y^\epsilon}\frac{\partial\psi}{\partial\beta}, \qquad q_\beta = -\frac{1}{\rho h_\alpha y^\epsilon}\frac{\partial\psi}{\partial\alpha} \tag{16}$$

Since the vorticity vector—i.e., rot $\boldsymbol{q}$—has only one component, say ζ, in the direction of γ in this case, dissolving Eq. (12) with the aid of Eq. (6), the formula of vorticity will be given by[26]

$$\zeta = \frac{p}{R}y^\epsilon\,(dS/d\psi) \tag{17}$$

where $\zeta = (\text{rot } \boldsymbol{q})_{\gamma\text{-component}}$

The vorticity equation expressed in the orthogonal curvilinear coordinates is immediately obtained from Eq. (17) as

$$\frac{1}{h_\alpha h_\beta}\left[\frac{\partial(q_\beta h_\beta)}{\partial\alpha} - \frac{\partial(q_\alpha h_\alpha)}{\partial\beta}\right] = \frac{p}{R}\, y^\epsilon \frac{dS}{d\psi} \tag{18}$$

q_α, q_β, ψ, p, ρ, and S will be determined by Eqs. (2), (16), (18), (11), and (6) with the aid of proper boundary conditions.

(c) *Energy Equation in Isoenergetic Flow*

When the flow conditions at upstream infinity are uniform, the total energy E is constant in the whole field, because no jumps of energy occur through the bow shock wave, as shown later in Eq. (26).

Introducing the velocity of sound, defined by

$$a = \sqrt{(\partial p/\partial\rho)_{S=\text{const.}}} = \sqrt{\gamma(p/\rho)} \tag{19}$$

the equation of energy can be expressed in several forms:

$$\begin{aligned} E \equiv \frac{1}{2}q^2 + \frac{\gamma}{\gamma-1}\frac{p}{\rho} &= \frac{1}{2}q_1^2 + \frac{\gamma}{\gamma-1}\frac{p_1}{\rho_1} \\ &= \frac{\gamma}{\gamma-1}\frac{p_0}{\rho_0} = \frac{1}{\gamma-1}a_0^2 = \frac{1}{2}\frac{\gamma+1}{\gamma-1}a_*^2 \\ &= \frac{1}{2}q_{max}^2 = \text{const.} \end{aligned} \tag{20}$$

Eliminating p by the use of the equation of state, Eq. (2), the formula of density is obtained from Eq. (20).

$$\begin{aligned} \frac{\rho}{\rho_0} &= e^{-[(S-S_0)/R]}\left[1 - \frac{\gamma-1}{2}\frac{q^2}{a_0^2}\right]^{1/(\gamma-1)} \\ &= e^{-[(S-S_0)/R]}\left[1 - \frac{\gamma-1}{\gamma+1}\frac{q^2}{a_*^2}\right]^{1/(\gamma-1)} \\ &= e^{-[(S-S_0)/R]}\left[\left(\frac{\rho}{\rho_0}\right)_{\text{isentropic}}\right] \end{aligned} \tag{21}$$

Boundary Conditions

(a) *Fixed Boundary Along the Surface of a Body*

Along the solid surface of the obstacle, the stream function must be constant. When the curvilinear coordinates are chosen as they contain the surface of fixed boundary, represented by $\beta = \beta_a = 0$, the boundary condition along it is given by

$$\psi = \psi_a = 0 \qquad \text{at} \qquad \beta = \beta_a = 0 \tag{22}$$

where $\beta = \beta_a$ can be chosen as the zero streamline without loss of generality.

(b) *Conditions Along the Bow Shock Wave*

Shock wave will be described in mathematical representation as a possible discontinuous surface through which fluid flows with reserving continuities of mass, momentum, and energy. Introducing the notations shown in Fig. 2, fundamental equations are given by continuity law:

$$\rho_1 q_{n1} = \rho_2 q_{n2} \tag{23}$$

momentum theorem:

$$\rho_1 q_{n1}^2 + p_1 = \rho_2 q_{n2}^2 + p_2 \tag{24}$$

$$\rho_1 q_{n1} q_{t1} = \rho_2 q_{n2} q_{t2} \tag{25}$$

and the law of conservation of energy:

$$\frac{1}{2}q_1^2 + \frac{\gamma}{\gamma-1}\frac{p_1}{\rho_1} = \frac{1}{2}q_2^2 + \frac{\gamma}{\gamma-1}\frac{p_2}{\rho_2} \tag{26}$$

In solving these equations, several relations are obtained, as follows:[27]

deflection angle:

$$\frac{1}{\tan\delta} = \left[\frac{\gamma+1}{2}\frac{M_1^2}{M_1^2\sin^2\omega_1 - 1} - 1\right]\tan\omega_1 \tag{27}$$

pressure and density ratios:

$$\frac{p_2}{p_1} = \frac{2\gamma}{\gamma+1}\left[M_1^2\sin^2\omega_1 - \frac{\gamma-1}{2\gamma}\right] \tag{28}$$

$$\frac{\rho_1}{\rho_2} = \frac{2}{\gamma+1}\left[\frac{1}{M_1^2\sin^2\omega_1} + \frac{\gamma-1}{2}\right] \tag{29}$$

and entropy change in different expressions:

$$e^{(S_2-S_1)/c_v} = \frac{p_2/p_1}{(\rho_2/\rho_1)^\gamma} \tag{30}$$

$$e^{(S_2-S_1)/c_p} = \frac{(p_2/p_1)^{1/\gamma}}{\rho_2/\rho_1}, \qquad e^{(S_2-S_1)/R} = \frac{(p_2/p_1)^{1/(\gamma-1)}}{(\rho_2/\rho_1)^{\gamma/(\gamma-1)}} \tag{30'}$$

The form of the shock wave will be represented by the use of curvilinear coordinates

$$\beta = \beta_s(\alpha) \tag{31}$$

similar to $y = y_s(x)$ in the case of Cartesian coordinates.

In the present computations, four fundamental equations, Eqs. (23)–(26), are replaced by the corresponding four independent relations, slightly deformed as follows.

The equation of continuity can be expressed by the form integrated from the zero streamline to the concerning point on the shock wave.

$$\psi = \psi_s = \rho_1 q_1 y_1 (y_1/2)^\epsilon \quad \text{at} \quad \beta = \beta_s(\alpha) \tag{32}$$

Two equations of momentum theory, Eqs. (24) and (25), are replaced by two formulas for deflection angle and entropy change—i.e., Eqs. (27) and (30) substituted by Eqs. (28) and (29).

Eq. (26) itself is used as the law of conservation of energy. Combining with the uniform condition at the upstream field, total energy holds a constant value throughout the whole field and the flow becomes isoenergetic, as mentioned previously.

(c) *Limiting Characteristics*

It is obvious that the region between the sonic line and limiting characteristics must be considered as it affects the subsonic field of flow through the sonic line, while the region behind the limiting characteristics can be ignored because no disturbances arise upward from this region. In an isentropic flow, limiting characteristics will be given in the hodograph plane, *a priori;* however, the limiting characteristics will not be given in rotational flow that contains entropy distributions.

In this connection, the approximate solution is first obtained in the physical plane by assuming the flow patterns. Then it is transformed into the hodograph plane for determining the sonic line and limiting characteristics. The principle is that the supersonic field will then be calculated by the theory of characteristics for rotational flow,[27] and the flow pattern in this region will be corrected. This form of calculation will not be suitable, however, for proceeding to further approximations with new coordinates, because the streamlines will not be smoothly connected through the sonic line. Besides, this process does not seem to have sufficient accuracy, because the region between the sonic line and limiting characteristics is so narrow in the physical plane. In practice, therefore, special calculations by the method of characteristics will not be applied, but flux analysis will be extended into the supersonic region, where the flow field is approximately solved by first assuming and then successively correcting flow patterns. This is equivalent to assuming and correcting the form of limiting characteristics, as mentioned later.

Principle of the Method

(a) *Characteristic Equation Referred to the Streamline Coordinates*

Taking suitably chosen curvilinear coordinates that coincide with the curve of solution about to be analyzed, it has been found that the partial differential equation can be formally transformed into an ordinary one in the general case and that it can be integrated along the coordinate curve perpendicular to the reference coordinate.[21] For this purpose, fundamental equations are expressed in the forms referred to the streamline coordinates in which a component of the coordinate axis, say β = constant, coincides with the streamline ψ = constant, as shown in Fig. 1.

Velocity components on such streamline coordinates are

$$q_\alpha = q, \qquad q_\beta = 0 \tag{33}$$

Since

$$\partial\psi/\partial\alpha = 0$$

from Eqs. (16) and (33), the stream function will be a function of β only, and the derivative for transformation is given by

$$\left.\begin{aligned} \frac{d\psi}{d\beta} &= \rho q h_\beta y^\epsilon \\ \text{or} \qquad \frac{d\beta}{d\psi} &= \frac{1}{\rho q h_\beta y} \end{aligned}\right\} \tag{34}$$

Similarly, the equation of vorticity is reduced from Eq. (18).

$$-\frac{1}{h_\alpha h_\beta}\frac{\partial(h_\alpha q)}{\partial\beta} = \frac{p}{R}y^\epsilon\frac{dS}{d\psi} \tag{35}$$

Unification of variables will be made by substituting Eq. (34) into Eq. (35) as follows:

$$\frac{\partial(h_\alpha q)}{\partial\beta} = -\frac{1}{R}\frac{p}{\rho}\frac{h_\alpha}{q}\frac{dS}{d\beta} \tag{36}$$

or

$$\frac{\partial(h_\alpha q)}{\partial\psi} = -\frac{1}{R}\frac{p}{\rho}\frac{h_\alpha}{q}\frac{dS}{d\psi} \tag{37}$$

both in the same form.

From the equation of energy, Eq. (20), the state quantity p/ρ is given by

$$\frac{p/\rho}{p_0/\rho_0} = 1 - \frac{\gamma - 1}{2}\left(\frac{q}{a_0}\right)^2 \tag{38}$$

where $$p_0/\rho_0 = a_0^2/\gamma$$

Then Eq. (37) can be transformed into the following expressions:

$$\frac{\partial[h_\alpha(q/a_0)]}{\partial\psi} = -\frac{h_\alpha}{\gamma - 1}\times \frac{1 - [(\gamma - 1)/2]\left(\frac{q}{a_0}\right)^2}{q/a_0}\frac{d(S/c_p)}{d\psi} \tag{39}$$

This differential equation between the velocity q and the parameter of flow pattern h_α under the known distribution of entropy S will be equivalent to the characteristic equation in the method of characteristics. Regarding Eq. (39) as the differential equation of the velocity q under the known distribution of h_α and S and rearranging in the following form:

$$\frac{\partial(q/a_0)^2}{\partial\psi} + \left[\frac{\partial \ln h_\alpha^2}{\partial\psi} - \frac{d(S/c_p)}{d\psi}\right]\left(\frac{q}{a_0}\right)^2 = -\frac{2}{\gamma - 1}\frac{d(S/c_p)}{d\psi} \tag{40}$$

integration is given by

$$\left(\frac{q}{a_0}\right)^2 = \frac{1}{h_\alpha^2}e^{S/c_p}\times\left[\int\frac{-2}{\gamma - 1}h_\alpha^2 e^{-(S/c_p)}\frac{d(S/c_p)}{d\psi}d\psi + F_n(\alpha)\right]$$

where the integral constant $F_n(\alpha)$ is an arbitrary function of α only.

Determining $F_n(\alpha)$ by the quantities on an adequately defined streamline $\psi = \psi_b$, the final form of

integration of the characteristic relation in a broad sense is given by

$$\left(\frac{q}{a_0}\right)^2 h_\alpha{}^2 e^{-(S/c_p)} = \left(\frac{q_b}{a_0}\right)^2 h_{\alpha b}{}^2 e^{-(S_b/c_p)} + \frac{2}{\gamma - 1}\int_{\psi_b}^{\psi} h_\alpha{}^2 \frac{de^{-(S/c_p)}}{d\psi}\, d\psi \quad (41)$$

or, with partial integration,

$$\left[\left(\frac{q}{a_0}\right)^2 - \frac{2}{\gamma - 1}\right] h_\alpha{}^2 e^{-(S/c_p)} = \left[\left(\frac{q_b}{a_0}\right)^2 - \frac{2}{\gamma - 1}\right] h_{\alpha b}{}^2 e^{-(S_b/c_p)} - \frac{2}{\gamma - 1}\int_{\psi_b}^{\psi} e^{-(S/c_p)} \frac{dh_\alpha{}^2}{d\psi}\, d\psi \quad (41')$$

For the practice of calculation, the following expression will be more convenient:

$$\left(\frac{q}{a_0}\right)^2 = \left(\frac{h_{\alpha b}}{h_\alpha}\right)^2 e^{[(S - S_b)/c_p]} \left(\frac{q_b}{a_0}\right)^2 + \frac{2}{\gamma - 1} \times \left(\frac{h_{\alpha b}}{h_\alpha}\right)^2 e^{S/c_p} \int_{\psi_b}^{\psi} \left(\frac{h_\alpha}{h_{\alpha b}}\right)^2 \frac{de^{-S/c_p}}{d\psi}\, d\psi \quad (42)$$

or, in the fully nondimensional form,

$$\left(\frac{q}{a_0}\right)^2 = \left(\frac{h_{\alpha b}/l}{h_\alpha/l}\right)^2 e^{[(S - S_b)/c_p]} \left(\frac{q_b}{a_0}\right)^2 + \frac{2}{\gamma - 1} \times \left(\frac{h_{\alpha b}/l}{h_\alpha/l}\right)^2 e^{S/c_p} \int_{[\psi_b/\rho_0 a_0 l(l/2)^\epsilon]}^{[\psi/\rho_0 a_0 l(l/2)^\epsilon]} \left(\frac{h_\alpha/l}{h_{\alpha b}/l}\right)^2 \times \frac{de^{-(S/c_p)}}{d\left[\dfrac{\psi}{\rho_0 a_0 l(l/2)^\epsilon}\right]} d\left[\frac{\psi}{\rho_0 a_0 l(l/2)^\epsilon}\right] \quad (42')$$

Eq. (41) or (42) is an exact relation in the isoenergetic rotational flow which gives velocity distribution along an orthogonal curve of streamlines and shows that the velocity is increased by the entropy gradients in the direction where the latter decrease. Since neither the flow pattern nor the entropy distribution is known in advance, calculations must be made by assuming them and correcting the approximate solutions successively.

If the effects of rotation are not large, as in many cases for the flow around thin obstacles, sufficient results will be available from one round of integration by substituting values of h_α and S from the irrotational solution. In such treatment, the velocity formula given by Eq. (42) will be regarded as a useful formula for vorticity correction to irrotational solutions.

For the special case of isentropic flow, where $S = S_b = S_0 =$ constant, Eq. (42) is deformed into

$$(q/a_0)^2 h_\alpha{}^2 = (q_b/a_0)^2 h_{\alpha b}{}^2$$

or

$$q/q_b = h_{\alpha b}/h_\alpha \quad (43)$$

and is reduced to the well-known relation between velocity and flow patterns in compressible potential flow.[21]

(*b*) *Approximate Method of Flux Analysis*

The flow field between the symmetrical obstacle and the detached bow shock wave as shown in Fig. 3 is considered. The form of the bow shock wave and the entropy distribution behind it are assumed to be temporarily determined by relaxing a condition of momentum conservation through the shock wave, while complete conditions are to be satisfied in the final stage.

Boundary conditions to satisfy continuity are

$$\psi = \psi_a = 0 \quad \text{at} \quad \beta = \beta_a = 0 \quad (22)$$

$$\psi = \psi_s = \rho_1 q_1 y_1 (y_1/2)^\epsilon \quad \text{at} \quad \beta = \beta_s(\alpha) \quad (32)$$

or, expressed in nondimensional form,

$$\frac{\psi_s}{\rho_0 a_0 l(l/2)^\epsilon} = \frac{\rho_1 q_1 y_1}{\rho_0 a_0 l}\left(\frac{y_1}{l}\right)^\epsilon \quad (44)$$

The flow patterns are conveniently assumed so that the boundary condition along the fixed surface is automatically satisfied—for example, by those of incompressible potential flow around the obstacle concerned, where the zero streamline along the body is chosen as the coordinate axis $\beta = \beta_a = 0$. Let an orthogonal coordinate (α = constant) through an arbitrary point Q be PQR, where R is the point of intersection with the bow shock wave determined by the method shown later, and its coordinates are (x, y_s) or (α, β_s).

If these flow patterns of zero approximation can be assumed to be sufficiently close to the final flow pattern, the β component of velocity will be sufficiently small that Eq. (33) can approximately hold. Neglecting terms containing the velocity component q_β as compared with q_α, the equations of continuity and vorticity are approximately reduced to Eqs. (34) and (35), respectively.

The latter is transformed into Eq. (36), and similar integration into Eq. (39) gives the following formula in the same form as Eq. (42), replacing boundary value b by state s on the shock line for the convenience of practical calculation.

$$\left(\frac{q}{a_0}\right)_m^2 = \left(\frac{h_{\alpha s}}{h_\alpha}\right)_{m-1}^2 e^{[(S - S_s)_{m-1}/c_p]} \left(\frac{q_s}{a_0}\right)_m^2 + \frac{2}{\gamma - 1}\left(\frac{h_{\alpha s}}{h_\alpha}\right)_{m-1}^2 e^{S_{m-1}/c_p} \int_{\beta_{s,m-1}}^{\beta_{m-1}} \left(\frac{h_\alpha}{h_{\alpha s}}\right)_{m-1}^2 \frac{de^{-S_{m-1}/c_p}}{d\beta_{m-1}}\, d\beta_{m-1} \quad (45)$$

where m is grade of approximation.

From the energy equation, Eq. (20) or (21), the density of mass flow is given by

$$\frac{\rho q}{\rho_0 a_0} = e^{-[(S - S_0)/R]}\left[\left(1 - \frac{\gamma - 1}{2}\frac{q^2}{a_0{}^2}\right)^{1/(\gamma - 1)} \frac{q}{a_0}\right] = e^{-[(S - S_0)/R]}\left(\frac{\rho q}{\rho_0 a_0}\right)_{\text{isentropic}} \quad (46)$$

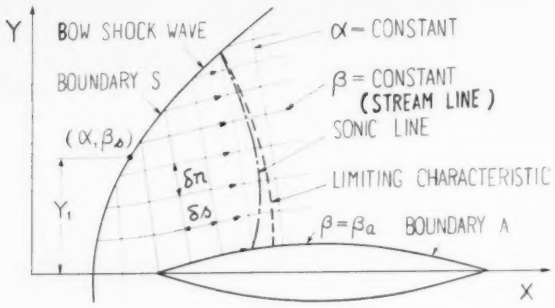

FIG. 1. Curvilinear coordinates.

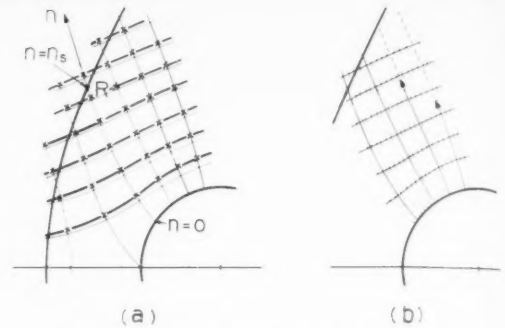

FIG. 6. Process of correction of flow patterns.

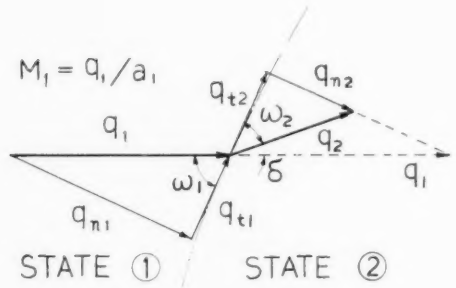

FIG. 2. Velocity diagram at shock boundary.

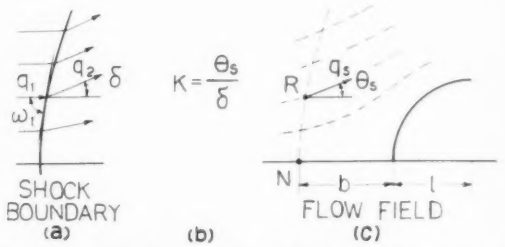

FIG. 7. Connection of the boundary condition on the bow shock wave: (a) deflection angle determined by the shock condition, (b) connection factor, and (c) direction of streamline determined by the flux calculation in the field of flow.

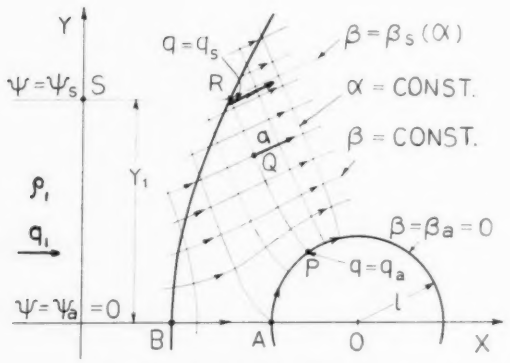

FIG. 3. Scheme of the flow pattern.

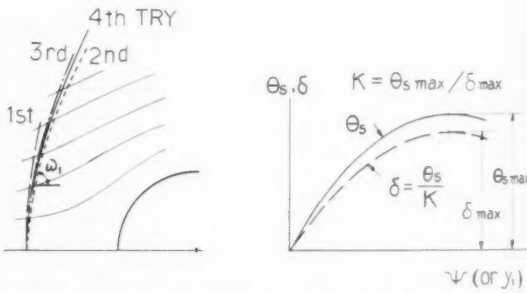

FIG. 8 (*left*). Determination of form of bow shock wave concerning fixed flow patterns. FIG. 9 (*right*). Determination of connection factor K in every step of approximation.

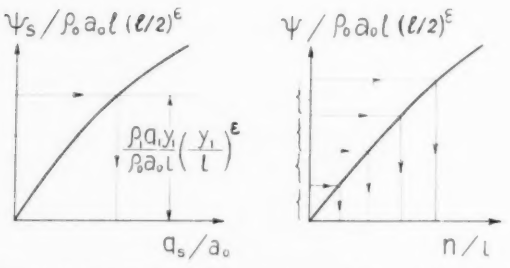

FIG. 4 (*left*). Flux between zero streamline and bow shock wave. FIG. 5 (*right*). Flux distribution along an orthogonal curve (α = constant).

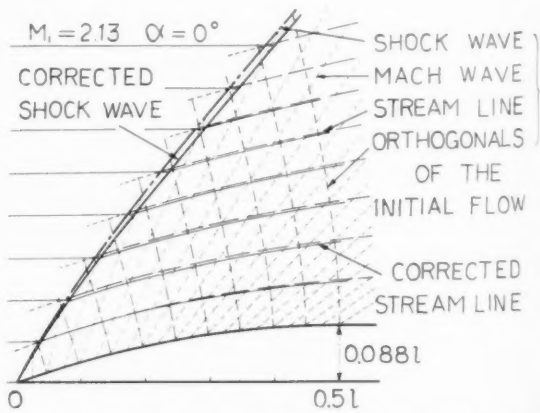

FIG. 10. Flow patterns of supersonic flow around a semiconvex airfoil.

The stream function can then be calculated by integrating the equation of continuity, Eq. (34), as follows:

$$\psi - \psi_a = \int_{\beta_a}^{\beta} pqy_\beta h_\beta d\beta$$

or, considering $\psi_a = 0$, $\beta_a = 0$,

$$\frac{\psi}{\rho_0 a_0 l/(l/2)^\epsilon} = \int_0^\beta \frac{\rho q}{\rho_0 a_0}\left(2\frac{y}{l}\right)^\epsilon \frac{h_\beta}{l}\, d\beta$$

$$= \int_0^{n/l} \frac{\rho q}{\rho_0 a_0}\left(2\frac{y}{l}\right)^\epsilon d\left(\frac{n}{l}\right) \qquad (47)$$

where $h_\beta d\beta = dn$ is substituted. The stream function will be expressed as a function of q_s/a_0.

Boundary conditions of continuity on the bow shock wave are given by integrating Eq. (47) into $\beta = \beta_s$.

$$\frac{\psi_s}{\rho_0 a_0 l/(l/2)^\epsilon} = \int_0^{n_s/l} \frac{\rho q}{\rho_0 a_0}\left(2\frac{y}{l}\right)^\epsilon d\left(\frac{n}{l}\right)$$

$$= \frac{\rho_1 q_1 y_1}{\rho_0 a_0 l}\left(\frac{y_1}{l}\right)^\epsilon \qquad (48)$$

The boundary value of velocity, q_s/a_0, immediately behind the shock wave will be determined by numerical calculation of Eq. (48). (See Fig. 4.)

Thus, substituting the determined value of q_s/a_0 into Eq. (47), distribution of the stream function along PQR can be obtained. From the relation ψ versus β or n shown in Fig. 5, values of β or n corresponding to stream functions can be corrected and, accordingly, the situation of intersection of the new streamline with the orthogonal curve concerned, α = constant, can be determined as shown schematically in Fig. 5. Getting these points on every orthogonal curve, corrected streamlines—namely, new coordinate curves—will be drawn graphically by connecting the corresponding points on adjacent orthogonals, as shown in Fig. 6(a).

New orthogonal curves are drawn by connecting the small divided line perpendicularly across the corrected streamlines as shown in Fig. 6(b), and flow patterns, which will be used as coordinate axes in the succeeding calculation, are completed in this step of approximation.

An approximate value of parameter h_α of corrected curvilinear coordinates will be given by replacing the derivatives in Eq. (15) by finite difference

$$h_\alpha = \delta s/\delta\alpha \qquad (49)$$

and, accordingly,

$$h_\alpha/h_{\alpha s} = \delta s/\delta s \qquad (50)$$

where δs is the arc length of the streamlines divided by two adjacent orthogonal curves.

The form of the bow shock wave and, consequently, the distribution of entropy, will be corrected according to the new streamlines as will be described in the next section.

The next stage of calculation will be performed by substituting these corrected values into Eq. (45) through Eq. (48) and repeating the same procedures. Successive calculations are continued until a convergent solution is finally obtained.

(c) *Fulfillment of the Boundary Condition Along the Bow Shock Wave*

Quantities behind the bow shock wave are assumed to vary along the shock polar monotonically from the state of the vertical shock wave to Mach wave corresponding to the uniform flow, and, accordingly, the deflection angle δ has a maximum value determined by the quantities of uniform flow.

Since flow patterns must first be assumed in the present theory, the angle of flow direction θ_s cannot generally coincide with the deflection angle δ immediately behind the shock wave. It is convenient, therefore, that the condition of the deflection angle, Eq. (27), is relaxed and not satisfied by θ_s in the first steps.

A parameter indicating the incompleteness of the shock condition is introduced by defining

$$K = \theta_s/\delta = \theta_{s\,max}/\delta_{max} \qquad (51)$$

or

$$\delta = \theta_s/K = (\theta_s/\theta_{s\,max})\delta_{max} \qquad (51')$$

where $\theta_{s\,max}$ is the maximum angle of flow direction immediately behind the shock wave, which must be corrected in every step of approximation, as shown in Fig. 7, while angle δ and δ_{max} are given as a fixed value from the exact condition through the oblique shock wave. (See Fig. 7.) If the solution of $K = 1$ is obtained, it will satisfy the shock condition completely. In the present method, the value of K is calculated for an arbitrarily chosen location N of the nose of the bow shock wave, and it is determined successively in the consequence of every step of approximation with a fixed location of point N. Starting from the chosen situation of point N, the form of the bow shock wave will be determined for the assumed or approximately drawn form of the streamlines as follows. The value of K is first assumed to be 1, and the line of the shock wave is extended by connecting the divided lines that intersect the uniform flow with the shock angle ω_1 given by Eq. (27) for $\delta = \theta_s/K$. Then, the value of K is calculated by dividing the greatest or maximum value of θ_s by δ_{max}, and the form of the shock wave is redrawn through the same process using the new value of K. These procedures are repeated successively, and the convergent value of K is determined when the form of the shock wave does not alter. (See Fig. 8.)

When the form of the bow shock wave with a definite value of the connection factor K is determined for a given form of flow patterns, solutions of further approximation are calculated by using the shock condition for $\delta(\delta = \theta_s/K$, as shown in Fig. 9) which will give the distribution of entropy, and the streamlines are corrected by the method described in the previous section. Then, fixing the detachment distance b of point N from the nose of the body, the form of the bow shock wave is redetermined with the new streamlines, adjusting the factor K by the processes mentioned

above. Calculations are repeated until the convergent solution is obtained for a fixed point N.

If the calculations for various values of b are made by starting with the identical patterns of flow as the zero approximation, the connection factor K will be given as a continuous function of detachment distance b. The correct situation of the nose of the bow shock wave corresponding to $K = 1$ will be determined from the relation of K versus b as obtained above (see Fig. 13). Final solutions are obtained by solving the problem for this value of b again through the same course of calculation as before.

(d) *Boundary Conditions Along the Sonic Line and Limiting Characteristics*

Since the form of the sonic line or limiting characteristics as a boundary condition cannot be given *a priori* in the physical plane, it will be convenient to start the approximation by assuming the form of flow patterns through these limiting lines, instead of assuming the form of these lines. If the flow patterns are assumed and other boundary conditions are considered, as previously mentioned, velocity distributions can be determined by integrating Eq. (45), as the principle, throughout the field concerned, and the form of the sonic line or limiting characteristics can be obtained. To give or assume the form of these limiting boundaries under the given flow patterns in the physical plane, therefore, seems to be an over-restriction with respect to the boundary condition.

In the present calculation neither the form of the sonic line nor the limiting characteristics are assumed, but the boundary conditions along these lines are replaced by equivalent conditions determined by assuming the flow patterns. The forms of these limiting lines will be obtained in the last step of every approximation, and their convergent forms will be determined by the final solution.

Rotational Flow Around a Semiconvex Airfoil with Attached Bow Shock Wave

In order to know the effect of rotation on the ordinary supersonic flow with a curved shock wave and to inspect the validity of the characteristic relation in a broad sense—i.e., Eq. (41) or (45)—application is first made to the supersonic flow of Mach Number $M_1 = 2.13$ around a semiconvex airfoil of 8.8 per cent thickness with an angle of attack of $\alpha = 0°$.

The basic streamline is given in the form of folding lines by the theory of characteristics for irrotational flow, where reflections of the Mach wave from the bow shock wave are neglected for the sake of simplicity. In connecting the sides of polygonal lines at mid-point, fair curves of the streamline and their orthogonals are drawn, with a slight extrapolation in front of the shock.

Approximate calculations previously mentioned are applied by fixing the starting point of the shock wave on the leading edge of the airfoil. Forms of the flow pattern and the bow shock wave initially given and corrected by the first approximation are shown in Fig. 10, where l is the chord length. Because the gradients of entropy in exponential form with respect to stream function do not exceed 4 per cent in this case, as shown in Fig. 11, correction terms for rotational flow—i.e., the second term in the right-hand side of Eq. (45)—are at most 10 per cent of the main part—i.e., the first term in the same side—in the present example. Moreover, the corrected streamlines hold almost parallel to the basic pattern, and, accordingly, the corrections in $h_\alpha/h_{\alpha s}$ will be as slight as less than 1 per cent; therefore, calculation seems to be practically convergent by one round approximation in such a small perturbation flow around thin bodies.

Pressure distributions along the wing surface are presented in Fig. 12 in comparison to the results of experiments made by Ferri.[28] The result shows that the deviation of the observed pressure coefficient from the theory of irrotational flow may be interpreted as the effect of rotation caused by the curved bow shock wave. Since vorticity rotates clockwise in the upper half plane, velocities along the wing surface tend to be diminished more than those far from the body, as compared with the irrotational solution, and, hence, the pressure coefficient is increased.

Supersonic Flow Around a Circular Cylinder with Detached Bow Shock Wave

Illustrative computations will be made for the supersonic flow ($M_1 = 2$) around a circular cylinder, which is the simplest sectional form among bodies with finite thickness and induces intense nonlinear disturbance to the field of flow. The flow patterns of irrotational flow around a circular cylinder of incompressible fluid extended to the infinity are chosen for starting the calculation. Comparing this with the last form of pattern, it will be found that the amount to be corrected is not so small that another pattern of flow—for example, that around a circular cylinder gushing out from a point source situated ahead of the cylinder—would be more profitable. For this reason, five or six rounds of approximation have been necessary to get a convergent solution for a fixed location of the nose point of the shock wave. As the value of the nose location, $b/d = 0.3$, 0.5, 0.6, and 0.55 have been chosen in order, and the relation of connection factor K versus b/d has been obtained as shown in Fig. 13, where at the first through the third approximation the effect of rotation expressed by the correction term in Eq. (45) has been omitted in order to simplify the process of calculation. Interpolation by putting $K = 1$ gives the correct value of distance of detachment as $b/d = 0.57$. Variation of forms of streamlines and bow shock waves in every step of approximation is shown in Fig. 14 for the case of $b/d = 0.57$ as an example. In the region near the sonic line, flux integration for the continuity in Eq. (48) sometimes cannot reach the boundary values $\rho_1 q_1 y_1$ by way of approximation, and, in such a case,

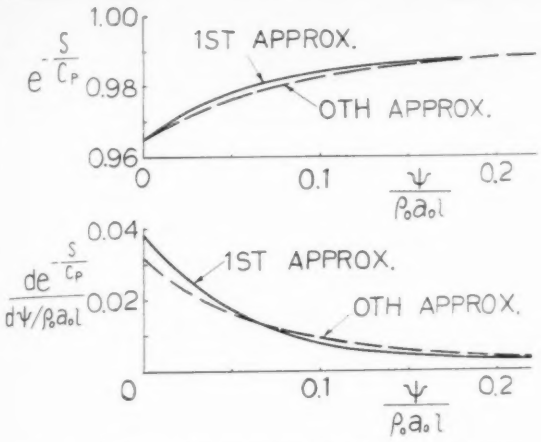

FIG. 11. Entropy distribution and its gradient (semiconvex airfoil).

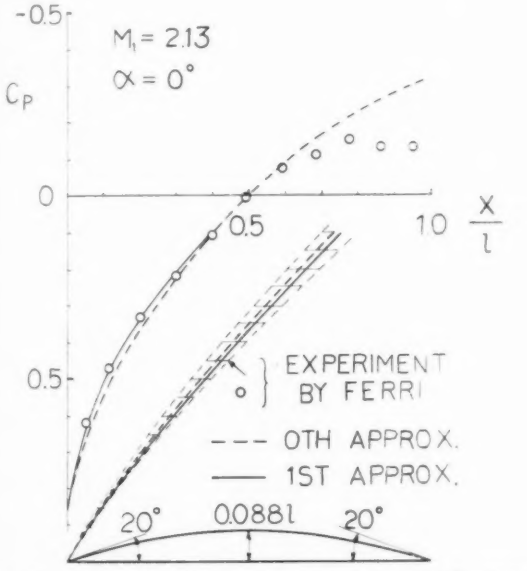

FIG. 12. Pressure coefficient and form of bow shock wave.

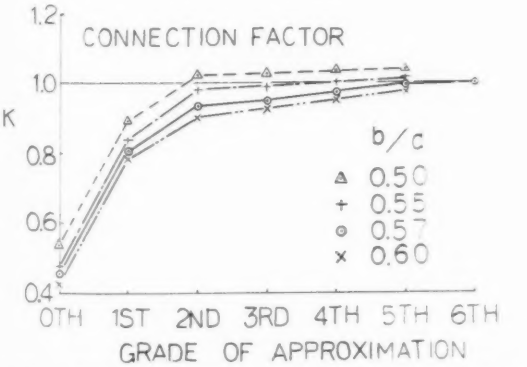

FIG. 13. Variation of connection factor in every step of approximation.

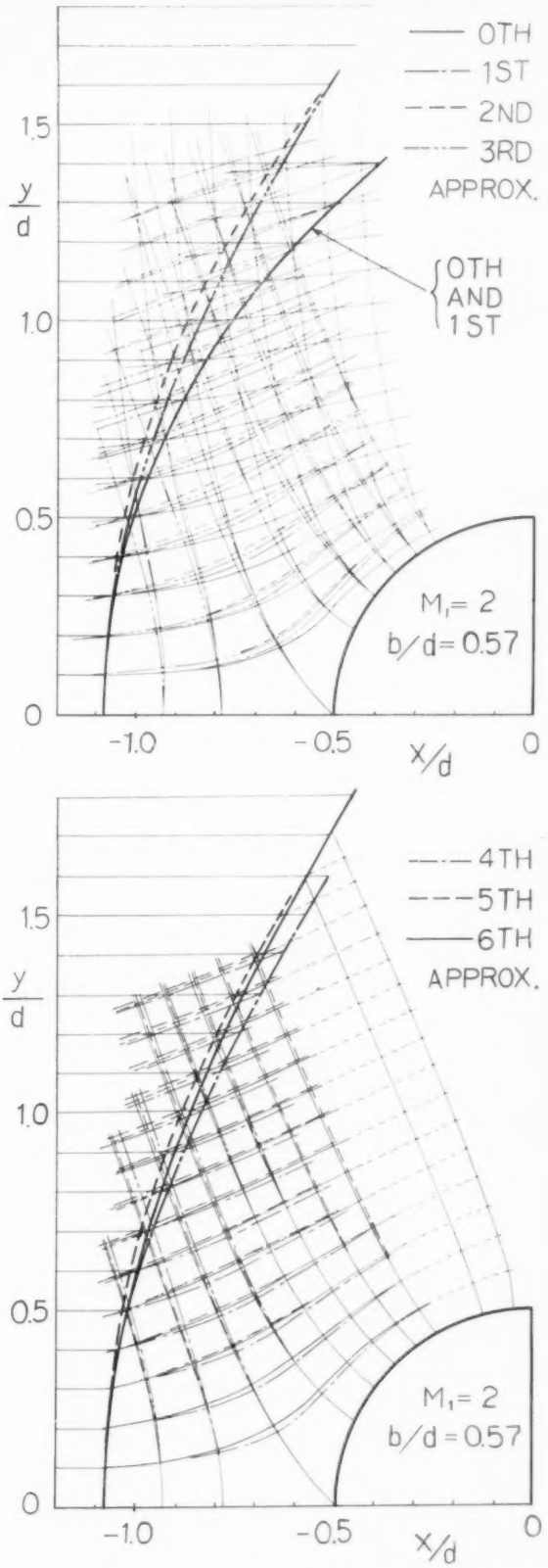

FIG. 14. Streamlines and form of bow shock waves in every stage of approximation for $b/d = 0.57$.

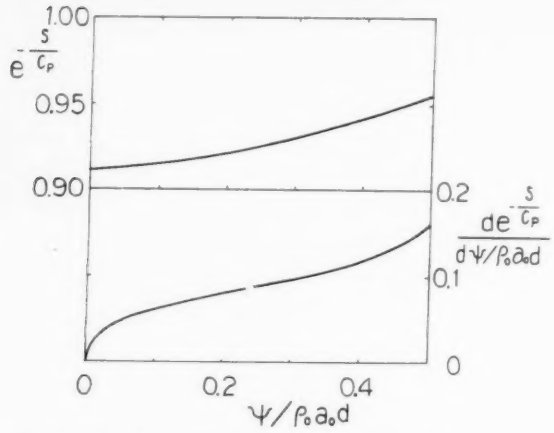

FIG. 15. Distribution of the entropy and its derivative (circular cylinder).

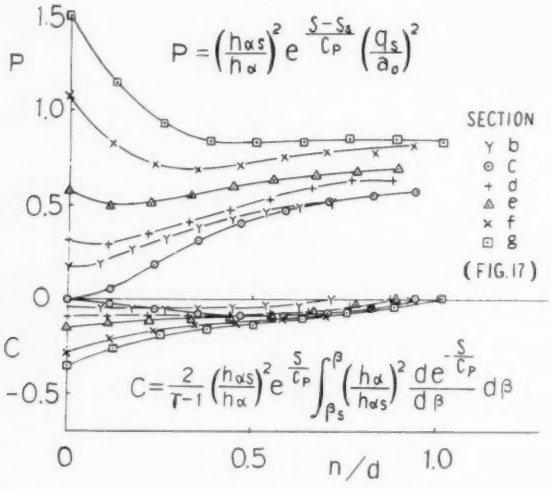

FIG. 16. Comparison of correction term of rotation with main term in $(q/a_0)^2$ (see Eq. 45).

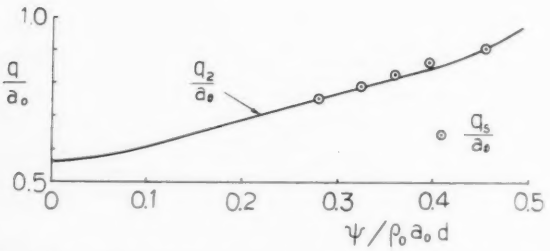

FIG. 18. Comparison of velocities immediately behind the bow shock wave obtained in the two different ways.

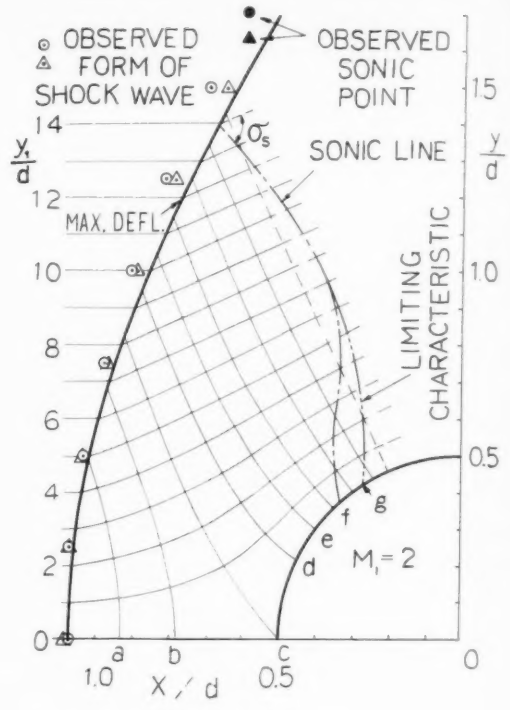

FIG. 17. Flow pattern.

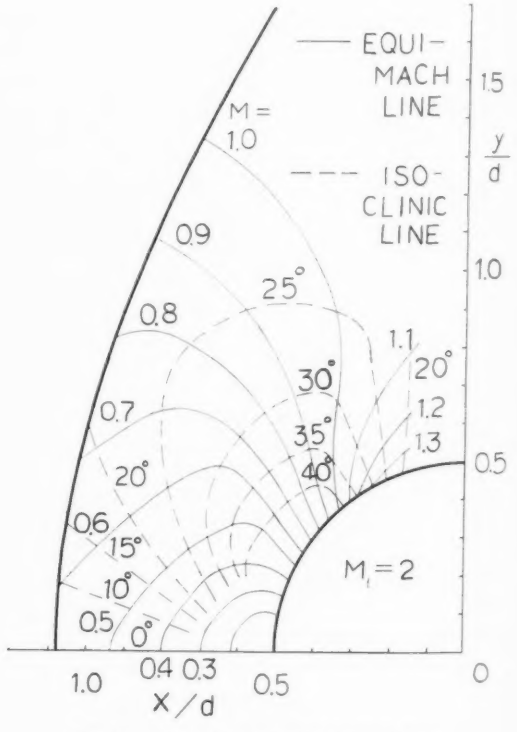

FIG. 19. Equi-Mach line and isoclinic line.

slight extrapolation of streamlines holding the curvature of upstream flow has been applied. Since the location of the shock wave is determined by the maximum flow angle, $\theta_{s\,max}$—which gives the connection factor K by $\theta_{s\,max}/\delta_{max}$—and not by the condition in the sonic point, it will not be affected directly by the superscripted obstacle. These inconveniences can be removed by choosing a more appropriate form of streamlines.

Distributions of entropy in exponential form and its derivatives with respect to the stream function are shown in Fig. 15. The magnitude of the correction term for rotation (C) reaches more than 40 per cent of the main term (P) in Eq. (45) as shown in Fig. 16.

A practically converged form of flow pattern is shown in Fig. 17 together with the sonic line and the limiting characteristics. In comparison with the observed form of the bow shock wave, which is marked by small circles and triangles, the present computation seems to give a fairly satisfactory configuration, excluding the area near the sonic region. The behavior of the sonic line will be the most remarkable one among these curves. The angle of intersection with the streamline, which is denoted by σ_s in Fig. 17, is 71° (±3°) immediately behind the shock wave and is less than a right angle, while perpendicular intersection takes place in the interior of the field. The magnitude of the angle has recently been obtained by Hashimoto,[29] who solved the local solution behind the shock wave in rigorous form. It has been found that the value of $\sigma_s = \pi/2$ is given when $M_1 = 1$ and $M_1 = 1.690$ ($\gamma = 1.4$) and $\sigma_s > \pi/2$ between $M_1 = 1 \sim 1.690$, while $\sigma_s < \pi/2$ when $M_1 > 1.690$. The exact value for $M_1 = 2$ is given by $\sigma_s = 73°34'$, and the present calculation shows fairly good agreement. Kim[30] has also supported this figure in his recent experiments.

Examination of the fulfillment of the boundary condition along the bow shock wave is made by comparing the boundary value of velocity, q_s/a_0—which is determined from the calculation of flow field—with the velocity immediately behind the shock wave, q_2/a_0—which is given from the shock angle and Mach Number of uniform flow by the shock conditions—and its result is shown in Fig. 18.

The Equi-Mach line, isoclinic line, and isopicnic line are presented in Figs. 19 and 20. Streamlines in the hodograph plane are also obtained as shown in Fig. 21. Pressure distributions along the surface of the circular cylinder are given in Fig. 22, comparing them with the observations.

The accuracy of the results will be fairly good in the field upstream of the region of maximum deflection, while it will not be good near the sonic region.

Experiments on the Supersonic Flow Around a Circular Cylinder

For the experimental investigations on the supersonic flow around a circular cylinder, pressure distributions along the surface of the cylinder were studied by

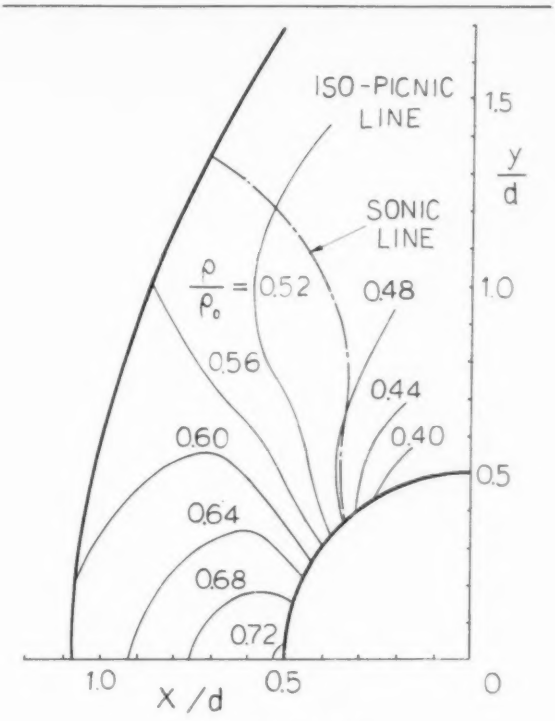

FIG. 20. Isopicnic line.

Eula,[31] Gowen and Perkins,[33] and Kim,[30] while the location of the detached shock wave was measured by Alperin[32] and Kim.[30] The present authors have also made several experiments on this problem to compare with the previous theory.

(a) *Wind Tunnel with a Multinozzle Grid*

Observation was made on supersonic flow produced by the multinozzle grid[34] which was devised first in Germany. It was fitted in the 20- by 12-cm. high-speed suction wind tunnel at the Institute of Science and Technology of the University of Tokyo, the plan of which is shown in Fig. 23. Passing through individual nozzles, the flow reaches supersonic velocity in the downstream portion of the grid. The shock wave of

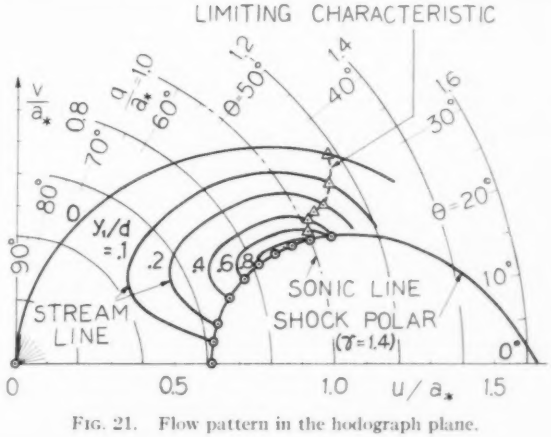

FIG. 21. Flow pattern in the hodograph plane.

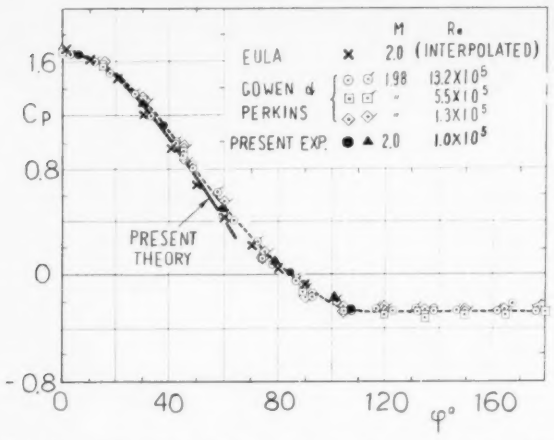

FIG. 22. Pressure distribution along the surface of circular cylinder.

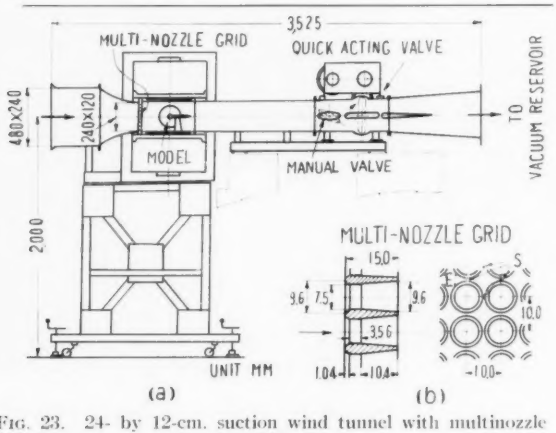

FIG. 23. 24- by 12-cm. suction wind tunnel with multinozzle grid.

narrow band produced at points S on the nozzle outlet [Fig. 23(b)] is so weakened by the expansion wave from points E that wavelets can be regarded as Mach waves in practice. This is shown by the fact that noticeable refraction by interference is not observed in schlieren photographs. Since the wake of region E will not be completely decayed, this form of multinozzle grid will not be suitable for the precise experiment of critical phenomena. The mean value of velocity distributions taken in the horizontal direction in the test section measured by the angle of Mach wave is shown in Fig. 24.

(*b*) *Model*

A circular cylinder of 10.02-mm. diameter made of brass was used. Along the surface ten holes were prepared for the measurement of pressure distributions. (See Fig. 25.)

(*c*) *Test on the End Effects*

In order to study the best end condition to realize two-dimensional flow, observations of the front of the bow shock wave were first made by setting the cylinder vertically at varying distance e from the wall. Schlieren photographs are presented in Fig. 26. When $e/d < 0.5$, compression effects by the existence of the cylinder recede within the boundary layer in the direction of upstream and a three-dimensional oblique shock wave is produced upstream, which interacts with the bow shock wave and slightly increases its detachment distance near the end. When $e/d > 0.7$, on the other hand, expansion of the flow around the end of the cylinder causes the depression and decreases the detachment distance. It is found that $e/d = 0.5 \sim 0.7$ will give a good configuration as the two-dimensional flow.

The measured value of the location of the shock wave is

$$b/d = 0.57$$

and is shown in Fig. 28 compared with other observations.

(*d*) *Results of Experiment and Comparison with the Theory and Other Experiments*

A schlieren photograph in the present experiment is shown in Fig. 27, the form of the bow shock wave being compared with the previous calculation in Fig. 17. The form of the sonic line could not be determined with sufficient accuracy; however, the sonic point on the bow shock wave is obtained for a more distant location than can be obtained with the theory.

The value of the pressure coefficient along the surface of the cylinder is obtained between those given by Eula[31] and Gowen and Perkins.[33] Despite the disagreement of the sonic point on the shock wave, the pressure distribution obtained by the present analysis is in fairly good agreement with the observations given in Fig. 22.

Asymptotic Solution of the Hypersonic Flow of Nonviscous and Nonheat-Conductive Fluid Along a Flat Plate

If the asymptotic solution along a flat plate is assumed to be given by the uniform parallel flow, its

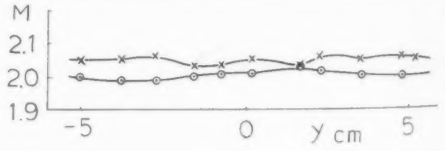

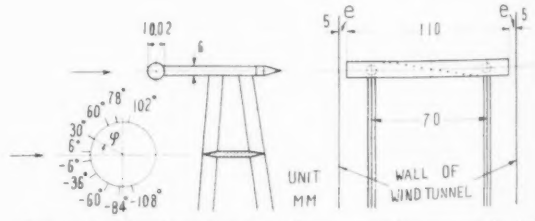

FIG. 24 (*top*). Distribution of Mach Number across the test section. FIG. 25 (*bottom*). Model and positions of pressure holes.

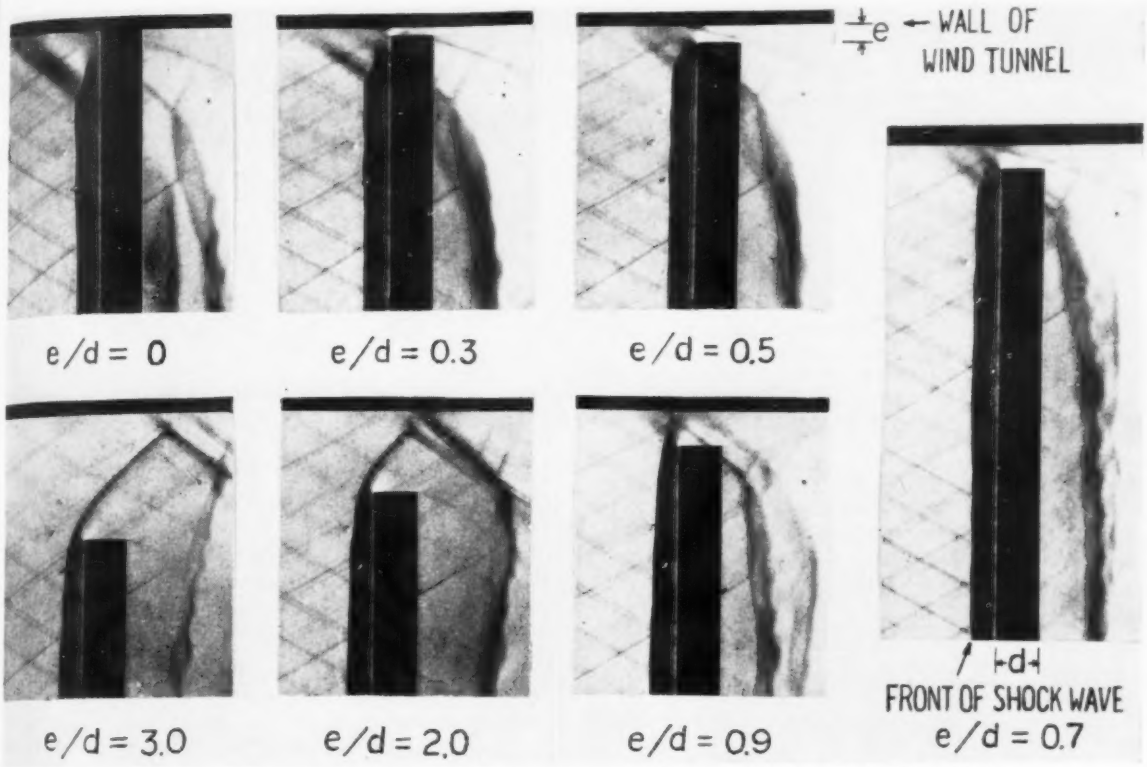

FIG. 26. Deformation and interference of the shock wave at the end of circular cylinder ($M_1 = 1.97$).

FIG. 27. Schlieren photograph of the flow around a circular cylinder ($M_1 = 1.97$).

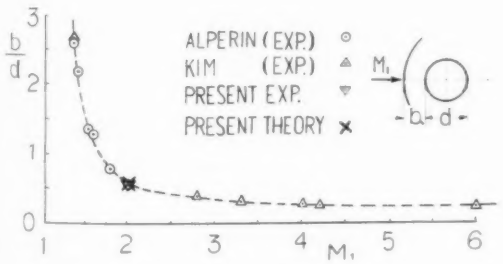

FIG. 28. Detachment distance of bow shock waves.

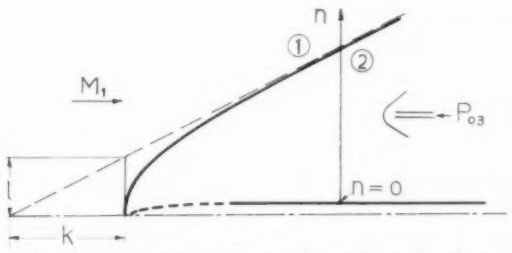

FIG. 29. Scheme of asymptotic flow along a flat plate.

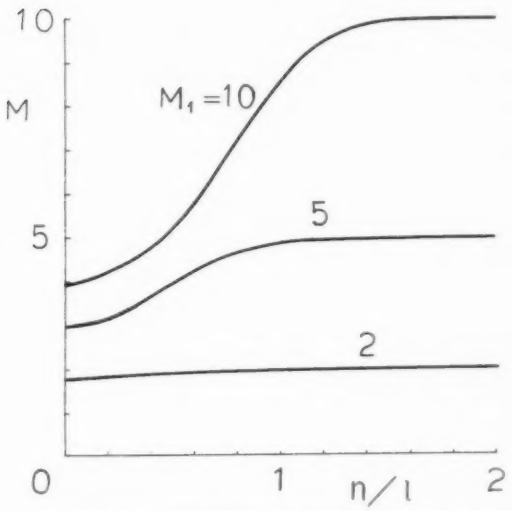

FIG. 30. Distribution of Mach Number.

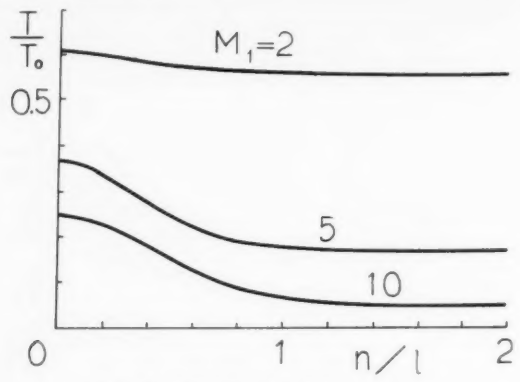

FIG. 31. Distribution of temperature.

solution will be obtained by integrating the superscripted characteristic relation in a broad sense.

Since the flow pattern is constructed by a grid of parallel straight lines, h_α is a constant along its orthogonal straight lines as shown in Fig. 29, and integration of Eq. (41) gives

$$\left[\frac{2}{\gamma-1}-\left(\frac{q}{a_0}\right)^2\right]e^{-(S/c_p)}=\left[\frac{2}{\gamma-1}-\left(\frac{q_b}{a_0}\right)^2\right]e^{-(S_b/c_p)} \tag{52}$$

The shock wave will be so weakened far from the leading edge in this case that it can be regarded as a Mach wave, and the flow can be directly connected with that of uniform upstream. If the range of integration reaches this boundary, invariant expression of it is given by

$$\left[\frac{2}{\gamma-1}-\left(\frac{q}{a_0}\right)^2\right]e^{-(S/c_p)}=\frac{2/(\gamma-1)}{1+[(\gamma-1)/2]M_1^2} \tag{53}$$

Substituting the entropy distribution

$$\frac{S-S_1}{c_p}=\frac{1}{\gamma}\ln\left[1+\frac{2\gamma}{\gamma+1}(M_1^2\sin^2\omega_1-1)\right]+\ln\left[1-\frac{2}{\gamma+1}\left(1-\frac{1}{M_1^2\sin^2\omega_1}\right)\right] \tag{54}$$

into Eq. (53), the velocity distribution is given by

$$\left(\frac{q}{a_0}\right)^2=\frac{2}{\gamma-1}\left[1-\frac{e^{[(S-S_1)/c_p]}}{1+[(\gamma-1)/2]M_1^2}\right]=\frac{2}{\gamma-1}-\frac{2/(\gamma-1)}{1+[(\gamma-1)/2]M_1^2}\left[\left\{1+\frac{2\gamma}{\gamma+1}(M_1^2\sin^2\omega_1-1)\right\}^{1/\gamma}\times\left\{1-\frac{2}{\gamma+1}\left(1-\frac{1}{M_1^2\sin^2\omega_1}\right)\right\}\right] \tag{55}$$

where ω_1 is given by the angle of tangent on the bow shock wave as

$$\omega_1=f(\psi) \tag{56}$$

The situation of the corresponding streamline is obtained by the equation of continuity, Eq. (34), as follows:

$$dn=h_\beta d\beta=d\psi/\rho q$$

or

$$d\left(\frac{n}{l}\right)=\frac{d(\psi/\rho_0 a_0 l)}{(\rho/\rho_0)(q/a_0)} \tag{57}$$

Substituting Eq. (46), integration of Eq. (57) gives

$$\frac{n}{l}=\int_0\left[1+\frac{2\gamma}{\gamma+1}(M_1^2\sin^2\omega_1-1)\right]^{1/(\gamma-1)}\times\left[1-\frac{2}{\gamma+1}\left(1-\frac{1}{M_1^2\sin^2\omega_1}\right)\right]^{\gamma/(\gamma-1)}\times\frac{d(\psi/\rho_0 a_0 l)}{\left[1-\frac{\gamma-1}{2}\left(\frac{q}{a_0}\right)^2\right]^{2-1/(\gamma-1)}\frac{q}{a_0}} \tag{58}$$

If the form of the bow shock wave is known, ω_1 is given as a function of ψ, and, accordingly, the velocities at the points arbitrarily distant from the flat plate will be obtained by Eqs. (55) and (58).

If the further assumptions that such an asymptotic solution can be realized with a known geometric form of the bow shock wave—say by a hyperbola, as shown in Fig. 29—by adjusting the sectional form of flat plate in the frontal part, the final form of the solution can be determined.

Calculating a few examples, distributions of Mach Number, flowing temperature, and the ratio of impact pressure p_{03} to the total pressure in the uniform upstream p_{01} are shown in Figs. 30, 31, and 32, respectively. It will be found that the remarkable deviation of these quantities from those of uniform upstream takes place mainly within the region $n/l = 1$.

CONCLUSIONS

Referring to the streamline coordinates, the vorticity equation in isoenergetic rotational flow is shown to be exactly integrated into Eq. (41) or (42), which gives a relation among velocity, flow pattern, and distribution of entropy across streamlines. It will be

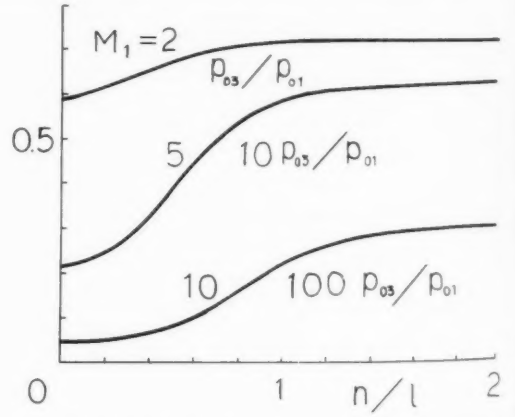

FIG. 32. Ratio of impulse pressure, p_{03}, to the total pressure in the uniform upstream, p_{01}.

valid as a formula for giving corrections of effects caused by rotation as shown in the example of semi-convex airfoils. The formula has also applied to the rotational flow with strong nonlinearity, which is given by the supersonic flow around a circular cylinder. The principle will be reasonable; however, higher accuracy cannot be expected in the practice of calculation, especially in the region adjacent to the sonic line. Compared with the observations, the sonic region seems to extend further from the cylinder. Flow patterns in the physical, as well as the hodograph, plane are, however, presented for the sake of references.

References

[1] Crocco, L., *Eine neue Stromfunktion für die Erforschung der Bewegung der Gase mit Rotation*, Zeitsch. Angew. Math. Mech., Vol. 17, No. 1, pp. 1–7, February, 1937.

[2] Lin, C. C., and Rubinov, S. I., *On the Flow Behind Curved Shocks*, J. Math. Phys., Vol. 27, No. 2, pp. 105–129, July, 1948.

[3] Dugundji, J., *An Investigation of the Detached Shock in Front of a Body of Revolution*, Journal of the Aeronautical Sciences, Vol. 15, No. 12, pp. 699–705, December, 1948.

[4] Thomas, T. Y., *The Distribution of Singular Shock Directions*, J. Math. Phys., Vol. 28, No. 3, pp. 153–172, October, 1949.

[5] Lin, C. C., and Shen, S. F., *An Analytic Determination of the Flow Behind a Symmetrical Curved Shock in a Uniform Stream*, NACA TN 2506, October, 1951.

[6] Melkus, H., *Über den abgelösten Verdichtungsstoss*, Ingenieur-Archiv, Vol. 19, No. 3, pp. 208–227, 1951.

[7] Cabannes, H., *Theoretical determination of the fluid flow behind a detached shock wave* (in French), ONERA Note tech. 5, 27 pp., 1951; AMR, Vol. 5, Rev. 781, March, 1952.

[8] Busemann, A., *A Review of Analytical Methods for the Treatment of Flows with Detached Shocks*, NACA TN 1858, April, 1949.

[9] Moeckel, W. E., *Approximate Method for Predicting Form and Location of Detached Shock Waves Ahead of Plane or Axially Symmetric Bodies*, NACA TN 1921, July, 1949.

[10] Vincenti, W. G., and Wagoner, C. B., *Transonic Flow past a Wedge Profile with Detached Bow Wave—General Analytical Method and Final Calculated Results*, NACA TN 2339, April, 1951; —*Details of Analysis*, NACA TN 2588, December, 1951.

[11] Goldstein, S., and Lighthill, M. J., *A Note on the Hodograph Transformation for the Two-dimensional Vortex Flow of an Incompressible Fluid*, Quart. J. Mech. Appl. Math., Vol. 3, Pt. 3, pp. 297–302, 1950.

[12] Pai, S. I., *On the Vorticity of the Flow Behind Curved Shock*, Readers' Forum, Journal of the Aeronautical Sciences, Vol. 17, No. 3, p. 188, March, 1950.

[13] Emmons, H. W., *The Theoretical Flow of a Frictionless, Adiabatic, Perfect Gas Inside of a Two-dimensional Hyperbolic Nozzle*, NACA TN 1003, 1946.

[14] Maccoll, J. W., and Codd, J., *Theoretical Investigations of the Flow around Various Bodies in the Sonic Region of Velocities*, Theor. Res. Rep., No. 17/45, Arm. Res. Dept., British MOS, September, 1945.

[15] Mitchell, A. R., *Application of Relaxation to the Rotational Field of Flow behind a Bow Shock Wave*, Quart. J. Mech. Appl. Math., Vol. 4, Pt. 3, pp. 371–383, September, 1951.

[16] Mitchell, A. R., *The Rotational Field behind a Bow Shock Wave in Axially Symmetric Flow using Relaxation Methods*, Proc. Roy. Soc. Edinburgh (A), Vol. 63, Pt. 4, No. 27, pp. 371–380, 1952.

[17] Laitone, E. V., *Location of Detached Shock Wave in Front of a Body Moving at Supersonic Speeds*, NACA RM A7B10, May, 1947.

[18] Tamada, K., *On Detached Shock Wave of Circular Cylinder and Sphere Moving with Supersonic Velocities*, Tomotika Lab., Tech. Memo., No. 25, Faculty of Physics, Univ. of Kyoto, September, 1950 (in Japanese).

[19] Kawamura, T., *A Note on the Detached Shock Wave in Front of a Body*, J. Japan Soc. Appl. Mech., Vol. 5, No. 30/31, pp. 162–165, December, 1952, January, 1953.

[20] Hida, K., *An Approximate Study on the Detached Shock Wave in Front of a Circular Cylinder and a Sphere*, J. Phys. Soc. Japan, Vol. 8, No. 6, pp. 740–745, November–December, 1953.

[21] Uchida, S., *A New Approximate Solution in Boundary Value Problems by the Use of Orthogonal Curvilinear Coordinates*, Rep. Inst. Sci. Tech., Univ. of Tokyo, Vol. 1, Nos. 7–8, pp. 101–105, July–August, 1947 (in Japanese); J. Phys. Soc. Japan, Vol. 3, No. 1, pp. 33–40, January–February, 1948.

[22] Uchida, S., *Calculation of Compressible Cascade Flow by the Method of Flux Analysis*, Journal of the Aeronautical Sciences, Vol. 21, No. 4, pp. 237–250, April, 1954.

[23] Meyer, R. E., *The Method of Characteristics for Problems of Compressible Flow Involving Two Independent Variables. Part I, The General Theory*, Quart. J. Mech. Appl. Math., Vol. 1, pp. 196–219, 1948.

[24] Fox, L., and Southwell, R. V., *On the Flow of Gas through a Nozzle with Velocities Exceeding the Speed of Sound*, Proc. Roy. Soc. London (A), Vol. 183, No. A 992, pp. 38–54, August, 1944.

[25] Green, J. R., and Southwell, R. V., *Relaxation Methods Applied to Engineering Problems, IX, High-speed Flow of Compressible Fluid through a Two-dimensional Nozzle*, Phil. Trans. Roy. Soc. London, Ser. A, Vol. 239, pp. 367–386, 1944; Math. Rev., Vol. 5, No. 9, p. 247, October, 1944.

[26] Vazsonyi, A., *On Rotational Gas Flow*, Quart. Appl. Math., Vol. 3, No. 1, pp. 29–37, April, 1945.

[27] Ferri, A., *Elements of Aerodynamics of Supersonic Flows*, The Macmillan Co., New York, 1949.

[28] Ferri, A., *Alcuni risultati sperimentali riguardanti profili alari provati alla galleria ultrasonora di Guidonia*, Atti di Guidonia No. 17, pp. 337–380, September, 1942.

[29] Hashimoto, J., *Characteristics of Flow near the Point of Intersection of Shock Wave and Sonic Line*, Preprint, Sectional Meeting of Appl. Math. Mech., Phys. Soc. Japan, p. 47, May, 1955 (to be published).

[30] Kim, C. S., *Experimental Studies of Supersonic Flow past a Circular Cylinder*, J. Phys. Soc. Japan, Vol. 11, No. 4, pp. 439–445, April, 1956.

[31] Eula, A., *L'influenza del numero di Reynolds ai grandi numeri di Mach*, Aerotecnica, Vol. 20, No. 1, pp. 20–29, January, 1940.

[32] Alperin, M., *Experimental Information on Two-dimensional Detached Shock Waves*, Jet Prop. Lab., Calif. Inst. Tech., Progress Rep. No. 4–44, pp. 1–26, May, 1950.

[33] Gowen, F. E., and Perkins, E. W., *Drag of Circular Cylinders for a Wide Range of Reynolds Numbers and Mach Numbers*, NACA TN 2960, June, 1953.

[34] Pankhurst, R. C., and Holder, D. W., *Wind-Tunnel Technique*, p. 110; Sir Isaac Pitman and Sons, Ltd., London, 1952.

On Equations of Motion for a Compressible Viscous Gas

E. V. LAITONE*

University of California at Berkeley

SUMMARY

It is first pointed out that, if Stokes relation is not used, the Navier-Stokes equations are better adapted for compressible viscous flow calculations than are the higher order kinetic theory approximations. The theoretical reasons underlying the introduction of the bulk viscosity into the Navier-Stokes equations are briefly discussed.

It is then shown that the higher order kinetic theory approximations attempting to improve the Navier-Stokes equations have not included all of the terms of the proper order because of the assumed form for the expansion of the distribution function. It is pointed out that the main term that can be legitimately added to the Navier-Stokes equations is the effect of thermal transpiration as first derived by Maxwell.

It is demonstrated that the first-order dynamic equations of continuum mechanics are relatively insensitive to the assumed physical model or molecular structure, since they only can affect an arbitrary constant.

Some comments and experimental observations on the effect of rigid body rotation are also included.

INTRODUCTION OF THE BULK VISCOSITY

ALTHOUGH THE FACT is not yet well known, it has been established that the usual form of the Navier-Stokes equations (see Lamb,[1] p. 577) for compressible flow are at best restricted to monatomic gases because of the use of Stokes[2] relation (see Lamb,[1] p. 574) between the shear viscosity μ and the dilatational viscosity λ (also called the volume, or compression, or second viscosity)

$$2\mu + 3\lambda = 0 \tag{1}$$

Tisza[3] was one of the first in this country to point out the severe restrictions implied in the use of Eq. (1) for other than monatomic fluids. Additional conclusive arguments and an extensive list of references are presented by Truesdell[4] and Rosenhead.[5]

Truesdell[6] showed that Stokes relation is valid only for a monatomic gas under the special conditions wherein it satisfies Maxwell's definitions of stress and temperature—that is, the pressure is a function of state alone and equal to the mean pressure, the stresses arise through transport of linear momentum by molecular diffusion, the temperature effect is directly related to the mean kinetic energy of translation only, and all properties are connected by the mean values of the molecules velocities relative to the mean motion of the gas. For this to be true it follows that Stokes relation is valid only for a monatomic gas that is sufficiently rare so that all triple or higher order collisions can be neglected, and yet not too rare so that the variation of any macroscopic quantities over a mean free path may also be neglected.

The proper forms of the Navier-Stokes equations for a polyatomic compressible fluid follow directly from Lamb[1] (pp. 574 and 576) if the dilatation viscosity is retained as an independent constant, as originally stated by Poisson (see reference 4, p. 228), so that one obtains

$$p_{xx} = -p + 2\mu u_x + \lambda(u_x + v_y + w_z) \tag{2}$$

$$p_{yx} = \mu(v_x + u_y) = p_{xy} \tag{3}$$

$$p_{zx} = \mu(u_z + w_x) = p_{xz} \tag{4}$$

and similarly for the other components. If the three normal stresses are averaged, one obtains the mean pressure

$$-\bar{p} = \frac{p_{xx} + p_{yy} + p_{zz}}{3} = -p + K(u_x + v_y + w_z) \tag{5}$$

where

$$K = \frac{2\mu + 3\lambda}{3} = -\frac{\rho(p - \bar{p})}{(\rho_t + u\rho_x + v\rho_y + w\rho_z)} \tag{6}$$

is the bulk viscosity (originally called the "second viscosity" by Lamb,[1] p. 645). The bulk viscosity is seen to be a direct indication of the departure from Stokes relation and of the deviation of the mean pressure $\bar{p}$ from the equation of state represented by the thermodynamic pressure p in an isotropic Newtonian fluid (see Lamb,[1] pp. 573 and 645, and Truesdell[4, 6]). It is obvious that for compressible flow only Eq. (1)—Stokes relation—makes the mean pressure $\bar{p}$ the same as the thermodynamic pressure p. Otherwise, the pressure is not an equation of state alone, but also depends upon the local dilatation. Then if we do not assume Stokes relation and retain λ as a separate constant as Poisson insisted, we obtain, in place of the present-day Navier-Stokes equations (following Lamb,[1] p. 576), for the x component of the motion in the absence of any body forces

$$\rho(u_t + uu_x + vu_x + wu_z) = \frac{\partial p_{xx}}{\partial x} + \frac{\partial p_{yy}}{\partial y} + \frac{\partial p_{zz}}{\partial z} =$$

$$\left[\begin{array}{r} -p_x + \mu(u_{xx} + u_{yy} + u_{zz}) + (\lambda + \mu)\dfrac{\partial}{\partial x} \times \\ (u_x + v_y + w_z) + \lambda_x(u_x + v_y + w_z) + \\ 2\mu_x u_x + \mu_y(v_x + u_y) + \mu_z(u_z + w_x) \end{array}\right] \tag{7}$$

Received July 1, 1955.

* Professor, Mechanical Engineering Department, College of Engineering.

or, for one-dimensional flow,

$$\rho(u_t + uu_x) = -p_x + (2\mu + \lambda)u_{xx} + u_x(\partial/\partial x)(2\mu + \lambda) \quad (8)$$

Consequently, for a monatomic gas that is not too dense, the use of the Stokes relation yields

$$K = 0, \qquad \lambda = -(2/3)\mu, \qquad (\lambda + \mu) = (1/3)\mu \quad (9)$$

reducing Eq. (7) to the usual form of the Navier-Stokes equations as given on page 577 of Lamb[1] when μ and λ are constant. However, Eq. (5) shows that Eq. (9) corresponds to the unwarranted assumption that the thermodynamic pressure is equal to the mean pressure. Truesdell[4, 6] points out that even the p represented in Eq. (5) may not be the thermodynamic pressure—that is, p is not necessarily an equation of state, as must be the density, for example, and its actual relationship must still be proved for specific applications (see also Lamb,[1] pp. 573 and 645).

Kinetic theory considerations show (see reference 5, p. 9) that a monatomic fluid with no bulk viscosity but with a so-called relaxation property has, in most acoustic applications if the frequency is not too high, a response identical to that of a fluid with a finite bulk viscosity. In addition, Enskog (see reference 10, pp. 286, 397) has shown that a dense monatomic gas tends to have a finite bulk viscosity. Because of these considerations, Eq. (9) is generally replaced by

$$(\lambda + \mu) = [(1/3)\mu + K] \geqq (1/3)\mu \quad (10)$$

However, this is not a rigorously valid assumption for relaxation effects, and it should be noted that this empirically defined bulk viscosity may not necessarily agree with that given in Eq. (6), since λ corresponds to a shear effect due to molecular transport (or perhaps only a transfer to rotational energy) in the direction of the moving boundary, whereas μ represents the better understood molecular transport normal to the mass transport. These two effects could conceivably have entirely different relaxation effects (see reference 5, pp. 41–42), a question which present day kinetic theory cannot answer, as pointed out by Truesdell,[4, 6] since to date no exact solution is available for a diatomic gas. On the other hand, the continuum derivation of the Navier-Stokes equations, in the form of Eq. (7), indicates that the bulk viscosity is a first-order continuum property of a diatomic gas, and may not necessarily have a relationship to a relaxation process. In addition, Eq. (7) shows that for two- or three-dimensional flow μ and λ enter in various other combinations than that given by Eq. (10). It is only in the one-dimensional case of Eq. (8) that a single grouping exists—namely,

$$(2\mu + \lambda) = [(4/3)\mu + K] \geqq (4/3)\mu \quad (11)$$

Although an "ersatz bulk viscosity" may be introduced for evaluating specific one-dimensional experimental relaxation results, as for the case of high frequency acoustic absorption in reference 5, still there is no assurance that the coefficient so determined is applicable to the steady-state one-dimensional hydrodynamic problem, let alone the two- or three-dimensional case.

The verification of Eq. (8) has been obtained[3, 4, 5] by its application to the measured values of acoustic absorption and attenuation for plane sound waves in polyatomic gases. Most of the experimental results for diatomic gases correlate with the application of Eq. (8) when $\lambda = 0$, a plausible value meaning pure dilatation produces no shear.

The corresponding measurements in liquids indicated that $\lambda \gg \mu$. However, as recently proved by Taylor (see reference 5, pp. 34–39), the extremely large values of the measured dilatation viscosity in a liquid can be due to the presence of a very minute fraction of suspended gas bubbles.

Gilbarg and Paolucci[7] applied Eq. (8) to the calculation of normal shock-wave thickness and showed that it gave very reasonable shock-wave thicknesses if measured values of the viscosity were allowed to vary with temperature through a power law corresponding to experimental data. Calculations in this manner with $\lambda = 0$ predicted the correct magnitude of the shock-wave thickness for air.

The experimental measurements of the actual plane shock profile by Sherman[8] have also confirmed Eq. (8), at least for Mach Numbers less than 2, by successfully predicting the temperature gradient measured with a wire probe traverse of a plane shock wave at low densities. On the other hand, Sherman's experimental data refute the various higher order kinetic theory approximations.

The latter finding is not surprising in view of the criticisms of kinetic theory that will be discussed later. It also agrees with similar comparisons with the experimental measurements of Greenspan[9] on the effect of viscosity on the attenuation and velocity of plane sound waves in helium. Better correlation can be obtained through Eq. (8) than by introducing higher order solutions of the Boltzmann equations, even for a monatomic gas.

Introduction of Higher Order Terms from Kinetic Theory

The third approximation of the kinetic theory development, as carried out by Burnett[11] in 1935 was hoped to provide some understanding of the effect of nonlinear terms upon the equations of motion. (See also reference 10, p. 260, noting that the so-called second-order equations of motion provide the next step after the Navier-Stokes linear viscosity terms, and for a rigorous solution require the complete third approximation to the velocity-distribution function f.) However, as just pointed out, a comparison of the second-order kinetic theory development with experimental data showed a discouraging lack of agreement.

It will now be shown that the failure of Burnett's[11] higher order kinetic theory development lies in the fact that his series expansion is incomplete because of the assumed form for the expansion of the distribution

function. Grad's solution[12] overcomes this objection but still fails to provide all the necessary second-order terms because the only terms evaluated by the use of Grad's improved method have been obtained from his "13-moment" approximation which again assumes a restricted form for the expansion of the distribution function f.

The form of the second approximation to the velocity distribution function f used in the Maxwell-Boltzmann integral equation by Burnett[11] had to be expressed as

$$f^{(1)} = f^{(0)} \left\{ 1 + F_1[UT_x + VT_y + WT_z] + F_2\left[\left(U^2 - \frac{C^2}{3}\right)u_x + \left(V^2 - \frac{C^2}{3}\right)v_y + \left(W^2 - \frac{C^2}{3}\right)w_z + UVd_1{}^2 + VWd_2{}^3 + WUd_3{}^1\right]\right\} \quad (12)$$

where $$d_j{}^i = (1/2)\left[(\partial u^i/\partial x_j) + (\partial u^j/\partial x_i)\right] \quad (13)$$

are the rates of shear deformation—that is,

$$d_1{}^2 = \left(\frac{v_x + u_y}{2}\right); \quad d_2{}^3 = \left(\frac{w_y + v_z}{2}\right); \quad d_3{}^1 = \left(\frac{u_z + w_x}{2}\right)$$

and the peculiar speed (see reference 10, pp. 26 and 49)

$$C = (U^2 + V^2 + W^2)^{1/2}$$

is the molecular velocity relative to the mean velocity of the gas $(u^2 + v^2 + w^2)^{1/2}$ so that the first-order or Maxwellian velocity distribution function is

$$f^{(0)} = \left(2\pi \frac{R}{m} T\right)^{-3/2} \exp\left(-\frac{mC^2}{2RT}\right) \quad (14)$$

The functions F_1 and F_2 are expressed by means of polynomials (of the argument C^2/T) whose numerical coefficients depend upon the law expressing the forces acting between two molecules.

This procedure is certainly valid for the second approximation, which leads to the usual Navier-Stokes equations, but to this order the form of the equations of motion are found to be entirely independent of the molecular forces that only affect the value of μ. However, Burnett used the same form for the third approximation of f by assuming that Eq. (12) could be generalized by replacing F_1 and F_2 by Sonine polynomials and assuming that the terms in the brackets could be continued as higher order spherical harmonic functions of (U, V, W) since the two brackets in Eq. (12) already correspond to spherical harmonics of degree one and two, respectively. It has not been shown that this expansion can prevent the loss of some higher order terms—even though it gives the correct answer for the second approximation for f—since the complete expression for the third approximation has never been obtained, let alone proved correct. There exists a forced symmetry about the principal axes for all squared and higher order velocity products, because of the symmetry of the spherical harmonics* and the method of evaluating the coefficients (see p. 386 of reference 11). This could cause the disappearance of some higher order terms even though the terms found may be correct. For example, Burnett determined the correct coefficient for $d_k{}^i d_j{}^k$, but most of the product terms predicted by Brillouin[14] and Truesdell[15] did not even occur. To illustrate, if we write for the rigid body rotation (the antisymmetric or vector part of the total displacement tensor)

$$\omega_j{}^i = \frac{1}{2}\left(\frac{\partial u^i}{\partial x_j} - \frac{\partial u^j}{\partial x_i}\right) \quad (15)$$

so that

$$\omega_1{}^2 = \left(\frac{v_x - u_y}{2}\right); \quad \omega_2{}^3 = \left(\frac{w_y - v_z}{2}\right); \quad \omega_3{}^1 = \left(\frac{u_z - w_x}{2}\right)$$

then such terms as $\omega_k{}^i \omega_j{}^k$, $d_k{}^i \omega_j{}^k$, etc. do form symmetric tensors invariant to rotation, even though $\omega_j{}^i$ itself does not possess this property, but could not occur in Burnett's expansion since the antisymmetric grouping expressed by Eq. (15) is not present. For example, out of the following three groups possible for two-dimensional flow

$$4(d_1{}^2)^2 = (v_x{}^2 + 2v_x u_y + u_y{}^2)$$
$$4(\omega_1{}^2)^2 = (v_x{}^2 - 2u_x u_y + u_y{}^2)$$
$$4d_1{}^2\omega_1{}^2 = (v_x{}^2 - u_y{}^2)$$

Burnett's method of expansion could only obtain the correct coefficient for the first possibility, or, as Truesdell points out (see reference 15, pp. 143–144), a restricted and artificial combination containing the last two.

Brillouin was the first to indicate (see reference 14, p. 450), that the complete expansion for f was assuredly obtained by multiplying *all* of the first derivatives of (u, v, w, t) by coefficients that are arbitrary functions of (U, V, W). Since the Maxwell-Boltzmann integral equation also contains the first derivatives as well as the integral of the product of f, it is evident that the higher approximations for f could contain all the possible combinations of the second derivatives and products of the first derivatives. This procedure would lead to a large number of terms, but as Brillouin[14] pointed out, only the few may be retained which are invariant—i.e., independent of choice or rotation of axes.

By extending Brillouin's method, but without using kinetic theory considerations, Truesdell[15] obtained a relation for the stress tensor in terms of all the possible symmetrical tensors derivable from the strain rate and the pressure and temperature gradients (see reference 15, p. 137, or reference 4, p. 249). Truesdell indicated that not only were product terms containing the rigid body rotation possible, but also further terms con-

* Instead of having an arbitrary coefficient for each individual velocity product as proposed by Maxwell,[13] certain groupings such as $(U^2 - V^2)$, $V(3U^2 - V^2)$, $U(U^2 - 3V^2)$, etc., occur, resulting in only one arbitrary coefficient for two velocity products.

taining products of the pressure gradient and derivatives of the external force field—altogether thirteen more terms than evaluated by Burnett (or only four more terms if it is further assumed that μ, λ, k are functions of the temperature only).

It will be shown later that the coefficients of the additional terms discovered by Brillouin and Truesdell are not necessarily all zero, at least for nonsymmetric molecules. Consequently, the Burnett expansion may not be complete.

The possibility of not obtaining all of the higher order terms because of the form assumed for the expansion for f does not occur in the exact expansion method developed by Grad,[12] at least for the special case of Maxwellian molecules. This new method is more in keeping with the original development introduced by Maxwell,[13] wherein all possible combinations of (U, V, W) were arranged in ascending powers, each ensuing term being multiplied by an arbitrary function of (ρ, T, u, v, w) or their derivatives (see reference 13, pp. 693–702). Maxwell had determined the relations to be satisfied by the arbitrary functions by substitution into the transport equations, keeping only the predominant terms until he finally had derived the thermal transpiration effect by a procedure that is only valid for the Maxwellian molecule.

Grad[12] improved and extended the possibilities for a converging series solution of the Maxwell-Boltzmann integral equation by noticing that the N-dimensional Hermite polynomials, having the velocity vector as their argument, would produce the appropriate separate products of the velocity components giving a general solution for f. The orthogonality property of these polynomials then allowed a representation of f as a convergent infinite series of Hermite functions, each multiplied by a coefficient which was an arbitrary function of (x, y, z, t) amenable to evaluation by means of an integration corresponding to the orthogonality relationship. This evaluation resulted in the coefficients being represented as moments which consisted of the integral of f multiplied by the corresponding velocity products—that is, as in Maxwell's equations of transfer the velocity squared terms corresponded to the pressure tensor and were called the second moment, while certain ones of the velocity cubed terms produced the heat flux vector as the contraction of the third moment, etc. At least twenty such moments are required for the evaluation of f to the first three terms of the Hermite expansion. The system of partial differential equations satisfied by these coefficients—expressed in terms of the moments as pressure tensor, heat flux vector, etc., rather than the velocity or temperature derivatives themselves—was found by then substituting this series expansion for f into the Maxwell-Boltzmann integral equation.

Because of the labor involved in even approximately solving the resulting infinite set of terms, Grad did all the calculations on the basis of his "13-moment" approximation (see reference 12, pp. 362–367, or reference 10, pp. 409–411). However, this simplified approximate solution of Grad's exact third-order expansion suffers from the same defect as Burnett's solution—namely, a restricted form for the distribution function which would prevent the evaluation of all the Brillouin-Truesdell[15] terms. This may be seen by comparing equation 5.6 with equation 4.10 of reference 12 (pp. 363 and 356).* The contracted Hermite polynomial used in the "13-moment" approximation again corresponds to the lack of an arbitrary coefficient for *each* velocity product, leading to a forced symmetry as already discussed in the Burnett case.

As a result, only the hitherto unsolved exact method of Grad,[12] or his limiting relation for slowly varying flow (equation 5.39, p. 374 of reference 12), may be considered to provide an improvement over the Navier-Stokes relations as expressed in Eq. (7). It is interesting to note that the additional terms contained in the limiting relation of Grad correspond almost identically to the "thermal transpiration" terms first derived by Maxwell,[13] the only difference being in the correction of a slight numerical error by Maxwell, and the retention of a separate coefficient of thermal conductivity (k).

The addition of Maxwell's[13] thermal transpiration effect to Eqs. (2), (3), and (4) would result in

$$\left.\begin{aligned}
p_{xx} &= -p + 2\mu u_x + \lambda(u_x + v_y + w_z) - \frac{4}{15} K_3 \frac{\mu}{p}\left[2\frac{\partial}{\partial x}(kT_x) - \frac{\partial}{\partial y}(kT_y) - \frac{\partial}{\partial z}(kT_z)\right] \\
p_{xy} &= p_{yx} = \mu(v_x + u_y) - \frac{2}{5} K_3 \frac{\mu}{p}\left[\frac{\partial}{\partial x}(kT_y) + \frac{\partial}{\partial y}(kT_x)\right] \\
p_{xz} &= p_{zx} = \mu(u_z + w_x) - \frac{2}{5} K_3 \frac{\mu}{p}\left[\frac{\partial}{\partial x}(kT_z) + \frac{\partial}{\partial z}(kT_x)\right]
\end{aligned}\right\} \quad (16)$$

The last term in each equation is the thermal transpiration effect as correctly rederived by Burnett (reference 11, p. 453) where the coefficient K_3 depends upon the molecular model assumed and becomes unity for the particular case of monatomic Maxwellian molecules. In the latter case, the transpiration term presented in Eq. (16) is in agreement with Grad[12] (p. 374), who also presents the correct form of the corresponding energy equation. It will be shown that these are probably the only rigorously valid equations available at present for the analysis of higher order effects as occurring in shock waves and in acoustic absorption at moderately high frequencies. Eq. (16) should provide a much better analysis of the structure of a shock wave since its form is such as to eliminate the anomalous predictions found by Sherman[8] when using Eq. (8) for Mach Number greater than 2. In addition, Eq. (16) should provide better solutions than those obtained using the addi-

* That is, the terms given by (UVW), ($UV^2 - U$), ($UW^2 - U$), ($U^3 - 3U$), etc., in the general Grad solution are contracted to $(U^2 + V^2 + W^2 - 5)U = U(C^2 - 5)$ in the "13-moment" approximation.

tional Burnett[11] terms, the "13-moment" method of Grad,[12] or the "cross-viscosity" term of Reiner as introduced by Gilbarg and Paolucci.[7]

The thermal transpiration term has a non-negligible effect since the heat conductivity coefficient k (in dynamic units) has a much greater order of magnitude than the viscosity coefficient μ; consequently, it should provide the predominant effect of the second derivative terms. If we follow Maxwell,[13] we should neglect products like $k_x T_x$ and, therefore, place k outside the brackets in Eq. (16). This would also make Eq. (16) agree with the form proposed by Brillouin[14] and Truesdell,[15] and finally agree with that given in Chapman and Cowling[10] for a monatomic gas since

$$K_3 = 1, \qquad K = 0, \qquad \lambda = -\frac{2}{3}\mu,$$

$$k = \frac{15}{4}\frac{R}{m}\mu = \frac{15}{4}\frac{p}{\rho T}\mu \qquad (17)$$

The thermal transpiration term provides the major correction to the Navier-Stokes equations since all of the remaining terms of the Burnett[11] or Grad[12] expansions are much smaller in magnitude, and even more important, as already indicated, all of the second-order terms actually have not yet been determined so it is impossible to evaluate the overall effect of all the remaining terms.

An inspection of the terms derived by Burnett (reference 11, p. 433, or reference 10, p. 265) shows immediately that the thermal transpiration effect is the major contribution for the usual aerodynamic problems since for steady adiabatic flow generally

$$\frac{\mu^2}{\rho T}|T_{xx}|_{\max} \gg \frac{\mu^2}{\rho T^2}T_x^2 > \frac{\mu^2}{\rho p T}|p_x T_x| > \frac{\mu^2}{p}|u_x^2|$$

because (independent of the degree of rarefaction)

$$0\left(\frac{\mu}{k}\right) = \frac{m}{R} = \frac{\rho T}{p} < 6 \times 10^{-4}\ \frac{\text{degrees}}{(\text{ft./sec.})^2} \qquad (18)$$

This not only indicates that Maxwell's thermal transpiration is the predominant effect, but that the products of temperature or pressure gradient terms cannot be neglected in comparison with the product terms of the velocity gradient as suggested in reference 7 (p. 640). All of these remaining terms of Burnett—that is, all those not included in Eq. (16)—are approximately the same order of magnitude and must all be retained whenever the thermal transpiration effect is not the predominant higher order effect. It must be borne in mind, however, that no general mathematical verification is available supporting Eq. (16) since the smallness in magnitude of a term in a differential equation does not guarantee that the resulting effect remains small.

If Eq. (16) is substituted into the proper equations of motion—e.g., reference 1, p. 576—the more general dynamic equations are obtained that contain the predominant higher order effect improving Eq. (7) as well as the first-order effect of a high degree of rarefaction. For example, for slowly varying one-dimensional flow, Eq. (16) would yield

$$\rho(u_t + uu_x) = -p_x + (2\mu + \lambda)u_{xx} + u_x\frac{\partial}{\partial x}(2\mu + \lambda) - \frac{8}{15}K_3\left(\frac{\mu k}{p}\right)T_{xxx} \qquad (19)$$

if we follow Maxwell[13] and neglect all the product terms in the thermal transpiration effect. This probably would provide the best equation for the analysis of shock-wave structure at Mach Numbers above 2, or the acoustic absorption at low pressures since in general $k \gg \mu$, so the thermal transpiration term may be considered as having the order of magnitude of (μ/p).

The corresponding predominant expression for the heat flux or energy equation may be obtained as

$$q_x = -kT_x + (4.5)[1 + (\lambda/2\mu)]\,(\mu k/p)Tu_{xx} \qquad (20)$$

The Effect of the Molecular Model upon the Equations of Motion

It is well known—e.g., see reference 10, pp. 118–123—that the assumed law of force acting during interaction of monatomic molecules has no direct effect upon the form of the first-order terms. That is, all molecular models lead to Eq. (2); the only ostensible effect lies in the determination of the value to be assigned to μ. However the second-order terms are directly affected by the assumed molecular model, as evinced by the appearance of the additional factor K_3 in Eq. (16)—also see reference 10, pp. 265–269. This indicates that only the first-order terms or Navier-Stokes equations of motion may be considered independent of the assumed physical model representing the viscous fluid.

The general applicability of the Navier-Stokes equations in the form corresponding to Eq. (7) for first-order effects is evident when one considers its basic derivation. Equivalent sets of first-order equations are obtained practically independent of the physical model assumed to represent the viscous fluid. For example, Stokes[2] concept of an elastic body, or the various and diverse molecular models of Navier, Poisson, and Maxwell all lead to analogous first-order effects. Even the basic consideration of a symmetric stress tensor linearly related to a symmetric strain tensor possessing the same principal axes leads almost directly to the Navier-Stokes equations.[4]

In order to illustrate the insensitivity of the Navier-Stokes equations to the physical model, a heuristic derivation will now be presented for a hypothetical compressible viscous gas that turns out to be considerably different in behavior when compared to the usual basic considerations of a symmetric tensor but still yields the same form for the dynamical equations. The foundation of this heuristic derivation stems from a direct application of the basic momentum principle and the assumption that a simple generalization of Newton's basic stress relation will predict the viscous stress for any departure from a uniform velocity so that

$$\frac{d}{dt}\int\int\int \rho\bar{V}dv = -\int\int p\bar{n}dS + \int\int \mu(\bar{n}\cdot\nabla)\bar{V}dS + \int\int \lambda_1(\nabla\cdot\bar{V})\bar{n}dS \quad (21)$$

The second integral on the right represents the viscous shear force on the bounding control surface S following the assumption that the shear stress is given by

$$\mu(d\bar{V}/dn) = \mu(\bar{n}\cdot\nabla)\bar{V} \quad (22)$$

The third integral on the right, as before, represents the compression viscosity due to dilatation. It must be noted that Eq. (22) corresponds to a first-order vortex friction due to rigid body rotation. This leads to a physically improbable behaviour that will be discussed later.

Then, using the general form of Gauss' theorem, Eq. (21) becomes

$$\frac{d}{dt}\int\int\int \rho\bar{V}\,dv = \int\int\int [-\nabla p + \nabla\cdot(\mu\nabla\bar{V}) + \nabla(\lambda_1\nabla\cdot\bar{V})]\,dv \quad (23)$$

These integral relations may be applicable in defining macroscopic effects having a steady mean flow. The question remains as to the proper way of defining p, μ and λ_1, for a given application. The pressure p is not the mean pressure $\bar{p}$ of Eq. (5), as originally defined by Stokes[2] (see Lamb,[1] p. 573), and may not even be the thermodynamic pressure, while μ may not have the same meaning as before. In any case, if Eq. (23) is directly integrated for slowly varying one-dimensional flow, we obtain

$$\rho(u_t + uu_x) = -p_x + (\mu + \lambda_1)u_{xx} + u_x(\partial/\partial x)(\mu + \lambda_1) \quad (24)$$

Then, if $\lambda_1 = \mu$, Eq. (24) becomes identical to that equation so successfully used for the analysis of plane shock waves in air by Sherman[8] and Gilbarg and Paolucci[7]—that is, for the case of $\lambda = 0$ in Eq. (8). This consistent agreement between Eqs. (8) and (24) actually must occur because the use of Eq. (24) in the comparison with the experimentally measured values in the linear range of sound absorption and attenuation would automatically yield $\lambda_1 = \mu$, as analogous to the predicted value of $\lambda = 0$ when using Eq. (8). This is obvious since the pertinent viscosity coefficient grouping remains in the one-dimensional dynamical equations as

$$2\mu + \lambda = \mu + \lambda_1 \approx 2\mu$$

$$\lambda \approx 0, \qquad \lambda_1 \approx \mu$$

in agreement with available experimental data on the acoustic absorption for diatomic gases in the linear range. The only possibility in distinguishing between the basic differences in the derivation of Eqs. (8) and (24) would be in the nonlinear high-frequency absorption data, because of the difference in the rate of energy dissipation in the two cases. However, the entire theory for this phenomenon is at present in a chaotic state. Heat conduction must be considered in the high-frequency equations, and even then a satisfactory agreement cannot be obtained without introducing empirical relaxation effects.[5]

In any case, there is no way at present to distinguish the dynamical equations of Navier-Stokes from those of Eq. (24) since they differ by an arbitrarily defined constant—only the rates of energy dissipation are dissimilar.

It is interesting to note that, at present, there exist no experimental data which could indicate whether or not the physical basis of Eq. (23) is valid. Kinetic theory considerations would show superficially that Eqs. (23) and (24) would be in agreement with the equations for a monatomic gas if $\lambda_1 = (1/3)\mu$ = constant, whereas first order kinetic theory directly provides $\lambda = -(2/3)\mu$.

However, from basic considerations it is obvious that Eq. (23) cannot be valid, at least for a Maxwellian monatomic gas, since the term containing μ has a direct physical relation to an unsymmetric tensor. This is so because it essentially contains the terms corresponding to the rigid body rotation ($\omega_j{}^i$), as well as the rate of deformation ($d_j{}^i$). That is, the stress tensor corresponding to Eq. (21) is written as

$$t_j{}^i = -p\delta_j{}^i + \mu(d_j{}^i + \omega_j{}^i) + \lambda_1 d_k{}^k\,\delta_j{}^i \quad (25)$$

in place of the usual Newton-Cauchy-Poisson relation (see reference 4, p. 126) corresponding to Eq. (2)—namely,

$$t_j{}^i = -p\delta_j{}^i + 2\mu d_j{}^i + \lambda\, d_k{}^k\,\delta_j{}^i \quad (26)$$

The direct shear strain in the isotropic case can be represented as a symmetric tensor, which has the same principal axes as the stress tensor, thereby allowing a linear relation between the stress and strain. On the contrary, the rigid body rotation is a vector or an antisymmetric—i.e., skew-symmetric—tensor that cannot be linearly related in an invariant manner to the symmetrical stress tensor. Physically this means that such a shear effect cannot be made to vanish through a rotation of the axes—that is, in this type of relation one cannot refer to any principal axes, and, therefore, there is no analogy to the stress ellipsoid. This would indicate a most implausible behavior, at least for first-order effects.

The elimination of this rigid body rotation provides the basic concept of a fluid in Stokes[2] principle (see reference 2, p. 80): "That the difference between the pressure on a plane in a given direction passing through any point P of a fluid in motion and the pressure which would exist in all directions about P if the fluid in its neighborhood were in a state of relative equilibrium depends only on the relative motion of the fluid immediately about P; and that the relative motion due to any motion of rotation may be eliminated without affecting the differences of the pressures above mentioned."

It is obvious that a rigid body rotation could not produce any shear force in a solid body. However, this

may be but one addition to the many reasons (see reference 4, p. 234) for a profound difference between an elastic body and a fluid, since there is absolutely no *a priori* reason why a polyatomic gas cannot produce such a shear effect, at least for second-order deformations. Even the second-order Burnett terms from kinetic theory can provide a somewhat similar shear strain for rigid body rotation, although in this case Truesdell[4] (see p. 251) has some valid objections. However, could a "rigid body rotation" of a gas be possible without any dissipation of energy? There seems to be a fundamental inconsistency in the fact that a rigid body rotation should produce no viscous resistance, or energy dissipation, and yet a rigid body rotation in *any* fluid is a nonpotential motion that must require an energy dissipation in order to create it. Perhaps it even requires a continual second-order energy dissipation in order to maintain it; if so, there must exist a so-called "vortex friction."

The question concerning rigid body rotation and first-order vortex friction had been raised by Mohr[16] on the basis of heuristic kinetic theory arguments which were correctly refuted by Fues[17] for the case of a monatomic Maxwellian gas. However, there still remains the possibility of a finite second-order vortex friction effect for a polyatomic gas because of the probability of a second-order deviation from a conservation of angular momentum in a nonuniform flow field. For example, the centrifugal force field conceivably could have some effect in a nonuniform flow. Fues' argument[17] that shows the centrifugal force cannot produce a shear effect is correct but is not complete since it does not eliminate the possibility that a velocity gradient, even in a steady mean flow, continually subjects new groups of molecules to a nonuniform centrifugal force field. The molecular movement resulting from the centrifugal force field may be negligible to the first order, but certainly not in all cases. For example, Maxwell[13] showed that a monatomic gas cannot rotate as a rigid body unless the density distribution varies exponentially. This effect is generally small since a tangential velocity of magnitude 1/10 the average molecular speed produces less than 1 per cent density variation in a rotating cylinder containing hydrogen. For a dense polyatomic gas, there may be a much stronger effect due to a second-order deviation from a conservation of angular momentum, effectively noncentral molecular forces, and non-conservative internal energy changes in a nonuniform flow field.

However, if the rigid body rotation produced only this type of a second-order friction effect, it would not justify Eq. (25) or Mohr's argument[16] since the rotational tensor is antisymmetric and could be related to the shear stress in an invariant manner only if it were introduced in a scalar form. The effect of this term certainly would be much smaller than the direct shear stress since it would be related to ω^2 as a second-order effect; therefore, as a Brillouin-Truesdell[15] term and not at all related to Eq. (25). That is, Eq. (26) and the Navier-Stokes equations would remain the proper first-order relations.

Rigid Body Rotation and the Brillouin-Truesdell Higher Order Terms

The likelihood of the previously mentioned Brillouin-Truesdell[15] terms will now be demonstrated in the simple example of a fluid contained in a vertical rotating circular cylinder. This will also illustrate the striking difference between a liquid and a gas whenever one considers the nonlinear terms (for the basic differences between an elastic body and a fluid see reference 4, p. 234).

In the rotating cylinder a liquid would maintain a constant density and temperature to a higher order of approximation, while only the pressure at a fixed elevation would vary as

$$p = p_0 + (1/2)\rho_0(r\omega)^2 \tag{27}$$

On the other hand, a gas could satisfy the Maxwell-Boltzmann equation, or the *first-order* quantum mechanics equilibrium conditions, only if the temperature were uniformly constant, so that at a fixed elevation the pressure and density both would vary as

$$\frac{p}{p_0} = \frac{\rho}{\rho_0} = \exp\left[\frac{(r\omega)^2}{2(R/m)T_0}\right] = 1 + \frac{(r\omega)^2}{2(R/m)T_0} + \frac{(r\omega)^4}{8(R/mT_0)^2} + \ldots \tag{28}$$

It is seen that to the order of ω^2 Eqs. (27) and (28) are identical since

$$p_0 = \rho_0(R/m)T_0 \tag{29}$$

Eq. (28) may be derived from either ordinary hydrostatics combined with Eq. (29), or the Navier-Stokes equations, or the Burnett equations, since $d_k{}^k \equiv 0$, $d_j{}^i \equiv 0$, and T = constant.

However, if the Burnett equations are applied to *any* other (p, ρ, T) relation, they will yield a shear stress (according to Truesdell,[15] p. 144). For example, if we assume constant density and Eq. (27) for the pressure variation, then the Burnett solution yields (see reference 11, p. 433)

$$p_{zz} + p = \left[\frac{4}{15}K_3\frac{\mu}{p}\frac{m}{R}(2k + xk_x + yk_y)\omega^2 - \frac{4}{15}K_4\frac{\mu k}{pT}\left(\frac{m}{R}\right)^2(x^2 + y^2)\omega^4\right] \tag{30}$$

$$p_{zx} = 0 = p_{zy}$$

$$p_{xy} = p_{yx} = (4/5)K_4(\mu k/pT)(m/R)^2\,xy\omega^4$$

which, to the order ω^2, agrees with Eq. (16) or Grad's solution (reference 12, p. 374). For Maxwellian molecules, Eq. (30) reduces to

$$p_{zz} + p = (\mu/p)(2\mu + x\mu_x + y\mu_y)\omega^2 \approx 2(\mu^2/p)\omega^2 \tag{31}$$

$$p_{zx} = p_{zy} = p_{xy} = 0$$

which agrees exactly with Grad's solution.

However, this is precisely the type of term predicted by the relation

$$\left.\begin{aligned} \frac{\mu^2}{p}\,\omega_k{}^i\omega_j{}^k &= \frac{\mu^2}{p}\begin{vmatrix}\omega^2 & 0\\ 0 & \omega^2\end{vmatrix} \\ \omega = |\,\omega_1{}^2\,| &= \left|\frac{v_x - u_y}{2}\right| \end{aligned}\right\} \tag{32}$$

indicating the possibility of the appearance of all the Brillouin-Truesdell[15] terms.

It is easily shown that the addition of Eq. (32) to the Burnett or Grad solutions, or to Eq. (16), makes it possible to modify the classical solution, given by Eq. (28), for the effect of nonconservative collisions in a centrifugal force field. This would certainly be required for polyatomic gases since Maxwell has already shown (see reference 13, p. 739) that Eq. (28) is an approximation that is valid only if the difference between the kinetic energy of the molecules and the internal energy of the gas is neglected. In addition, the dissipation indicated by Eq. (32) would be in complete agreement with Jeans' concept[18] of the persistence of velocity. Since the outer molecules on the average are actually moving faster in space than the inner ones, therefore the persistence of velocity after a collision would tend to produce an increase in the speed of the inner molecules, and likewise a decrease in the speed of the outer molecules. This would lead to a slip condition at the wall and a continual dissipation of energy, in agreement with Eq. (32), since it would be a higher order effect, directly dependent on the assumed intermolecular forces.

A simple experiment, determining whether or not the persistence of velocity could produce a slip at the boundary and a shear effect varying with ω^2 or ω^4, would be to measure the temperature increase of a gas at various low pressures when contained in a cylinder rotating in a vacuum.

On a somewhat reduced scale similar considerations should also apply in a liquid flow. For example, the rotating cylinder containing a liquid would eventually approach a steady state if Stokes principle[2] were always true. However, if a rigid body rotation created an effective second-order energy dissipation, then the steady state would never be attained, slip would occur at the cylinder walls, and an internal oscillation of the fluid could occur in order to dissipate the angular momentum.

The author believes he has observed this oscillation in water contained in a vertical rotating circular cylinder with a free surface. When a dye was streaked across the free water surface in such a manner that spiral configurations were formed, then after a long period of rotation, although no appreciable radial diffusion of the dye was apparent, still the central annuli of water exhibited a slowly varying rotation speed that became alternately greater or less than the rotation of the cylinder. However this experiment would be extremely critical to external vibrations and thermal convection, and the author is not certain that all such external disturbances were negligible.

In addition, the free water surface did not maintain a smooth parabolic profile but had a slowly varying perturbation of finite length. This may have been related to the inviscid "cellular inertia waves" investigated by Bjerknes and Solberg.[19] In order to determine whether or not viscosity or surface tension had a role in this phenomenon, the experiment was repeated using a light oil in the rotating cylinder. The parabolic surface was not very smooth and no oscillations were apparent. However observations with small paper fibers that were slowly sinking to the bottom of the rotating cylinder indicated that the annuli less than midway to the cylinder wall could rotate more rapidly than the wall itself.

This phenomenon would be in complete agreement with Jeans' persistence of velocity effect[18] as previously discussed. In any case, its existence would show that Reiner's "cross-viscosity" term[20] by itself could not represent all the possible second-order effects in a general liquid. As a matter of fact, the same mathematical arguments used by Reiner[20] to introduce the term $d_k{}^i d_j{}^k$ would also apply for $\omega_k{}^i\omega_j{}^k$ and $d_k{}^i\omega_j{}^k$ since they form symmetric tensors invariant to any rotation or translation of the axes.

Therefore, the generalized liquid that possessed a second-order vortex friction must have a symmetric stress tensor represented by

$$t_j{}^i = F_0\delta_j{}^i + F_1 d_j{}^i + F_2 d_k{}^i d_j{}^k + F_3\omega_k{}^i\omega_j{}^k + F_4 d_k{}^i\omega_j{}^k \tag{33}$$

This would, of course, define a non-Stokesian liquid since the stress is now dependent on the vorticity. Brillouin[14] and Truesdell[15] include all the terms of Eq. (33) in their more general fluid relation, which also includes other effects such as those produced by temperature and pressure gradients in gases. However, both thought it probable that F_3 would be zero, Brillouin's[14] argument being that no stresses could be created by a rigid body rotation when the rate of deformation vanished, at least for the case of conservative intermolecular forces (see reference 14, p. 453). Yet the only possibility of explaining the preceding experimental behavior (provided the phenomenon still occurs in steady rotation when *all* external disturbances are eliminated) is by means of the term containing F_3 since all of the remaining terms vanish (except $F_0 = -p$), because $d_k{}^i = 0$ for any rotating fluid.

For a gas, Eq. (32) indicates that F_3 would be related to (μ^2/p). If this were true then Maxwell's thermal transpiration effect would still remain the predominant term, as indicated by the inequalities preceding Eq. (18), and Eq. (16) would still provide the best general solution for most cases other than the rotating container. At least, as previously pointed out, it would not be justifiable to retain any of the remaining second-order Burnett[11] or "13-moment" Grad[12] terms since those corresponding to F_3 and F_4 in Eq. (33) seem to have been lost in the process of obtaining a solution.

Addendum*

In the *Journal of Rational Mechanics and Analysis*, Vol. 5, pp. 1–128, 1956, Ikenberry and Truesdell present a rigorous mathematical analysis of the erroneous behavior of the Burnett expansion method and the Grad "13-moment" approximation. Truesdell shows, by comparison with the exact solution for a simple shearing flow defined by u_x/y = constant, that the Maxwellian iteration process only converges for $\mu u_x/py < \sqrt{2}/3$. Also, by comparison with a mathematical model simulating the exact equations of motion for a Maxwellian molecule, Truesdell indicates that in general no universal formulas, valid for all initial or boundary conditions, can result beyond the Navier-Stokes order of approximation and that in a specific case the Navier-Stokes equations more closely approximate the true asymptotic solution than does any finite sum of higher order approximations.

References

[1] Lamb, H., *Hydrodynamics*, 6th Ed., pp. 571–581, 645. Cambridge Univ. Press, Cambridge, England, 1932.

[2] Stokes, G. G., *Mathematical and Physical Papers*, Vol. I, pp. 78–93, 116–120, 182–185, Vol. III, pp. 69–71, p. 136, Cambridge Univ. Press, Cambridge, England, 1880.

[3] Tisza, L., *Supersonic Absorption and Stokes' Viscosity Relation*, Physical Review (Ser. 2), Vol. 61, pp. 531–536, April, 1942.

[4] Truesdell, C., *The Mechanical Foundations of Elasticity and Fluid Dynamics*, Journal of Rational Mechanics and Analysis, Vol. 1, pp. 125–300, 1952.

[5] *A Discussion on the First and Second Viscosities of Fluids*, Proceedings of the Royal Society (Ser. A), Vol. 226, pp. 1–69. (October, 1954).

[6] Truesdell, C., *On the Viscosity of Fluid According to the Kinetic Theory*, Zeitschrift für Physik, Vol. 131, pp. 272–289, 1952.

[7] Gilbarg, D., and Paolucci, D., *The Structure of Shock Waves in the Continuum Theory of Fluids*, Journal of Rational Mechanics and Analysis, Vol. 2, pp. 617–642, 1953.

[8] Sherman, F. S., *A Low Density Wind Tunnel Study of Shock Wave Structure and Relaxation Phenomena in Gases*, University of California, Berkeley, Institute of Engineering Research Report HE-150-122, May, 1954.

[9] Greenspan, Martin, *Propagation of Sound in Rarefied Helium*, Journal of the Acoustical Society of America, Vol. 22, No. 5, pp. 568–571, September, 1950.

[10] Chapman, S., and Cowling, T. G., *The Mathematical Theory of Non-Uniform Gases*, 2nd Ed.; Cambridge Univ. Press, Cambridge, England, 1952.

[11] Burnett, D., *The Distribution of Molecular Velocities and the Mean Motion in a Non-Uniform Gas*, Proceedings of the London Mathematical Society, Ser. 2, Vol. 40, pp. 382–435, December, 1935.

[12] Grad, H., *On the Kinetic Theory of Rarefied Gases*, Communications in Pure and Applied Mathematics, Vol. 2, pp. 331–407, December, 1949.

[13] Maxwell, J. C., *Scientific Papers*, Cambridge Univ. Press, Vol. II, pp. 26–78, 681–741, 1890. Reprinted by Dover Publications, N. Y.

[14] Brillouin, M., *Théorie Moléculaire des Gaz. Diffusion du Mouvement et de l'Energie*, Annales de Chemie et de Physique, Ser. 7, Vol. 20, pp. 440–485, 1900.

[15] Truesdell, C., *A New Definition of a Fluid. II. The Maxwellian Fluid*, Journal Mathematiques Pures et Appliquees, Vol. 30, pp. 111–158, April, 1951.

[16] Mohr, Ernst, *The Navier-Stokes Stress Principle for Viscous Fluids*, NACA TM. 1029. See also Zeitschrift für Physik, Vol. 119, pp. 575–580, 1942.

[17] Fues, E., *Gibt es Wirbelreibung?*, Zeitschrift für Physik, Vol. 118, pp. 409–415, 1941, and Vol. 121, pp. 58–62, 1943.

[18] Jeans, J., *The Dynamical Theory of Gases*, 4th Ed., Cambridge Univ. Press, 1925. Reprinted by Dover Publications, N. Y.

[19] Bjerknes, V., and Solberg, H., *Avhandlinger utgitt av Det.*, Norske Videnskapl Akademie i Oslo, I Matem. Naturrid Klasse, 1929; No. 7 (See *Hydrodynamics*, pp. 271–279, Bulletin No. 84, National Research Council, Washington, D. C., 1931).

[20] Reiner, M., *A Mathematical Theory of Dilatancy*, American Journal of Mathematics, Vol. 67, pp. 350–362, July, 1945.

* Note added March, 1956.

Stiffness and Deflection Analysis of Complex Structures

(*Continued from page 823*)

[2] Levy, S., *Computation of Influence Coefficients for Aircraft Structures with Discontinuities and Sweepback*, Journal of the Aeronautical Sciences, Vol. 14, No. 10, p. 547, October, 1947.

[3] Lang, A. L., and Bisplinghoff, R. L., *Some Results of Sweptback Wing Structural Studies*, Journal of the Aeronautical Sciences, Vol. 18, No. 11, p. 705, November, 1951.

[4] Langefors, B., *Analysis of Elastic Structures by Matrix Transformation with Special Regard to Semimonocoque Structures*, Journal of the Aeronautical Sciences, Vol. 19, No. 8, p. 451, July, 1952.

[5] Rand, T., *An Approximate Method for the Calculation of Stresses in Sweptback Wings*, Journal of the Aeronautical Sciences, Vol. 18, No. 1, p. 61, January, 1951.

[6] Wehle, L. B., and Lansing, W., *A Method for Reducing the Analysis of Complex Redundant Structures to a Routine Procedure*, Journal of the Aeronautical Sciences, Vol. 19, No. 10, p. 677, October, 1952.

[7] Fung, Y. C., *Bending of Thin Elastic Plates of Variable Thickness*, Journal of the Aeronautical Sciences, Vol. 20, No. 7, p. 455, July, 1953.

[8] Reissner, E., and Stein, M., *Torsion and Transverse Bending of Cantilever Plates*, NACA TN 2369, 1951.

[9] Benscoter, S., and MacNeal, R., *Equivalent Plate Theory for a Straight Multicell Wing*, NACA TN 2786, 1952.

[10] Levy, S., *Structural Analysis and Influence Coefficients for Delta Wings*, Journal of the Aeronautical Sciences, Vol. 20, No. 7, p. 449, July, 1953.

[11] Schuerch, H. U., *Delta Wing Design Analysis*, Paper presented at SAE National Aeronautic Meeting, Los Angeles, September 29–October 3, 1953, Preprint No. 141.

[12] Hrennikoff, A., *Solution of Problems of Elasticity by the Framework Method*, Journal of Applied Mechanics, Vol. 8, No. 4, December, 1941.

[13] Hemp, W. S., *On the Application of Oblique Coordinates to Problems of Plane Elasticity and Swept Back Wings*, Report No. 31, The College of Aeronautics, Cranfield, England, 1950.

[14] Reissner, E., *Analysis of Shear Lag in Box Beams by the Principle of Minimum Potential Energy*, Quart. Appl. Math., Vol. IV, No. 3, October, 1946.

An Investigation of the Noise Produced by a Subsonic Air Jet*

J. H. GERRARD†
University of Manchester

SUMMARY

To investigate the theoretical predictions of Lighthill[2] on aerodynamic sound, measurements have been made of the sound field of a 1 in. air jet issuing from a long pipe. The measurements have been made over a wide frequency band (30 to 10,000 cycles/sec.) and in 1/3 octave bands in this frequency range. The mean Mach Number at the pipe orifice was varied from 0.3 to 1.0.

The dependence of the apparent position of the noise sources on frequency and jet speed was investigated. At a given frequency a source is situated farther from the jet orifice the higher the jet speed. Lower frequency sources appear farther downstream than ones of higher frequency, consistent with their association with larger eddies. The directional characteristics of the sound field at different frequencies and jet speeds are illustrated by means of scale diagrams showing lines of constant sound intensity. These sound fields are analyzed in terms of the moving quadrupole sources of Lighthill's theory and good agreement obtained. It is shown that the apparent spread of the sources at low frequencies is due to the Doppler effect. At low frequency (relative to the frequency of maximum power output) the radiation is predominantly that of three mutually orthogonal longitudinal quadrupoles which, except for the effect of convection upon it, has a sound field like a monopole source. At higher frequencies the sound fields of lateral and longitudinal quadrupoles predominate.

The dependence of the noise intensity upon jet speed is examined in terms of the power law relation; $\bar{p}^2 \propto M^n$. The exponent (n) depends upon the Mach Number (M_c) of convection of the sources which is a function of frequency; because of this dependence n also varies with direction, being greater in downstream directions than in upstream directions. From this variation with direction it is concluded that at a given jet speed there is a frequency at which M_c is a maximum; this maximum frequency increases with jet speed. The values of M_c are comparable with unity, and therefore the Doppler effect has to be considered when analyzing the sound field. For radiation at right angles to the direction of motion of the source the exponent is the same as for a stationary source: thus a more direct comparison with theory is made.

The spectrum of the acoustic power output of the jet derived by integration of the measured noise intensity is found to be extremely flat. The maximum power output lies at about 4 kc./sec. and is almost independent of jet speed. This independence is thought to be partly due to the convection of the noise sources and partly to acoustic radiation damping.

The acoustic efficiency of the jet is found to be very small: $10^{-4}\ M^{6.2}$ in the frequency band from 30 to 10,000 cycles/sec. The values of the efficiency (η) per 1/3 octave are derived and from these the quotient η/M^{n_1-3}: the latter is independent of M and has a maximum at 4 kc./sec. and below this frequency increases as the square of the frequency.

The observed noise field is well represented, qualitatively, by the Lighthill theory. Measurements of complex turbulent velocity correlations are necessary before a rigorous comparison with theory can be made.

Received June 23, 1955.

* The author was in receipt of a maintenance grant from the Department of Scientific and Industrial Research while engaged on the work reported in this paper. Much invaluable help and encouragement have been given by Prof. M. J. Lighthill, Prof. W. A. Mair, and P. R. Owen. Much of the electronic equipment was designed by V. H. Attree. The author's grateful acknowledgment is made to all the above-named.

† Fluid Motion Laboratory.

NOTATION

$\bar{p}^2$	=	mean square sound pressure (intensity $I = \bar{p}^2/\rho_0 a_0$)
U	=	jet velocity
M	=	mean Mach Number at pipe orifice
M_c	=	Mach Number of convection of source
M_x	=	mean Mach Number at distance x downstream of orifice
x_0	=	distance downstream from orifice of source position
d	=	pipe diameter (= 2.513 cm.)
r	=	distance of point of observation from source
ϑ	=	angle between r and the downstream direction of the jet axis
$\vartheta_{max.}$	=	angle ϑ corresponding to direction of maximum intensity
N	=	frequency
S	=	Nd/Ma_0 = nondimensional frequency (Strouhal Number)
ρ_0	=	air density
a_0	=	speed of sound in atmosphere surrounding jet
n	=	exponent in $\bar{p}^2 \propto M^n$—i.e., $n = \partial \log \bar{p}^2/\partial \log M$
m	=	value of n at $\vartheta = 90°$; equals value when $M_c = 0$
P	=	acoustic power output
$\overline{(\bar{p}^2)}$	=	average mean square sound pressure over the surface of a sphere of radius r surrounding the source
$\overline{(\bar{p}^2)_0}$	=	free-field value of $\overline{(\bar{p}^2)}$
n_1	=	exponent in relation $\overline{(\bar{p}^2)_0} \propto M^{n_1}$
$\bar{n}_1$	=	average of n_1 over range $0.3 < M < 1.0$
η	=	acoustic efficiency

(1) INTRODUCTION

The noise emitted by jet engines has become a compelling problem and has led in the past few years to experimental studies of the noise radiated by small cold turbulent jets in many laboratories in Britain and the United States.[1] The main stimulus to this experimental work was Lighthill's theory,[2] which related the noise radiation to the characteristics of the turbulence within the jet. Lighthill derives from the equations of continuity and momentum a wave equation with a right-hand side equal to the second space derivative of the fluctuating stress tensor in the flow field. At low Mach Numbers this stress tensor (T_{ij}) approximates to $\rho_0 v_i v_j$ where v_i is the turbulent velocity component. This wave equation has a retarded potential solution which is the fluctuating density outside the flow field. At large distances the solution takes the

TABLE 1
Apparent Source Position and Angle of Maximum Intensity

Frequency Cycles/sec.	Strouhal Number	M	$\vartheta_{max.}$°	x_0/d
8,500	0.672	0.955	41.7	9.75
	0.808	0.794	41.6	8.15
	1.02	0.631	43	7.15
	1.28	0.501	41.3	5.95
	1.61	0.398	42	2.6
	2.03	0.316	40.6	0.6
5,500	0.523	0.794	35	8.05
	1.04	0.398	35.7	5.5
2,630	0.250	0.794	26	10.35
	0.499	0.398	24.5	4.7
1,300	0.124	0.794	23	11.95
	0.156	0.631	19.5	9.55
	0.196	0.501	19	6.75
	0.246	0.398	18.5	4.4
640	0.061	0.794	17	12.35
	0.121	0.398	16	1.4
30 to 10,000	...	0.5 to 1.0	27	14

form of an integral, over the flow, containing the second time-derivative of the tensor T_{ij}.

The stress tensor represents the strength per unit volume of a field of quadrupoles which arise from oscillations in the rate of momentum flux across surfaces fixed in the fluid. Simple source (or monopole) and dipole distributions are absent from the jet because at any instant the integrated flux of mass and, since there are no solid boundaries, the integrated flux of momentum over the whole field must be zero. Lighthill suggests that the most significant analysis of the tensor T_{ij} is into a pressure and a pure shearing stress, and he shows that these radiate like a monopole (produced by three mutually orthogonal longitudinal quadrupoles) and a lateral quadrupole, respectively. In Part II of his paper, Lighthill shows that the important term in the rate of change of momentum flux at a point is the product of the excess pressure and the rate of strain, thus illustrating how the lateral quadrupole is produced by shear.

A detailed prediction of the noise field requires a knowledge of the correlations between values of $\rho_0 v_i v_j$ separated in space and time, but the main features of the noise radiation can be deduced from a dimensional argument. Thus Lighthill relates the sound intensity (proportional to the mean square of density fluctuations) to the eight power of a typical velocity in the jet and to the square of a typical length such as the jet diameter, and he goes on to show that the total acoustic power output from similar jets is approximately proportional to $\rho_0 U^8 a_0^{-5} d^2$; the relevant dimensionless frequency parameter is the Strouhal Number (Nd/U).

When the source of sound is convected with the flow, at Mach Number M_c, a factor $(1 - M_c \cos \vartheta)^{-6}$ must be included in the intensity: thus a lateral quadrupole which, when stationary, produces a maximum in intensity at 45° to the flow, has this angle decreased by convection; also, owing to the Doppler effect a convected source of frequency N radiates a frequency $N(1 - M_c \cos \vartheta)^{-1}$. Another effect of the convection is to alter the power law for the intensity by an amount depending on the angle ϑ.

These dimensional considerations and their extension to apply to a convected source are sufficient for a preliminary comparison between theory and experiment. The results given here, as well as those of other workers, in general support this theory.

The similarity in the sound fields of small jets issuing from pipes and nozzles[3, 4] and the sound fields of stationary jet engines[5, 6] indicates that the production of noise is due mainly to turbulent mixing of the jet with the surrounding atmosphere. The results of all workers confirm that the sound intensity varies according to a high power of the jet speed, and Hubbard and Lassiter[6] have shown that the intensity is proportional to the square of the orifice diameter. The sound field possesses highly directional properties, consequently comparison of *intensity* measurements by different workers may be misleading. Fitzpatrick and Lee[4] have determined the acoustic power output of small jets from measurements in a reverberation chamber. Their spectra of acoustic power output agree well with those found by the author from an integration of the measured intensity. Fitzpatrick and Lee and also Westley and Lilley[3] found that the frequency of maximum power output was almost independent of jet speed, whereas it was expected that the Strouhal Number corresponding to maximum power output should show this independence. The author finds that some increase in the frequency of the maximum with increasing jet speed would be produced if the speed of convection of the sources was independent of frequency; this effect when supplemented by Lighthill's suggestion[7] of acoustic radiation damping has the effect of producing the almost constant frequency of maximum power output.

The manner in which the intensity and acoustic power output vary with jet speed is discussed in some detail in terms of the exponents in the relations $I \propto M^n$ and $P \propto M^{n_1}$. n has been determined at constant frequency and n_1 at both constant frequency and Strouhal Number. The variation of the exponents can be partly accounted for by their dependence upon the speed of convection of the sources.

Hubbard and Lassiter[6] and Westley and Lilley[3] have shown that the high-frequency sources are situated close to the jet orifice while the low-frequency sources are located further downstream. The positions of the sources are also determined here: the variation of position with jet speed as well as frequency is investigated.

Lines of constant sound intensity have been plotted to study the directional characteristics of the sound field. For small jets Westley and Lilley[5] showed strong evidence for the existence of lateral quadrupole sources at high frequencies. The angle of maximum intensity is known to increase with increasing frequency (see Table 1); von Gierke et al.[5] have shown that at very high frequencies (relative to that of maximum power output) the angle of maximum intensity approaches the direction perpendicular to the jet axis. An explanation of the observation is suggested here.

The sound field is analyzed in more detail and found to be well represented by quadrupole fields, although certain discrepancies still exist.

Measurements have been made in a wide frequency band (30 to 10,000 cycles/sec.) and in $^1/_3$ octave frequency bands in this frequency range. The wide frequency-band measurements were made first to obtain an overall picture of the sound field and to plan the method of experiment. The range of mean Mach Number at the jet orifice covered in these experiments was 0.3 to 1.0.

(2) Apparatus

The jet investigated in these experiments was produced by exhausting a reservoir of compressed air, 4,500 ft.^{3} capacity, through a cylindrical pipe of 1 in. internal diameter and 36 diameters long. The flow at the end of the pipe approximated to fully developed turbulent pipe flow. Another pipe of the same internal diameter but 54 diameters in length was used in some experiments. The increased turbulence produced an increase in the total sound radiated of 2 or 3 db. in all directions. The experiments were made in a large aircraft hangar (180 by 90 by 35 ft.) with the jet pipe fixed horizontally in the middle of the hangar and 12 ft. above the floor.

A Standard Telephones and Cables Ltd. dynamic microphone (type 4021E) was used for the preliminary measurements, thus restricting the frequency range between 30 and 10,000 cycles/sec. Later measurements were made in $^1/_3$ octave frequency bands, and a Bruel and Kjaer condenser microphone (type 4111) was used because the dynamic microphone was found unsuitable for measurements close to the source of sound.

The microphone signal was amplified by a conventional variable gain amplifier followed by a feedback-amplifier[8] of high linearity as output stage. The 1/3 octave filters and one valve circuit of a Siemens-Halske spectral analyzer could be inserted between these two amplifier stages. The r.m.s. output was indicated by a vacuo-junction and galvanometer. This square-law measuring circuit had a long time constant which was advantageous for noise measurements. A short time-constant valve voltmeter circuit was incorporated in the amplifier to enable the gain adjustment to be made rapidly.

The amplifier hum and noise level was always more than 30 db. below the measured jet noise signal. The hum level was kept low by running the valve heaters in series from a d.c. power supply. The amplifier gain varied by roughly 0.1 db. during each series of measurements. The gain was measured at the beginning and end of each run. The constant voltage input used for this calibration was obtained from a nonlinear bridge.[9]

(3.1) Method of Measurement

In order that the sound pressure level could be related to the jet speed, simultaneous measurements were made of the sound pressure and the pressure at the inlet to the jet pipe. The pipe was calibrated by determining the mean Mach Number (M) at the pipe orifice as a function of the ratio of the pipe inlet pressure to the atmospheric pressure. The mean Mach Number was found from a transverse across the orifice with pitot and static tubes; small corrections were applied for the effect of turbulence[10] and for the displacement of the effective center of the pitot tube.[11] The Mach Number was calculated on the assumption that the flow was isenergetic.

Mach Number distributions were also measured downstream of the orifice. The mean Mach Number (M_x) across the jet at a distance x downstream of the orifice was found to obey the relation

$$M_x/M = 2.22/[2.22 + (x/d)]$$

in the range $0 \leq (x/d) \leq 20$, where d is the orifice jet diameter.

The air was compressed into the reservoirs and the compressor stopped. The air was fed to the jet pipe through a 12 in. main and then through 4 in. pipes. Two methods of exhausting the air through the jet pipe were used; in the one a gate valve in the 12 in. main was used to control the flow and reduce the rate of fall of pressure at the jet exit so that noise measurements within a narrow range of jet speeds could be made: in the other the gate valve was fully opened. Measurements at the same jet speed for a range of reservoir pressures showed that the noise produced in the gate valve was negligible compared with that of the jets.

Preliminary measurements showed that the jet sound field possessed axial symmetry; namely, that reflections from one particular direction did not predominate. The measurements reported here were all made in the horizontal plane through the jet axis. For measurements which were not made close to the source of sound a correction for the reverberant sound level was necessary to reduce them to their free-field value. The reverberant sound level calculated from the reverberation time, assuming that the hangar was a rectangular box and that its surfaces reflected diffusely, was found to be too high by an amount depending upon frequency; it was therefore determined directly, for each frequency band, as a function of jet speed, from measurements made at large distances from the jet.

(3.2) Accuracy of Results

The electronic equipment was calibrated to ± 0.1 db., and measurements were read to the nearest 0.05 db. The gain of the amplifier and filters was measured at the beginning and end of each run. Noise measurements were repeatable to within 1 db. in all cases. The dynamic microphone calibration was checked by the N.P.L. mobile acoustics laboratory at low frequencies and found to be accurate to within 1 db. A comparison of the two microphones used showed their calibrations agreed to within 1 db. at all frequencies. The absolute accuracy was governed mainly by the

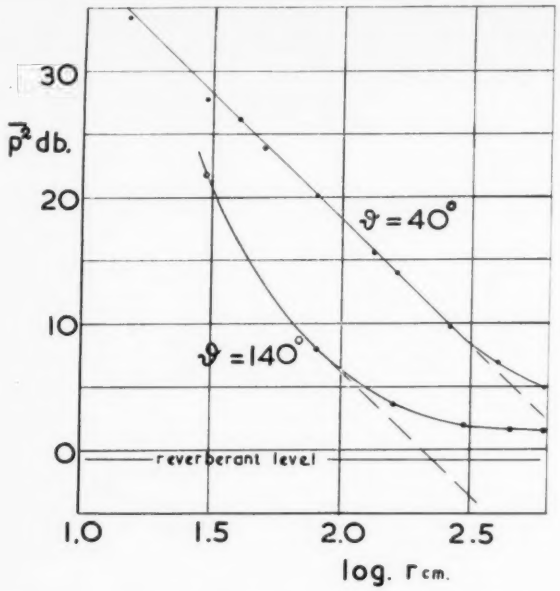

FIG. 1. Intensity as a function of distance; 1,300 cycles/sec., $M = 0.794$.

distortion of the sound field from its free-field form by the presence of reflecting surfaces. The uncertainty of measurements, including the correction for the reverberant sound level, was estimated to be about ±2 db.

(4) VARIATION OF INTENSITY WITH DISTANCE FROM SOURCE

At positions close to the jet the measured sound field is the same as would be measured in a free-field: that is to say, in the absence of all reflecting surfaces except the jet pipe. At large distances from the source of sound, reflecting surfaces are the controlling factors and the measured intensity is sensibly the reverberant sound level. In a radiation field the sound intensity falls off as the inverse square of the distance. The observed mean square sound pressure may be represented by $\bar{p}^2 \propto 1/r^s$ where r is the distance of the point of observation from the source and s is a function of distance, frequency, and direction. In the "near-field" s was greater than 2 in upstream directions and less than 2 in downstream directions. At larger distances s approaches 2 in a free sound field. The limit of the radiation field depended upon direction and frequency.

Four curves of sound intensity as a function of distance are shown in Figs. 1 and 2. The measured reverberant sound levels at these speeds for the high and low frequency were −41.25 db. and −0.75 db. relative to 1 μ-bar,* respectively. The limits of the radiation fields at these same two frequencies are shown in Fig. 3. These are the limits of the region in which $s = 2$ in the free-field and were obtained from measurements along lines radiating from the effective source position (marked with an asterisk in Fig. 3). Measurements at 1,300 cycles/sec. and $M = 0.794$ showed that the limit was of the order of 100 cm. from the source, except at $\vartheta = 40°$. The curves are very roughly the same shape as the lines of constant intensity, with some significant divergences. Outside the inner limit of the radiation field the lines of constant intensity cannot change shape as distance from the source increases. It follows, therefore, that if a source is concentrated at a point, the limit of the radiation field has the same shape as the radiation field lines of constant intensity. The low frequency curve shows the composite nature of the radiation field and indicates the possibility that the sources are distributed along the jet. The point marked with the asterisk is the position of the most intense source. From the curves obtained at the higher frequency it appears that the radiation (in the upstream direction at least) is emitted by distributed sources: these may, in fact, be due to radiation from the pipe walls.

The variation in size of the region bounded by the inner limits of the radiation field, with frequency and jet speed, was difficult to assess from the small amount of data. The region appeared to increase in size with decreasing frequency as was expected. The variation in size with jet speed is unaccountable. There are, however, many factors which may be relevant, such as the volume occupied by the source distribution, the speed of convection of the sources, and the type of the source.

Wide frequency-band measurements have not been made close to the jet. At larger distances the departure from the inverse square law could be accounted for by the reflected sound.

(5) POSITION OF SOUND SOURCES

Each turbulent eddy contained in the jet radiates noise like a system of acoustic quadrupole sources which, in certain circumstances, may reduce to a simple

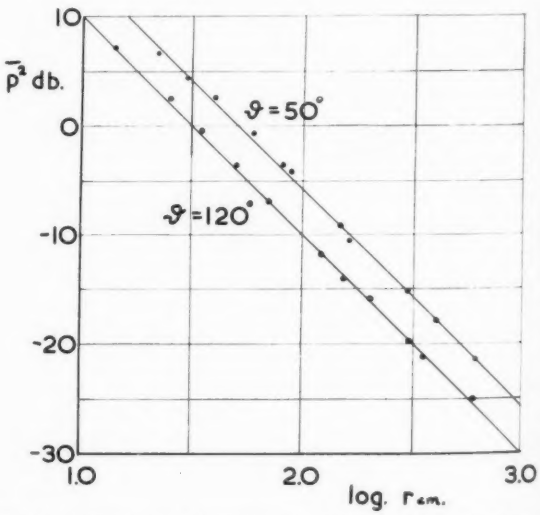

FIG. 2. Intensity as a function of distance; 8,500 cycles/sec., $M = 0.398$.

* 1 μ-bar ≡ 1 dyne cm.$^{-2}$.

source.[2] The total noise field is the aggregate of the fields of the individual sources, with the included effect of Doppler shift in frequency due to the convection of the sources which will vary from one eddy to another. It is, nevertheless, convenient and instructive to approximate to the source distribution associated with a given frequency of noise by a discrete source or a small number of sources: but, owing to the Doppler effect the source positions deduced from the acoustic measurements are only *apparent* positions.

There are several reasons why it is desirable to determine, at least approximately, the positions of the sound sources early in the investigation. At high frequencies the microphones possess directional properties. An error is introduced if the microphone is not directed towards the source. This is unavoidable when measuring over a wide frequency band but can be eliminated from the narrow frequency-band measurements.

The center of the sphere, over which the intensity is integrated to obtain the acoustic power output, must be taken at the source position if no error is to be introduced. The proportionate error in acoustic power output is $y^2/2z^2$, where y is the misplacement of the center of the sphere (of radius z) from the source; clearly, this error is not significant unless y/z is large.

The speed of convection of the source determines the pattern of the radiation field, and a speed must be chosen in order to fit the theoretical expressions for the sound field to the measured intensities. A knowledge of the range of speeds present in the vicinity of the source is therefore desirable.

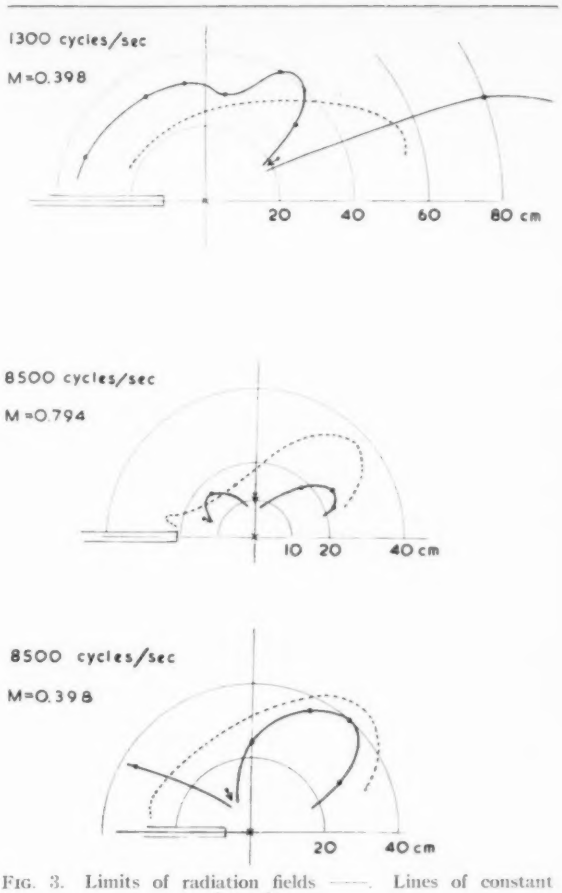

FIG. 3. Limits of radiation fields ——. Lines of constant intensity – – –.

(5.1) Method of Determining Source Position

Except at the lowest frequencies the sound field of a jet possesses a pronounced maximum in the downstream quadrant. The source position can, therefore, be determined from a plot of the lines of constant intensity in the horizontal plane through the jet axis. Using the analogy between lines of constant intensity and contours of equal height, a line followed "up the spur of the hill" leads to the source. At low frequencies, for which the microphone was omnidirectional, the intensity was measured as a function of position as the microphone traversed the maximum. This was repeated at various distances from the jet. When the positions of maximum intensity were plotted on a scale diagram they were found to be on a straight line which was extrapolated to give the source position. At high frequencies the microphone had to be directed towards the source and thus the source position had first to be estimated. Measurements along two arcs served to show whether the initial estimate was a good one or not, and with the accumulation of information the first guess at the source position was usually fairly accurate.

At low frequencies there is evidence that the sources are distributed over a large volume (but not large compared with a wave length). The angle which the direction of maximum intensity makes to the jet axis decreases with decreasing frequency. These two factors make the determination of source position very inaccurate at low frequencies. It appears that the difficulty can only be overcome by plotting the complete near-field.

(5.2) Results

At any given frequency, as the speed of the jet decreased the source moved nearer to the orifice, and it was found that the jet Mach Number at the source position was approximately the same for all jet speeds. From this one would have expected the speed of convection of the source to remain approximately constant with change in jet speed and thus the direction of maximum intensity to be at the same angle to the jet axis: this was, in fact, found to be the case.

The variation of source position with frequency was not a simple one. Sources of a given low frequency were more spread in the direction of the jet axis than those of higher frequency (see Section 6) as might be expected if the low-frequency sources were monopole in character and so did not require to be in a region of strong mean-flow shear in order to radiate.

The most intense component of a given low-frequency radiation field had its origin at smaller distances (x_0)

downstream of the jet orifice than the other sources of the same frequency. It will be seen in Section 6 that these low-frequency sources are predominantly monopole in character. The values of x_0 corresponding to this most intense component are the ones discussed here. This is also the value of x_0 obtained by drawing a line "up the spur of the hill." The manner in which x_0 varies with frequency depends upon jet speed and is shown in Table 1 together with the angles at which the maxima occur. The source position determined at the lowest frequency is in some doubt (see Figs. 8 and 9).

Measurements in a wide frequency band indicated that the effective source position in the 30 to 10,000 cycles/sec. range was about 14 diameters downstream of the orifice for the range of jet Mach Number, $0.5 < M < 1.0$. The angle of maximum intensity observed in wide frequency-band measurements was 27° and was independent of jet speed.

The values of the nondimensional frequency or Strouhal Number are included in Table 1 because it is this rather than frequency which is fundamental when considering aerodynamic sound. It is assumed that the frequency is related to frequencies characteristic of the energy bearing eddies in the turbulence, which would be roughly proportional to a typical velocity (Ma_0) divided by a typical length (d). It appears, nevertheless that the angle of maximum intensity depends upon frequency rather than Strouhal Number.

(6) Lines of Constant Intensity

A consideration of the directional characteristics of the sound field followed naturally from the determination of source position. The measurements of the last section formed a basis for the observations required. The lines of constant intensity are plotted on scale diagrams in Figs. 4 to 10. Measurements have been made at the points shown by small circles. The numbers on the figures indicate sound pressure in decibels relative to 1 μ-bar and were determined by interpolation. The apparent source position and direction of maximum intensity are shown on the figures. The wave-length of the sound is also drawn on the same scale. The reverberant sound level lies at least 10 db. below the lowest sound pressure contour except at 640 cycles/sec. (Figs. 8 and 9) where it is about 6 db. below. No correction has been applied for the reverberant sound because it would not alter the diagrams significantly.

At the highest frequency investigated the sound field possesses a maximum at an angle ($\vartheta_{max.}$) a little less than 45° to the jet axis and another at an angle (ϑ) of about 160°. As the frequency decreases, the angle $\vartheta_{max.}$ decreases and the maximum in the upstream direction disappears. At the lowest frequencies, the direction of maximum intensity lies at a small angle to the jet axis and the intensity at a fixed distance (r) from the source decreases as ϑ increases. When measurements were made in a wide frequency band (30 to 10,000 cycles/sec.), $\vartheta_{max.}$ was 27°. This value of $\vartheta_{max.}$ did not depend upon the jet speed. In the range of ϑ from 90 to 180° the wide frequency-band intensity was approximately constant for a given value of r.

When the distance from the source is of the order of a wave length of the sound, it appears from the diagrams that the maximum of intensity is divided into two peaks. This is probably due to the sources of sound being spread over a length of the jet comparable with the sound wave length.

Figs. 4 and 5 show the sound fields at 8,500 cycles per sec. at two jet speeds. They possess a maximum in the downstream quadrant in the position which would be expected from a lateral quadrupole. The radiation at right angles to the jet at the source position, however, shows that other types of sources are also present since a lateral quadrupole would not radiate in this direction. If we restrict our choice of sources to fourth-order multipoles, the form of the lines of constant intensity in the range $15° < \vartheta < 45°$ shows that the source responsible for the radiation at $\vartheta = 90°$ must be a longitudinal quadrupole with its axis perpendicular to the jet. An expression for the intensity can be derived which agrees with the observed field to within 2 db. for values of ϑ up to 110°. The best fit was obtained by using the following expressions

$$M = 0.794 \qquad \bar{p}^2 = \frac{A \sin^2 2\vartheta + B \sin^4 \vartheta}{r^2(1 - M_{c_1} \cos \vartheta)^6} \tag{1}$$

$$M = 0.398 \qquad \bar{p}^2 = \frac{C \sin^2 2\vartheta + D \sin^4 \vartheta}{r^2 (1 - M_{c_2} \cos \vartheta)^6} \tag{2}$$

The part containing $\sin^2 2\vartheta$ represents a lateral quadrupole radiation field and the other, containing $\sin^4 \vartheta$, a longitudinal quadrupole field. The Mach Numbers of convection (M_c) of the two types of source were taken to be the same because the sources were in the same small region of the jet. When r is in centimeters, the va'ues of the constants in db. relative to 1 μ-bar, are

$$A = 51.1 \text{ db.}$$
$$B = 53.5 \text{ db.} \qquad M_{c_1} = 0.32$$
$$C = 31.8 \text{ db.}$$
$$D = 31.0 \text{ db.} \qquad M_{c_2} = 0.16$$

These values were determined by solving the simultaneous equations obtained by fitting Eqs. (1) and (2) to the experimental curves at particular values of ϑ. The solutions are not to be considered as unique: in fact, the determination of a unique solution simply from measurement of intensity is not possible.

If we assume that $\bar{p}^2 \propto M^n$, then Eqs. (1) and (2) give for the lateral quadrupole $n = 6.4$, and for the longitudinal quadrupole $n = 7.5$. Considering the errors which must necessarily arise, the mean of these two values of n (viz., 7.0) compares very favorably with the value of the mean exponent ($\bar{n}_1$) determined for this frequency (viz., 7.2, see Fig. 12). The Mach Numbers of convection are not at variance with the measured structure of the jet. Their ratio to the maximum

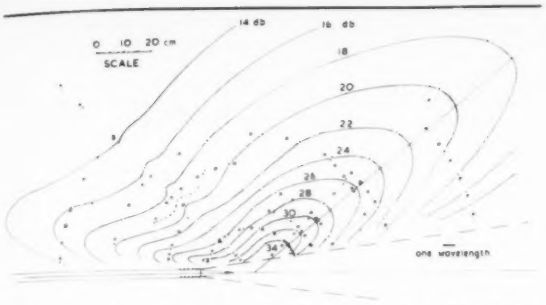

FIG. 4. Lines of constant intensity; 8,500 cycles/sec., $M = 0.794$.

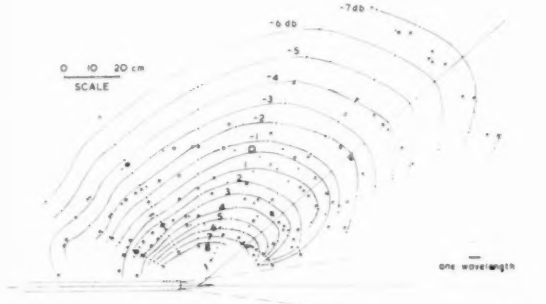

FIG. 5. Lines of constant intensity; 8,500 cycles/sec., $M = 0.398$.

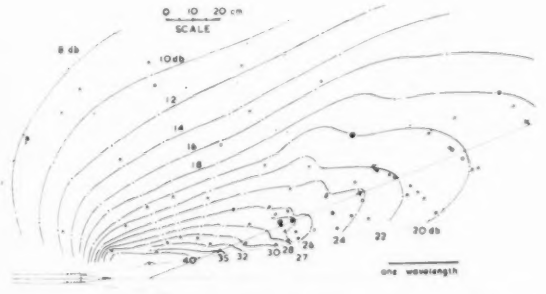

FIG. 6. Lines of constant intensity; 1,300 cycles/sec., $M = 0.794$.

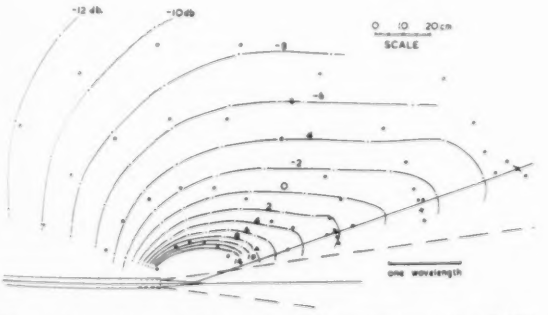

FIG. 7. Lines of constant intensity; 1,300 cycles/sec., $M = 0.398$.

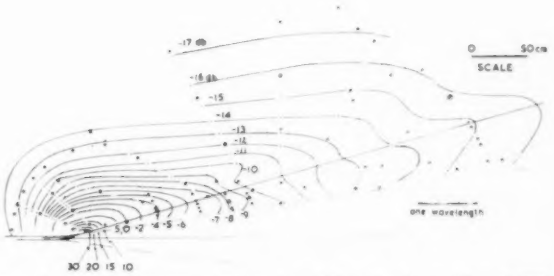

FIG. 8. Lines of constant intensity; 640 cycles/sec., $M = 0.398$.

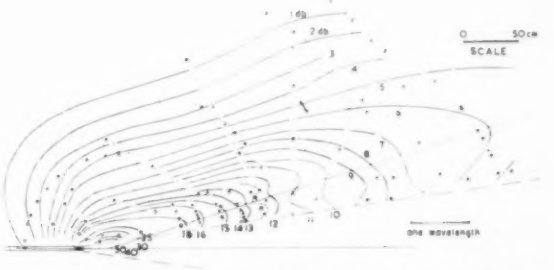

FIG. 9. Lines of constant intensity; 640 cycles/sec., $M = 0.794$.

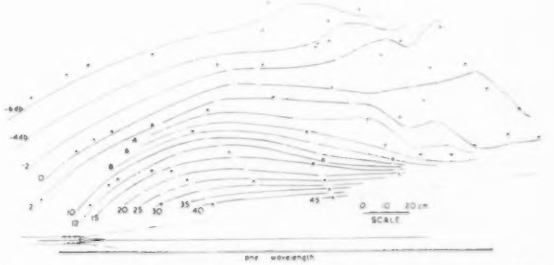

FIG. 10. Lines of constant intensity; 172 cycles/sec., $M = 0.955$.

Mach Number at the section of the jet at the source position are 0.43 and 0.36 for the high and low jet speed, respectively. The values of M_c for other jet speeds have been determined at this frequency and are well represented by the relation $M_c = 0.4M$, where M is the mean Mach Number at the jet pipe orifice.

At this frequency of 8,500 cycles/sec., a maximum in the upstream direction remains to be explained. The factors which may contribute to its production are radiation from the pipe walls due to the turbulent pipe-flow within, the possibility of higher order multipoles,[7] the diffraction of sound by the jet pipe which may cast a shadow at this frequency,[12] and the distribution of sources along the jet (due to the Doppler effect).

It is interesting to note, in connection with the distribution of the sources, that a maximum in the intensity of the radiation appears and increases with increasing frequency and Mach Number. At very high frequencies and at Mach Numbers greater than unity, Powell[13] has discovered radiation predominantly in the upstream direction. He postulates, on strong evidence, that the sound is so directed by the distribution of monopole sources, which are stationary and spaced at distances equal to the wave length of the sound. Powell's sources, however, are produced by the passage of eddies through shock waves, a mechanism which is impossible in the subsonic jet investigated here.

The fact that the sources of sound are convected at an appreciable Mach Number produces a decrease in the radiated frequency with increasing angle, (ϑ), (Doppler effect). We might expect, therefore, that Eqs. 1 and 2 which agree with the observed field at 8,500 cycles/sec. in the downstream quadrant but fall well below in the upstream quadrant, would agree with the observed fields in the upstream quadrant at some lower frequency. In fact the radiation at 5,500 and 4,185 cycles/sec. is less than 2 db. different in intensity from that at 8,500 cycles/sec. in the range of ϑ from 130 to 160°. The discrepancy between Eqs. (1) and (2) and the observed fields does not, therefore, appear to be due to the Doppler effect.

A comparison between a theoretical field and that observed has also been made at 1,300 cycles/sec. at a jet Mach Number of 0.631. A distribution of monopole sources appears to be the only combination which reproduces the observed field. Combinations of sources of longitudinal and lateral quadrupole type have been tried without success. Radiation of the monopole type is expected, as Proudman has shown,[14] when the source is situated in a region of small shear and the turbulence is approximately isotropic. A monopole source was assumed at the position obtained by tracing back the position of maximum intensity as explained in Section 5. A second monopole source was assumed to be situated at another point further downstream, the position of which was estimated from the form of the lines of constant intensity. The expression used was, therefore,

$$\bar{p}^2 = \frac{A}{r_1^2(1 - M_{c_1}\cos\vartheta_1)^6} + \frac{B}{r_2^2(1 - M_{c_2}\cos\vartheta_2)^6} \qquad (3)$$

where the term with suffixes 1 refers to the source at $x_0 = 24$ cm. and the other to the second source which was placed 55 cm. further downstream. When r is measured in centimeters, the values of the parameters—in db. relative to 1 μ-bar—are

$$A = 42.2 \text{ db.} \qquad M_{c_1} = 0.52$$
$$B = 40.9 \text{ db.} \qquad M_{c_2} = 0.13$$

The Mach Numbers of convection are very close to the measured Mach Numbers on the axis at the two source positions: 0.14 ± 0.04 and 0.514. This agrees with the radiation being like that of a monopole source (produced by three mutually orthogonal longitudinal quadrupoles) which we should expect from the absence of shear on the axis. The theoretical expression lies within 3 db. of the observed intensity for all values of ϑ. The theoretical expression has a maximum at $\vartheta = 0°$, however, and the observed field falls off as the axis is approached. It is possible that this loss in intensity close to the axis is due to refraction: thus, if the source moves nearer to the jet axis and becomes more monopole in character as the frequency decreases, this will be accompanied by greater refraction effects.

The spread of the apparent sources at this frequency can be shown to be due to the Doppler effect. A source of a given frequency radiates higher frequencies in downstream directions and lower frequencies in upstream directions; thus measurements at a single frequency should be related to sources of different frequencies which will be in different positions. The source at $x_0 = 24$ cm. was found to be convected at a Mach Number of about 0.5 and thus the Doppler effect is to separate the frequencies in upstream and downstream directions in the ratio of 3:1. The first term in Eq. (3), which represents the radiation field of this source, approximates to the observed field (at 1,300 cycles/sec.) in the downstream quadrant. Because of the Doppler effect the sound intensity given by this term in the upstream quadrant should fit the measured field at a frequency of about 300 or 400 cycles/sec. The sound field measured at 340 cycles/sec. did in fact lie within 2 db. of that predicted by the first term of Eq. (3) at angles (ϑ) close to 180°.

Although a fit between theory and experiment at this frequency is possible by considering only monopole sources, it is likely that lateral quadrupole radiation still exists but is considerably less intense than the monopole radiation. We will return to a consideration of the types of sources and their relative intensity after discussing the spectrum of the jet noise.

(7) Variation of Intensity with Jet Speed: The Exponent in $\bar{p}^2 \propto M^n$

The intensity of sound radiated from a flow field is expected to possess a marked dependence upon the

Mach Number of the flow; the exponent in the relation

$$\bar{p}^2 \propto M^n \tag{4}$$

is of the order of 8. When the source of sound is convected with a Mach Number M_c, n will depend upon M_c and the direction of radiation of the sound. The exponent may be expected to depend upon frequency and jet speed since it has been shown that M_c is a function of these parameters. It is important to notice that n is determined from the manner in which $\bar{p}^2$ varies with M *at constant frequency*. The manner in which the acoustic power output of the jet varies with jet speed at constant Strouhal Number is considered in Section 8.

If it is assumed that the sound reaching the point of observation comes from a single region and that the sources in this region are convected with the same speed, we may write

$$\bar{p}^2 = \frac{M^m f(\vartheta)}{r^2(1 - M_c \cos \vartheta)^6} \tag{5}$$

where m is the value of n when $\vartheta = 90°$ or when $M_c = 0$, and $f(\vartheta)$ depends upon the type of source. The exponent n is given by

$$n = \partial \log \bar{p}^2 / \partial \log M = m + k[6M_c \cos \vartheta / (1 - M_c \cos \vartheta)] \tag{6}$$

where $k = \partial \log M_c / \partial \log M$, which was found (Section 6) to be equal to unity at 8,500 cycles/sec. If we put $n_0 - m = a$ and $m - n_{180} = b$ then it may easily be shown that

$$\left.\begin{aligned} M_c &= (a - b)/(a + b) \\ k &= (ab\ 3)(a - b) \end{aligned}\right\} \tag{7}$$

The values of n were determined from the slopes of curves relating the sound pressure (in db.) to the logarithm of M. Measurements were made in the radiation field at various angles, at a fixed distance from some point on the axis, and over the whole jet-speed range. This point was chosen to be within the range of source positions, but since the source position changed with jet speed, some error was introduced by this procedure. The curvature of these plots was in most cases not great. In a range of $\log_{10} M$ of 0.1 there were from 2 to 4 experimental points. The values of n were determined without applying a correction for the reverberant sound. The accuracy of the values of n was estimated to be about ± 0.3. A qualitative comparison between theory and experiment is all that is possible. It was found that n depended upon direction, frequency, and jet speed. At a constant frequency and jet speed—that is, when only direction was varied—the greatest range of n observed was 4. The values of n determined in all the experiments varied between 4.3 and 10.3.

In all cases n decreased as the angle ϑ increased. If, however, a theoretical curve, [Eq. (6)] was made to fit the observations over the range $0 < \vartheta < 90°$ it fell below the experimental points in the range $90° < \vartheta < 180°$. This is not surprising because it was found (Section 6) that the source responsible for the predominant radiation in the downstream quadrant only contributed a small amount to the upstream radiation. It can now be inferred from this behavior of n that the source responsible for the predominant radiation in the upstream quadrant is convected with a much lower velocity for the high as well as the low frequencies.

TABLE 2

M	Frequency at which M_c is greatest (downstream radiation) cycles/sec.
0.794	4,000
0.631	2,600 to 4,000
0.501	1,300 to 2,600
0.398	830 to 1,300

Eq. (6) shows that the variation of n with frequency and jet speed may be considered in two parts. The variation of m with jet speed was not systematic, and its variation with frequency was found to be fairly well represented by

$$m = \log_{10} N + 3.1 \tag{8}$$

where N is the frequency in cycles/sec. The manner in which the variation of n with angle depends upon frequency is determined by the frequency dependence of k and M_c (see Eq. 6). Since it was found that $k = 1$ for radiation in the downstream quadrant at 8,500 cycles/sec., the variation of M_c with frequency may be deduced if we assume that k is independent of frequency. The difference in the value of n at 0 and 90° is an indication of the magnitude of M_c. At a given jet speed this difference was found to possess a maximum value as the frequency was varied. The rough positions of these maxima are tabulated in Table 2.

The values of n for the different frequency bands were spread over a larger range at the higher jet speeds. This is probably due to M_c being spread over a wider range.

The values of n determined from wide frequency-band measurements were in agreement with the average properties of the values of n determined in narrow frequency bands. The values of n varied between 5.5 and 8.5. The determined values of m lay between 6.2 and 6.8; the value 6.5 corresponds, by Eq. (8), to a frequency of 2,500 cycles/sec. which is consistent with the value deduced from $\vartheta_{max.}$ in the wide and narrow frequency-band measurements given in Table 1.

(8) Acoustic Power Output of Jet

The spectrum of the radiated sound is of little significance unless it is referred to the integrated energy. Since the sound field possesses highly directional properties, the spectrum measured at one point in the sound field may be quite different from that measured at another point. Similarly, comparison of results of different workers is more likely to be informative when referred to the integrated acoustic output and may in

TABLE 3

Values of Exponent in $p \propto M^{n_1}$ Determined at Constant Strouhal Number, Averaged over Mach Number Range

S	0.1	0.2	0.3	0.4	0.5	0.6	0.7	0.8	0.9	1.0
$\bar{n}_1$	8.0	7.6	7.5	7.4	7.7	7.3	7.2	7.2	6.7	6.7

fact be misleading if measurements at dissimilar positions are compared.

The acoustic power output (P) may be defined by the expression

$$P = \frac{2\pi r^2}{\rho_0 a_0} \int_0^\pi \bar{p}^2 \sin \vartheta \, d\vartheta = \frac{4\pi r^2}{\rho_0 a_0} \overline{(\bar{p}^2)} \qquad (9)$$

where $\overline{(\bar{p}^2)}$ is the average of the mean square sound pressure over the surface of a sphere of radius r surrounding the source. The computed value of $\overline{(\bar{p}^2)}$ was corrected by subtracting the reverberant sound level, thus giving the free-field value $\overline{(\bar{p}^2)_0}$.

It was found that the integrated sound pressure could be represented by

$$\overline{(\bar{p}^2)_0} \; \alpha \; M^{n_1} \qquad (10)$$

where n_1 depended but little upon M. This is illustrated in Fig. 11. The curves for different frequencies as shown here bear no relation to one another; they have been plotted solely to show how well a straight line may be fitted to the points. The slopes of these lines (i.e., the values of $\bar{n}_1$, where the bar denotes an average over the Mach Number range) have been determined numerically and are plotted in Fig. 12. The values of $\bar{n}_1$ determined in a wide frequency band lay between 7.0 and 7.4 which again correspond to a frequency between 2 and 3 kc./sec. The limits attached to the points indicate the magnitude of the root mean square deviation of the n_1 values averaged to produce $\bar{n}_1$. The wider the limits shown the more the curve deviates from a straight line. This departure from linearity may be attributed to the variation of M_c with M. The variation of $\bar{n}_1$ with frequency may be accounted for by the change of M_c with frequency.

The values of acoustic power output were also plotted as a logarithmic function of jet speed at constant Strouhal Number. The number of points on these curves was restricted by the number of frequency bands investigated, and thus the values of n_1 determined were subject to larger error. The dependence of n_1 upon M was about the same as when it was determined at constant frequency. The values of $\bar{n}_1$ determined by fitting the best straight line to the logarithmic plots are tabulated in Table 3. The exponent is seen to decrease with increasing Strouhal Number and is fairly well represented by

$$\bar{n}_1 = 8 - 1.2\,S \qquad (11)$$

The variation of $\bar{n}_1$ could be partly accounted for by a variation of M_c with Strouhal Number or entirely by Lighthill's suggested mechanism of acoustic radiation damping which is discussed in Section 10.

(8.1) Spectrum of Jet Noise

The spectrum of the acoustic power output of the jet per $^1/_3$ octave frequency band is shown in Fig. 13. Since this noise intensity is proportional to the product of turbulent fluctuations, the broadness of the spectrum was expected. There is no noticeable change in the frequency of maximum power with jet speed. This may be partly due to the extreme flatness of the spectra. Lines passing through the points where the power is 3 db. below the maximum indicate the spectral width. They show that the width increases with decreasing jet speed. As the parameter of importance in determining aerodynamic sound spectra is the Strouhal Number, it was expected that the frequency of maximum power would be proportional to the jet speed. This anomaly would be partly removed if M_c did not depend upon frequency. If such was the case, the only variation of the exponent $\bar{n}_1$ with frequency would be due to the frequency dependence of m. The exponent m increases monotonically with frequency (Eq. 8) whereas $\bar{n}_1$ has a maximum at 4 kc./sec. It is because $\bar{n}_1$ possesses a maximum at the frequency of maximum power output that the latter is independent of jet speed. It must be stressed that this mechanism does not entirely account for the constancy of the frequency of maximum power output and that it is also necessary to consider Lighthill's suggestion of the mechanism of radiation damping. The spectrum of the jet noise related to Strouhal Number is shown in Fig. 14. Again the spectrum is extremely flat and there is evidence that the peak moves to higher frequencies with decreasing jet speed whereas it is expected to be independent of jet speed. This shift to higher frequencies follows from Eq. 11. The flatness of the spectrum shows why the measurements in the frequency band from 30 to 10,000 cycles/sec. correspond to a frequency (ca. 3,000 cycles/sec.) only a little less than the frequency of maximum intensity (4,000 cycles/sec.).

(9) Acoustic Efficiency

The efficiency of a quadrupole source as a producer of sound is known to be very low. It is much lower than that of monopole and dipole sources and is also a function of the wave length of the radiation as was explained by Stokes.[15] The acoustic efficiency in a given frequency band is defined as the ratio of the acoustic power output in this frequency band to the rate of expenditure of mechanical energy required to produce it. The mechanical energy is taken as the kinetic energy flowing per second from the jet pipe orifice, and thus the efficiency (η) is given by

$$\eta = 16r^2 \int_0^\pi \bar{p}^2 \sin \vartheta d\vartheta / \rho_0{}^2 a_0{}^4 d^2 M^3 \qquad (12)$$

The acoustic power output may be represented by Eq. (10), and thus the efficiency must satisfy the relation

$$\eta = F M^{n_1 - 3} \qquad (13)$$

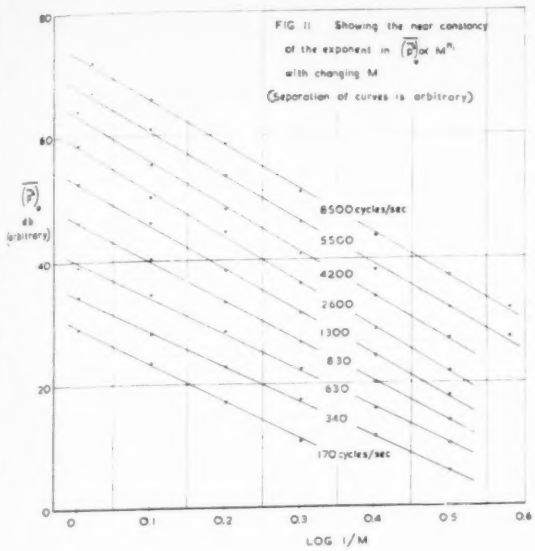

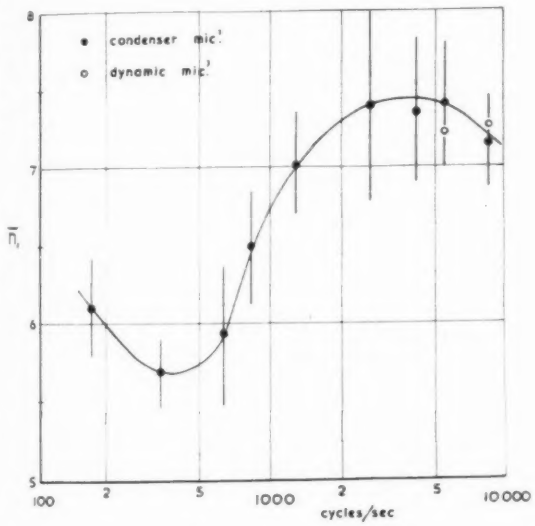

FIG. 12. $\bar{n}_1$ as a function of frequency.

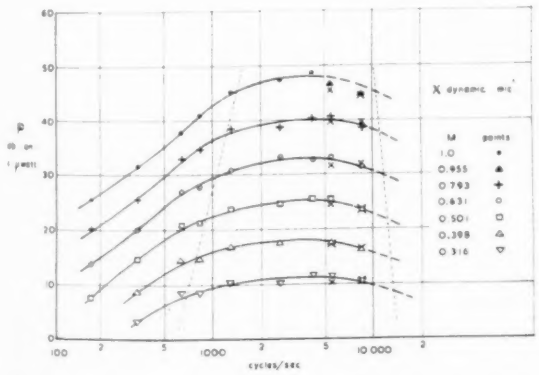

FIG. 13. Spectrum of acoustic power output per 1/3 octave.

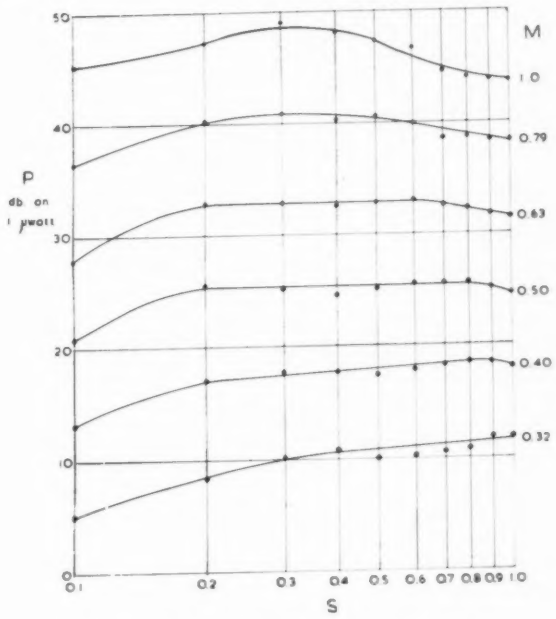

FIG. 14. Spectrum related to Strouhal Number.

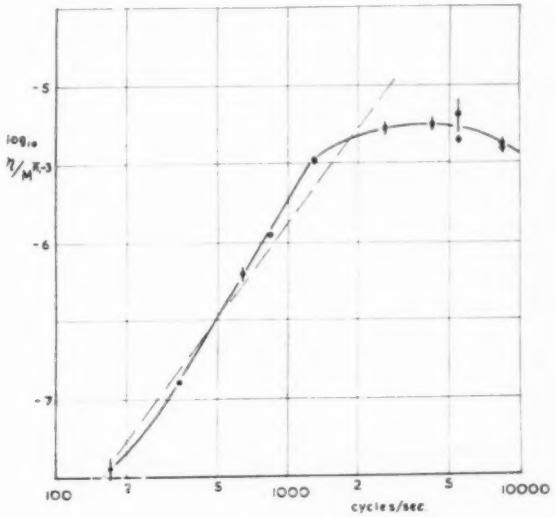

FIG. 15. Acoustic efficiency / $M^{\bar{n}_1+3}$.

where F is a function of frequency. The function F is plotted against frequency in Fig. 15. It increases approximately as the square of the frequency at frequencies below about 2 kc./sec. and possesses a maximum at about 4 kc./sec. The relation $F \alpha N^2$ is indicated by a dashed line. The points in Fig. 15 were determined from the mean of the values of F at 6 or 7 jet speeds. The r.m.s. deviations are indicated by the limits attached to the points. Wide frequency-band measurements, of course, gave a value of η much in excess of the $^1/_3$ octave frequency-band measurements. For the same jet pipe the result was

$$\eta = 1.0 \times 10^{-4} M^{4.2} \tag{14}$$

When the pipe length was increased from 36 diameters to 54 diameters, the resulting efficiency was

$$\eta = 2.0 \times 10^{-4} M^{4.4} \tag{15}$$

which indicates that the flow at the orifice of the pipe used in the bulk of these experiments was not quite fully developed turbulent pipe flow.

(10) Discussion of Results

The general character of the noise field agrees with that predicted by Lighthill. The intensity and acoustic power output vary as a high power of the jet velocity. The main types of radiation field expected from Lighthill's theory are those of lateral and longitudinal quadrupoles, the latter producing, in certain circumstances, the radiation field of a monopole (or simple) source. The observed radiation field of the jet can be interpreted in terms of these three types of source as modified by the effects of convection of the sources.

The types of acoustic sources and their positions in the jet inferred from intensity measurements can be related to the flow pattern in the jet. Low-frequency noise is produced by turbulence in the center of the jet where the mean flow shear is low and the turbulence is approximately isotropic. At these frequencies the noise is found to be monopole in character, which is consistent with the theory of Proudman[14] on the radiation of sound by isotropic turbulence. The low-frequency sources are spread over a comparatively long length of the jet. The increase in turbulent eddy size corresponding to larger noise wave length only partly contributes to this spreading which is also due to the fact that sources of different "source-frequency" radiate the same noise frequency (in different directions) because of the motion of the sources (Doppler effect).

Higher frequency noise is produced in the mixing region of the jet where M_c is approximately 0.4 M: the mixing region may be considered as a kind of vortex layer in which eddies travel downstream with roughly half the jet speed. Due to shear the sources are lateral quadrupoles. Longitudinal quadrupole sources with their axes perpendicular to the jet are also present at these frequencies.

At the very highest frequencies[5] radiation is predominantly perpendicular to the jet which suggests longitudinal quadrupole sources. These are produced by rapid fluctuations in the radial component of the turbulent velocity which are evidently connected with the flow of atmospheric air into the mixing region. Rapid fluctuations in the inflow are produced near the orifice where the turbulent eddies are small.

The convection of the noise sources has a considerable effect upon the radiated noise field producing, as Lighthill has explained, a preference for forward emission as well as complicating frequency relations by the Doppler effect. For a stationary source, the exponent n in the relation $\bar{p}^2 \alpha M^n$ does not depend upon direction; but for a moving source, values of n in the downstream direction are greater than those in upstream directions by an amount depending upon M_c: this amount is as much as 4 at some frequencies. The value of n determined at $\vartheta = 90°$ is uninfluenced by the motion of the source and is found to lie between 6.5 and 7.0. Lighthill[7] has suggested that the decrease from the theoretical value of 8 may be due to the fact that the growth of turbulent energy in the mixing region suffers acoustic radiation damping at the higher Mach Numbers. He suggests also that the effect should be greatest at the higher Strouhal Numbers, which is found to be the case (see Table 3). The change in shape of the spectrum of the acoustic power output with changing speed is governed by the dependence of $\bar{n}_1$ upon frequency, where $\bar{n}_1$ is the exponent in the relation $P \alpha M^{n_1}$ and the bar denotes an average over the range of M investigated. The fact that $\bar{n}_1$ possesses a maximum at 4 kc./sec. corroborates the finding that the spectrum of acoustic power output also possesses a maximum at 4 kc./sec. which is independent of jet speed. It is a fundamental assumption of the theory that frequencies should depend upon the value of the Strouhal Number (Nd/Ma_0). If the sources of noise were not convected ($M_c = 0$), the frequency of maximum power output ($N_{max.}$) would increase with increasing jet speed; a further factor must, however, be included before the relation $N_{max.} \alpha M$ is obtained. This factor, which would be mainly responsible for the constancy of $N_{max.}$, is the acoustic radiation damping suggested by Lighthill and referred to above.

Further evidence that the sources of sound are quadrupoles comes from the extreme smallness of the acoustic efficiency of the jet. Over a wide frequency band this is found to be of the order of $10^{-4} M^{4.2}$.

It appears from this qualitative comparison of theory and experiment that Lighthill's theory of aerodynamic sound is valid. A quantitative verification of the theory requires measurements of the turbulent structure of the jet.

References

[1] Symposium on Aircraft Noise, JASA, Vol. 25, (3), pp. 363-442, 1953.

[2] Lighthill, M. J., *On Sound Generated Aerodynamically—*

(Continued on page 873)

Inelastic Column Buckling*

L. HANNES LARSSON†
Finland Institute of Technology

SUMMARY

In this paper the inelastic buckling process is examined rigorously in order to compare the maximum load with the tangent modulus and reduced modulus loads. First, the results of the analysis of the idealized H-section column which was carried out according to Duberg and Wilder[4] are presented as large graphical tables. The material properties are defined by Ylinen's analytical stress-strain law.[5] Then an exact theory of the centrally compressed, initially slightly curved column is developed. An approximate method of solution based on the assumption that the deflection curve is a half sine wave is proposed and illustrated in a numerical example for a straight column. The results show that the tangent modulus theory in most cases, and, particularly, in the most important cases, yields a better approximation for the maximum load supported by a centrally loaded initially straight column than does the reduced modulus theory.

INTRODUCTION

IN 1947, F. R. Shanley showed that the classical reduced modulus theory of the inelastic column buckling does not give all possible equilibrium paths of a perfect column.[1] According to Shanley, the lowest load at which a bifurcation of equilibrium positions can occur—if the axial load is allowed to increase during the transition from the initial straight configuration to a slightly bent configuration—is given by the tangent modulus formula. When the tangent modulus load is exceeded, there will be, near the convex side of the column, a region where a decrease of strain corresponds to an increase of axial load. The region of strain reversal begins at the outer fibers of the mid-section and spreads toward the interior and the ends of the column as the load increases. Of course, such a region of strain reversal will be produced also in eccentrically loaded columns and columns with initial deflections, at least if the imperfections are small. The reversal of strain then occurs even before the tangent modulus load has been reached.

To treat the above process mathematically is very difficult. For columns with an idealized H-section, Duberg and Wilder have developed an approximate method of solution.[4] They showed that the maximum load of a perfect H-section column in most cases remains closer to the tangent modulus load than to the reduced modulus load. Columns with general cross sections have been treated approximately by Tung-Hua Lin[2] and C. E. Pearson.[3] In the following, a general theory of the behavior of an inelastic column will be presented. The column is assumed to be centrally compressed but initially slightly curved. An approximate method of solution, based on the assumption that the deflection curve is a half sine wave, is developed. The material properties are defined by Ylinen's analytical stress-strain law.[5] Ylinen's stress-strain function is briefly accounted for, and it is used in the analysis of the idealized H-section column according to Duberg and Wilder.

Received July 21, 1955. Revised and received January 12, 1956.

* This paper is a condensation of the author's diploma work at the Finland Institute of Technology, Helsinki, Finland. The author wants to express his gratitude to Prof. P. Laasonen of the Finland Institute of Technology for his valuable advice and constant encouragement during the preparation of the work.

† Master of Science in Mechanical Engineering. Now associated with the Tampella Engineering Works, Tampere, Finland.

THE IDEALIZED H-SECTION COLUMN

The mathematical treatment of the buckling process of columns according to the principles of Shanley mentioned in the Introduction is very complicated, as shown by previous investigators.[2, 3] An exceptional case is the column with an idealized H-section for which Duberg and Wilder have developed an approximate method of solution fit for use with any desired degree of accuracy. Duberg and Wilder defined the material properties by the Ramberg-Osgood stress-strain relationship. The writer made a similar investigation in his diploma work using Ylinen's stress-strain function[5]

$$\epsilon = (1/E)\left\{c\sigma - (1-c)\,\sigma_0 \log\left[1 - (\sigma/\sigma_0)\right]\right\} \quad (1)$$

where ϵ signifies the compressive strain, σ the compressive stress, and E Young's modulus of elasticity. For simplicity, compressive stresses and compressive strains, which are considered as positive quantities, are described simply as stresses and strains in the following: The free parameter c in Eq. (1) counts for the form of the stress-strain curve, $c < 1$ (see Fig. 1). When $c = 1$, Eq. (1) changes to Hooke's law. Values of $c = 0.98\ldots 0.99$ correspond to high strength steels, whereas, for Finnish pine wood, $c = 0.875$ on an average. σ_0

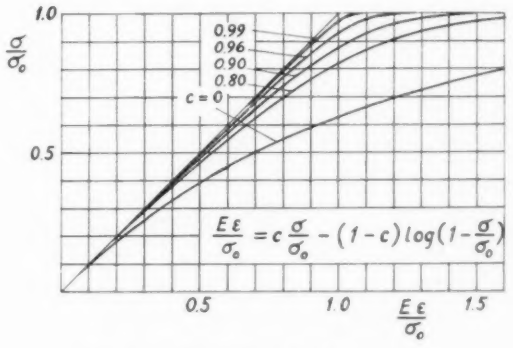

FIG. 1. Ylinen's stress-strain function.

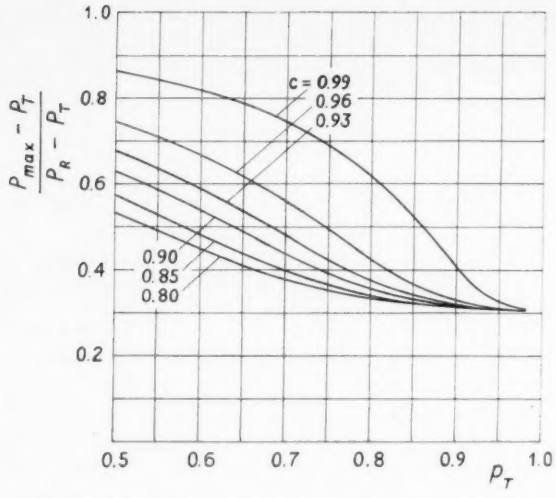

FIG. 2. Maximum load of H-section column compared with reduced modulus load and tangent modulus load as a function of $p_T = \sigma_T/\sigma_0 = P_T/A\ \sigma_0$.

signifies that value of the stress at which (for the first time) the stress-strain curve becomes horizontal. For materials with a pronounced yield point $\sigma_0 = \sigma_{Y.P.}$, and for materials which have no clear yield point σ_0 should be replaced by the ultimate strength. The expression of the tangent modulus is obtained from Eq. (1).

$$E_T = d\sigma/d\epsilon = E[(\sigma_0 - \sigma)/(\sigma_0 - c\sigma)] \qquad (2)$$

The deflection curve of the column was expressed by a finite series of m odd sine terms, the coefficients of which were solved, for each value of the column load, from a system of transcendental equations obtained by satisfying the proper differential equation at m equidistant stations on the half column length. There are two differential equations, the one applying to stations at which the stress in the outer flange is continually increasing, the other to the reversed part of the column and depending on the maximum value of the outer flange stress. Therefore, it was necessary to proceed stepwise in the solution. It turned out that the approximation of the deflection curve by one single sine term gave a satisfactorily accurate value for the maximum load P_{max} of the column. The solutions obtained with two and three sine terms in the expression of the deflection curve were already almost identical. Duberg and Wilder arrived at similar results by making use of the Ramberg-Osgood stress-strain law.

On the basis of the above results, the maximum load was calculated by assuming the deflection curve of the column to be a half sine wave, varying systematically the form of the stress-strain curve (c) and the ratio $p_T = P_T/A\ \sigma_0 = \sigma_T/\sigma_0$, where P_T is the tangent modulus load and A the cross-sectional area of the column. Small values of p_T correspond to slender columns, values of p_T near unity to short columns. For each value of c and p_T the resulting transcendental equation between the column load P and the deflection a at the middle of the column could easily be solved for P, and so the maximum load P_{max} was calculated. In order to compare the maximum load with the tangent modulus load P_T and the reduced modulus load P_R the ratio $(P_{max} - P_T)/(P_R - P_T)$ was calculated in each case. The results are given graphically in Fig. 2.

With a given P_T, P_R can be computed as follows. The equations

$$P_T = [(\pi^2 E\ A\ h^2)/(4\ L^2)]\ [(1 - p_T)/(1 - c\ p_T)] \qquad (3)$$

$$P_R = [(\pi^2 E\ A\ h^2)/(4\ L^2)]\ [(2\ \eta)/(1 + \eta)] \qquad (4)$$

where L is the column length, h the depth of the cross section and η the value of E_T/E as defined in Eq. (2) corresponding to the stress $\sigma_R = P_R/A$, yield for $p_R = P_R/(A\ \sigma_0)$ the second degree equation

$$(1 + c)p_R^2 - 2\{1 + p_T[(1 - c\ p_T)/(1 - p_T)]\}p_R + 2\ p_T[(1 - c\ p_T)/(1 - p_T)] = 0 \qquad (5)$$

Fig. 3 shows the ratio $(P_R - P_T)/P_T$ as a function of p_T for different values of c. From Fig. 2 it is seen that, for values of p_T near unity, the maximum load will remain nearer to the tangent modulus load than to the reduced modulus load. The dotted curve in Fig. 3 gives the limiting cases when the ordinates of Fig. 2 are equal to 1/2. On the right-hand side of the dotted curve P_{max} is nearer to P_T, on the left-hand side nearer to P_R. All maximum points of the curves in Fig. 3 lie to the right of the dotted curve, and hence P_{max} is close to the tangent modulus load. If, for instance, $c = 0.9$, the value of p_T corresponding to $(P_{max} - P_T)/(P_R - P_T) = 0.5$ is approximately 0.64. For smaller values of p_T the stress-strain curve in Fig. 1 practically coincides with the straight line given by Hooke's law. Thus, from this investigation, we can draw the conclusion that the tangent modulus theory in most cases, and in the most important cases, gives a better approximation for the maximum load supported by an idealized H-section column compressed in the inelastic range than

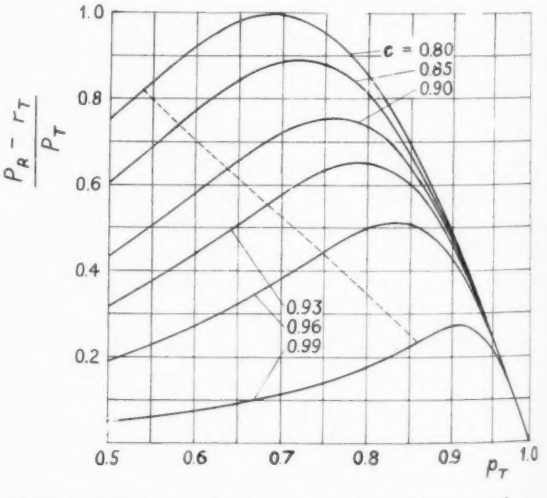

FIG. 3. Ratio $(P_R - P_T)/P_T$ for H-section column as a function of $p_T = \sigma_T/\sigma_0 = P_T/A\ \sigma_0$. The ordinate should vary from 0 to 0.10 and not from 0 to 1.0 as marked in the drawing.

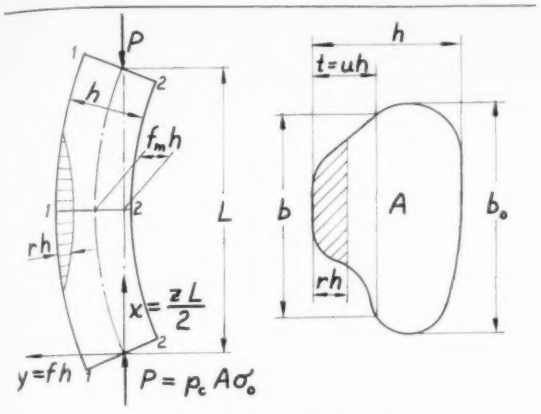

FIG. 4. Centrally compressed column.

the reduced modulus theory. This statement is in agreement with the results of Duberg and Wilder. However, Fig. 2 shows appreciable differences compared with the corresponding curves obtained by Duberg and Wilder. This comes evidently from the different signification of constants in Ramberg-Osgood's and Ylinen's stress-strain laws.

MATHEMATICAL ANALYSIS OF THE CENTRALLY COMPRESSED COLUMN

Let us consider a centrally compressed column of constant cross section with hinged ends. For simplicity, only bending in the principal plane perpendicular to the axis of least moment of inertia is discussed. The deflection is denoted by y (see Fig. 4), and the axial coordinate x is measured from one end along the line of action of the forces P. The cross-sectional properties are area A, width perpendicular to the plane of bending b, and depth h. The width ratio, b/b_0, where the reference width b_0 can be chosen arbitrarily, is, in general, a function of the distance t measured from the extreme fibers on the convex side. Our purpose is to show how the column behaves under increasing load, and especially to determine the maximum load.

In order to make the equations nondimensional, the following notations are introduced:

$$\left.\begin{aligned} z &= 2x/L, \quad f = y/h, \quad u = t/h \\ e &= E\epsilon/\sigma_0, \quad p = \sigma/\sigma_0, \quad p_c = \sigma_c/\sigma_0 = P/A\sigma_0 \end{aligned}\right\} \tag{6}$$

where σ_0 is one of the constants in Ylinen's stress-strain law, Eq. (1). In the last of Eqs. (6), σ_c signifies the average stress P/A and p_c the nondimensional average stress. The following basic assumptions are made: (1) planes perpendicular to the column axis before loading remain plane and perpendicular, and (2) at each fiber the relationship between stress and strain is the same as in simple compression and tension tests. From the first assumption it follows that the strain distribution across the column depth is a straight line,

$$e = e_1 + u(e_2 - e_1) \tag{7}$$

where e_1 and e_2 denote the nondimensional strains in the outermost fibers on the convex and the concave sides of the column, respectively. The unknown quantities e_1 and e_2 are considered as functions of z and p_c.

In considering the stress-strain relationship in a particular cross section we have to distinguish two different zones—one where the strain is continually increasing with increasing axial force, and the other near the outer edge of the cross section where the strain is decreasing after having reached a certain maximum. Fig. 4 shows how the width of the reversed zone is supposed to vary along the column length under a given value of the load. As long as the strain is continually increasing, the stress will be given by the stress-strain curve, while in the reversed zone a different law is followed. After the maximum value of the strain has been reached, the stress decreases according to the elastic modulus, $d\sigma = E\,d\epsilon$, or $dp = de$. At a fixed value of z the strain distribution lines of Eq. (7) depend on the parameter p_c. Fig. 5 shows a part near the outer edge of the cross section of the strain distribution lines corresponding to some values (p_{c1}, p_{c2}, ...) of the nondimensional axial load. The abscissa r of the tangent point A of the envelope of the strain distribution lines and the strain distribution line corresponding to the nondimensional load p_{ci} (Fig. 5) gives the nondimensional width of the reversed zone under this value of the load, and the ordinate e_r of point A gives the maximum value that the nondimensional strain can reach at the distance r from the outer fibers in the cross section under consideration. The parametric representation of the envelope is expressed by the two following equations:

$$e_1(p_c, z) + u[e_2(p_c, z) - e_1(p_c, z)] - e = 0 \tag{8a}$$

$$\frac{\partial}{\partial p_c} e_1(p_c, z) + u \frac{\partial}{\partial p_c} [e_2(p_c, z) - e_1(p_c, z)] = 0 \tag{8b}$$

Solved for u, Eq. (8b) gives $r(p_c, z)$; this expression, inserted in Eq. (8a), yields $e_r(p_c, z)$:

$$r = -\{(\partial e_1/\partial p_c)/[(\partial/\partial p_c)(e_2 - e_1)]\} \tag{9a}$$

$$e_r = e_1 + r(e_2 - e_1) = e_r(r) \tag{9b}$$

In a particular cross-section, strain reversal will occur if $r > 0$.

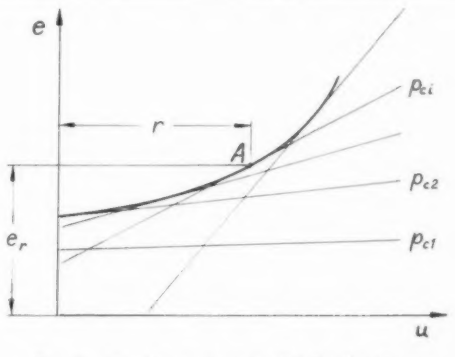

FIG. 5. Envelope of strain distribution lines.

TABLE 1
Expressions of e_1 and e_2 for $c = 0.9$, $p_c = 0.8$

Range	e_1 and e_2 in the Mid-Section of the Column
$0.800 \leqq p_c \leqq 0.805$	$e_1 = 0.880944 - 78.92\ (p_c - 0.8)^2$ $e_2 = 0.880944 + 2.8\ (p_c - 0.8) + 87.08\ (p_c - 0.8)^2$
$0.805 \leqq p_c \leqq 0.810$	$e_1 = 0.878971 - 0.7892\ (p_c - 0.805) - 47.16\ (p_c - 0.805)^2$ $e_2 = 0.897121 + 3.6708\ (p_c - 0.805) + 62.84\ (p_c - 0.805)^2$
$0.810 \leqq p_c \leqq 0.815$	$e_1 = 0.873846 - 1.2608\ (p_c - 0.810) - 123.28\ (p_c - 0.810)^2$ $e_2 = 0.917046 + 4.2992\ (p_c - 0.810) + 150.72\ (p_c - 0.810)^2$
$0.815 \leqq p_c \leqq 0.820$	$e_1 = 0.86446 - 2.4936\ (p_c - 0.815) - 233.28\ (p_c - 0.815)^2$ $e_2 = 0.94231 + 5.8064\ (p_c - 0.815) + 305.92\ (p_c - 0.815)^2$
$0.820 \leqq p_c \leqq 0.822$	$e_1 = 0.84616 - 4.8264\ (p_c - 0.820) - 1174.3\ (p_c - 0.820)^2$ $e_2 = 0.97899 + 8.8656\ (p_c - 0.820) + 1524.2\ (p_c - 0.820)^2$
$0.822 \leqq p_c \leqq 0.8226$	$e_1 = 0.83181 - 9.5236\ (p_c - 0.822) - 3405\ (p_c - 0.822)^2$ $e_2 = 1.002818 + 14.9624\ (p_c - 0.822) + 4496\ (p_c - 0.822)^2$

Let $p = S(e)$ signify the compressive stress-strain diagram of the material. Furthermore, denote by p_1 the nondimensional stress in the reversed zone and by p_2 the nondimensional stress in the remaining part of the cross section. From the above statements it follows that

$$(0 \leqq u \leqq r) \qquad p_1 = S[e_r(u)] - \{e_r(u) - [e_1 + u(e_2 - e_1)]\} \tag{10a}$$

$$(r \leqq u \leqq 1) \qquad p_2 = S[e_1 + u(e_2 - e_1)] \tag{10b}$$

The equations of force and moment equilibrium will read

$$p_c = \frac{b_0 h}{A}\left[\int_0^r p_1 \frac{b}{b_0}\,du + \int_r^1 p_2 \frac{b}{b_0}\,du\right] \tag{11}$$

$$p_c f = \frac{b_0 h}{A}\left[\int_0^r (p_1 - p_c)\frac{b}{b_0}\,u\,du + \int_r^1 (p_2 - p_c)\frac{b}{b_0}\,u\,du\right] \tag{12}$$

From Eq. (12) we obtain the expression

$$f = \frac{b_0 h}{A p_c}\left[\int_0^r (p_1 - p_c)\frac{b}{b_0}\,u\,du + \int_r^1 (p_2 - p_c)\frac{b}{b_0}\,u\,du\right] \tag{13}$$

for the nondimensional deflection.

Let us assume now that the column has a small initial deflection, denoted by $y_0 = y_0(x)$ or $f_0 = f_0(z)$, where $f_0 = y_0/h$. The curvature is then

$$1/\rho_0 = -(4h/L^2)\ (d^2 f_0/dz^2) \tag{14}$$

The radius of curvature is here considered positive when the column is bent in the positive direction of the y-axis, as in Fig. 4. From geometrical considerations, we obtain

$$1/\rho = (\sigma_0/E)\ [(e_2 - e_1)/h] + (1/\rho_0) \tag{15}$$

On the other hand, the expression for the curvature is

$$\frac{1}{\rho} = -\frac{(4h/L^2)\ (\partial^2 f/\partial z^2)}{\{1 + [(2h/L)\ (\partial f/\partial z)]^2\}^{3/2}} \tag{16}$$

The two previous equations yield

$$(e_2 - e_1)\frac{\sigma_0}{E}\frac{1}{h} + \frac{1}{\rho_0} = -\frac{(4h/L^2)\ (\partial^2 f/\partial z^2)}{\{1 + [(2h/L)\ (\partial f/\partial z)]^2\}^{3/2}} \tag{17}$$

Eqs. (11) and (17) define the solution of the problem represented by the functions $e_1(p_c, z)$ and $e_2(p_c, z)$. The quantities f, p_1, p_2, r, and e, involved in these equations are, however, connected to each other and to the variables p_c and z in a rather complicated manner as can be seen from Eqs. (9a), (9b), (10a), (10b), and (13).

AN APPROXIMATE METHOD FOR THE INITIALLY STRAIGHT COLUMN

As long as the strain on the convex side of the mid-section of the originally slightly curved column is continually increasing with increasing average stress the deformations can be found as follows. On the basis of Eq. (15) and the known compressive stress-strain diagram of the material a family of curves is constructed which gives the relationship between the curvature $1/\rho$ and the eccentricity $y = f h$ of the axial load, the nondimensional average stress p_c being a parameter. These curves make it possible to find the deflection curve of the column for different values of p_c using some graphical or numerical method of integration, as von Kármán has shown.[6] Thus also e_1 (p_c, z) and e_2 (p_c, z) are found up to that value of p_c by which e_1 begins to diminish in the mid-section. After the occurrence of strain reversal the above-mentioned method does not give the correct result, but then Eqs. (11) and (17) must be used.

Since, in the case of the originally curved column, the real difficulties begin only after the strain reversal has begun on the convex side, the following theory will consider only originally straight columns for which $y_0(x) = 1/\rho_0 = 0$. Such columns will remain straight until the axial load has reached the tangent modulus value. The treatment of initially curved columns after strain reversal has occurred would not contain any essential increase of difficulties. The cross section is assumed to be rectangular for simplicity.

Eq. (11) of the equilibrium of axial forces reads, for the rectangular cross section,

$$p_c = \int_0^1 p\,du = \int_0^r p_1\,du + \int_r^1 p_2\,du \qquad (18)$$

The nondimensional deflection is obtained from Eq. (13),

$$\left.\begin{aligned} f &= \frac{1}{p_c}\int_0^1 (p - p_c)u\,du \\ &= \frac{1}{p_c}\left[\int_0^r (p_1 - p_c)u\,du + \int_r^1 (p_2 - p_c)\,u\,du\right] \end{aligned}\right\} \qquad (19)$$

From the geometrical condition, Eq. (17), it follows, when the right-hand side is linearized for small deflections,

$$\partial^2 f/\partial z^2 = -(L^2/4\,h^2)\,(\sigma_0/E)\,(e_2 - e_1) \qquad (20)$$

The unknown functions $e_1(p_c, z)$ and $e_2(p_c, z)$ are required to satisfy Eqs. (18) and (20).

Let us suppose now that the deflection of the column can be approximated with sufficient accuracy by a half sine wave,

$$f = f_m \sin(\pi/2)z \qquad (21)$$

where f_m signifies the deflection of the middle of the column divided by the depth of the cross section. According to Eq. (20) the difference $e_2 - e_1$ is then, also, sinusoidal, and it will be sufficient to consider its value $(e_2 - e_1)_m$ in the mid-section of the column. From Eq. (20) it follows

$$f_m = [L^2/(\pi^2 h^2)]\,(\sigma_0/E)\,(e_2 - e_1)_m \qquad (22)$$

Let the compressive stress-strain curve of the material be expressed by Ylinen's stress-strain function [from Eq. (1)]

$$e = \Phi(p) = c\,p - (1 - c)\log(1 - p) \qquad (23)$$

from which

$$dp/de = E_T/E = \eta(p) = (1 - p)/(1 - c\,p) \qquad (24)$$

By making use of the tangent modulus formula

$$p_T = [(\pi^2 E\,h^2)/(12\,\sigma_0 L^2)]\,\eta(p_T) \qquad (25)$$

Eq. (22) can be written

$$f_m = \tfrac{1}{4}(1 - p_T)/[12\,p_T\,(1 - c\,p_T)]\,(e_2 - e_1)_m \qquad (26)$$

To find a first approximation for the solution, the following method is proposed. The curves describing e_1 and e_2 in the mid-section of the column as functions of the nondimensional average stress p_c are approximated in the ranges (p_T, p_{c1}), (p_{c1}, p_{c2}) etc. (see Fig. 6), by convenient analytical expressions which are determined in the way that the curve parts have the same slope at the connection points p_{c1}, p_{c2}, etc., and that Eqs. (18) and (26) are satisfied at these points. Calculations become very simple by assuming the curve parts to be parabolic.

A Numerical Solution

In order to illustrate the above-mentioned procedure, the numerical solution in a typical case of the inelastic buckling, with the values of $c = 0.9$, $p_T = 0.8$, is given here. Table 1 shows the chosen ranges of p_c and the obtained equations of the nondimensional compressive strains on the convex and concave sides of the mid-section of the column. The result is plotted in Fig. 6.

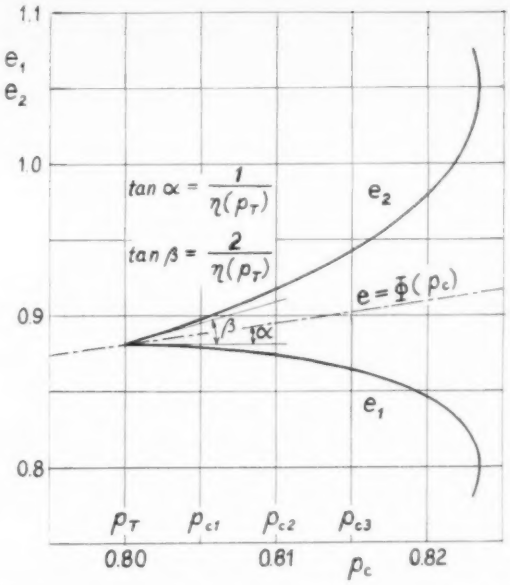

FIG. 6. Strains on convex and concave sides of column mid-section as functions of nondimensional average stress $p_c = \sigma_c/\sigma_0 = P/A\,\sigma_0$ for $c = 0.9$, $p_T = 0.8$ (rectangular cross section).

Let us consider the range $0.8 \leqq p_c \leqq 0.805$. For values of p_c smaller than p_T the column remains straight—that is, e_1 and e_2 are given by the inverse stress-strain function $e = \Phi(p_c)$. For $p_c = p_T = 0.8$, Eq. (23) yields (with $c = 0.9$) $e_1 = e_2 = 0.880944$.

At the beginning of the bending, $(d\,e_1/d\,p_c) = 0$ in the column mid-section. When p_c exceeds the tangent modulus value p_T by an infinitely small amount Δp_c the stress distribution across the column depth is a straight line. The increase of strain at the middle of the cross section is $\Delta p_c/\eta(p_T)$. The increase of strain at the concave side of the cross section is then equal to $2[\Delta p_c/\eta(p_T)]$. Thus the slope of the curve $e_2 = e_2(p_c)$ at $p_c = p_T$ is two times the slope of the inverse stress-strain curve $e = \Phi(p_c)$ at this point (see Fig. 6). The initial conditions of the buckling process have been derived more rigorously by Duberg and Wilder.[4] For $p_c = p_T = 0.8$, the slope of the stress-strain curve $e = \Phi(p_c)$ is [from Eq. (24)]

$$\frac{1}{\eta(p_T)} = \frac{1 - 0.9 \times 0.8}{1 - 0.8} = 1.4 \qquad (27)$$

and the slope of the curve $e_2 = e_2(p_c)$ is equal to 2.8 (see Fig. 6).

From the conditions at $p_c = 0.8$ it follows that the assumed parabolic expressions of e_1 and e_2 for $0.8 \leqq p_c \leqq 0.805$ take the form

$$e_1 = 0.880944 - a_1(p_c - 0.8)^2 \qquad (28a)$$

$$e_2 = 0.880944 + 2.8(p_c - 0.8) + a_2(p_c - 0.8)^2 \qquad (28b)$$

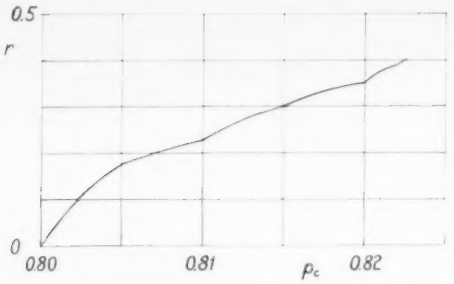

FIG. 7. Width of reversed zone in column mid-section as a function of nondimensional average stress $p_c = \sigma_c/\sigma_0 = P/A\,\sigma_0$ for $c = 0.9$, $p_T = 0.8$ (rectangular cross section).

The coefficients of the second degree terms have to be determined by trial and error so that Eqs. (18) and (26) are satisfied for $p_c = 0.805$. Here it is shown that Eqs. (18) and (26) are satisfied for $p_c = 0.805$ by the expressions appearing in Table 1.

For the calculation of the stress distribution the envelope of the strain distribution lines has to be known. Eq. (9a) yields the nondimensional width of the reversed zone in the mid-section of the column, $r = 0.177$. In particular, e_r corresponding to $r = 0.1$ is found by trial and error by varying the parameter p_c in Eqs. (9a) and (9b); the result is $e_r(0.1) = 0.881259$. Table 2 shows the calculation of the stress pattern in the mid-section of the column for $p_c = 0.805$. The cross section was divided into ten equal intervals. Detailed calculations proved that this was sufficient even for higher values of the average stress. In order to facilitate the calculation of values of p corresponding to given values of e from the stress-strain curve a table was prepared to permit interpolation. Columns 8 and 9 in Table 2 give the coefficients for the use of Simpson's rule for Eqs. (18) and (19). The result is

$$\int_0^1 (p - 0.805)\,du = 0.000000 \tag{29}$$

$$\left.\begin{aligned} f_m &= \frac{1}{p_c}\int_0^1 (p - 0.805)\,u\,du \\ &= \frac{1}{0.805}\int_0^1 (p - 0.805)\,u\,du = 0.001350 \end{aligned}\right\} \tag{30}$$

On the other hand, Eq. (26) yields

$$f_m = f\,\frac{1 - 0.8}{12 \times 0.8 \times (1 - 0.9 \times 0.8)} \times 0.018150 = 0.001350 \tag{31}$$

Thus, Eqs. (18) and (26) are satisfied.

The above-mentioned method of trial and error in calculating the coefficients of the second degree terms of e_1 and e_2 was briefly as follows. First, a_1 in Eq. (28a) was chosen arbitrarily (a_1') and several values were given to a_2. With each of these values and a_1' the stress pattern in the mid-section of the column was calculated. Then, in general, the average stress of this stress pattern, obtained from Eq. (18), differed from the value 0.805 by an amount Δ_1. The value a_2', for which $\Delta_1 = 0$, was accepted as a couple for a_1'. With a_1' and a_2', f_m was calculated from Eq. (19). In general, this f_m differed from the value given by Eq. (26) by an amount Δ_2. Now another value a_1'' was given to a_1 and the corresponding value a_2'' of a_2 was found as above, so that the average value of the nondimensional stress pattern was 0.805. With a_1'' and a_2'' the quantity Δ_2 was calculated again, and, continuing in this manner, a couple of values for a_1 and a_2 were found for which also $\Delta_2 = 0$.

The inaccuracy of the above method can be clearly visualized from Fig. 7. The plot of the nondimensional width of the reversed zone in the mid-section, r, against the nondimensional average stress, p_c, is a continuous curve, but its slope changes stepwise at the junctions. Between these points the curve consists of hyperbolas. By reducing the length of the intervals of Table 1—that is, by satisfying the fundamental equations for a greater number of values of p_c—the curve would, of course, become smoother. Then the results would be nearer to the exact solution (based on the assumption of a sinusoidal deflection curve). Calculations made at the middle of an interval, $p_c = 0.8075$, showed that Eqs. (18) and (26) are approximately satisfied at this point. The approximation made by increasing p_c stepwise can be considered as not significant.

As can be seen from Table 1, the above explained approximate method was applied only up to the nondimensional average stress $p_c = 0.8226$. After that the method was essentially simplified by making the as-

TABLE 2

Calculation of the Stress Pattern for $c = 0.9$, $p_T = 0.8$ ($z = 1$, $p_c = 0.805$)

(1) u	(2) e Eq. (7)	(3) e_r Eqs. (9)	(4) $S(e_r)$	(5) $e_r - e$ (3) − (2)	(6) p Eqs. (10)	(7) $p - 0.805$	(8)	(9)
0.0	0.878971	0.880944	0.800000	0.001973	0.798027	−0.006973	1	0
0.1	0.880786	0.881259	0.800225	0.000473	0.799752	−0.005248	4	0.4
0.2	0.882601				0.801182	−0.003818	2	0.4
0.3	0.884416				0.802475	−0.002525	4	1.2
0.4	0.886231				0.803764	−0.001236	2	0.8
0.5	0.888046				0.805050	+0.000050	4	2
0.6	0.889861				0.806333	+0.001333	2	1.2
0.7	0.891676				0.807613	+0.002613	4	2.8
0.8	0.893491				0.808890	+0.003890	2	1.6
0.9	0.895306				0.810163	+0.005163	4	3.6
1.0	0.897121				0.811434	+0.006434	1	1

sumption that the nondimensional width of the reversed zone in the column mid-section would not reach the value $r = 0.5$. This assumption seems rather justified from Fig. 7. For each value of p_c exceeding 0.8226 it was necessary only to determine e_1 and e_2 to satisfy Eqs. (18) and (26). Table 3 shows the results for $p_c = 0.823$ and $p_c = 0.8234$, two solutions in each case. The first of these solutions corresponds to increasing load, the second to decreasing load after the maximum value of the load has been reached.

The maximum abscissa $p_{c\,max}$ of the curves in Fig. 6 is 0.8235. The critical value predicted by the reduced modulus theory is $p_R = 0.86351$. The interesting ratio $(p_{c\,max} - p_T)/(p_R - p_T)$ becomes

$$(p_{c\,max} - p_T)/(p_R - p_T) = 0.0235/0.06351 = 0.370 \quad (32)$$

For the H-section column the corresponding value (Fig. 2) is 0.350.

When the axial force has reached its maximum value the width of the reversed zone in the mid-section is approximately $r = 0.42$. According to the reduced modulus theory, it would be $r = 0.459$ and constant along the column length.

Conclusions

The above theory is based on the assumption that the deflection curve is a half sine wave. The solution becomes very laborious if the form of the deflection curve is considered as unknown. However, the results obtained for the H-section column showed that the deflection was very near to a sine curve. The maximum load, particularly, calculated on the basis of a supposed sine-wave deflection, did not differ significantly from the correct solution. By extending the conclusions gained from the analysis of the idealized H-section column, we can condense the results of this investigation as follows: the maximum load supported by a straight uniform column centrally compressed in the inelastic range in most cases, and, particularly, in the most important cases, remains nearer to the tangent modulus load than to the reduced modulus load. Therefore, it is recommended that the tangent modulus theory be used even in theoretical considerations.

Table 3

Values of e_1 and e_2 for $p_c = 0.823$ and $p_c = 0.8234$ in Column Mid-Section

$p_c = 0.823$	$e_1 = 0.81825$	$e_1 = 0.7785$
	$e_2 = 1.02309$	$e_2 = 1.0755$
$p_c = 0.8234$	$e_1 = 0.805$	$e_1 = 0.793$
	$e_2 = 1.041$	$e_2 = 1.057$

References

[1] Shanley, F. R., *Inelastic Column Theory*, Journal of the Aeronautical Sciences, Vol. 14, No. 5, pp. 261–267, May, 1947.

[2] Lin, Tung-Hua, *Inelastic Column Buckling*, Journal of the Aeronautical Sciences, Vol. 17, No. 3, pp. 159–172, March, 1950.

[3] Pearson, C. E., *Bifurcation Criterion and Plastic Buckling of Plates and Columns*, Journal of the Aeronautical Sciences, Vol. 17, No. 7, pp. 417–424, July, 1950.

[4] Duberg, J. E., and Wilder, T. W., III, *Inelastic Column Behavior*, NACA TN 2267, January, 1951.

[5] Ylinen, A., *A Stress-Strain Function for Simple Compression and Corresponding Buckling Formula* (in Finnish with English abstract), Teknillinen Aikakauslehti (Helsinki), Vol. 38, No. 1, pp. 9–14, January, 1948.

[6] Timoshenko, S., *Theory of Elastic Stability*, p. 54; McGraw-Hill Book Company, Inc., New York, 1936.

An Investigation of the Noise Produced by a Subsonic Air Jet

(*Continued from page 866*)

l General Theory. Proc. Roy. Soc. A, vol. 211, pp. 564–587, 1952.

[3] Westley, R., and Lilley, G. M., *An Investigation of the Noise Field from a Small Jet and Methods for Its Reduction*, A.R.C. Report 14,719, 1952 (unpublished).

[4] Fitzpatrick, H. M., and Lee, R., *Measurement of the Noise Radiated by Subsonic Air Jets*, David W. Taylor Model Basin, Report 835, November, 1952.

[5] von Gierke, H. E., et al., *The Noise Field of a Turbo-Jet Engine*, J. Acous. Soc. Amer., Vol. 24, p. 169–174, 1952.

[6] Hubbard, H. H., and Lassiter, L. W., *Experimental Studies of Noise from Subsonic Jets in Still Air*, NACA Tech. Note 2757, 1952.

[7] Lighthill, M. J., *On Sound Generated Aerodynamically—II Turbulence as a Source of Sound*, Proc. Roy. Soc. A, Vol. 222, pp. 1–32, 1954.

[8] Attree, V. H., *A Feedback-Pair Video Amplifier*, Electronic Engrg., Vol. 24, p. 504, 1952.

[9] Attree, V. H., *Precision Voltage Source*, Wireless Engr., Vol. 29, p. 226, 1952.

[10] Goldstein, S., *Note on the Measurement of Total-head and Static Pressure in Turbulent Streams*, Proc. Roy. Soc. A, Vol. 155, p. 570, 1936.

[11] Young, A. D., and Maas, J. N., *The Behaviour of a Pitot Tube in a Transverse Total-Pressure Gradient*, A.R.C. R & M No. 1770, 1937.

[12] Morse, P. M., *Vibration and Sound*, Ch. 7, McGraw-Hill, 1948.

[13] Powell, A., *The Noise of Choked Jets*, J. Acous. Soc. Amer., Vol. 25, pp. 385–389, 1953.

[14] Proudman, I., *The Generation of Noise by Isotropic Turbulence*, Proc. Roy. Soc. A, Vol. 214, pp. 119–132, 1952.

[15] Rayleigh, *Theory of Sound*, Vol. II, §324; Macmillan, 1896.

Aspect Ratio Influence at High Subsonic Speeds*

GORDON F. ANDERSON†
Brown University

SUMMARY

The velocity induced by the thickness of a thin infinite wing in a parallel flow can be calculated, at some distance from the wing, by linearized subsonic compressible flow theory. If now, a portion of the infinite wing is removed from the flow, the velocity at any point on the wing will be less by the velocity induced by the portion of the wing which was removed. Furthermore, if the part removed is relatively far away from the point on the wing for which the induced velocity is being calculated, linearized subsonic compressible flow theory is valid.

Utilizing such a scheme, the velocity at the location of a finite wing can be considered as being the same as for the infinite wing, reduced by the amount which would have been contributed by the portions of the infinite wing which were removed from the flow. The difference in the induced velocity can be averaged over the area of the finite wing and the average applied as a correction to the free-stream velocity. At this increased free-stream velocity, the finite wing should have approximately the same pressure distribution as the infinite wing at the uncorrected free-stream velocity.

SYMBOLS

D	= drag
F, G	= auxiliary functions
M	= Mach Number
U	= free-stream velocity in x-direction
a	= speed of sound
c	= chord of wing
c_D	= drag coefficient
d	= maximum thickness of wing profile
g	= function representing strength of source-sink distribution
g_0	= auxiliary function
k	= ratio of specific heats, c_p/c_v
q	= dynamic pressure
u	= induced or perturbation velocity in x-direction
x, y, z	= Cartesian coordinates
β	= $\sqrt{1 - M^2}$
δ	= dimensionless geometric parameter
λ	= wing aspect ratio
φ	= velocity potential
ξ	= auxiliary coordinate in x-direction
ζ	= auxiliary coordinate in z-direction
τ	= thickness ratio of wing profile = d/c

Subscripts

0	= zero streamline
i	= incompressible
c	= compressible
∞	= infinity, far away from disturbances
x	= partial derivative with respect to x
A	= dependent on wing profile area
I	= dependent on wing profile moment of inertia
$corr$	= corrected

Received June 3, 1955.

* This investigation was performed under the sponsorship of the United States Air Force through the Office of Scientific Research of the Air Research and Development Command under Contract AF 18(600)-664.

† Research Associate, Division of Engineering.

(I) INTRODUCTION

EXPERIMENTAL DATA have shown that a decrease in aspect ratio of a wing decreases the adverse effects of compressibility on the wing. This paper presents an approximate method by which the quantitative effect of variation of aspect ratio can be predicted.

Goethert[3] has already determined the effect of compressibility on the velocities induced by small angles of attack of the finite wing. Throughout this paper references to induced velocities refer only to the velocities induced by the thickness of the finite wing.

At any point on the infinite wing, the velocity is that of the free stream far upstream plus the velocity induced by the presence of the wing in the flow. If we consider a finite portion of the infinite wing, which contains this same point at which the velocities are being considered, and remove from the flow the remaining portions of the infinite wing, the velocity at that point will now be the same as for the infinite wing less the velocity that would be induced by the portions of the wing that were removed from the flow. If we assume that the decrease in the induced velocity does not differ greatly from point to point on the finite wing, it is possible to average the effect over the whole of the finite wing and apply the result as a correction to the free-stream velocity.

The result of this reasoning is that the finite wing will be considered to experience the same static pressure to total pressure ratio at corresponding points as the infinite wing, but only when measured at a free-stream velocity which is greater, by the correction calculated, than the free-stream velocity over the infinite wing. Schlieren pictures[1] of wings of different aspect ratio at high Mach Numbers qualitatively substantiate the validity of this approach. Furthermore, a comparison with experimental drag data[2] produced reasonable quantitative agreement.

The justification for applying linear theory to this problem and expecting validity well into the transonic range (which is indeed necessary if drag coefficients are to be compared) lies in the fact that the correction calculated is concerned with that part of the flow field for which the linear theory is valid. The point in the flow which is being considered may lie close to or on the finite wing, but the effect we are calculating is due to a portion of the infinite wing which is relatively far

removed from the point. This reasoning is similar to that used by Goethert[4] in the calculation of wind-tunnel wall corrections at high subsonic speeds.

If experimental data are available for a given profile at any one aspect ratio, the performance at another aspect ratio may be predicted. The nonlinear characteristics of the profile are determined by the experimental data, and the effect of variation of the aspect ratio is a nearly linear phenomenon which is approximated by the linear theory presented in this paper.

(II) Linear Theory

The potential of a finite wing at zero lift in a free stream of velocity U_∞ can be represented by the potential of the free-stream velocity plus the potential of a source-sink distribution.

$$\varphi = U_\infty x - \int_{-1}^{+1}\int_{-\lambda}^{+\lambda} \frac{g(\xi,\zeta)}{4\pi} \times d\xi d\zeta / \sqrt{(x-\xi)^2 + y^2 + (z-\zeta)^2} \quad (1)$$

The strength of the source-sink distribution $g(\xi, \zeta)$ should be such that the zero streamline

$$\left.\begin{aligned} &-1 \le x \le 1 \\ y_0 = y_0(x, z) \quad & \\ &-\lambda \le z \le \lambda \end{aligned}\right\} \qquad (2)$$
$$y_0 = 0 \quad \text{everywhere else}$$

defines the boundaries of the finite wing.

With the assumption that the wing is a straight rectangular wing with constant airfoil section in the spanwise direction

$$y_0 = y_0(x) \quad \text{in the interval} \quad (-\lambda \le z \le \lambda) \quad (3)$$

The linearized distribution then becomes

$$g(x, \xi) = 2U_\infty y_{0x} = 2U_\infty y_0' \quad (4)$$

and, therefore,

$$\varphi = U_\infty x - \int_{-1}^{+1}\int_{-\lambda}^{+\lambda} 2U_\infty \times \frac{y_0'}{4\pi} \frac{d\xi d\zeta}{\sqrt{(x-\xi)^2 + y^2 + (z-\zeta)^2}} \quad (5)$$

The above potential can also be represented by an infinite (in the spanwise direction) source-sink distribution less the part of the distribution which lies in the intervals $(-\infty < z < -\lambda)$ and $(\lambda < z < \infty)$.

$$\varphi = U_\infty x - \int_{-1}^{+1}\int_{-\infty}^{+\infty} 2U_\infty \frac{y_0'}{4\pi} \times \frac{d\xi\, d\zeta}{\sqrt{(x-\xi)^2 + y^2 + (z-\zeta)^2}} + \int_{-1}^{+1}\int_{-\infty}^{-\lambda} 2U_\infty \frac{y_0'}{4\pi} \times \frac{d\xi d\zeta}{\sqrt{(x-\xi)^2 + y^2 + (z-\zeta)^2}} + \int_{-1}^{+1}\int_{\lambda}^{\infty} 2U_\infty \frac{y_0'}{4\pi} \times \frac{d\xi d\zeta}{\sqrt{(x-\xi)^2 + y^2 + (z-\zeta)^2}} \quad (6)$$

letting

$$F(\lambda, x, y, z) = \int_{-1}^{+1}\int_{-\infty}^{-\lambda} \frac{y_0'}{2\pi} \times \frac{d\xi d\zeta}{\sqrt{(x-\xi)^2 + y^2 + (z-\zeta)^2}} + \int_{-1}^{+1}\int_{\lambda}^{\infty} \frac{y_0'}{2\pi} \times \frac{d\xi\, d\zeta}{\sqrt{(x-\xi)^2 + y^2 + (z-\zeta)^2}} \quad (7)$$

then

$$\varphi = U_\infty \left[x + \int_{-1}^{+1} \frac{y_0'}{\pi} \ln \sqrt{(x-\xi)^2 + y^2}\, d\xi + F(\lambda, x, y, z) \right] \quad (8)$$

The velocity, at any point on the wing, in the free-stream direction will then be

$$u = U_\infty + u_{\lambda=\infty} + U_\infty F_x(\lambda, x, y, z) \quad (9)$$

or

$$u = U_\infty [1 + F_x(\lambda, x, y, z)] + u_{\lambda=\infty} \quad (10)$$

If the average value of $F_x(\lambda, x, y, z)$ can be found

$$u = U_\infty [1 + \bar{F}_x(\lambda)] + u_{\lambda=\infty} \quad (11)$$

The finite wing and the infinite wing will have the same ratio of static to total pressure at corresponding chordwise positions only when

$$u_{finite\ wing} = u_{infinite\ wing}$$

$$U_\infty\ [1 + \bar{F}_x(\lambda)]_{finite\ wing} = U_{\infty\ infinite\ wing}$$

and therefore, the two wings will experience the same force per unit span only when the free-stream velocities far from the wings have the above relationship.

(III) Evaluation of the Correction to the Free-Stream Velocity

$$F_x = -\int_{-1}^{+1}\int_{-\infty}^{-\lambda} \frac{y_0'}{2\pi} \frac{(x-\xi)d\xi d\zeta}{[(x-\xi)^2 + y^2 + (z-\zeta)^2]^{3/2}} - \int_{-1}^{+1}\int_{\lambda}^{\infty} \frac{y_0'}{2\pi} \frac{(x-\xi)d\xi d\zeta}{[(x-\xi)^2 + y^2 + (z-\zeta)^2]^{3/2}} \quad (12)$$

integrating Eq. (12) over z from $-\infty < z < -\lambda$ and $\lambda < z < \infty$

$$F_x = \int_{-1}^{+1} \frac{y_0'}{2\pi} \frac{(x-\xi)}{(x-\xi)^2 + y^2} \times \left\{ \frac{\lambda - z}{\sqrt{(x-\xi)^2 + y^2 + (\lambda - z)^2}} + \frac{\lambda + z}{\sqrt{(x-\xi)^2 + y^2 + (\lambda + z)^2}} - 2 \right\} d\xi \quad (13)$$

The average value of F_x at the location of the finite wing is represented by

$$\bar{F}_x = \frac{1}{4\lambda} \int_{-1}^{+1}\int_{-\lambda}^{+\lambda} F_x dx dz \quad (14)$$

$$\bar{F}_x = \frac{1}{4\lambda}\int_{-1}^{+1}\int_{-1}^{+1}\frac{y_0'(x-\xi)}{2\pi[(x-\xi)^2+y^2]}\times \int_{-\lambda}^{+\lambda}\left\{\frac{\lambda-z}{\sqrt{(x-\xi)^2+y^2+(\lambda-z)^2}}+\frac{\lambda+z}{\sqrt{(x-\xi)^2+y^2+(\lambda+z)^2}}-2\right\}dxdzd\xi \quad (15)$$

$$\bar{F}_x = \int_{-1}^{+1}\frac{y_0'}{2\pi}\left\{\sqrt{1+\left(\frac{1-\xi}{2\lambda}\right)^2}-\sqrt{1+\left(\frac{1+\xi}{2\lambda}\right)^2}+\frac{\xi}{\lambda}-\ln\frac{1+\sqrt{1+[(1-\xi)/2\lambda]^2}}{1+\sqrt{1+[(1+\xi)/2\lambda]^2}}\right\}d\xi \quad (16)$$

Denoting the term in the brackets by $G(\xi)$ and approximating it by a Taylor series

$$\left.\begin{aligned} G(\xi) &= G(0)+\xi G'(0)+\frac{\xi^2}{2}G''(0)+\ldots+\frac{\xi^n}{n!}G'^n(0)\\ G(0) &= G''(0)=G''''(0)\equiv 0\\ G(\xi) &= \xi G'(0)+\frac{\xi^3}{3!}G'''(0)+\frac{\xi^5}{5!}G'(0)+\ldots \end{aligned}\right\} \quad (17)$$

$$\bar{F}_x = \int_{-1}^{+1}\frac{y_0'}{2\pi}\left\{\xi G'(0)+\frac{\xi^3}{3!}G'''(0)+\frac{\xi^5}{5!}G'^5(0)\ldots\right\}d\xi \quad (18)$$

$$\left.\begin{aligned} G'(0) &= \frac{1}{\lambda}\left\{2\lambda-\sqrt{1+4\lambda^2}+1\right\}\\ G'''(0) &= 4\left\{\frac{4\lambda^3}{\sqrt{(1+4\lambda^2)^3}}-\frac{3\lambda}{\sqrt{1+4\lambda^2}}+1\right\}\\ G'^5(0) &= 48\left\{-\frac{5\lambda}{\sqrt{1+4\lambda^2}}+\frac{25\lambda^3}{\sqrt{(1+4\lambda^2)^3}}-\frac{72\lambda^5}{\sqrt{(1+4\lambda^2)^5}}+\frac{80\lambda^7}{\sqrt{(1+4\lambda^2)^7}}+1\right\} \end{aligned}\right\} \quad (19)$$

let

$$\left.\begin{aligned} g_1(\lambda) &= G(0)\\ g_2(\lambda) &= \frac{G'''(0)}{3!}\\ g_3(\lambda) &= \frac{G'^5(0)}{5!} \end{aligned}\right\} \quad (20)$$

$$\bar{F}_x = g_1(\lambda)\frac{1}{2\pi}\int_{-1}^{+1}y_0'\xi d\xi + g_2(\lambda)\frac{1}{2\pi}\int_{-1}^{+1}y_0'\xi^3 d\xi + g_3(\lambda)\frac{1}{2\pi}\int_{-1}^{+1}y_0'\xi^5 d\xi \quad (21)$$

The functions $g_1(\lambda)$, $g_2(\lambda)$ and $g_3(\lambda)$ have been calculated and are plotted in Fig. 1. For $\lambda > 1$, $g_2(\lambda)$ and $g_3(\lambda)$ are negligible and for $\lambda > 0.4$, $g_3(\lambda)$ is negligible. In subsequent calculations $g_3(\lambda)$ is omitted. (See Fig. 2.)

$$\bar{F}_x = g_1(\lambda)\frac{1}{2\pi}\int_{-1}^{+1}y_0'\xi d\xi + g_2(\lambda)\frac{1}{2\pi}\int_{-1}^{+1}y_0'\xi^3 d\xi \quad (22)$$

$$\int_{-1}^{+1}y_0'\xi d\xi = -\int_{-1}^{+1}y_0 d\xi \quad (23)$$

$$\int_{-1}^{+1}y_0'\xi^3 d\xi = -\int_{-1}^{+1}3y_0\xi^2 d\xi \quad (24)$$

If the profile is compared to the rectangle as in Fig. A:

$$2\int_{-1}^{+1}y_0 d\xi = \text{area of airfoil}$$

dc = area of rectangle

let

$$\delta_A = 2\int_{-1}^{+1}y_0 d\xi / dc \quad (25)$$

then

$$\int_{-1}^{+1}y_0 d\xi = 2\frac{d}{c}\delta_A \quad (26)$$

likewise

$$\int_{-1}^{+1}2y_0\xi^2 d\xi = \text{moment of inertia of profile about } y\text{-axis}$$

$dc^3/12$ = moment of inertia of rectangle about y-axis

let

$$\delta_I = \frac{\int_{-1}^{+1}2y_0\xi^2 d\xi}{dc^3/12} \quad (27)$$

then

$$\int_{-1}^{+1}y_0\xi^2 d\xi = \frac{2}{3}\frac{d}{c}\delta_I \quad (28)$$

and, therefore,

$$\bar{F}_x = -g_1(\lambda)(1/\pi)(d/c)\delta_A - g_2(\lambda)(1/\pi)(d/c)\delta_I \quad (29)$$

$$\bar{F}_x = -(\tau/\pi)\{g_1(\lambda)\delta_A + g_2(\lambda)\delta_I\} \quad (30)$$

so that

$$u = U_\infty\{1-(\tau/\pi)[g_1(\lambda)\delta_A + g_2(\lambda)\delta_I]\} + u_{\lambda=\infty} \quad (31)$$

$$u_{\infty_{corr}} = U_\infty\{1-(\tau/\pi)[g_1(\lambda)\delta_A + g_2(\lambda)\delta_I]\} \quad (32)$$

$$U_{\infty_{corr}} = U_\infty + \Delta u \quad (33)$$

$$\Delta u/U_\infty = -(\tau/\pi)[g_1(\lambda)\delta_A + g_2(\lambda)\delta_I] \quad (34)$$

for $\lambda > 1$

$$g_2(\lambda) \doteq 0, \qquad g_1(\lambda) \doteq (1/\lambda)[1-(1/4\lambda)] \quad (35)$$

$$\Delta u/U_\infty \doteq -(\tau/\pi\lambda)[1-(1/4\lambda)]\delta_A \quad (36)$$

Employing the Prandtl-Glauert approximation for compressible flow, we obtain

$$\frac{\Delta u_c}{U_\infty} = \frac{\Delta u_i}{U_\infty}\frac{1}{\beta^2} = -\frac{1}{\pi\beta^2}\tau_i\{g_1(\lambda_i)\delta_A + g_2(\lambda_i)\delta_I\} \quad (37)$$

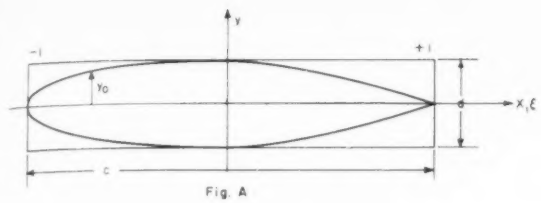

Fig. A

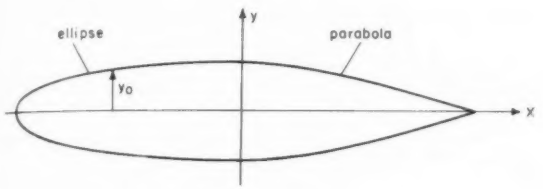

Fig. B

FIG. 1
VARIATION OF FUNCTIONS
$g_n(\lambda)$ WITH λ

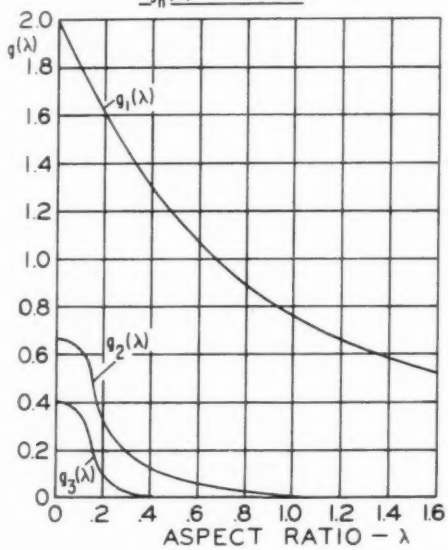

FIG. 2
COMPARISON OF $g_1(\lambda)$ EXACT AND $g_1(\lambda)$ APPROX.

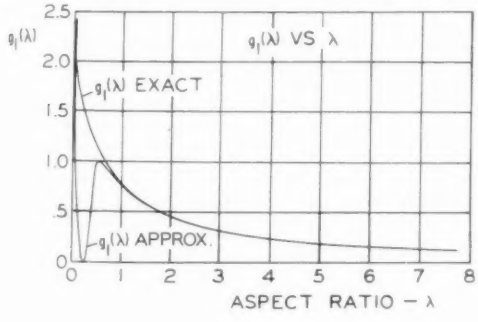

FIG. 3 FREE STREAM MACH NO. CORRECTION FOR VARIOUS VALUES OF λ
$\frac{\Delta M}{M}\frac{1}{\tau}$ VS M

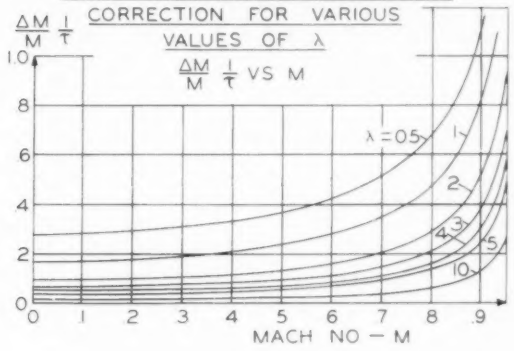

FIG 4 DRAG COEFFICIENT CORRECTION FOR VARIOUS VALUES OF FREE STREAM MACH NO. CORRECTION

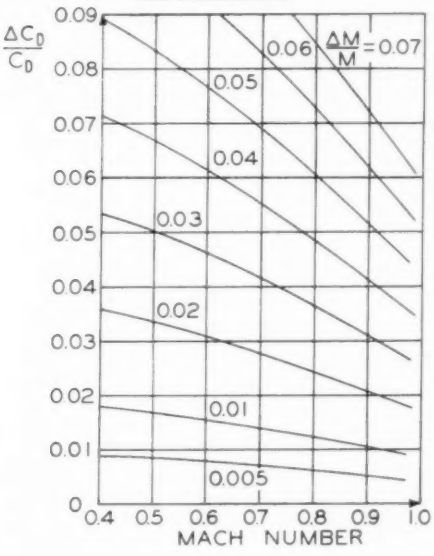

FIG 5 CORRECTED EXPERIMENTAL DATA
$C_D = f(M)_\lambda$ (REF 2 FIG. 58)
NACA 0 0012-1.1·30 PROFILE

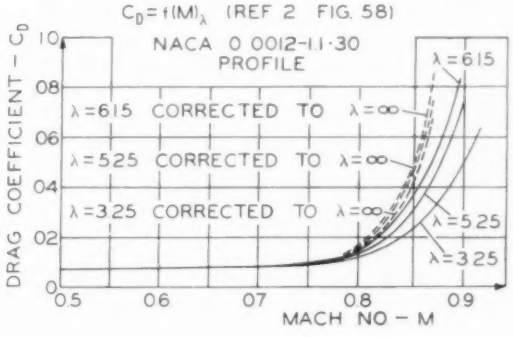

FIG 6 CORRECTED EXPERIMENTAL DATA

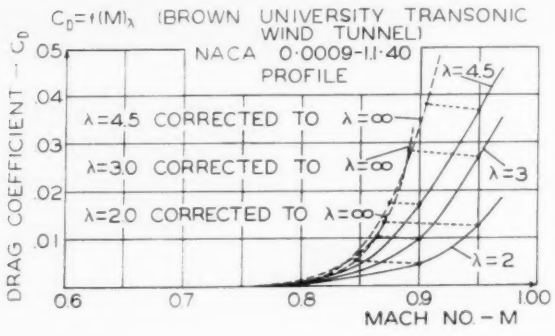

$$\frac{\Delta u_c}{U_\infty} = -\frac{1}{\pi\beta}\tau_c\left\{g_1(\beta\lambda_c)\delta_A + g_2(\beta\lambda_c)\delta_I\right\} \tag{38}$$

and for $\beta\lambda_c > 1$

$$\frac{\Delta u_c}{U_\infty} \doteq -\frac{1}{\pi\beta^2\lambda_c}\tau_c\left(1 + \frac{1}{4\beta\lambda_c}\right)\delta_A \tag{39}$$

(IV) Approximate Values for δ_A and δ_I

The usual airfoil sections have limitations which prevent large variations in the terms δ_A and δ_I. Therefore, the airfoil section is approximated by an ellipse for the nose section and parabolic arcs for the rear portion as shown in Fig. B.

$$\delta_A = \frac{\int_{-1}^{+1} 2y_0 dx}{d \cdot c} = 0.7270 \tag{40}$$

$$\delta_I = \frac{\int_{-1}^{+1} 2y_0 x^2 dx}{dc^3/12} = 0.4945 \tag{41}$$

(V) Correction for Change of Dynamic Pressure

In the formulation of this theory, it was assumed that if the proper correction could be applied to the free-stream velocity approaching the finite wing, the force on the finite wing could be compared to the force on the infinite wing. Since the dynamic pressure shall not be the same for the two wings, the force coefficients shall also be different.

It is more convenient to express the result as a function of the Mach Number. The correction to the free-stream velocity and the correction to the drag coefficient become

$$\Delta M/M_\infty = (\Delta u/U_\infty)\left\{1 + [(k-1)/2]M_\infty^2\right\} \tag{42}$$

$$\frac{\Delta c_D}{c_D} = -\left(\frac{2 - M_\infty^2}{1 + [(k-1)/2]M_\infty^2}\right)\frac{\Delta M}{M_\infty} \tag{43}$$

Using the approximate values of δ_A and δ_I, as found in Section (IV) above, $(\Delta M/M_\infty)(1/\tau)$ vs. M_∞ is plotted in Fig. 3 for various values of the aspect ratio. $\Delta c_D/c_D$ vs. M for various $\Delta M/M_\infty$ is plotted in Fig. 4.

(VI) Comparison of Theory with Experimental Results

Experimental data presented in reference 2 were compared with the theory presented in this paper. The data for aspect ratio 6.25, 5.25, and 3.28 were corrected to infinite aspect ratio. Ideally, the data should then coincide. The results of this comparison are shown in Fig. 5.

Recently, additional experimental data on wings of different aspect ratio have been obtained in the Brown University transonic wind tunnel. The friction drag was subtracted and the data were compared at aspect ratio equal to infinity. The results are given in Fig. 6.

It can be seen that the theory agrees favorably with experimental data. Therefore, if data for a wing of one aspect ratio are available, it is possible to predict, with reasonable accuracy, the performance of a wing of the same profile at any other aspect ratio. Reasonable accuracy is expected only for wings of aspect ratio greater than unity and Mach Numbers for which the Prandtl-Glauert corrections are valid reasonably far from the wing.

References

[1] Lindsey, W. F., and Humphreys, M. D., *Effects of Aspect Ratio at High Subsonic Mach Numbers*, NACA TN 2720, July, 1952.

[2] Feldman, Fritz K., *Untersuchung von symmetrischen Tragflügelprofilen bei hohen Unterschallgeschwindigkeiten in einem geschlossenen Windkanal*, Mitteilungen aus dem Institut für Aerodynamik an der ETH, No. 14, 1948.

[3] Goethert, B., *Plane and Three-Dimensional Flow at High Subsonic Speeds*, NACA TM 1105, October, 1946.

[4] Goethert, B., *Windkanal Korrecturen bei hohen Luftgeschwindigkeiten*, Lilienthal Gesellschaft für Luftfahrtforschung, Report No. 127, p. 114, 1940.

A Creep Buckling Hypothesis

GEORGE GERARD*
New York University

SUMMARY

Published work on creep buckling has implied that failure of columns after a critical time is caused by initial imperfections. Such analyses are relatively complex and ultimately leave the choice of selecting the proper value of the initial imperfection to the designer. Furthermore, recent test results on creep buckling of columns have indicated that there is a random and relatively unimportant effect of small initial imperfections on the critical time.

To avoid the difficulties associated with initial imperfections, a formulation of the creep buckling phenomenon in terms of classical stability theory is presented. The theory permits the extension of known solutions for plastic buckling of certain thin plates and shells to creep buckling problems.

SYMBOLS

b = width
C_i = plasticity coefficients
D = bending rigidity
e_i = strain intensity
E_s = secant modulus
E_t = tangent modulus
G_s = shear secant modulus
h = thickness
K = buckling coefficient
L = length
R = radius
t = time
w = lateral deflection
x, y = coordinates
β = plasticity factor
ϵ = strain
σ = stress
σ_i = stress intensity
τ = shear stress
ν = Poisson's ratio

Subscript

cr = critical

INTRODUCTION

THE PROBLEM OF creep buckling of columns, plates, and shells has become of increasing importance in the design of aircraft for thermal flight. Thus far, theories and experimental data have appeared in the literature only for creep buckling of columns.

In spite of the fact that research has progressed on creep buckling of columns since approximately 1949, a survey of the literature indicates that there are almost more theories than reliable test points which can be used to check the theories. Furthermore, much of the available test data cannot be used to check theory because of the simple fact that the compressive creep properties of the materials used were not obtained.

In this paper, a unified theory is presented for estimating creep buckling of plates, cylinders, and columns, based on available theories for plastic buckling of such elements. Available test data on creep buckling of columns, for which the compressive creep properties are known, are used to check the theory.

THEORY

Assumptions

In the following development, it is assumed that a perfect plate element is subjected to a load less than that which would produce short-time buckling at elevated temperature. Under the applied load, the element deforms time dependently without any deflection out of its plane. As a result of the time-dependent deformation under the constant applied stress, the axial stiffness of the element decreases so that, at the critical time, lateral deflections out of the plane of the element develop suddenly.

The loading and assumed deformation sequence is illustrated in Fig. 1. Aside from the fact that each value of strain is associated with a prescribed time value, the stress-strain relations of Fig. 1 corresponding to creep buckling are formally equivalent to those encountered in plastic buckling problems.

Equilibrium Equation

It is pertinent to consider the following equilibrium differential equation obtained by Stowell[1] for time-independent plastic buckling of flat plates.

$$D\,[C_1(\partial^4 w/\partial x^4) - C_2(\partial^4 w/\partial x^3 \partial y) + 2C_3(\partial^4 w/\partial x^2 \partial y^2) - C_4(\partial^4 w/\partial x \partial y^3) + C_5(\partial^4 w/\partial y^4)] = -h[\sigma_x(\partial^2 w/\partial x^2) + \sigma_y(\partial^2 w/\partial y^2) + 2\tau(\partial^2 w/\partial x \partial y)] \quad (1)$$

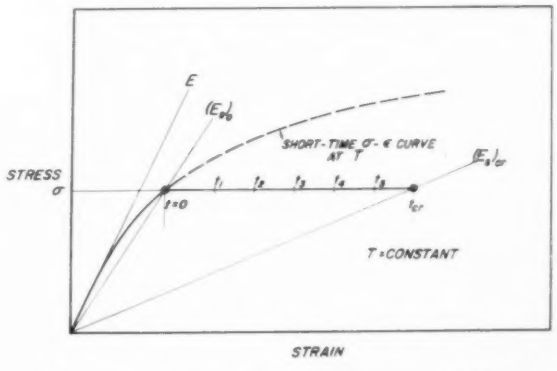

FIG. 1. Stress-strain relations leading to creep buckling.

Received July 18, 1955.

* Assistant Director, Research Division, College of Engineering.

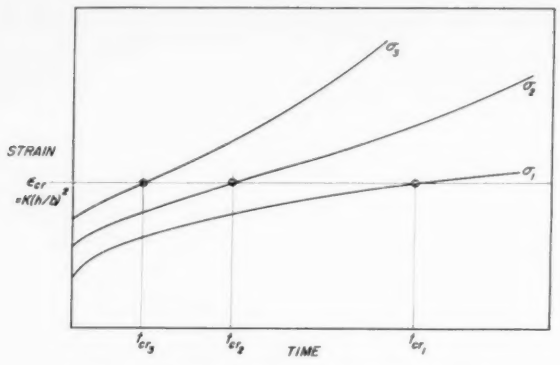

FIG. 2. Critical time solution for hinged flanges.

where

$$
\begin{aligned}
D &= E_s h^3/9 \\
C_1 &= 1 - (\alpha/4)\,\sigma_x^2 \\
C_2 &= \alpha\,\sigma_x\tau \\
C_3 &= 1 - (\alpha/4)\,(\sigma_x\sigma_y + 2\tau^2) \\
C_4 &= \alpha\,\sigma_y\tau \\
C_5 &= 1 - (\alpha/4)\,\sigma_y^2
\end{aligned}
$$

$$
\alpha = \frac{3[1 - (E_t/E_s)]}{\sigma_x^2 + \sigma_y^2 - \sigma_x\sigma_y + 3\tau^2}
$$

Eq. (1) is based on the assumptions that $\nu = 1/2$ in the elastic and plastic regions, that deformation-type stress-strain relations apply, and that the plate remains plastic during the buckling process. The derivation of Eq. (1) depends only upon the assumption that

$$E_s = \sigma_i/e_i \tag{2}$$

where σ_i and e_i are stress and strain intensities, respectively. They are rotationally invariant functions and are defined according to the octahedral shear law.

To permit use of Eq. (1) for creep buckling problems, the following assumption is used to replace the assumption of Eq. (2):

$$E_s[t] = \sigma_i/e_i[t] \tag{3}$$

where $e_i[t]$ is now a time-dependent strain intensity.

Thus, the constant stress state existing prior to creep buckling produces time-dependent deformations which are analogous to the plastic deformations produced by the increasing stress state existing prior to short-time buckling. At buckling, the superimposed incremental stress state associated with Eq. (1) is time independent since buckling is assumed to occur suddenly for creep buckling as well as for short-time buckling.

Consequently, the equilibrium condition represented by Eq. (1) can be satisfied by a suitable reduction in E_s to permit creep buckling as well as an increase in stress for short-time buckling. To be strictly correct, since the applied stress is constant for creep buckling, lateral bending must proceed according to the reduced modulus model rather than the tangent modulus model. This is a point which may have relatively little effect on the results. Moreover, for a unified treatment of creep and short-time buckling, it is convenient to adopt also the tangent modulus for creep buckling.

To summarize then, in Eq. (1), the stresses σ_x, σ_y, and τ are prescribed and therefore are time independent. The deflection w is time independent since buckling is assumed to occur suddenly. The bending rigidity D is time dependent since it contains E_s, and the coefficients C_1 to C_5 may also be time dependent if the quantity E_t/E_s varies with time.

APPLICATIONS

Hinged Flange

The short-time plastic buckling of a long hinged flange has been determined by Stowell.[1] The short-time buckling stress solution satisfying Eq. (1) is

$$\sigma_{cr} = KE_s(h/b)^2 \tag{4}$$

Eq. (1) can also be satisfied by a value of $(E_s)_{cr}$ given by

$$(E_s)_{cr} = (\sigma/K)\,(h/b)^2 \tag{5}$$

Thus, for creep buckling under a value of compressive stress σ less than σ_{cr} of Eq. (4), Eq. (3) reduces to

$$E_s[t] = \sigma/\epsilon[t] \tag{6}$$

and, therefore, Eq. (5) can be written as

$$\epsilon_{cr}[t] = K(h/b)^2 \tag{7}$$

Eq. (7) implies that, after a sufficient period of time at elevated temperature, the axial stiffness of the hinged flange has decreased sufficiently because of creep to permit buckling. Critical times can be found directly from compression creep curves by determining the critical strain according to Eq. (7). The method of determining t_{cr} is illustrated in Fig. 2. These data can be cross-plotted with σ as a function of t_{cr} for various constant values of ϵ_{cr} or with σ as a function of ϵ_{cr} for various constant values of t_{cr}.

Plates

The short-time plastic buckling of long flat plates with various boundary conditions has been considered by Stowell.[1] The buckling stress can be found from the following equation and the values of β listed in Table 1.

$$\sigma_{cr} = \beta KE_s(h/b)^2 \tag{8}$$

TABLE 1
Values of β for Long Flat Plates

Boundary Conditions	β	β_0 for $E_t/E_s = 0$
Compression—clamped flange[1]	$0.330 + \dfrac{0.335}{(1 + 3E_t/E_s)^{1/2}}$	0.665
Compression—simply supported plate[1]	$0.500 + \dfrac{0.250}{(1 + 3E_t/E_s)^{1/2}}$	0.750
Compression—clamped plate[1]	$0.352 + \dfrac{0.324}{(1 + E_t/E_s)^{1/2}}$	0.676
Shear-elastically restrained plate[2]	$3G_s/E_s$	

By following the analysis used for the hinged flange, the critical strain for plates can be written as

$$\epsilon_{cr}[t] = \beta K(h/b)^2 \tag{9}$$

It can be observed that the limiting values of β vary between unity and those listed in the last column of Table 1 for $E_t/E_s = 0$.

To evaluate E_t/E_s and therefore β for a creep buckling problem, it is necessary to know the stress-strain relations for the material at the critical time. Since the incremental stress state associated with buckling has assumed to be a time-independent process, the pertinent stress-strain relations at the critical time could be evaluated presumably from the following test procedure. Subject a specimen to compressive creep at elevated temperature. After a prescribed time, unload the specimen and then determine the stress-strain characteristics at the test temperature by loading beyond the stress level used for the creep test.

From another viewpoint, buckling has been assumed to occur suddenly, and, therefore, it may be argued that the superimposed incremental stress state should follow an elastic loading path. However, in short-time buckling tests at elevated temperatures as well as at room temperature, the incremental stress state follows the tangent modulus and not the elastic modulus. Therefore, the argument that creep buckling should follow an elastic path does not appear to be valid.

From a conservative standpoint, one could assume that $E_t/E_s = 0$ and use the β_0 values given in Table 1 in conjunction with Eq. (9). A conservative value of a critical time could then be found by utilizing the critical strain determined from Eq. (9) in conjunction with creep data as illustrated in Fig. 2 for the hinged flange.

Short-time tests on extruded H-sections have indicated that plate assemblies generally possess some reserve strength beyond buckling. For sections which buckle plastically, the failing strength is adequately predicted by taking $\beta = 1$ in Eq. (8). As a possible upper limit for the critical time, Eq. (9) may be used with $\beta = 1$.

Cylinders

The short-time plastic buckling of long cylinders under compressive or torsional loads has been considered in reference 3. The plastic buckling stress of a compressed cylinder is given by

$$\sigma_{cr} = \beta K E_s(h/R) \tag{10}$$

where $$\beta = (E_t/E_s)^{1/2}$$

For a long cylinder subjected to torsion

$$\tau_{cr} = \beta K E_s(h/R)^{3/2} \tag{11}$$

where $$\beta = 1$$

The critical strain can be expressed in the form

$$\epsilon_{cr}[t] = \beta K(h/R)^n \tag{12}$$

where $n = 1$ for compression and $n = 3/2$ for torsion. Since $\beta = 1$ for torsional buckling of a cylinder, the critical time can be found directly as shown in Fig. 2 if the compressive stresses are converted into shear stresses by use of the pertinent affinity relation.

Compressive buckling of a cylinder is strongly dependent upon the value of E_t/E_s. Therefore, the suggested approach for plates cannot be used in this case. Since columns also depend primarily upon E_t/E_s, further discussion of compressed cylinders is reserved for the next section.

Columns

The short-time plastic buckling of columns depends upon the tangent modulus. In terms of β,

$$\sigma_{cr} = \beta K E_s(b/L)^2 \tag{13}$$

where $$\beta = E_t/E_s$$

Thus, for columns as well as compressed cylinders, the values of β must be known in order to determine the critical stress for short-time buckling or the critical time for creep buckling. For the latter, it is necessary to know the stress-strain relations after a given amount of creep has occurred as discussed in the section on plates. This can be found from tests or from a mathematical formulation of the creep law. It may be possible to obtain an estimate of the critical time for columns and compressed cylinders by assuming that $\beta = 1$ and then determining the critical strain from Eq. (12) for cylinders and the following for columns.

$$\epsilon_{cr}[t] = K(b/L)^2 \tag{14}$$

Early estimates of the importance of initial imperfections indicated that theoretically perfect columns would not creep buckle.[4] This result is probably due to neglect of the decrease in axial stiffness as the element creeps. Consequently, theoretical work on creep buckling of columns has implied that initial imperfections provide the mechanism by which failure occurs at the critical time. Libove[5, 6] has found that, theoretically, initial imperfections seriously influence the column life. Kempner found that a linear viscoelastic column has an infinite life regardless of the initial imperfections. A finite life was obtained by Kempner[8] when nonlinear viscoelastic behavior was assumed.

Recent tests on creep buckling of columns[9] have indicated, however, that there is a random and relatively unimportant influence of small initial imperfections upon the critical time. Furthermore, failure occurs suddenly and after relatively small lateral deflections. These test results suggest that the approach used herein in which perfect elements are considered may yield a satisfactory approximation to the critical time.

Experimental Data

In the preceding sections, it was indicated that compressed flat plates with various boundary conditions and flat plates and cylinders under shear loadings are

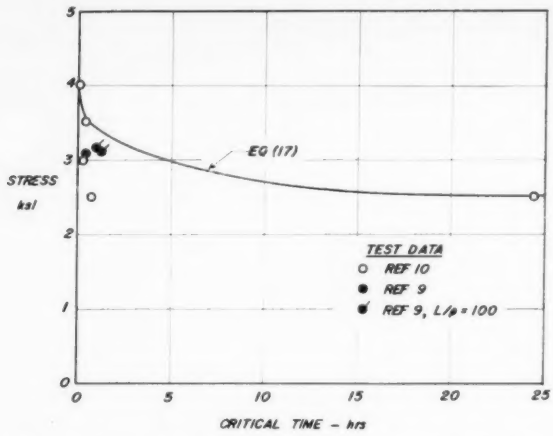

FIG. 3. Critical time comparisons of critical elastic strain approach and test data on 75S-T6 columns of $L/\rho = 110$ at 600°F.

not particularly sensitive to the values of E_t which appear in the β term. Columns and circular cylinders under compression, on the other hand, depend directly upon E_t. In the absence of test data on creep buckling of plates, use of test data on columns to check the predictions of the approach suggested herein provides a particularly severe test of the method. Because of the sensitivity to E_t, it would be anticipated that, if the method failed for columns, it may still be of value for those plates and cylinders which depend upon E_t in a minor way.

In reference 10, test data are presented on creep buckling of columns of 75S-T6 aluminum alloy at 600°F. In addition, compressive creep data under constant load conditions were obtained in the stress range of 4.5 to 5.5 ksi. The data for this stress range and a temperature of 600°F. were quite accurately represented by the following empirical equation:

$$\epsilon = (\sigma/E) + Ae^{B\sigma}t^{K} \tag{15}$$

where

$$A = 2.64 \times 10^{-7}\ \text{hr.}^{-1}$$
$$B = 1.92 \times 10^{-3}\ \text{psi}^{-1}$$
$$E = 5.2 \times 10^{6}\ \text{psi}$$
$$K = 0.66$$

By employing the assumption of Eq. (14),

$$\epsilon_{cr} = (\pi\rho/L)^2 \tag{16}$$

Together with Eq. (16), the critical time for creep buckling under a prescribed compressive stress can be determined by rearranging Eq. (15)

$$t_{cr} = \left[\frac{\epsilon_{cr} - (\sigma/E)}{Ae^{B\sigma}}\right]^{1/K} \tag{17}$$

In Fig. 3, computed data involving Eqs. (16) and (17) for columns of $L/\rho = 110$ are shown together with test data of references 9 and 10. The agreement between Eq. (17) and the upper test points is good. For the other test points in the region of 1 hour, the agreement is not so satisfactory. However, it should be noted that both the basic creep data and column test points are of sufficient variability to require statistical analysis to establish correlation between theory and experiment. In this respect, creep problems are very similar to fatigue problems.

In Fig. 4, additional test data on columns of several slenderness ratios[9] are compared with the predictions of Eqs. (16) and (17). It can be observed that fair agreement is obtained between the heavy line and the test data. The light lines in Fig. 4 were obtained by using σ/E_t in Eq. (17) in place of σ/E in order to obtain agreement with the time-independent behavior of columns. It can be seen that little change occurs.

In closing, it must be emphasized that before the various theories which have been proposed for creep buckling can be evaluated it is necessary that satisfactory tests be conducted. Such tests would require that several creep curves be obtained for a given stress level and temperature in order that the variability of the basic creep data be established. Then, a sufficient number of creep buckling tests should be run under presumably identical conditions to establish the varia-

(Continued on page 887)

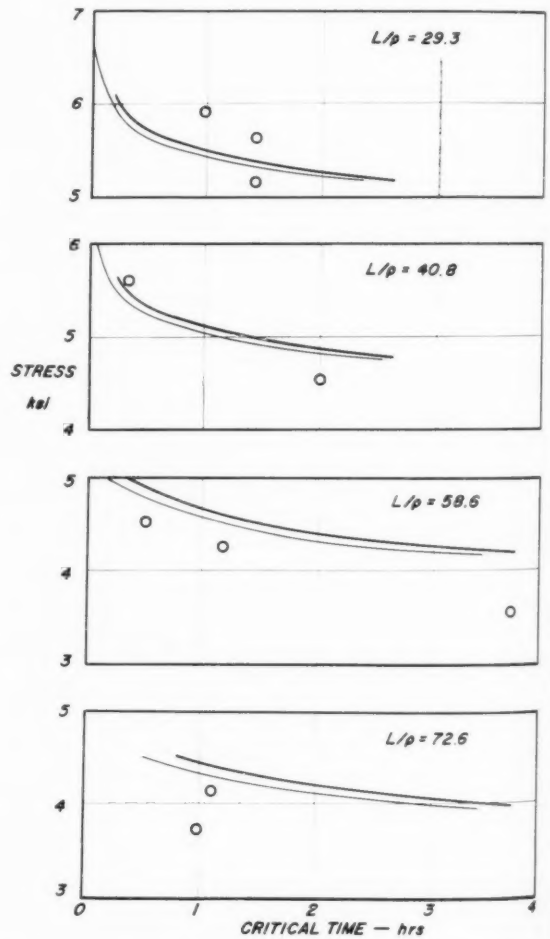

FIG. 4. Critical time comparisons of critical strain approach and test data on 75S-T6 columns at 600°F.

Creep Deflection of Viscoelastic Plate Under Uniform Edge Compression

T. H. LIN*

University of Detroit

SUMMARY

The stress-strain-time relationship of a viscoelastic body under plane stress system is given. This relationship is expressed in its Laplace transform form. Equilibrium condition for the viscoelastic plate with simply supported edges under edge thrust in terms of lateral deflections is shown. The initial deflection of the plate is expressed in double sine series. The method of calculating the magnification of each term of the series at different instants is derived. The sum of these terms gives the deflection-time curve of a viscoelastic plate under edge thrust. The shape of the deformed surface generally changes with time. An illustrative example is shown in the Appendix.

SYMBOLS

a	= length of plate
b	= width of plate
a_k, b_m	= constants
A_{mn}, B_{mn}	= constants
c	= damping constant
ϵ	= volumetric strain or hydrostatic strain component
ϵ_{ij}	= components of strain tensor
ϵ'_{ij}	= components of deviated strain tensor
E	= Young's modulus of elasticity
f, F	= functions
G	= elastic modulus of rigidity
h	= thickness of plate
I	= moment of inertia of unit width of the plate
K	= curvature, constant
k	= spring constant, constant
M	= moment
N_x	= direct stress on the edge of plate per unit length
m, n	= integral numbers
P, Q	= linear operators $a_k\ (\partial^k/\partial t^k)$ and $b_m\ (\partial^m/\partial t^m)$ respectively
S	= Laplace transform variable
t	= time
x	= axis parallel to the length of plate
y	= axis parallel to the width of plate
z	= axis perpendicular to the plane of plate
u, v	= displacements along the x-, and y-axis, respectively
w_0	= initial deflection of plate
w	= additional deflection of plate
$w + w_0$	= total deflection of plate
μ	= Poisson's ratio in elastic range
σ	= the hydrostatic component of stress
σ_{ij}	= components of stress tensor
σ'_{ij}	= components of deviated stress tensor
φ	= a function
τ	= a variable, shear stress
γ	= shear strain

Bar on top of the symbol denotes Laplace transform of the expression

Dot denotes differentiation with respect to time

δ_{ij} = Kronecker delta $= \begin{cases} 1 & = ij \\ 0 & \neq ij \end{cases}$

Received April 5, 1955. Revised and received May 14, 1956.

* Professor of Aeronautical Engineering, University of Detroit. Now, Professor of Engineering, University of California, Los Angeles.

INTRODUCTION

THE RECENT INCREASE in the use of structures under elevated temperatures has made the creep problem increasingly important. Progress has been made in the determination of the behavior of beams and columns under conditions subject to creep in the past few years,[1–8] but there is apparently very little published literature on the creep deflection of plate under compressive loadings.[9] It is the purpose of this paper to extend the analytical method of calculating creep deflection of viscoelastic columns[7] to calculate the creep deflection of plates which can be assumed to have linearly viscoelastic properties either at room or elevated temperatures.

Viscoelastic material[10] has the general linear inelastic behavior of a combination of the behavior of solid and liquid phases, with the limiting cases being that of the elastic solid and of ideal viscous liquid. This viscoelastic behavior can be represented by a number of mechanical springs and dampers to form mechanical models.[7, 10] The general stress-strain relations of volume-constant linear viscoelastic materials may be written in the general form[10]

$$P\sigma'_{ij} = Qe'_{ij}$$

where σ'_{ij} and e'_{ij} are the components of the deviated stress and strain tensors, respectively; P and Q are, respectively, the linear operators, $a_k(\partial^k/\partial t^k)$ and $b_m(\partial^m/\partial t^m)$; and a_k and b_m are constants.

Alfrey[11] has shown that the distribution of deviatoric stress within any volume-constant linear viscoelastic body is identical with that of a volume-constant elastic material subject to the same surface forces. The deviatoric strain at any point in the linear viscoelastic body is proportional to the deviatoric strain at the corresponding point in the elastic body. The deformed shapes of the two bodies will be the same although the magnitude may be different. However, this analogy between the elastic and the linear viscoelastic bodies does not hold when the structure is subject to buckling—as in the case of columns, or plates under compression. In the following, a viscoelastic plate with simply supported edges under uniform edge compression is analyzed. This analysis is based on small deflection theory and gives results without substantial error with the deflections not exceeding 0.4 times the thickness of the

plate.[12] Plates with large deflections are not considered in the present paper.

Mathematical Analysis

Stress-Strain-Time Relationship

Creep deformation is independent of hydrostatic stress.[13] Therefore, the creep stress-strain relationship is expressed only in terms of deviated stress and deviated strain:[14]

$$_1\sigma = (1/3)\,\sigma_{ii} \tag{1}$$

$$_1e = (1/3)e_{ii} \tag{2}$$

$$\sigma'_{ij} = \sigma_{ij} - \delta_{ij}\,{}_1\sigma \tag{3}$$

$$e'_{ij} = e_{ij} - \delta_{ij}\,{}_1e \tag{4}$$

Brull[14] has shown that the deviator's stress-strain-time relationship of linear viscoelastic material can be represented by

$$\bar{\sigma}'_{ij} = 2G\,\bar{\epsilon}'_{ij}\,(1 - \bar{\varphi}) \tag{5}$$

With $\sigma_{z=0}$, Eq. (5) is written in the following form:

$$(2/3)\bar{\sigma}_x - (\bar{\sigma}_y/3) = 2G\{(2\bar{\epsilon}_x/3) - [(\bar{\epsilon}_y + \bar{\epsilon}_z)/3]\}\,(1 - \bar{\varphi}) \tag{6}$$

$$(2/3)\bar{\sigma}_y - (\bar{\sigma}_x/3) = 2G\{(2\bar{\epsilon}_y/3) - [(\bar{\epsilon}_x + \bar{\epsilon}_z)/3]\}\,(1 - \bar{\varphi}) \tag{7}$$

$$(\bar{\sigma}_x + \bar{\sigma}_y)/3 = -2G\{(2\bar{\epsilon}_z/3) - [(\bar{\epsilon}_x + \bar{\epsilon}_y)/3]\}\,(1 - \bar{\varphi}) \tag{8}$$

From Eqs. (6) to (8),

$$\bar{\sigma}_x - \bar{\sigma}_y = 2G(1 - \bar{\varphi})\,(\bar{\epsilon}_x - \bar{\epsilon}_y) \tag{9}$$

$$\bar{\sigma}_x + \bar{\sigma}_y = -2G(1 - \bar{\varphi})\,(2\bar{\epsilon}_z - \bar{\epsilon}_x - \bar{\epsilon}_y) \tag{10}$$

The bulk modulus does not change due to creep

$$(\bar{\sigma}_x + \bar{\sigma}_y)/3 = K(\bar{\epsilon}_x + \bar{\epsilon}_y + \bar{\epsilon}_z) \tag{11}$$

where

$$K = E/[3(1 - 2\mu)] = [2G(1 + \mu)]/[3(1 - 2\mu)]$$

and μ is the same as that for the elastic case.[14]
From Eqs. (10) and (11),

$$\bar{\epsilon}_z = \{[-f(\mu) + (1 - \bar{\varphi})]/[f(\mu) + 2(1 - \bar{\varphi})]\} \times (\bar{\epsilon}_x + \bar{\epsilon}_y), \quad \text{where} \quad f(\mu) = (1 + \mu)/(1 - 2\mu) \tag{12}$$

From Eqs. (9), (10), and (12),

$$\begin{aligned} \bar{\sigma}_x &= F_1\,\bar{\epsilon}_x + F_2\,\bar{\epsilon}_y \\ \bar{\sigma}_y &= F_1\,\bar{\epsilon}_y + F_2\,\bar{\epsilon}_x \\ \bar{\tau}_{xy} &= F_3\,\bar{\gamma}_{xy} \end{aligned} \tag{13}$$

where

$$F_1 = G\,(1 - \bar{\varphi})\,(\{[3f(\mu)]/[f(\mu) + 2(1 - \bar{\varphi})]\} + 1)$$

$$F_2 = G\,(1 - \bar{\varphi})\,(\{[3f(\mu)]/[f(\mu) + 2(1 - \bar{\varphi})]\} - 1)$$

and

$$F_3 = G(1 - \bar{\varphi})$$

$$F_2 + 2F_3 = F_1 \tag{14}$$

Resisting Moment and Lateral Deflection

Assuming that the normals to the neutral surface of the plate before bending remain straight during bending,

$$\bar{\epsilon}_x = \bar{K}_x z + \bar{\epsilon}_{x_0}; \qquad \bar{\epsilon}_y = \bar{K}_y z + \bar{\epsilon}_{y_0} \tag{15}$$

where e_{x_0} and e_{y_0} are strains at median surface.

$$\bar{M}_x = \int \bar{\sigma}_x z\,dz = \int (F_1\bar{K}_x z^2 + F_2 K_y z^2)\,dz = (F_1\bar{K}_x + F_2\bar{K}_y)I \tag{16}$$

where $I = \int z^2 dz$.

$$\bar{M}_y = (F_1\bar{K}_y + F_2\bar{K}_x)I \tag{17}$$

$$\gamma_{xy} = (\partial u/\partial y) + (\partial v/\partial x)$$

$$\bar{\tau}_{xy} = F_3\bar{\gamma}_{xy} = F_3[(\partial\bar{u}/\partial y) + (\partial\bar{v}/\partial x)]$$

$$u = u_0 - z(\partial w/\partial x) \qquad v = v_0 - z(\partial w/\partial y)$$

Where u_0 and v_0 are the displacements along the x- and y-axes of the points on the median surface.

$$\bar{M}_{xy} = \int \bar{\tau}_{xy} z\,dz = \int -2F_3 z^2 \bar{w}_{xy}\,dz = -2F_3 I\bar{w}_{xy} \tag{18}$$

Creep Deflection of the Plate

Since no plate is absolutely flat and homogeneous, the initial curvature and the nonhomogeneity of the material are here represented by an initial deflection w_0, and $w + w_0$ is the total deflection of the plate at any instant. For a plate under uniform thrust N_x per unit length on two opposite edges, the differential equation for equilibrium may be written as follows:[12]

$$\partial^2 M_x/\partial x^2 - 2(\partial^2 M_{xy}/\partial x\partial y) + (\partial^2 M_y/\partial y^2) = -N_x[\partial^2(w + w_0)/\partial x^2] \tag{19}$$

From Eqs. (15) to (19),

$$I[F_1\bar{w}_{xxxx} + 2F_2\bar{w}_{xxyy} + F_1\bar{w}_{yyyy} + 4F_3\bar{w}_{xxyy}] = -N_x[\bar{w}_{xx} + (1/S)w_{0xx}] \tag{20}$$

From Eqs. (14) and (20),

$$IF_1[\bar{w}_{xxxx} + 2\bar{w}_{xxyy} + \bar{w}_{yyyy}] = -N_x[\bar{w}_{xx} + (1/S)w_{0xx}] \tag{21}$$

Let the plate of length a and width b be simply sup-

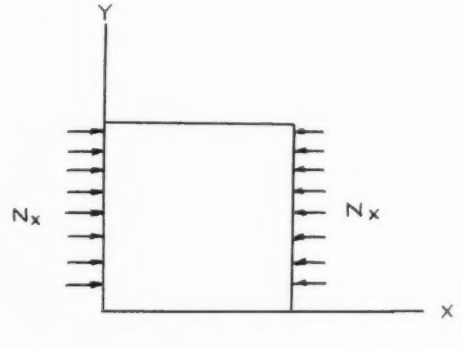

Fig. 1

Square Plate under Edge Thrust

ported on four edges, and let w_0 be expressed in double sine series.

$$w_0 = \Sigma\Sigma A_{mn} \sin (m\pi x/a) \sin (n\pi y/b)$$

$$w_{0xx} = -\Sigma\Sigma A_{mn} (m^2\pi^2/a^2) \sin (m\pi x/a) \sin (n\pi y/b)$$

$$\{F_1\Sigma\Sigma\}[(m\pi/a)^4 + 2(m\pi/a)^2 (n\pi/b^2) + (n\pi/b)^4] - (N_x/F_1)(m\pi/a)^2\}B_{mn} \sin (m\pi x/a) \sin (n\pi y/b) = +(N_x/F_1)\Sigma\Sigma(A_{mn}/S)(m^2\pi^2/a^2)[\sin (m\pi x/a) \times \sin (n\pi y/b)] \quad (22)$$

Multiplying the above equation by $\sin (m\pi x/a) \sin (n\pi y/b)\, dxdy$ and integrating from $x = 0$ to a and $y = 0$ to b,

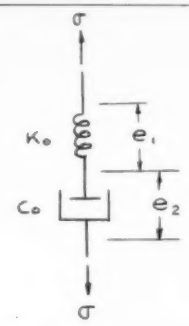

Fig. 2 Maxwell Model

$$\bar{B}_{mn} = \frac{+A_{mn}(m\pi/a)^2 (1/S)}{[(m\pi/a)^4 + 2(m\pi/a)^2 (n\pi/b)^2 + (n\pi/b)^4](F_1/N_x) - (m\pi/a)^2}$$

$$\bar{B}_{mn} = \frac{(A_{mn}/S)(m\pi/a)^2 N_x [f(\mu) + 2(1 - \bar{\varphi})]}{C_{mn} IG(1 - \bar{\varphi})[4f(\mu) + 2(1 - \bar{\varphi})] - (m\pi/a)^2 N_x[f(\mu) + 2(1 - \bar{\varphi})]} \quad (23)$$

Where

$$C_{mn} = [(m\pi/a)^4 + 2(m\pi/a)^2 (n\pi/b)^2 + (n\pi/b)^4]$$

For the Maxwell model (see Appendix),

$$1 - \bar{\varphi} = S/(S + \alpha) \quad (24)$$

The constant α for the Maxwell model or the constants for more complex models can be determined from the properties of the material.

By Heaviside's expansion,[15] B_{mn} is obtained from the inverse transform of $\bar{B}_{mn}$. Substituting B_{mn} into Eq. 22, the deflection w of the plate is obtained.

An illustrative example is given in the Appendix. Deflection-time curves were calculated for initial deflections of two different harmonics; one with $m = 1$, $n = 1$ and the other with $m = 3$ and $n = 1$. The former initial deflection grows much faster than the latter. Hence a plate with initial deflection composed of different harmonics will have different stress distributions at different instants.

This analysis also shows that infinite rate of deflections is produced only at infinite time, so long as the stress in the plate is within the elastic limit of the instantaneous stress-strain curve of the material. The creep strain in the plate or column is similar to additional initial curvature and does not change the critical compressive strength of the member. That is why viscoelastic plates or columns, with the slope of the instantaneous stress-strain curve taken as constant, has no critical time of collapse.

Appendix

A viscoelastic plate 8 in. square, and $\frac{3}{16}$ in. thick is subject to a compressive load of 4,500 psi on two opposite edges (see Fig. 1). All the four edges are simply supported. The viscoelastic properties of the plate are represented by a Maxwell's model as shown in Fig. 2.

$$e_1 = \sigma/k_0 \qquad \dot{e}_2 = \sigma/c_0$$

$$e = e_1 + e_2$$

$$\dot{e} = \dot{e}_1 + \dot{e}_2 = (\dot{\sigma}/k_0) + (\sigma/c_0) = (1/k_0)[\dot{\sigma} + (k_0/c_0)\sigma]$$

With $k_0 = E$ and $k_0/c_0 = \alpha$

$$\dot{e} = (1/E)(\dot{\sigma} + \alpha\sigma) \quad (A\text{-}1)$$

$$S\bar{e} = (1/E)(S\bar{\sigma} + \bar{\sigma})$$

$$\bar{\sigma} = E[S/(S + \alpha)]\bar{e}$$

$$1 - \bar{\varphi} = S/(S + \alpha)$$

E for 75ST aluminum alloy at 600°F. is 5.2×10^6 psi and the average rate of creep for the first 10 hours under a constant stress of 4,500 psi is 0.00056 hour (see Fig. 17.3 of reference 5).

$$\dot{e} = \alpha\sigma/E$$

$$\alpha = E\dot{e}/\sigma = \frac{0.00056 \times 5.2 \times 10^6}{4{,}500} = 0.647 \text{ hour}$$

This viscoelastic plate is assumed to have the same values of E and α.

From Eq. (23),

$$B_{mn} = \frac{A_{mn}/S}{C_{mn} IG \dfrac{S}{S + \alpha}\left[4f(\mu) + \dfrac{2S}{S + \alpha}\right]} - 1 \quad (A\text{-}2)$$
$$\left(\frac{m\pi}{a}\right)^2 N_x\left[f(\mu) + \frac{2S}{S + \alpha}\right]$$

μ is taken to be 0.3

$$G = E/[2(1 + \mu)] = (5.2 \times 10^6)/(2 \times 1.3) = 2 \times 10^6 \text{ psi}$$

plate.[12] Plates with large deflections are not considered in the present paper.

Mathematical Analysis

Stress-Strain-Time Relationship

Creep deformation is independent of hydrostatic stress.[13] Therefore, the creep stress-strain relationship is expressed only in terms of deviated stress and deviated strain:[14]

$$_1\sigma = (1/3)\,\sigma_{ii} \tag{1}$$

$$_1e = (1/3)e_{ii} \tag{2}$$

$$\sigma'_{ij} = \sigma_{ij} - \delta_{ij}\,{}_1\sigma \tag{3}$$

$$e'_{ij} = e_{ij} - \delta_{ij}\,{}_1e \tag{4}$$

Brull[14] has shown that the deviator's stress-strain-time relationship of linear viscoelastic material can be represented by

$$\bar{\sigma}'_{ij} = 2G\,\bar{e}'_{ij}\,(1 - \bar{\varphi}) \tag{5}$$

With $\sigma_{z=0}$, Eq. (5) is written in the following form:

$$(2/3)\bar{\sigma}_x - (\bar{\sigma}_y/3) = 2G\{(2\bar{e}_x/3) - [(\bar{e}_y + \bar{e}_z)/3]\}\,(1 - \bar{\varphi}) \tag{6}$$

$$(2/3)\bar{\sigma}_y - (\bar{\sigma}_x/3) = 2G\{(2\bar{e}_y/3) - [(\bar{e}_x + \bar{e}_z)/3]\}\,(1 - \bar{\varphi}) \tag{7}$$

$$(\bar{\sigma}_x + \bar{\sigma}_y)/3 = -2G\{(2\bar{e}_z/3) - [(\bar{e}_x + \bar{e}_y)/3]\}\,(1 - \bar{\varphi}) \tag{8}$$

From Eqs. (6) to (8),

$$\bar{\sigma}_x - \bar{\sigma}_y = 2G(1 - \bar{\varphi})\,(\bar{e}_x - \bar{e}_y) \tag{9}$$

$$\bar{\sigma}_x + \bar{\sigma}_y = -2G(1 - \bar{\varphi})\,(2\bar{e}_z - \bar{e}_x - \bar{e}_y) \tag{10}$$

The bulk modulus does not change due to creep

$$(\bar{\sigma}_x + \bar{\sigma}_y)/3 = K(\bar{e}_x + \bar{e}_y + \bar{e}_z) \tag{11}$$

where

$$K = E/[3(1 - 2\mu)] = [2G(1 + \mu)]/[3(1 - 2\mu)]$$

and μ is the same as that for the elastic case.[14]
From Eqs. (10) and (11),

$$\bar{e}_z = \{[-f(\mu) + (1 - \bar{\varphi})]/[f(\mu) + 2(1 - \bar{\varphi})]\} \times (\bar{e}_x + \bar{e}_y), \quad \text{where} \quad f(\mu) = (1 + \mu)/(1 - 2\mu) \tag{12}$$

From Eqs. (9), (10), and (12),

$$\begin{aligned} \bar{\sigma}_x &= F_1\,\bar{e}_x + F_2\,\bar{e}_y \\ \bar{\sigma}_y &= F_1\,\bar{e}_y + F_2\,\bar{e}_x \\ \bar{\tau}_{xy} &= F_3\,\bar{\gamma}_{xy} \end{aligned} \tag{13}$$

where

$$F_1 = G\,(1 - \bar{\varphi})\,(\{[3f(\mu)]/[f(\mu) + 2(1 - \bar{\varphi})]\} + 1)$$

$$F_2 = G\,(1 - \bar{\varphi})\,(\{[3f(\mu)]/[f(\mu) + 2(1 - \bar{\varphi})]\} - 1)$$

and

$$F_3 = G(1 - \bar{\varphi})$$

$$F_2 + 2F_3 = F_1 \tag{14}$$

Resisting Moment and Lateral Deflection

Assuming that the normals to the neutral surface of the plate before bending remain straight during bending,

$$\bar{e}_x = \bar{K}_x z + \bar{e}_{x_0}; \qquad \bar{e}_y = \bar{K}_y z + \bar{e}_{y_0} \tag{15}$$

where e_{x_0} and e_{y_0} are strains at median surface.

$$\bar{M}_x = \int \bar{\sigma}_x z\,dz = \int (F_1\bar{K}_x z^2 + F_2 K_y z^2)\,dz = (F_1\bar{K}_x + F_2\bar{K}_y)I \tag{16}$$

where $I = \int z^2 dz$.

$$\bar{M}_y = (F_1\bar{K}_y + F_2\bar{K}_x)I \tag{17}$$

$$\gamma_{xy} = (\partial u/\partial y) + (\partial v/\partial x)$$

$$\bar{\tau}_{xy} = F_3\bar{\gamma}_{xy} = F_3[(\partial\bar{u}/\partial y) + (\partial\bar{v}/\partial x)]$$

$$u = u_0 - z(\partial w/\partial x) \qquad v = v_0 - z(\partial w/\partial y)$$

Where u_0 and v_0 are the displacements along the x- and y-axes of the points on the median surface.

$$\bar{M}_{xy} = \int \bar{\tau}_{xy} z\,dz = \int -2F_3 z^2 \bar{w}_{xy}\,dz = -2F_3 I\bar{w}_{xy} \tag{18}$$

Creep Deflection of the Plate

Since no plate is absolutely flat and homogeneous, the initial curvature and the nonhomogeneity of the material are here represented by an initial deflection w_0, and $w + w_0$ is the total deflection of the plate at any instant. For a plate under uniform thrust N_x per unit length on two opposite edges, the differential equation for equilibrium may be written as follows:[12]

$$\partial^2 M_x/\partial x^2 - 2(\partial^2 M_{xy}/\partial x\partial y) + (\partial^2 M_y/\partial y^2) = -N_x[\partial^2(w + w_0)/\partial x^2] \tag{19}$$

From Eqs. (15) to (19),

$$I[F_1\bar{w}_{xxxx} + 2F_2\bar{w}_{xxyy} + F_1\bar{w}_{yyyy} + 4F_3\bar{w}_{xxyy}] = -N_x[\bar{w}_{xx} + (1/S)w_{0xx}] \tag{20}$$

From Eqs. (14) and (20),

$$IF_1[\bar{w}_{xxxx} + 2\bar{w}_{xxyy} + \bar{w}_{yyyy}] = -N_x[\bar{w}_{xx} + (1/S)w_{0xx}] \tag{21}$$

Let the plate of length a and width b be simply sup-

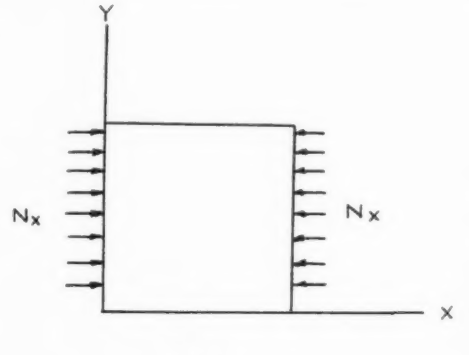

Fig. 1

Square Plate under Edge Thrust

ported on four edges, and let w_0 be expressed in double sine series.

$$w_0 = \Sigma\Sigma A_{mn} \sin (m\pi x/a) \sin (n\pi y/b)$$

$$w_{0,xx} = -\Sigma\Sigma A_{mn} (m^2\pi^2/a^2) \sin (m\pi x/a) \sin (n\pi y/b)$$

$$\{F_1\Sigma\Sigma[(m\pi/a)^4 + 2(m\pi/a)^2 (n\pi/b^2) + (n\pi/b)^4] - (N_x/F_1) (m\pi/a)^2\} B_{mn} \sin (m\pi x/a) \sin (n\pi y/b) = +(N_x/F_1)\Sigma\Sigma(A_{mn}/S) (m^2\pi^2/a^2) [\sin (m\pi x/a) \times \sin (n\pi y/b)] \quad (22)$$

Multiplying the above equation by $\sin (m\pi x/a) \sin (n\pi y/b)\, dxdy$ and integrating from $x = 0$ to a and $y = 0$ to b,

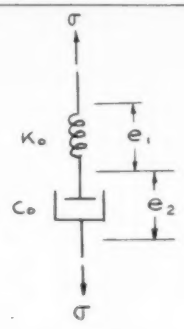

Fig. 2 Maxwell Model

$$\bar{B}_{mn} = \frac{+ A_{mn}(m\pi/a)^2 (1/S)}{[(m\pi/a)^4 + 2(m\pi/a)^2 (n\pi/b)^2 + (n\pi/b)^4] (F_1/N_x) - (m\pi/a)^2}$$

$$\bar{B}_{mn} = \frac{(A_{mn}/S) (m\pi/a)^2 N_x [f(\mu) + 2(1 - \bar{\varphi})]}{C_{mn} IG(1 - \bar{\varphi}) [4f(\mu) + 2(1 - \bar{\varphi})] - (m\pi/a)^2 N_x[f(\mu) + 2(1 - \bar{\varphi})]} \quad (23)$$

Where

$$C_{mn} = [(m\pi/a)^4 + 2(m\pi/a)^2 (n\pi/b)^2 + (n\pi/b)^4]$$

For the Maxwell model (see Appendix),

$$1 - \bar{\varphi} = S/(S + \alpha) \quad (24)$$

The constant α for the Maxwell model or the constants for more complex models can be determined from the properties of the material.

By Heaviside's expansion,[15] B_{mn} is obtained from the inverse transform of $\bar{B}_{mn}$. Substituting B_{mn} into Eq. 22, the deflection w of the plate is obtained.

An illustrative example is given in the Appendix. Deflection-time curves were calculated for initial deflections of two different harmonics; one with $m = 1$, $n = 1$ and the other with $m = 3$ and $n = 1$. The former initial deflection grows much faster than the latter. Hence a plate with initial deflection composed of different harmonics will have different stress distributions at different instants.

This analysis also shows that infinite rate of deflections is produced only at infinite time, so long as the stress in the plate is within the elastic limit of the instantaneous stress-strain curve of the material. The creep strain in the plate or column is similar to additional initial curvature and does not change the critical compressive strength of the member. That is why viscoelastic plates or columns, with the slope of the instantaneous stress-strain curve taken as constant, has no critical time of collapse.

Appendix

A viscoelastic plate 8 in. square, and $^3/_{16}$ in. thick is subject to a compressive load of 4,500 psi on two opposite edges (see Fig. 1). All the four edges are simply supported. The viscoelastic properties of the plate are represented by a Maxwell's model as shown in Fig. 2.

$$e_1 = \sigma/k_0 \qquad \dot{e}_2 = \sigma/c_0$$

$$e = e_1 + e_2$$

$$\dot{e} = \dot{e}_1 + \dot{e}_2 = (\dot{\sigma}/k_0) + (\sigma/c_0) = (1/k_0) [\dot{\sigma} + (k_0/c_0)\sigma]$$

With $k_0 = E$ and $k_0/c_0 = \alpha$

$$\dot{e} = (1/E) (\dot{\sigma} + \alpha\sigma) \quad (A\text{-}1)$$

$$S\bar{e} = (1/E) (S\bar{\sigma} + \bar{\sigma})$$

$$\bar{\sigma} = E[S/(S + \alpha)]\, \bar{e}$$

$$1 - \bar{\varphi} = S/(S + \alpha)$$

E for 75ST aluminum alloy at 600°F. is 5.2×10^6 psi and the average rate of creep for the first 10 hours under a constant stress of 4,500 psi is 0.00056/hour (see Fig. 17.3 of reference 5).

$$\dot{e} = \alpha\sigma/E$$

$$\alpha = E\dot{e}/\sigma = \frac{0.00056 \times 5.2 \times 10^6}{4{,}500} = 0.647 \text{ hour}$$

This viscoelastic plate is assumed to have the same values of E and α.

From Eq. (23),

$$B_{mn} = \frac{A_{mn} S}{C_{mn} IG \dfrac{S}{S + \alpha}\left[4f(\mu) + \dfrac{2S}{S + \alpha}\right]} \quad (A\text{-}2)$$
$$\left(\frac{m\pi}{a}\right)^2 N_x \left[f(\mu) + \frac{2S}{S + \alpha}\right] - 1$$

μ is taken to be 0.3

$$G = E/[2(1 + \mu)] = (5.2 \times 10)^6 (2 \times 1.3) = 2 \times 10^6 \text{ psi}$$

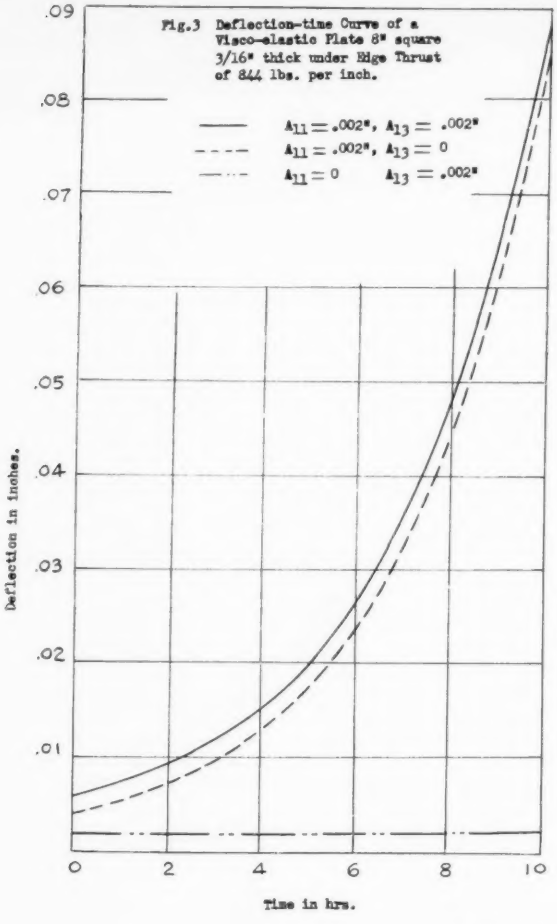

$$I = (1/12)(3/16)^3 \qquad N_x = 844 \text{ lbs. in.}$$

$$e_{11} = \pi^4/32^2$$

$$C_{11}IG/[(\pi^2/a^2)N_x]$$

$$f(\mu) = (1+\mu)(1-2\mu) = 3.25$$

$$\bar{B}_{11} = \frac{A_{11}\,S}{\dfrac{0.802S\,[13(S+\alpha)+2S]}{(S+\alpha)\,[3.25(S+\alpha)+2S]} - 1} \tag{A-3}$$

After simplifying and factoring the denominator,

$$\bar{B}_{11} = \frac{A_{11} \times 0.775\,(S+\alpha)\,(S+0.619\alpha)}{S\,(S+0.976\alpha)\,(S-0.492\alpha)} \tag{A-4}$$

By Heaviside expansion,

$$B_{11} = A_{11} + 0.775 \sum_{1}^{n} \frac{p(\beta_n)}{q'(\beta_n)}\, e^{\beta_n t} \tag{A-5}$$

$$p(S) = (S+\alpha)\,(S+0.619\alpha) \tag{A-6}$$

$$q(S) = S(S+0.976\alpha)\,(S-0.492\alpha)$$

$$q'(S) = (S+0.976\alpha)\,(S-0.492\alpha) + S(S+0.976\alpha) + S\,(S-0.492\alpha) \tag{A-7}$$

$$\beta_1 = 0 \qquad \beta_2 = -0.976\alpha \qquad \beta_3 = 0.492\alpha \tag{A-8}$$

From Eq. (A-5), for $A_{11} = 0.002$ in.,

$$B_{11} = 0.002 \times 0.775\,(-1.29 - 0.0060e^{-0.976\alpha t} + 2.30\,e^{0.492\alpha t}) \tag{A-9}$$

For $m = 1$, $n = 3$,

$$C_{13} = (\pi^4/8^4)\,[1 + 2 \times 1 \times 3^2 + 3^4] = (\pi^4/8^4) \times 100$$

$$C_{13}IG/[(\pi^2/a^2)N_x] = 0.802 \times 25$$

$$\bar{B}_{13} = \frac{A_{13}(S+\alpha)\,(5.25S+3.25\alpha)/S}{0.802 \times 25\,(15S+13\alpha) - (S+\alpha)\,(5.25S+3.25\alpha)}$$

$$= \frac{A_{13}}{56.3}\,\frac{(S+\alpha)\,(S+0.619\alpha)}{S(S+0.866\alpha)\,(S-0.012\alpha)} \tag{A.10}$$

For $A_{13} = 0.002$ in.

$$B_{13} = (0.002/56.3)\,[-59.6 - 0.043e^{-0.866\alpha t} + 60.6e^{0.012\alpha t}] \tag{A-11}$$

B_{11} and B_{13} at $t = 0$ to 10 hours are calculated with α of 0.647/hour as shown in Table 1, and the center deflections vs. time due to A_{11} and A_{13} are plotted in Fig. 3.

TABLE 1

(1) t Hours	(2) B_{11} In.	(3) $A_{11}+B_{11}$ In.	(4) B_{13} In.	(5) $A_{13}+B_{13}$ In.	(6) Center Deflection In.
0	0.00155	0.00355	0.000035	0.00204	0.00559
2	0.00471	0.00671	0.000071	0.00207	0.00878
4	0.01076	0.01276	0.000106	0.00211	0.01487
6	0.02216	0.02416	0.000142	0.00214	0.02630
8	0.0436	0.0456	0.000178	0.00218	0.0478
9	0.0606	0.0626			
10	0.0842	0.0862	0.000234	0.00223	0.0884

References

[1] Marin, J., *Creep Deflections in Columns*, Journal of Applied Physics, Vol. 18, pp. 103–109, January, 1947.

[2] Rosenthal, D., and Baer, H. W., *An Elementary Theory of Creep Buckling of Columns*, Proc. First U. S. National Congress of Applied Mechanics, pp. 603–611, June, 1951.

[3] Marin, J., Pao, Y. H., and Cuff, C., *Creep Properties of Lucite and Plexiglass for Tension, Compression, Bending and Torsion*, Trans. A.S.M.E., Vol. 73, No. 5, pp. 705–718, July, 1951.

[6] Kempner, J., *Creep Bending and Buckling of Linearly Visco-Elastic Columns*, NACA TN 3136, January, 1954.

[7] Higgins, T. P., Jr., *Effect of Creep on Column Deflection*, Chapter 10 of reference 17.

[8] Libove, Charles, *Creep Buckling of Columns*, Journal of the Aeronautical Sciences, Vol. 19, No. 7, pp. 459–467, July 1952.

[9] Lin, T. H., *Stresses in Columns with Time Dependent Elasticity*, Proceedings of the First Mid-Western Conference on Solid Mechanics, 1953.

[10] Kempner, J., and Patel, S. A., *Creep Buckling of Columns*, NACA TN 3138, January, 1954.

[11] Gerard, G., *Life Expectancy of Aircraft Under Elevated Temperature Conditions*, Wright Air Development Center Tech. Report 53-493, p. 15, October, 1953.

[12] Freudenthal, A. M., *The Inelastic Behavior of Engineering Materials and Structures*, pp. 220–242; John Wiley and Sons, Inc., New York, 1950.

[13] Alfrey, T., *Mechanical Behavior of High Polymer*, pp. 557–564; Interscience Publishers, Inc., New York, 1948.

[14] Timoshenko, S., *Theory of Elastic Stability*, p. 322; McGraw-Hill Book Co., Inc., New York, 1936.

[15] Johnson, A. E., *Creep Under Complex Stress Systems at Elevated Temperatures*, Proceedings of the Institute of Mechanical Engineering, London, England, Vol. 164, pp. 423–442, 1951.

[16] Brull, M. A., *A Structural Theory Incorporating the Effect of Time-Dependent Elasticity*, Doctoral dissertation at the University of Michigan, 1952; Proceedings of the First Midwestern Conference on Solid Mechanics, 1953.

[17] Churchill, R. V., *Modern Operational Mathematics in Engineering*, pp. 44–45; McGraw-Hill Book Co., Inc., New York, 1949.

[18] Lin, T. H., *Creep Deflections and Stresses in Columns*, presented at the Applied Mechanics Division, A.S.M.E., November 14, 1955. Paper No. 55-A-43. To be published in the Journal of Applied Mechanics.

[19] Shanley, F. R., *Weight Strength Analysis of Aircraft Structures*, pp. 310–316; McGraw-Hill Book Co., Inc., New York, 1952.

[20] Southwell, R. V., *Theory of Elasticity*, p. 461; The Clarendon Press, Oxford, England, 1936.

Forced Responses of Two Elastic Beams . . .

(*Continued from page 829*)

speaking, the input force is not sinusoidal. However, the arbitrary input force can be represented by functions with the only restriction that they are finite and integrable in a suitable interval. For such cases, the responses can be obtained by using the method shown herein and the well-known technique of replacing the arbitrary input by a Fourier series expansion. The total reaction forces—i.e., R_c and R_d—are then obtained as a summation of the reaction forces originating from input forces corresponding to the individual terms of the Fourier expansion.

Reference

[1] Myklestad, N. O., *Vibration Analysis;* McGraw-Hill Book Company, Inc., New York, 1944.

A Creep Buckling Hypothesis

(*Continued from page 882*)

bility in the creep buckling process. Finally, by use of statistical techniques, the degree of correlation between theory and experiment can be determined. The inadequacy of the currently available test data only serves to indicate the necessity for statistically planned experiments.

References

[1] Stowell, E. Z., *A Unified Theory of Plastic Buckling of Columns and Plates*, NACA Rep. 898, 1948.

[2] Gerard, G., *Critical Shear Stress of Plates Above the Proportional Limit*, J. Appl. Mech.; Vol. 15, No. 1, pp. 7–12, March, 1948.

[3] Gerard, G., *Compressive and Torsional Buckling of Thin-Wall Cylinders in the Yield Region*, N.Y.U. Report to NACA, October, 1954 (to be published as an NACA TN).

[4] Gerard, G., *Note on Creep Buckling of Columns*, Readers' Forum, Journal of the Aeronautical Sciences, Vol. 19, No. 10, p. 714, October, 1952.

[5] Libove, C., *Creep Buckling of Columns*, Journal of the Aeronautical Sciences, Vol. 19, No. 7, pp. 459–467, July, 1952.

[6] Libove, C., *Creep Buckling Analysis of Rectangular-Section Columns*, NACA TN 2956, 1953.

[7] Kempner, J., *Creep Bending and Buckling of Linearly Visco-elastic Columns*, NACA TN 3136, 1954.

[8] Kempner, J., *Creep Bending and Buckling of Nonlinearly Visco-elastic Columns*, NACA TN 3137, 1954.

[9] Mathauser, E. E., and Brooks, W. A., Jr., *An Investigation of the Creep Lifetime of 75S-T6 Aluminum Alloy Columns*, NACA TN 3204, 1954.

[10] Shanley, F. R., *Weight-Strength Analysis of Aircraft Structures*, pp. 307–322; McGraw-Hill Book Company, Inc., New York, 1952.

Readers' Forum

BRIEF REPORTS of investigations in the aeronautical sciences and discussions of papers published in the JOURNAL are presented in this special department. Entries must be restricted to a maximum of 1,300 words or the equivalent of one JOURNAL page including formulas and illustrations. Publication is completed as soon as possible after receipt of the material. The Editorial Committee does not hold itself responsible for the opinions expressed by the correspondents.

Contents

Determination of the Stationary Flow Field in Front of a Supersonic Cascade.....P. SCHWAAR 888

Comments on Vortex-Core Measurements.....ROBERT W. TRUITT 889

Note on Photoelastic Study of Swept Wings.....C. L. AMBA RAO 889

The Hot-Film Anemometer: A New Device for Fluid Mechanics Research....S. C. LING AND P. G. HUBBARD 890

Variational Method in the Theory of Axisymmetric Rotational Flow of a Compressible Fluid.....BOHDAN KRAJEWSKI 891

Errata—"Applied Aerodynamics and Flight Mechanics".....W. BAILEY OSWALD 892

Plastic Buckling of Circular Cylinders.S. RADHAKRISHNAN 892

Note on "On the Stability Theory of Flow with Finite Disturbances".....J. T. STUART 894

Remarks on Chaplygin Functions.....VIVIAN O'BRIEN 894

Asymptotic Suction Characteristics of the Boundary Layer over a Circular Cylinder.....H. G. LEW 895

Stall Propagation in a Cascade of Airfoils.....ANTHONY R. KRIEBEL 897

Tip-Bluntness Effects on Cone Pressures at $M = 6.85$...MITCHEL H. BERTRAM 898

Determination of the Stationary Flow Field in Front of a Supersonic Cascade

P. Schwaar

Société Nationale d'Etude et de Construction de Moteurs d'Aviation (SNECMA), Villaroche, France

April 12, 1956

KANTROWITZ[1] has shown that, in the case of subsonic axial velocities, pressure waves may propagate upstream of a supersonic cascade only if they are cancelled subsequently by waves of opposite sign. Determining the flow velocity and direction far upstream of the cascade for given entry conditions is then easily performed by means of Prandtl-Busemann's graphical characteristics method. Boxer, Sterrett, and Wlodarski[2] discussed the same flow phenomenon and used it for creating finite leading-edge angles, stating, however, that the graphical method fails in solving the inverse problem, which consists of determining the cascade entry conditions from given uniform upstream flow conditions. They consequently developed an analytical procedure.

However, the inverse problem may be solved actually in a very simple manner by the graphical method. Let us consider (Fig. 1) the case of a cascade with a leading-edge shock starting on the suction side and neutralized upstream by expansion waves of the same family issued from the wedges O_1 and O_2. The flow field may be characterized by the direction angle θ and the Prandtl-Meyer expansion angle ν of the velocity vector. Within the approximation of the method, it is possible to cancel the whole perturbation system at a finite distance from the leading edge, resulting in the prescribed uniform flow conditions (θ, ν) far upstream of the cascade. Indeed, choosing two adjacent wedge apexes O_1, O_2 and assuming, for example, computation steps of 1°, one finds that the shock originating at the leading edge F (of still unknown location) must be cancelled as a 2° compression wave at the intersection point A_1 of two 1° expansion waves

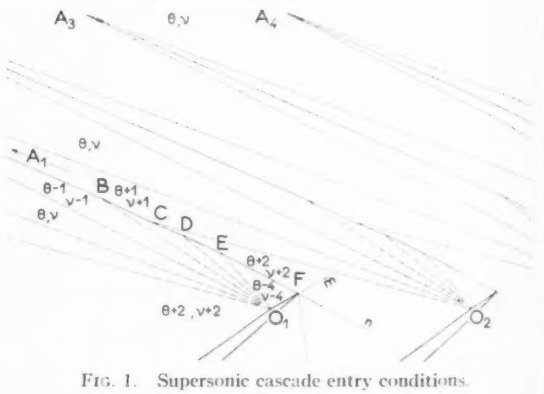

FIG. 1. Supersonic cascade entry conditions.

starting, respectively, from O_1 and O_2—namely $\overline{O_1A_1}$ $(\theta - 1, \nu - 1)/(\theta, \nu)$ and $\overline{O_2A_1}$ $(\theta, \nu)/(\theta + 1, \nu + 1)$. Therefore, the 2° compression wave $\overline{A_1B}$ $(\theta + 1, \nu + 1)/(\theta - 1, \nu - 1)$ may be drawn as a straight segment until it intersects at B with a further expansion wave—in our case $\overline{O_1B}$ $(\theta - 2, \nu - 2)/(\theta - 1, \nu - 1)$—thus determining the 3° shock-wave segment $\overline{BC}$ $(\theta + 1, \nu + 1) \div (\theta - 2, \nu - 2)$, etc. On the figure, the construction has been performed for an arbitrarily chosen 6° leading-edge shock, resulting in the cascade entry conditions $(\theta + 2, \nu + 2)/(\theta - 4, \nu - 4)$ on the suction side. Finally, the leading edge is located at the intersection point F of the straight lines $\overline{O_1m}$ of $(\theta - 4)°$ direction and $\overline{E\,n}$ of the 6° leading-edge shock front.

Thus, the inverse problem is solved for the case of a concentrated expansion at O. Should the forepart of the blade suction side have a continuous curvature instead of a corner, one obtains immediately an infinite family of particular solutions by drawing the streamlines in the vicinity of O and taking them as contours for the suction-side forepart.

References

[1] Kantrowitz, A., *The Supersonic Axial-Flow Compressor*, NACA Rep. 974, 1950.

[2] Boxer, E., Sterrett, J. R., and Wlodarski, J., *Application of Supersonic Vortex-Flow Theory to the Design of Supersonic Impulse Compressor- or Turbine-Blade Sections*, NACA RM L52B06, 1952.

Comments on Vortex-Core Measurements

Robert W. Truitt

Professor of Aeronautical Engineering, Virginia Polytechnic Institute, Blacksburg, Va.

April 23, 1956

In a recent Readers' Forum note,[1] Hopkins and Sorensen described a device for exploring vortex fields which they referred to as a new technique. The writer has used successfully this identical technique in research and in undergraduate aeronautical laboratory experiments for over 10 years.

The writer and his undergraduate students presented papers on the use of a Vortexmeter[2,3] in which the results of a series of experiments in vortex fields were reported. In addition to those indicated in reference 1, references 2 and 3 describe the following techniques and experiments using a Vortexmeter:

(1) Experimental results of Vortexmeter rotational speed (r.p.m.) vs. angle of attack for a finite wing. The plot of Vortexmeter r.p.m. vs. angle of attack showed the same straight-line variation and stalling characteristics as the C_L vs. α curve. The angle of attack for zero lift determined by use of the Vortexmeter (zero r.p.m.) was found to be in excellent agreement with the experimental results of C_L vs. α.

(2) Technique for determining the origin and roll-up characteristics of the trailing vortex system of a finite lifting wing. The Vortexmeter was also used to find the "effective span," trace the downstream location of the core of the trailing vortex, and measure its strength at a series of chord stations.

(3) Technique for detecting misalignment and warping of a wind-tunnel model wing. By exploring the right and left wing tip regions with the Vortexmeter, asymmetric locations or strengths of the trailing vortex system are detected readily.

It may be interesting to note that the writer found the most satisfactory rotating element to be a straight flat "paddle" or "shovel-shaped" vane. This type of vane was found to give better quantitative results for the measurement of the strength of a vortex than the type used in reference 1. The reason for this is that the paddle-type vane acts, in principle, like the cup-type anemometer—i.e., the flat vane area is concentrated at a given radius.

Although the writer developed the Vortexmeter technique independently, it has been developed to a high degree by other investigators in this country and abroad as both an instructional and research tool. A Yugoslavian textbook[4] describes a paddle-bladed Vortexmeter (Fig. 1)* as standard laboratory equipment for vortex-core measurements. In 1951, Dr. August Raspet of the Aerophysics Department, Mississippi State College, measured, in a free-flight investigation, the spanwise distribution of circulation on a sailplane wing, with a set of 15 three-bladed Vortexmeters located at stations along the trailing edge. Raspet found that a two-bladed Vortexmeter lacks discrimination for low vorticities when used on wakes which are not axially symmetric—viz., behind a wing.

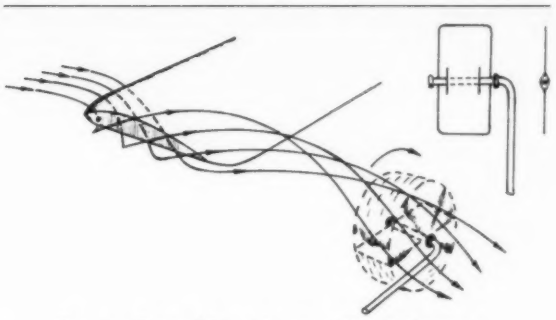

Fig. 1. Copy of Fig. 164, page 161 of reference 4.

References

[1] Hopkins, Edward J., and Sorensen, Norman E., *A Device for Vortex-Core Measurements*, Journal of the Aeronautical Sciences, Readers' Forum, Vol. 23, No. 4, pp. 396–398, April, 1956.

[2] Truitt, Robert W., *The Use of a Vortexmeter*, paper presented at the Annual Meeting of the Aeronautical Engineering Section, American Society of Engineering Education, Dartmouth College, June 25, 1952.

[3] Deutsch, Jeffrey S., and Palatine, Richard E., *A Vortexmeter For Flow Studies*, paper presented at the Third Annual Southeastern Conference, Student Branches, Institute of the Aeronautical Sciences, Georgia Institute of Technology, April 17, 1952.

[4] Obad, Stanko, *Mechanika* Vazduhoplova, published in Belgrade, Yugoslavia, 1950.

* Courtesy of Professor Raspet.

Note on Photoelastic Study of Swept Wings

C. L. Amba Rao

Department of Aeronautical Engineering, Indian Institute of Science, Bangalore 3, India

April 24, 1956

Introduction

A survey of recent literature indicates some work done by Gerard and Papirno[1] and Coiley.[2] If the aerodynamic load is applied about the elastic axis of the wing, the problem reduces to the bending of a plate as the thickness chord ratio is small. Hence one of the following standard methods[3] is used. Otherwise, the optical birefringence due to tensile stresses cancels off with that due to compressive stresses.

(a) Combinations of materials of different stress optical coefficients.[4] (b) Reflecting surfaces or layers at the neutral surface.[5] (c) Superposition of bending on initial frozen tension.[6] (d) The one strip method in which, after freezing, half the thickness is removed.

Symbols

E_s	=	Young's modulus of (optically birefringent) sensitive plastic
E_i	=	Young's modulus of insensitive plastic
b_i	=	width of the sensitive plastic in the transformed section
h	=	total thickness of sheet
p, q	=	principal stresses
σ_1, σ_2	=	principal stresses on the outermost fiber at A

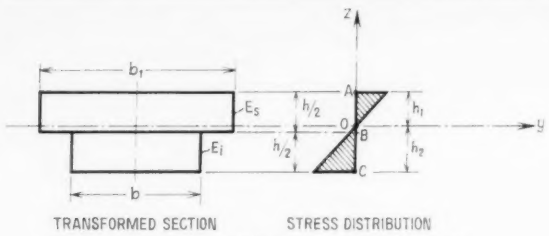

FIG. 1. Stress distribution in sandwich plate.

M_1, M_2 = principal bending moments
R_t = phase difference or relative retardation in fringes
C_s = stress optic constant in sensitive material
C_i = stress optic constant in insensitive material
I = moment of inertia of the section about neutral axis

THEORY

In case (a) above and in composite structures[7] in all the previous work, it is said that the Young's modulus of both the materials should be the same, which may not always be possible. An expression is derived for the case when the Young's modulus is different for the two.

The transformed section principle is used[8] (Fig. 1). Let $E_s > E_i$. Assuming there is no sliding between the two, during bending, the theory of solid beams can be used—i.e., the elongations of longitudinal fibers are proportional to the distance from the neutral axis. Hence

$$b_1 = b(E_s/E_i) \tag{1}$$

There is a shift in the neutral axis location, and

$$h_1 = (h/4)\{[(E_s/E_i) + 3]/[(E_s/E_i) + 1]\} \tag{2}$$

The maximum stress at the bottommost fiber at distance h_2 from the neutral axis $= Mh_2/I$. The maximum stress at the topmost fiber at distance h_1 from the neutral axis $= (Mh_1/I)(E_s/E_i)$. Similarly it can be derived even if $E_s < E_i$.

The integrated retardation[3] over a considerable thickness is interpreted in terms of the maximum stress difference on the boundary, as the law of stress variation is known.
In OA,

$$\left.\begin{aligned} R_t &= \int_0^{h_1} (p - q)C_s\,dz = \frac{1}{2}(\sigma_1 - \sigma_2)h_1C_s \\ &= (1/2)[(M_1 - M_2)/I](E_s/E_i)C_sh_1^2 \end{aligned}\right\} \tag{3}$$

In OB,

$$R_t = (1/2)[(M_1 - M_2)/I]C_s[h_2 - (h/2)]^2 \tag{4}$$

Similarly, in BC,

$$R_t = (1/2)[(M_1 - M_2)/I]C_i(h/2)[2h_2 - (h/2)] \tag{5}$$

The total retardation consists of three parts, and the retardation in the insensitive material (in BC) is usually neglected. If not,

$$R_t = (1/2)[(M_1 - M_2)/I]\{(E_s/E_i)C_sh_1^2 - C_s[h_2 - (h/2)]^2 - C_i(h/2)[2h_2 - (h/2)]\} \tag{6}$$

REFERENCES

[1] Gerard, G., and Papirno, R., *Note on Photoelastic Study of a Swept-Wing Model*, Journal of the Aeronautical Sciences, Readers' Forum, Vol. 21, No. 12, pp. 846, 847, December, 1954.

[2] Coiley, G. M., *Stress Concentration in Swept Wing Panels Using Photoelastic Models*, The College of Aeronautics, Cranfield, Rep. No. 78.

[3] Hetenyi, M. (Ed.), *Handbook of Experimental Stress Analysis*, p. 927; John Wiley & Sons, Inc., New York, 1950.

[4] Solakian, A. G., *Photoelastic Models with Cemented Elements*, Photoelastic Journal, Vol. 1, No. 1, pp. 14–17, 1938.

[5] Goodier, J. N., and Lee, G. H., *An Extension of the Photoelastic Method of Stress Measurement to Plates in Transverse Bending*, J. Appl. Mech., Trans. ASME, Vol. 63, pp. A-27–A-29, Discussion, p. A-187, 1941.

[6] Drucker, D. C., *The Photoelastic Analysis of Transverse Bending of Plates in the Standard Transmission Polariscope*, J. Appl. Mech., Trans. ASME, Vol. 64, pp. A-161–A-164, 1942.

[7] Lamble, J. H., and Bayoumi, S. E. A., *A Room Temperature Photo-Elastic Technique for Three Dimensional Problems*. Proc. (B) The Institution of Mechanical Engineers, Vol. 1B, No. 12, pp. 575–579, 1952–1953.

[8] Timoshenko, S., and MacCullough, G. H., *Elements of Strength of Materials*, 3rd Ed., p. 241; D. Van Nostrand Company, Inc., New York, 1949.

The Hot-Film Anemometer: A New Device for Fluid Mechanics Research*

S. C. Ling and P. G. Hubbard
Iowa Institute of Hydraulic Research, State University of Iowa, Iowa City

April 25, 1956

A NEW HEAT-TRANSFER TYPE of sensing element consisting of a very thin platinum film fused to a glass surface has been developed for the study of flow characteristics in both gases and liquids. The platinum film is the sensing element, while the glass acts as a supporting body for the film. Its operation is very similar to that of the well-known hot-wire anemometer, inasmuch as both are heated by passing an electrical current through them; the resulting heat exchange between the wire or film and the fluid is detected electrically as a function of flow parameters. However, the hot-film anemometer has several superior characteristics which make it suitable for use in situations for which the hot wire is impracticable—such as the flow of liquids and either the supersonic or high-temperature flow of gases.

The outstanding characteristics of the hot-film anemometer as a transducer are its excellent mechanical characteristics, its superior dynamic response, and the high signal-to-noise ratio. An infinite variety of geometrical forms is feasible depending on the nature of the application, and a typical 30°-wedge type of hot-film probe is illustrated in Fig. 1. The wedge form minimizes the collection of microscopic dirt carried by the fluid and provides a more efficient and uniform heat-transfer surface so that the small amount of dirt which does collect has less effect on its rate of heat transfer. In the case of the hot-wire anemometer, heat transfer is concentrated at the front stagnation zone, making it very sensitive to minute surface contamination in this area. For a fluid carrying fibrous debris, a cone-shaped probe could be utilized to minimize the collection of these impurities on the sensing surface. In certain applications—e.g., in studies of boundary-layer transition where any disturbance due to the detecting instrument is to be avoided—a plane hot-film element can be mounted flush with a flow boundary. For applications in high-temperature flow, a film of rhodium fused on a quartz surface would be preferable because of the resistant properties of these materials at elevated temperatures.

Although the sectional width of the hot-film probe shown in

* All phases of the project described herein were supported by the Office of Naval Research under Contract N8-onr-500 with the Iowa Institute of Hydraulic Research.

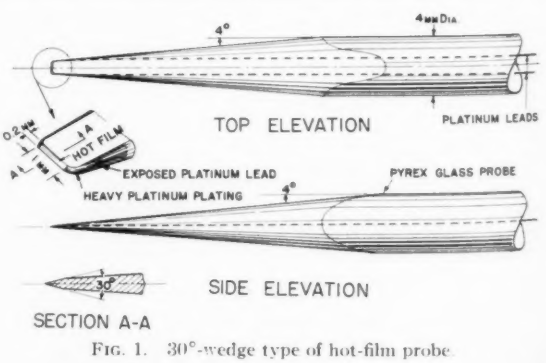

FIG. 1. 30°-wedge type of hot-film probe.

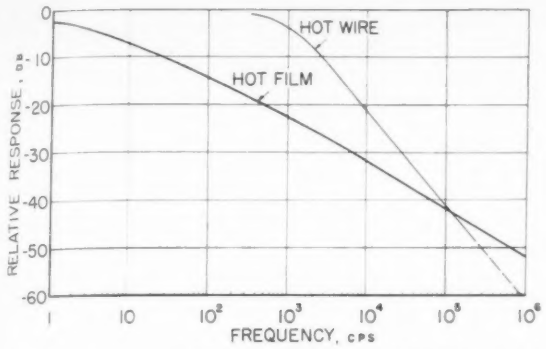

FIG. 2. Uncompensated frequency response of hot film and hot wire.

Fig. 1 is approximately 50 times the diameter of a typical hot-wire sensing element, the curves of Fig. 2 show that the dynamic response is comparable; these data represent operation of the two types at the same mean velocity and overheating ratio. At high frequencies the response of the film is superior, but at low frequencies the wire gives the greater relative response. This low-frequency deficiency of the hot film is more than compensated, however, by its higher signal level. An important detail of this comparison is the decrease in response of 3 db. per octave for the hot film with a maximum phase lag of 45° as contrasted with 6 db. per octave and 90° for the hot wire. This peculiar characteristic is due to the nature of the heat exchange between the film and its supporting material. Because of this special dynamic response, the simple R-C or R-L circuits frequently used with hot-wire anemometers cannot be used to compensate the signal from a hot film. However, this characteristic is especially adaptable to constant-temperature operation wherein a servocontrol circuit is used.

Several factors are responsible for the high signal-to-noise ratio of the hot-film anemometer. Because the mechanical strength of a hot-film element depends only on its glass or ceramic supporting base, the thickness of the film can be varied at will to control the total resistance independently of its linear dimensions. Resistance values from a few ohms up to several thousand ohms are practicable on a probe whose size is governed by the requirements of space resolution; a probe of several hundred ohms will match the equivalent-noise resistance of present vacuum-tube amplifiers. Another factor is the improved mechanical arrangement of a film supported by a glass or ceramic base instead of a thin wire supported at its ends. The extraneous signal due to stress and local vibration is thereby eliminated. The low asymptotic phase lag of the hot-film element also contributes to a low overall noise in constant-temperature operation because of the sharper high-frequency cutoff which can be used in the control circuits. When all of these factors are taken into account, the signal-to-noise ratio of the hot-film anemometer is superior to that of a hot wire operating under similar conditions.

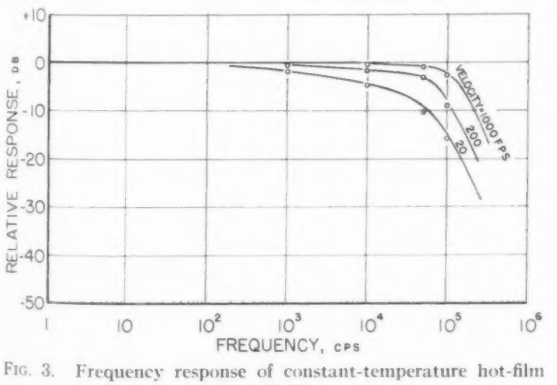

FIG. 3. Frequency response of constant-temperature hot-film anemometer.

Several instruments have been built by the authors for various research organizations. The typical dynamic response of one of these instruments is shown in Fig. 3. A special circuit is included to convert the nonlinear response of the sensing element to a voltage and a panel-meter indication which are linear functions of the fluid velocity. This greatly increases both the simplicity and the accuracy of use of such an instrument.

A comprehensive theoretical treatise on the dynamic and thermodynamic properties of hot films on a plane, a cylinder, or a wedge, the analysis of the servocontrol amplifiers, and additional performance data are to be found in reference 1. A mathematical treatment of the dynamic response of different forms of sensing elements and an operating manual for the instrument as a whole will appear as separate publications at a later date.

REFERENCE

[1] Ling, S. C., *Measurement of Flow Characteristics by the Hot-film Technique*, Ph.D. Dissertation, State University of Iowa, June, 1955.

Variational Method in the Theory of Axisymmetric Rotational Flow of a Compressible Fluid

Bohdan Krajewski
Research Engineer, Warsaw, Poland
May 7, 1956

INTRODUCTION

IN THE STUDY of flow through turbomachines, such as compressors and turbines, steady axisymmetric flow is assumed. Introducing the so-called "stream function" Ψ and changing variables, the problem can be reduced to the first variation of the function Ψ. Further calculations can be carried out using one of the well-known methods of Ritz, Trefftz, and Galerkin.

BASIC ASSUMPTIONS AND EQUATIONS

For an axisymmetric steady inviscid flow, the gradient of total enthalpy H can be expressed in cylindrical coordinates [see reference 2, pages 9, 10, Eqs. (7a), (7b), (7c)] by the relation

$$\partial H/\partial r = F_r + T(\partial s/\partial r) + (C_u/r)\,[\partial(rC_u)/\partial r] - C_z[(\partial C_r/\partial x) - (\partial C_z/\partial r)] \quad (1)$$

$$0 = F_u - (C_r/r)\,[\partial(rC_u)/\partial r] - C_z(\partial C_u/\partial x) \ldots \quad (2)$$

$$\partial H/\partial x = F_x + T(\partial s/\partial x) + C_r[(\partial C_r/\partial x) - (\partial C_z/\partial r)] + C_u(\partial C_u/\partial x) \quad (3)$$

where

H = total enthalpy per unit mass
C_u, C_r, C_z = components of the absolute velocity, tangential, radial, and axial, respectively
r, x = cylindrical coordinates, radial and axial, respectively
F_u, F_r, F_z = tangential, radial, and axial force exerted on gas particles by blades, respectively
s = entropy per unit mass
T = absolute temperature of gas

The equation of continuity under similar conditions becomes

$$[\partial(\rho rC_z)/\partial x] + [\partial(\rho rC_r)/\partial_r] = 0 \quad (4)$$

Eq. (4) shows that it is possible to define a stream function Ψ, of r and x, such that

$$\rho rC_r = -\rho_0(\partial\Psi/\partial x) \ldots \quad (5)$$

$$\rho rC_z = \rho_0(\partial\Psi/\partial_r) \ldots \quad (6)$$

wehre ρ_0 is a constant reference density.

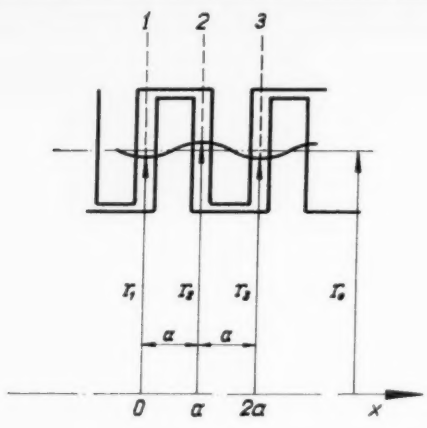

FIG. 1.

Because there is no blade force acting in the gap between two blade rows and because the principal effect is due to the radial component of the gradient H, further considerations will be confined to Eq. (1). In general, the effect of the radial motion on the calculations is due chiefly to the term $\partial C_r/\partial x$ in Eq. (1).

This term is expected to be significant mainly because of the oscillatory motion, which may involve important changes in C_r in a row of blades. The curve of intersection of a stream surface with an axial plane is referred to as "the radial flow path." Because of the axial symmetry, the radial flow path is the same in any axial plane.

In such a case, the sinusoidal curve is believed to represent the principal effect of the radial motion (see Fig. 1). This assumption is made by many authors.[1, 2, 3] Therefore, Eq. (1) may be rewritten as an ordinary differential equation:

$$dH/dr = T(ds/dr) + (C_u/r)\,[d(rC_u)/dr] - C_r[(dC_r/dx) - (dC_x/dr)] \quad (7)$$

and now the stream function may be expressed in the form

$$\Psi = \Psi_1 + f(x)p(r) \ldots \quad (8)$$

where $f(x)$ is a function determining the form of the radial flow path.

The function $f(x)$ satisfies the following conditions:

$$x = 0, a; \qquad f(0) = 0; \qquad f(a) = 1$$

Thus, the stream function in sections 1 and 2 of Fig. 1 may be expressed in the form

$$\Psi = \Psi_1 \quad \text{for } x = 0$$
$$\Psi = \Psi_1 + p(r) \quad \text{for } x = a$$

where Ψ_1 and $p(r)$ are functions of r alone.

Introducing the transformation

$$dH/d\Psi = (dH/dr)\,(dr/d\Psi); \quad ds/d\Psi = (ds/dr)\,(dr/d\Psi); \quad d(rC_u)/d\Psi = [d(rC_u)/dr]\,(dr/d\Psi) \quad (9)$$

Eq. (7) may be rewritten as

$$dH/d\Psi = T(ds/d\Psi) + (C_u/r)\,[d(rC_u)/d\Psi] - (\rho_0/\rho r)\,[(dC_r/dx) - (dC_x/dr)] \ldots \quad (10)$$

or

$$(\rho r/\rho_0)\,(dH/d\Psi) - (\rho r/\rho_0)T(ds/d\Psi) - (\rho/r\rho_0) \times \{d[(C_u r)^2/2]/d\Psi\} + [(dC_r/dx) - (dC_x/dr)] = 0 \quad (11)$$

Substituting Eqs. (5), (6), and (8) in Eq. (11) we have

$$(\rho r/\rho_0)\,(dH/d\Psi) - (\rho r/\rho_0)T(ds/d\Psi) - (\rho d/r\rho_0)\,\{[(C_u r)^2/2]/d\Psi\} - (\rho/r\rho_0)f''(x)p(r) - (d/dr)\,[(\rho_0/\rho r)\,(d\Psi/dr)] = 0 \quad (12)$$

It is known that for the function Ψ the first variation is determined by the relation

$$F\langle r\rangle = \int_{r_1}^{r_2} g\left[r_1\Psi(r), \frac{d\Psi}{dr}\right] dr = \text{extremum} \quad (13)$$

where the condition

$$(\partial g/\partial\Psi) - (d/dr)\,(\partial g/\partial\Psi_r) = 0 \quad (14)$$

where $\Psi_r = (d\Psi/dr)$ should be satisfied. It can easily be seen that Eq. (12) satisfies the condition determined by Eq. (14), where the initial equation is expressed as

$$\int_{r_1}^{r_2}\left[\frac{\rho}{\rho_0} rH - \frac{\rho}{\rho_0} rTs - \frac{\rho}{r\rho_0}\frac{(rC_u)^2}{2} - \frac{\rho}{r\rho_0}f''(x)p(r)\Psi + \frac{\rho_0}{2\rho r}\left(\frac{d\Psi}{dr}\right)^2\right] dr = \text{extremum} \quad (15)$$

The quantities such as H, s, rC_u are in practical problems given functions of Ψ and r:

$$H = F(\Psi_1 r); \quad s = G(\Psi_1 r); \quad rC_u = K(\Psi_1 r) \ldots \quad (16)$$

REFERENCES

[1] Traupel, W., *Neue allegemeine Theorie der mehrstufigen axialen Turbomaschine*, Vol. 1 p. 135; Leemann & Co., Zürich und Leipzig, 1942.

[2] Wu, Chung-Hua, and Wolfenstein, L., *Application of Radial Equilibrium Condition to Axial-Flow Compressors and Turbine Design*, NACA TN 1795, pp. 17–20, 1949.

[3] Eckert, B., *Axialkompressoren und Radialkompressoren*. Vol. 1, p. 183; Julius Springer, Berlin, Göttingen, Heidelberg, 1953.

Errata—"Applied Aerodynamics and Flight Mechanics"

W. Bailey Oswald
Chief—Aerodynamics Section, Santa Monica Division, Douglas Aircraft Company, Inc., Santa Monica, Calif.
June 26, 1956

A FEW ERRORS have been found in the manuscript of my paper.[1] In order to avoid confusion of diligent readers who might wish to make use of relations therein, corrections for these errors are listed below:

(1) Delete $1/V_b$ from the last term of Eq. (17) on page 478.

(2) Change W_a to W_r in the expression for Term No. (4) in Table 1 on page 479.

(3) In the second line following Eq. (23) on page 482, insert the words "twice the " before the words "kinetic energy."

The text, discussion, and calculations relating to the above material were correctly presented in the paper.

REFERENCE

[1] Journal of the Aeronautical Sciences, Vol. 23, No. 5, pp. 469–484, May, 1956.

Plastic Buckling of Circular Cylinders*

S. Radhakrishnan†
College of Engineering, New York University, New York
May 28, 1956

THE PLASTIC BUCKLING of circular cylinders under single and combined loads is solved by starting with Donnell's[1] equations of equilibrium and using the following assumptions: (a)

* This is a brief summary of some of the results of a thesis submitted to the College of Engineering, New York University, in partial fulfillment of the requirements for the degree of Doctor of Engineering Science. The author wishes to express his deep gratitude to Dr. George Gerard who was his thesis adviser. Complete results will be published later.

† Now, Aeronautical Engineer, Hindustan Aircraft Ltd., Bangalore, India.

Expressions for strains and curvatures in terms of displacements used in elastic thin-shell theory are retained, (b) the secant shear modulus in the plastic region is defined as the ratio of octahedral shear stress to octahedral shear strain, (c) the Hencky-Nadai stress-strain law is used to relate the stresses and strains along with the assumption of ν (Poisson's ratio) = 1/2, and (d) the entire cross section of the shell remains plastic during the infinitesimal buckling. The last assumption overcomes the mathematical objections usually raised in the use of deformation theory laws.

Following a procedure analogous to that adopted by Stowell,[2] the equations of equilibrium in terms of the displacements u, v, and w in the plastic region were obtained by Gerard.[3] These three equations are reduced to yield a single eighth-order differential equation in w. The final equations for two cases of loading in terms of w are:

(a) Torsional buckling

$$\frac{E_s h^3}{9}\left[\frac{E_t}{E_s}\frac{\partial^4}{\partial x^4}+\left(3-\frac{E_t}{E_s}\right)\frac{\partial^4}{\partial x^2\partial y^2}+\frac{E_t}{E_s}\frac{\partial^4}{\partial y^4}\right]\left[\frac{\partial^4}{\partial x^4}+\left(1+\frac{E_t}{E_s}\right)\frac{\partial^4}{\partial x^2\partial y^2}+\frac{\partial^4}{\partial y^4}\right]w+\frac{E_s h}{r^2}\frac{\partial^4 w}{\partial x^4}+2\tau_{cr}h\times$$
$$\left[\frac{E_t}{E_s}\frac{\partial^4}{\partial x^4}+\left(3-\frac{E_t}{E_s}\right)\frac{\partial^4}{\partial x^2\partial y^2}+\frac{E_t}{E_s}\frac{\partial^4}{\partial y^4}\right]\frac{\partial^2 w}{\partial x\partial y}=0 \quad (1)$$

(b) Buckling under combined lateral pressure and axial load.

$$\frac{E_s h^3}{9}\left[A_1\frac{\partial^4}{\partial x^4}+(4A_1A_2-A_{12}-A_{12}^2)\frac{\partial^4}{\partial x^2\partial y^2}+A_2\frac{\partial^4}{\partial y^4}\right]\left[A_1\frac{\partial^4}{\partial x^4}+(A_{12}+1)\frac{\partial^4}{\partial x^2\partial y^2}+A_2\frac{\partial^4}{\partial y^4}\right]w+$$
$$\frac{4E_s h}{3r^2}\left(A_1A_2-\frac{A_{12}^2}{4}\right)\frac{\partial^4 w}{\partial x^4}+\left[A_1\frac{\partial^4}{\partial x^4}+(4A_1A_2-A_{12}-A_{12}^2)\frac{\partial^4}{\partial x^2\partial y^2}+A_2\frac{\partial^4}{\partial y^4}\right]\left(\sigma_{xcr}h\frac{\partial^2 w}{\partial x^2}+\sigma_{ycr}h\frac{\partial^2 w}{\partial y^2}\right)=0 \quad (2)$$

In the above equations, x is the coordinate along the axis of the cylinder, y the coordinate along the circumference of the cylinder, r the radius of the cylinder, h the thickness of the cylinder, w the normal displacement of the shell, E_s the secant modulus, E_t the tangent modulus, τ_{cr} the critical shear stress, σ_{xcr} the critical axial compressive stress, σ_{ycr} the critical circumferential compressive stress from lateral pressure p ($\sigma_y = pr/h$), and A_1, A_2, and A_{12} the plasticity coefficients defined by

$$A_1 = 1-(3/4)\left[1-(E_t/E_s)\right]\left[\sigma_x^2/(\sigma_x^2-\sigma_x\sigma_y+\sigma_y^2)^{1/2}\right]$$
$$A_2 = 1-(3/4)\left[1-(E_t/E_s)\right]\left[\sigma_y^2/(\sigma_x^2-\sigma_x\sigma_y+\sigma_y^2)^{1/2}\right]$$
$$A_{12} = 1-(3/2)\left[1-(E_t/E_s)\right]\left[\sigma_x\sigma_y/(\sigma_x^2-\sigma_x\sigma_y+\sigma_y^2)^{1/2}\right]$$

Eqs. (1) and (2) reduce to the corresponding Donnell's equations for the elastic case when E_t and E_s are replaced by E and 1/2 is replaced by ν at the appropriate places [e.g., $E_s h^3/9$ will become, in the elastic case, $Eh^3/12(1-\nu^2)$, the bending rigidity].

Only boundary conditions on w can be prescribed since the differential equations are in terms of w while the boundary conditions on u and v are implied by their respective relation to w. The buckling problem is solved for the case of the simply supported cylinder ($w = \partial^2 w/\partial x^2 = 0$ at both ends of the cylinder) using the following nondimensional parameters:

$$Z = (L^2/rh)\sqrt{1-\nu^2} = (3/2)(L^2/rh)$$

k_s = shear stress coefficient = $N_{xy}L^2/\pi^2 D = 9\tau_{xy}L^2/\pi^2 E_s h^2$

k_x = axial stress coefficient = $N_x L^2/\pi^2 D = 9\sigma_x L^2/\pi^2 E_s h^2$

k_y = circumferential stress coefficient = $N_y L^2/\pi^2 D = 9\sigma_y L^2/\pi^2 E_s h^2$

where L is the length of the cylinder.

The torsional buckling case corresponding to Eq. (1) is solved by using Galerkin's method as used by Batdorf[1] for the elastic case. The results after minimization with respect to the number of circumferential buckles are given in Fig. 1. In all the buckling problems in the plastic region, the parameter E_t/E_s plays an important role.

The combined loads case corresponding to Eq. (2) is solved for the simply supported cylinder by using $w = w_0 \sin(m\pi x/L)\sin(\pi y/\lambda)$ where m is the number of half waves in the axial direction and λ the number of half waves in the circumferential direction. The resulting expression after substitution for w is solved for k_{ycr} for chosen values of σ_x/σ_y, E_t/E_s, and Z by minimizing with respect to m and λ. For most cylinders ($Z > 300$), the minimum value of m was found to be 1. In Fig. 2, the critical values of k_y against k_x are plotted for both compressive and tensile axial load for three values of E_t/E_s with $Z = 9{,}000$. Fig.

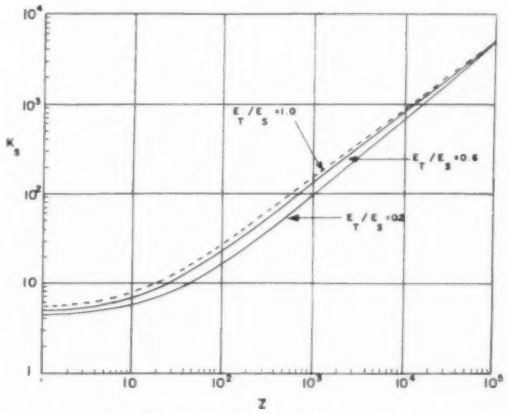

FIG. 1. Critical shear-stress coefficients in the plastic region for simply supported cylinders in torsion.

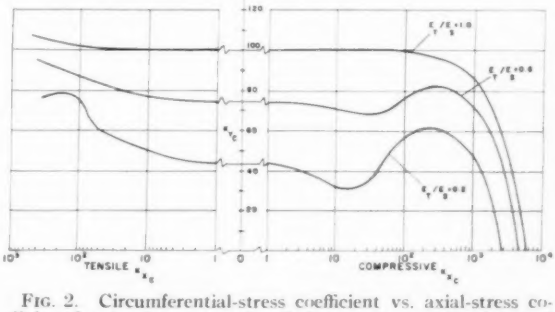

FIG. 2. Circumferential-stress coefficient vs. axial-stress coefficient for simply supported cylinders under combined lateral pressure and axial load for $Z = 9{,}000$ under various E_t/E_s values.

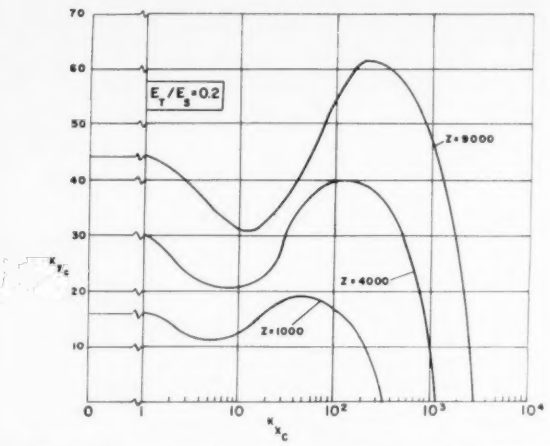

FIG. 3. Circumferential-stress coefficient vs. axial-stress coefficient for simply supported cylinders under combined lateral pressure and axial load for various Z values.

3 shows the variations of k_x and k_y for various Z's at $E_t/E_s = 0.2$.

From Figs. 2 and 3 it is seen that an unusual behavior is predicted by the theory in the case of the combined loads—viz., that in certain ranges the critical lateral pressure increases with the application of axial compressive load. This effect is accentuated at low E_t/E_s values. Suitable experimental data are not available to check the theoretical predictions in the combined loads case.

REFERENCES

[1] Donnell, L. H., *Stability of Thin-walled Tubes under Torsion*, NACA TR 479, 1934.

[2] Stowell, E. Z., *A Unified Theory of Plastic Buckling of Columns and Plates*, NACA TR 898, 1948.

[3] Gerard, G., *Compressive and Torsional Buckling of Thin-Wall Cylinders in the Yield Region*, to be published as an NACA Technical Note.

[4] Batdorf, S. B., *A Simplified Method of Elastic Stability Analysis for Thin Cylindrical Shells*, NACA TR 874, 1947.

Note on "On the Stability Theory of Flow with Finite Disturbances"

J. T. Stuart
Aerodynamics Division, National Physical Laboratory, Teddington, England
May 7, 1956

IN A RECENT NOTE, Pai[1] rejects my criticisms[2] of his proof[3] that laminar flows are stable against finite disturbances. He asks what I mean by stability of a laminar flow. I agree with the definition given by Lin[4] and with that given by Pai himself,[1] so it is clear that the source of the controversy does not lie here. Furthermore, he states that Eq. (7) of reference 2 will not reduce to Eq. (6) if the components of disturbance velocity, u' and v', are put equal to zero, because of the term $\partial\bar{u}/\partial t$. However, if $u' = v' = 0$, no energy is being transferred between the mean flow, $\bar{u}$, and the disturbance flow, and since there is no other source of unsteadiness, $\bar{u}$ must be independent of time. Consequently the mean flow equation takes its steady laminar form, and Eq. (7) does in fact degenerate into Eq. (6).

Let us turn now to the basic point of the analysis of reference 3, from which Pai concludes that two-dimensional flows are stable against finite disturbances. Pai assumes there that the disturbance of a laminar flow can be purely harmonic in x [see reference 3, Eq. (22)]. The vital thing which I have tried to show in reference 2 is that a disturbance of a laminar flow cannot, according to the Navier-Stokes equations, be purely harmonic in x. In particular, the disturbance must contain a mean motion part, which physically we know to arise from the action of Reynolds stresses.

Thus, the error in reference 3 can either be regarded physically, as being due to the neglect of the effect of the Reynolds stresses on the mean motion, or mathematically, as being due to the assumption that the nonlinear equations of motion can exhibit purely-harmonic solutions. Whether one looks at the problem physically or mathematically, the conclusion that laminar flows are stable is therefore seen to be fallacious. That laminar flows *are unstable* is, of course, borne out empirically by a wealth of experimental evidence on the subject.

Author's Reply

In reply to Stuart's note, I would like to make the following two remarks.

Since he agrees with my definition of stability of laminar flow, his treatment does not indicate anything of the stability of the original steady solution of laminar flow because his disturbance is a deviation from a mean flow differing from the original flow.

One should remember that the mean velocity distribution of a turbulent flow is nothing but a solution of Navier-Stokes equations if Reynolds stresses are included. It is well known that turbulent flows are stable. Hence, there is no basis that the mean velocity including the Reynolds stresses should be unstable as Stuart claims.

REFERENCES

[1] Pai, S. I., *On the Stability Theory of Flow with Finite Disturbances*, Journal of the Aeronautical Sciences, Vol. 23, No. 3, p. 274, March, 1956.

[2] Stuart, J. T., *On the Role of Reynolds Stresses in Stability Theory*, Journal of the Aeronautical Sciences, Vol. 23, No. 1, p. 86, January, 1956.

[3] Pai, S. I., *On the Stability of Parallel Flows with Respect to Periodic Disturbances*, J. Franklin Inst., Vol. 259, No. 3, p. 197, March, 1955.

[4] Lin, C. C., *The Theory of Hydrodynamic Stability*, p. 1, Cambridge University Press, Cambridge, England, 1955.

Remarks on Chaplygin Functions

Vivian O'Brien
Associate Physicist, Applied Physics Laboratory, The Johns Hopkins University, Silver Spring, Md.
April 30, 1956

INTRODUCTION

IT IS WELL KNOWN that the solutions of Chaplygin's equation for compressible flow[1, 2] are $\psi = \tau^{k/2} F(a_k, b_k, c_k; \tau) \sin k\theta$, the parameters of the hypergeometric functions arising from the fluid and k, a real number, dependent upon the physical boundaries. The following facts are less well known.

SPECIAL CASES OF THE LOG SOLUTION

For certain cases ($c_k = -m$, m an integer ≥ 1), the ordinary hypergeometric series $F(a_k, b_k, c_k; \tau)$ diverges and a logarithmic solution must be found [Eq. (13) of reference 1]. For the regular series, if a_k or b_k is a negative integer, the series terminates—i.e., becomes a polynomial in τ. However, if a_k or b_k becomes a negative integer when c_k is a negative integer, the logarithmic solution still contains an infinite series (cf. a misstatement page 4, reference 1 which does not distinguish the two cases). Both cases are included in the list of the pathological cases of general hypergeometric functions on page 69, reference 3.

For both c_k, a negative integer, and b_k, a negative integer, the complete solution can be written (following the notation of reference 1)

$$\psi_{-k} = \tau^{-k/2} \begin{matrix} \sin \\ \cos \end{matrix} (k\theta) \Gamma_{-k}(\tau)$$

$$Y_{-k}(\tau) = 1 + \sum_{m=1}^{k-1} \frac{(m + a_k - k - 1)\ldots(a_k - k)(m + b_k - k - 1)\ldots(b_k - k)}{m!(m-k)!(m-k)\ldots(1-k)}\tau^m + \frac{(a_k - 1)\ldots(a_k - k)(b_k - 1)\ldots(b_k - k)}{k!(k-1)!(-1)^{k-1}}\tau^k \log \tau Y(a_k, b_k, k+1; \tau) + (-1)^{k-1}\sum_{m=k+1}^{k-b_k}\times \frac{(m-1+a_k-k)\ldots(a_k-k)(m-1+b_k-k)\ldots(b_k-k)}{m!(k-1)!(m-k)!}\tau^m\left\{\frac{1}{a_k}+\ldots+\frac{1}{a_k+m-k-1}+\frac{1}{b_k}+\ldots+\frac{1}{b_k+m-k-1}-\frac{1}{k+1}-\ldots-\frac{1}{m}-\frac{1}{1}-\ldots-\frac{1}{m-k}\right\} + (-1)^{-1-b_k}\sum_{m=1-b_k+k}^{\infty}\times \frac{(m-1+a_k-k)\ldots(a_k-k)(m-1+b_k-k)!(k-b_k)!}{m!(k-1)!(m-k)!}\tau^m \quad (1)$$

a_k, b_k = functions of (γ, k); $c_k = -k + 1$

If air is the fluid, $\gamma = 1.4$, and the condition for both c_k and b_k negative integers may be expressed as the Diophantine equation

$$6(k^2 + 1) = n(n + 1) \qquad k, n \text{ integers}; (n - k) \text{ odd} \qquad (2)$$

The first few k's which satisfy Eq. (2) are 2, 5, 12, 119, . . .

Values of $Y_{-k}(\tau)$ for the first three of these special cases were included in the extensive tables of reference 4. Apparently all were calculated from a truncated series, the last summation being neglected. Obviously, the error is most serious at the largest tabulated τ—i.e., $\tau = 0.5$. For $k = 2$, the value of the final series for $\tau = 0.5$ was calculated and equals just the difference between the values given in references 4 and 5. The correction is about 1.5 per cent of the tabulated value of reference 4.

For $k = 5$, the correction for $\tau = 0.5$ was found to be about 19.5 per cent of the tabulated value. For $k = 12$, the sum of the final series for the same $\tau = 0.5$ exceeds the tabulated value by an order of 10.

For $k = 5$ and 12, the errors in the derivatives $dY_{-k}(\tau)/d\tau$ calculated by the truncated series are even more serious since each term of the final series is multiplied by a sizable number. The derivative for the $k = 2$ case is somewhat different (cf. page 4, reference 1), and the small difference between values given by references 4 and 5 is probably due to some other cause.

The corrections are negligible for subsonic τ so the tables of reference 6 are unaffected. The transonic flow for $k = 2$, calculated using reference 4, may be compared with Davies.[5]

Zeros

The number of zeros between $0 \leq \tau \leq 1$ for the hypergeometric series can be calculated easily by Hurwitz's formulas.[7] The actual locations of the zeros of the Chaplygin functions for air as functions of k are somewhat interesting.

For $c_k > 0$, $(k \leqq -1)$, $F(a_k, b_k, c_k; \tau)$ may be considered a continuous surface $F(k, \tau)$ erected on a section of the k, τ, plane $(0 \leq \tau \leq 1)$. Its intersections with the k, τ plane are the lines of zeros $\tau_{n,k}$, each continuous curve being well located by the roots of the polynomial cases and the zeros of the Gauss function $F(a_k, b_k, c_k; 1)$.

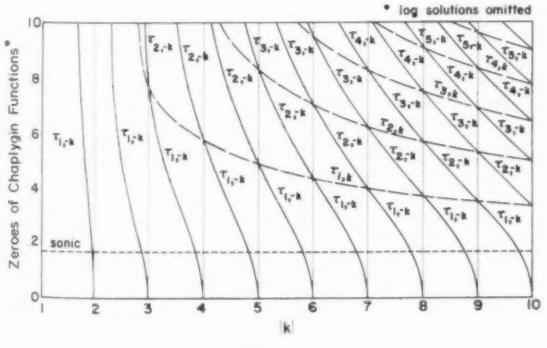

FIG. 1.

For $c_k < 0$, $(-k < -1)$, the surface $F(a_k, b_k, c_k; \tau) \equiv F(-k, \tau)$ is continuous between integers but discontinuous at every integer. The discontinuous lines of zeros $\tau_{n,-k}$ form a peculiar pattern with the first zero $\tau_{1,-k}$ tending rapidly to zero as c_k (or $-k$) approaches a negative integer. Thus, in the neighborhood of the integers, the first zero occurs at a *subsonic* τ. At the integer, the nth zero becomes the $(n-1)$st zero.

Since $F(k, \tau)$ and $F(-k, \tau)$ each multiplied by always positive factors are the independent solutions ψ of the same differential equation,[1, 2] the above cases may be combined by "folding" at $k = 0$ resulting in Fig. 1. (The logarithmic solutions for integral k do not fall in these lines, of course.)

References

[1] Garrick, I. E., and Kaplan, C., *On the Flow of a Compressible Fluid by the Hodograph Method; II, Fundamental Set of Particular Flow Solutions of the Chaplygin Differential Equation*, NACA TR 790, 1944.

[2] Lighthill, M. J., *The Hodograph Transformation in Transonic Flow*, Pts. I–III, Proc. Roy. Soc. (London), Series A., Vols. 191, 192, 1946, 1947.

[3] *Higher Transcendental Functions*, Vol. 1, Bateman Manuscript Project, California Institute of Technology; McGraw-Hill Book Co., Inc., New York, 1953.

[4] Huckel, Vera, *Tables of Hypergeometric Functions for Use in Compressible Flow Theory*, NACA TN 1716, 1948.

[5] Davies, N. J., *The Two-Dimensional Irrotational Flow of a Compressible Fluid Around a Corner*, Quart. Jour. Mech. and Appl. Math., Vol. VI, Pt. 1, March, 1953.

[6] Chang, C. C., and O'Brien, V., *Some Exact Solutions of Two-Dimensional Flows of Compressible Fluid with Hodograph Method*, NACA TN 2885, February, 1953.

[7] Hurwitz, A., *Ueber die Nullstellen der hypergeometrischen Reihe*, Math. Ann., Bd. 38, p. 452, 1891.

Asymptotic Suction Characteristics of the Boundary Layer over a Circular Cylinder*

H. G. Lew

Department of Aeronautical Engineering, The Pennsylvania State University, University Park, Pa.

May 11, 1956

IN A RECENT NOTE,[1] the asymptotic behavior of the boundary layer over a porous circular cylinder subjected to a uniform suction was considered. Under a small uniform suction, the behavior was obtained in a very simple way as an exact solution of the Navier-Stokes equations. The important parameter obtained appeared to be a Reynolds Number composed of the magnitude of the suction velocity at the wall and the radius of the cylinder. The skin friction was found to be independent of the radius of the cylinder; in fact, it had the same form as the flat-plate case. The shearing force per unit length of these cylinders was directly proportional to the suction Reynolds Number

* This research was supported by the U.S. Air Force through the Office of Scientific Research of the ARDC.

The checking of the algebraic work by J. B. Fanucci is gratefully acknowledged.

parameter. If α is the suction Reynolds Number, then

$$\alpha = -v_0 a/\nu \tag{1}$$

where v_0 is the suction velocity at the wall, a the radius of the cylinder, and ν the kinematic viscosity. A calculation of the displacement area and momentum defect area (Glauert and Lighthill)[2] defined, respectively, by

$$\Delta = 2\pi \int_a^\infty \left(1 - \frac{u}{U}\right) r\, dr \tag{2}$$

and

$$\theta = 2\pi \int_a^\infty \left(1 - \frac{u}{U}\right) \frac{u}{U} r\, dr \tag{3}$$

shows that, for these integrals to yield finite results, it is sufficient that $\alpha > 2$. In fact, the dependence of these quantities on α is given by

$$\Delta/\pi a^2 = 2/(\alpha - 2) \tag{4}$$

$$\theta/\pi a^2 = \alpha/[(\alpha - 2)(\alpha - 1)] \tag{5}$$

The displacement thickness would be given by the expression $[a(-1 + \sqrt{1 + \Delta/\pi a^2})]$. The ratio of this displacement thickness to that of the two-dimensional asymptotic suction profile is given by $[\alpha\{-1 + \sqrt{1 + 2/(\alpha - 2)}\}]$. This ratio is greater than 1 for $\infty > \alpha > 2$ and equal to 1 for $\alpha = \infty$.

Evidently, a certain amount of suction is needed for a given cylinder to obtain finite values of these quantities far downstream of the cylinder. It is remembered that, on a flat plate, finite values are obtained upon the application of suction. Thus the presence of a finite a in α minimizes the effect of v_0. It is evident, also, that increasing α values decrease the $\Delta/\pi a^2$, $\theta/\pi a^2$ values and that the effect of finite transverse curvature is essentially to increase the displacement thickness if there is suction present. It is also noted that, because of the suction, the skin friction at the wall is the same as that of the two-dimensional case so that the velocity starts at the same rate at the wall as the two-dimensional case.

With the help of the results of Lew and Fanucci,[3] it is not difficult to extend these results to the flow of a compressible heat-conducting boundary layer over a porous circular cylinder with uniform suction. However, it is noted that the boundary-layer approximation is used only in the energy equation; the momentum equation is still the Navier-Stokes equation. The equations of motion for this case are

$$\rho v(du/dr) = (1/r)(d/dr)[\mu r(du/dr)] \tag{6}$$

$$d(\rho v r)/dr = 0 \tag{7}$$

$$\rho c_p v(dT/dr) = (c_p/P_r)\cdot(1/r)(d/dr)[\mu r(dT/dr)] + \mu(du/dr)^2 \tag{8}$$

where u, v are the velocity components in the axial and radial directions, respectively, and r is the radial distance from the origin. In addition, the coefficient of viscosity and coefficient of heat conductivity are functions of the temperature and may be the power law expressions [e.g., Eq. (37) of reference 3]. The integrals of the above equations follow in the fashion of references 1 and 3. Thus, for Eq. (7), one obtains

$$\rho v r = \rho_0 v_0 a = \text{constant} \tag{9}$$

and, for Eq. (6),

$$(\rho v r)(u - U) = \mu r(du/dr) \tag{10}$$

Now, by allowing u to be the independent variable, Eq. (8) becomes

$$(1 - P_r)c_p(dT/du) - (U - u)\cdot\{c_p(d^2T/du^2) + P_r\} = 0 \tag{11}$$

with the boundary conditions that

$$\begin{aligned} &\text{at } u = 0: \quad T = T_0 \\ &\text{at } u = U: \quad T = T_1 \end{aligned} \tag{12}$$

Eqs. (11) and (12) are exactly the same as the two-dimensional case [in fact, they are Eqs. (41) and (42) of reference 3]. Thus, the solution from reference 3 is

$$[1 - (T/T_1)] = [1 - (u/U)]^{P_r}\{1 - (T_0/T_1) + [(\gamma - 1)/2]M_1^2\} + [(\gamma - 1)/2][M_1^2 P_r/(2 - P_r)] \times \{[1 - (u/U)]^2 - (2/Pr)[1 - (u/U)]^{P_r}\} \tag{13}$$

It is noted that a change of the wall condition to that of zero heat transfer will retain only the second part of the right side of Eq. (13). The solution for zero heat transfer in the two-dimensional case was given by Young.[4] The relation of the velocity u to the physical coordinate r may be given by

$$\frac{u}{U} = 1 - \exp\cdot\left[\rho_0 v_0 a \int_a^r \frac{dr}{\mu r}\right] \tag{14}$$

which can be explicitly determined once the dependence of μ on temperature is specified. In fact, if the new variable ζ is defined by

$$\zeta = -\alpha \int_0^\eta \frac{\mu_0}{\mu}\cdot\frac{d\eta}{\alpha + \eta} \tag{15}$$

where the substitution $r = a + y$ and $\eta = -(v_0 y)/\nu_0$ have been used and $\alpha = -v_0 a/\nu_0$, then

$$u/U = 1 - \exp(\zeta) \tag{16}$$

and Eq. (46) of reference 3 is valid here. The relation between the two-dimensional case and this case comes through the transformation

$$\eta = \alpha\cdot\{\exp[(\mu_1/\mu_0)\cdot(\eta_{\text{T.D.}}/\alpha)] - 1\} \tag{17}$$

where it is remembered that $\eta_{\text{T.D.}}$ was defined as $(-v_1 y/\nu_1)$ and T.D. = two-dimensional.

The gradient of the temperature at the wall can be determined without using Eq. (14) and is given by

$$dT/dr|_{r=a} = -(P_r v_0 T_1/\nu_0)\cdot\{1 - (T_0/T_1) + [(\gamma - 1)/2]M_1^2\} \tag{18}$$

which is exactly that of the two-dimensional case—that is, no effect of the radius appears. It is more interesting that the skin friction is still given by

$$\tau_0 = -\rho_0 v_0 U \tag{19}$$

independent of the transverse curvature and having the same form as the two-dimensional case and of the incompressible circular-cylinder case. The nondimensional equivalents of Eqs. (18) and (19) may be more convenient at times. These may be obtained by multiplying Eq. (18) by the ratio $\delta/(T_1 - T_0)$ and Eq. (19) by $2/\rho_0 U^2$ where δ is a characteristic length such as the displacement thickness. Thus, the local skin-friction coefficient $2\tau_0/\rho_0 U^2$ so obtained is dependent on the ratio of suction velocity to the free-stream velocity only. The dependence of the local heat-transfer coefficient so defined on all parameters as temperature ratio, Mach Number, etc., is obvious then from Eq. (18). It is easily seen from Eq. (17) that the temperature and velocity layers with suction are increased under the effect of a finite transverse curvature since $\eta > \eta_{\text{T.D.}}$ for $\alpha < \infty$ and $\eta = \eta_{\text{T.D.}}$ for $\alpha = \infty$. A considerable amount of detail information is given in reference 5.

The effect of compressibility with otherwise constant physical properties of the fluid can be determined easily. From Eq. (14), the velocity profile is

$$u/U = 1 - (r/a)^{\rho_0 v_0 a/\mu} \tag{20}$$

having the same form as the incompressible case. The dependence of the temperature on the distance r follows directly from Eq. (13). Moreover, the velocity and temperature gradients are the same as Eqs. (18) and (19).

References

[1] Lew, H. G., *The Asymptotic Behavior of the Boundary Layer to Transverse Curvature*, Journal of the Aeronautical Sciences, Readers' Forum, Vol. 23, No. 3, pp. 276, 277, March, 1956.

[2] Glauert, M., and Lighthill, M. J., *The Axisymmetric Boundary Layer on a Long Thin Cylinder*, Proc. Royal Soc., A, Vol. 230, pp. 188–203, 1955.

[3] Lew, H. G., and Fanucci, J. B., *On the Laminar Compressible Boundary Layer over a Flat Plate with Suction or Injection*, Journal of the Aeronautical Sciences, Vol. 22, No. 9, pp. 589–597, September, 1955.

[4] Young, A. D., *Note on the Velocity and Temperature Distributions Attained with Suction on a Flat Plate of Infinite Extent in Compressible Flow*, Quart. J. Mech. & Appl. Math., Vol. 1, Pt. 1, March, 1948.

[5] Lew, H. G., *The Asymptotic Suction Characteristics of the Boundary Layer on a Circular Cylinder*, Tech. Rep. No. 7, Dept. of Aeronautical Engineering, The Pennsylvania State University, January, 1956.

Stall Propagation in a Cascade of Airfoils

Anthony R. Kriebel

Research Assistant, Gas Turbine Laboratory, Massachusetts Institute of Technology, Cambridge, Mass.

May 7, 1956

Introduction

In order to observe and measure optically a stable pattern of stall propagation in the simplest possible type of flow, a radial outflow circular cascade was installed in the closed circuit wind tunnel at the M.I.T. Gas Turbine Laboratory under the sponsorship of the National Advisory Committee for Aeronautics. Interferometer and schlieren pictures of the flow through a section of the cascade were taken at 6,000 frames per sec. These pictures have suggested a new avenue of analytical approach to the problem which is not restricted to small unsteady perturbations or an assumed simplified cascade geometry.

Experimental Results

Fig. 1 is a section of one of the interferometer films of the flow over two blades of the cascade where the lines indicate constant air density. From the large collection of such pictures, it can be concluded that for all the cascade configurations, Reynolds Numbers, and Mach Numbers tested, the airfoils stalled from the leading edges during stall propagation and periodically shed nearly all their bound vorticity. The vorticity shed downstream from the cascade airfoils was largely concentrated into discrete vortices which accumulated at and departed from the leading and trailing edges of the airfoils as they stalled and unstalled. There is experimental evidence that these same conclusions are valid for a single stage research compressor from which stall propagation data were taken also.

Hot-wire velocity measurements from the research compressor assembled as an isolated rotor indicate that, as the flow was throttled, one stall cell appeared which included from two to five of the 44 rotor blades. With further throttling the number of cells increased consecutively to four.

There was small axial flow through the portion of the rotor included in stall cells, and the cells extended downstream from the rotor in a direction almost normal to the plane of the rotor.

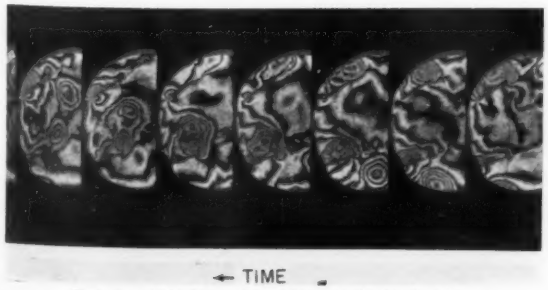

Fig. 1. Interferometer pictures (6,000/sec.).

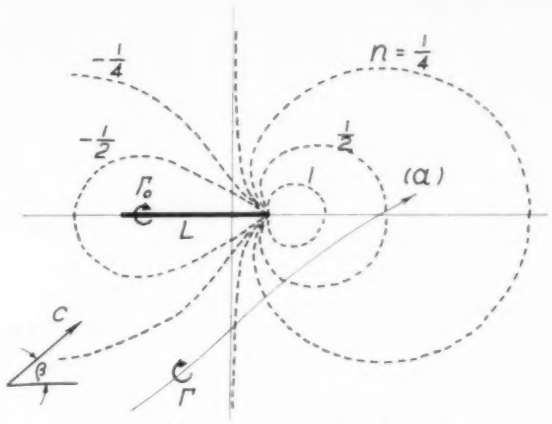

Fig. 2. Effect of vortex on plate circulation.

Outline of Proposed Theory

In Fig. 1 it is noted that in the circular cascade whenever a vortex was shed from the leading edge of an airfoil the succeeding airfoil stalled as the vortex passed under it. If one considers the potential flow around a flat plate, a theoretical explanation becomes evident. For uniform streaming flow over a flat plate with the Kutta condition satisfied and with an adjacent potential vortex, the dashed curves in Fig. 2 are loci of the vortex for constant plate circulation given by

$$\Gamma_0 = \pi LC \sin \beta + n\Gamma$$

It is evident from Fig. 2 that the theoretical plate circulation goes through a maximum value as the vortex passes under the plate along line (a) after it has been shed from the adjacent airfoil in the cascade. In Fig. 1 it is observed that a blade stalled as the shed vortex, Γ, approached the location for maximum Γ_0 on the blade. This qualitative description indicates a mechanism by which stalling can propagate along the cascade and that there should be a finite time delay between the stalling of succeeding airfoils even if boundary-layer time delays are neglected.

It is hypothesized that for a single stall cell the flow relative to the rotor may have been similar to that sketched in Fig. 3, where the "bound vortices" are indicated on the blades and located along line (b) after they have been shed downstream. The "starting vortices," shed when the airfoils unstall, are shown located along line (c). Lines (b) and (c) are the boundaries of what is called the stall cell, are of shape constant in time, and move relative to the cascade with velocity of propagation, V_p. The shed vortices move downstream along path lines (b) and (c) with velocity V_a. In a coordinate system fixed to the stall cell, the flow is steady except for the local effects of the finite spacing of the vortices and moving blades.

As shown in Fig. 3, lines (b) and (c) far downstream must become straight and parallel and the vortices uniformly spaced along them by distance a. Local velocities are those induced by two infinite vortex streets oriented at the angle ϕ and spaced na apart.

More than a distance a away from the vortex streets the velocity induced by them may be taken as zero outside the cell, while in the center of the cell, if $n > 2$,

$$V_i = \Gamma/a$$

Each vortex moves with velocity V_2, and from Fig. 3 the velocity of propagation of the stall cell along the cascade is

$$V_p = C_{\theta_2} - C_{z_2} \tan \phi \qquad (1)$$

From the rotor experimental data, it appears to be a good

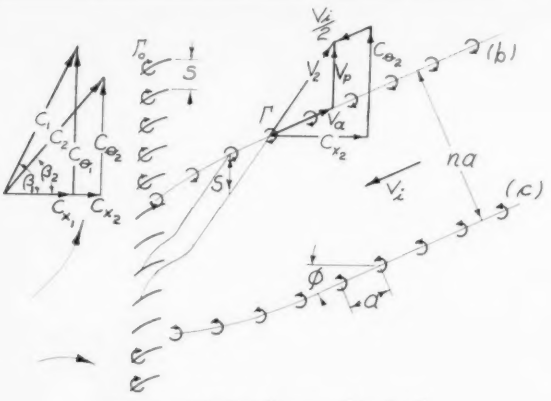

FIG. 3. Velocity diagram of stall cell.

approximation to assume no flow through the stall cell, or

$$V_i \cos \phi = C_{x2}$$

and $$\Gamma = \Gamma_0 = s(C_{x1} \tan \beta_1 - C_{x2} \tan \beta_2)$$

Then $$V_i = \Gamma/a = (s/a)(C_{x1} \tan \beta_1 - C_{x2} \tan \beta_2) \quad (2)$$

Since the vortices pass any downstream point on line (b) or (c) of Fig. 3 with the same frequency with which they are shed onto the lines from the blades

$$s/a = V_p/V_a = (C_{\theta 2} - C_x \tan \phi)/[(C_{x2}/\cos \phi) - (V_i/2)] \quad (3)$$

Eliminating s/a from Eqs. (2) and (3) gives

$$(\tan \beta_2 - \tan \phi) \cos^2 \phi = \frac{1}{[2(C_{x1}/C_{x2}) \tan \beta_1 - 2 \tan \beta_2]} \quad (4)$$

Solving Eq. (4) for ϕ and substituting in Eq. (1) gives

$$V_p/C_{x1} = \tan \beta_1 \pm \sqrt{\tan^2 \beta_1 - [(\tan^2 \beta_2 + 1)C_{x2}^2/C_{x1}^2]} \quad (5)$$

The plus sign for the last term implies that ϕ is a large negative angle which can be shown to be impossible physically. Therefore,

$$V_p/C_{\theta 1} = 1 - \sqrt{1 - (C_2/C_{\theta 1})^2} \quad (6)$$

Eq. (6) indicates that stall cells of the type assumed are impossible if $C_2 > C_{\theta 1}$. This has been verified experimentally. The blockage effect of the stall cells after the onset of propagation was such that $C_2/C_{\theta 1}$ remained almost constant with further throttling of the rotor, and cells propagated with approximately half wheel speed in agreement with Eq. (6).

The assumptions made in the analysis imply that the airfoils outside the cell have no drag and those in the cell have no lift. It may be noted that in the case of no axial flow in the cell, the model is similar to a flat plate translating along the cascade at velocity V_p and blocking the flow through a portion of it. The stall cell corresponds to the wake behind the plate, and there is a "head loss" in the cell given by the velocity defect.

Analyses of the model for small perturbations ($V_i/C_x << 1$) indicate that a flow with small disturbances is possible only for a narrow range of blade stall characteristics, which may indicate why small perturbation stall cells seldom are observed experimentally.

The vortex flow model of Fig. 3 gives a qualitative explanation for the observed splitting of the stall cell into two as the flow was throttled. With throttling, n was observed to increase before splitting occurred. If the lines (b) and (c) are not infinitely long, the induced velocity V_i at the blade in the center of the stall cell decreases as n increases. When V_i becomes small at the center blade it tends to unstall, thereby splitting the cell into two stall cells which become distributed axisymmetrically around the rotor. Experimental data have been taken which support this description.

Tip-Bluntness Effects on Cone Pressures at $M = 6.85$

Mitchel H. Bertram
Langley Aeronautical Laboratory, NACA, Langley Field, Va.
May 22, 1956

THERE IS, at present, considerable interest in the characteristics of blunted bodies from both an aerodynamic and a heat-transfer standpoint. The use of blunt shapes is contemplated to reduce the heat-transfer problem at body noses, but there are also applications for blunt noses which occur from mainly aerodynamic considerations. An actual reduction in drag may be the beneficial result of blunting the nose of a cone or a similar slender shape under certain conditions.[1] Although the sphere has received considerable treatment, the nose shapes are not necessarily tangent spheres. In the case, let us say, of a total head tube situated in the nose of a given body, the blunting may be quite flat, and nose sections blunter than spherical shape may conceivably be desirable, in some cases, from the heat-transfer standpoint.

The purpose of the present investigation is to examine the aerodynamic effect of a simple type of nose blunting on a basic body. The body chosen was a 10° half-angle cone with a base diameter of 2.00 in., and the blunting consisted of a plane cut normal to the cone axis. This is similar to the blunting previously investigated by this writer for the two-dimensional case.[2] The model was fitted with five rows of pressure orifices. There was one orifice at the first station, two orifices at the second and fourth stations, and four orifices at the third and fifth stations. Successive blunting of this cone supplied a large number of data points. The tests were conducted in the nominal Mach 7 Invar nozzle of the Langley 11-in. hypersonic tunnel. Because of variations in pressure and the times at which data were taken during a run, the calibration Mach Number varied between 6.84 and 6.87, the value of 6.85 being a good average for all the data. Some calibration data for this nozzle may be found in reference 3. The data were obtained at supply pressures in the range 22 to 34 atmospheres and at supply temperatures between 1065°R. and 1170°R., and the corresponding Reynolds Numbers per in. were in the range 2.4×10^6 to 3.8×10^6.

In this investigation, surface pressures were measured, and schlieren pictures were taken to enable measurement of the shock shape and thus to evaluate the various parameters immediately behind the bow shock. Typical schlieren photographs of an essentially sharp-pointed cone and the same cone blunted are shown in Figs. 1 and 2. Fig. 3 is a schlieren photograph of a flat-ended circular cylinder with the axis of the cylinder aligned with the free-stream flow direction. This configuration is included for the comparison of its shock shape with that for the blunted cone in the tip region.

Perhaps the most significant difference between the shock on the sharp and blunted cones, aside from the expected detached shock at the nose of the blunted cone, is the inflection in the shock from the blunted cone 20 to 30 tip diameters from the nose. This nonmonotonicity in the slope of the shock wave from the blunted cone is shown in Fig. 4a. There is apparently an overexpansion after the leading tip so that, at between 20 and 25 tip diameters from the nose, the slope of the shock decreases to a value about 2° less than the slope obtained from cone theory; from this low value it rapidly increases to the value given by cone theory. The shock slope in the tip region is given by Fig. 4b. In this figure, for the blunted cone, only measurements from the largest diameter cone tip have been utilized because of difficulties apparently arising from optical refraction and resolution with shock measurements from the smaller tips. Such difficulties are illustrated by comparison of the shock detachment distance for the several configurations. Measurements of the ratio of axial shock detachment distance to nose diameter D for the relatively large flat-nosed cylinders, whose dimensions are given in Fig. 4a, gave a value of 0.269; however the blunted cone with D =

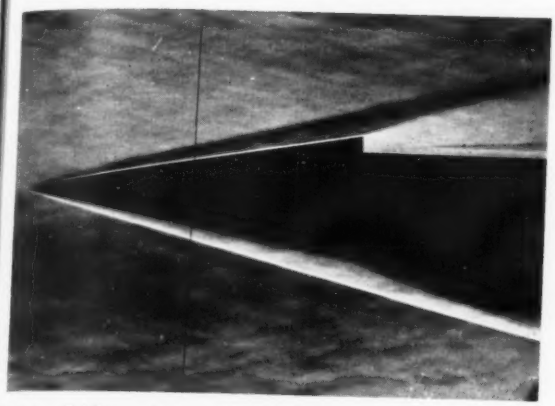

FIG. 1. Schlieren photograph of 10° half-angle cone. $M_\infty = 6.85$

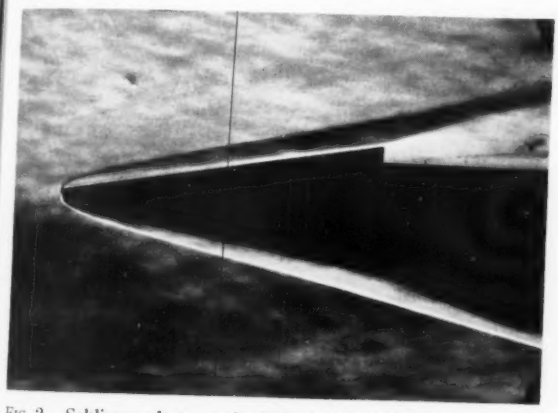

FIG. 2. Schlieren photograph of blunted-tip 10° half-angle cone. $M_\infty = 6.85$.

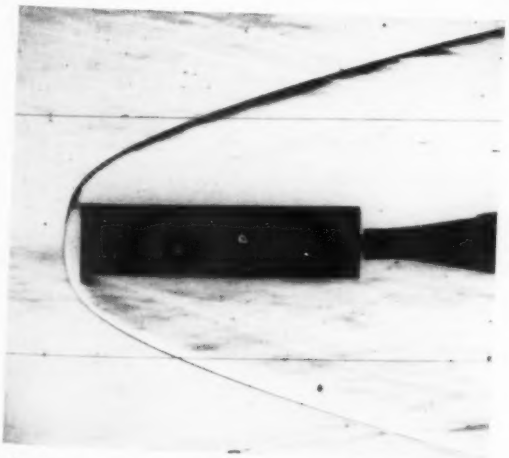

FIG. 3. Schlieren photograph of flat-nosed cylinder. $M_\infty = 6.85$.

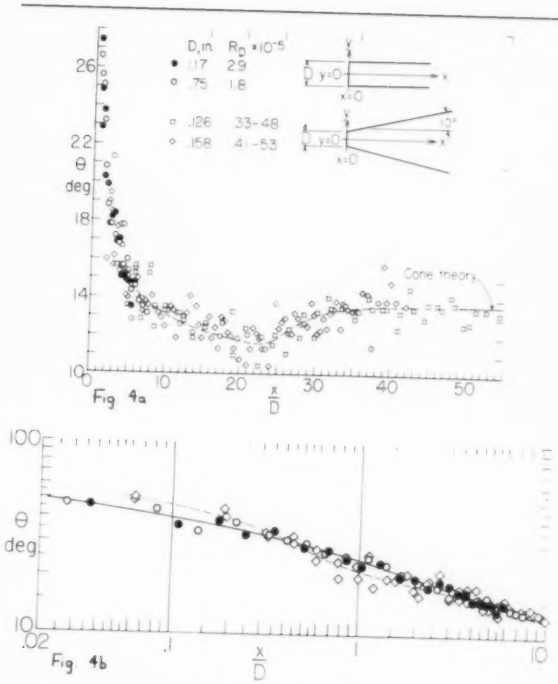

FIG. 4. Local inclination of the shock from a flat-nosed cylinder and a blunted cone. $M_\infty = 6.85$.

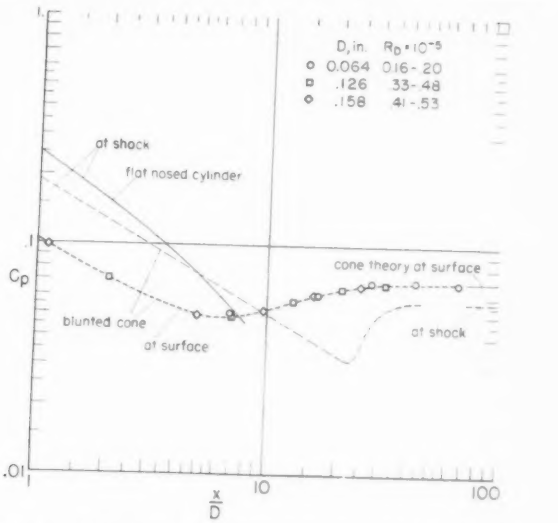

FIG. 5. Pressure coefficients immediately behind shock from a flat-nosed cylinder and a blunted cone and at the surface of a blunted cone. $M_\infty = 6.85$.

0.126 in. gave an average value 0.37 for this ratio with a scatter of 14 per cent (from average of 2 runs). With the diameter of the blunted cone tip increased to 0.158 in., the nondimensionalized detachment distance was 0.26 (from 2 runs) with an estimated measuring accuracy of 5 per cent, a reasonable agreement with the flat-nosed cylinder result.

Utilizing the shock-shape (Fig. 4) and surface-pressure measurements, the pressure coefficients immediately behind the shock and at the surface were obtained. These results are shown in Fig. 5. The data points shown for the surface-pressure measurements are averages for a given station. The dip in the results from the blunted-cone shock and surface pressures is quite pronounced with the surface pressures reaching a minimum value well ahead of the minimum in the pressures at the shock. At low values of x/D, waves from the vicinity of the shock appear to determine the surface pressures. The reflection of these waves from the surface eventually turns the shock so as to approach the shock strength given by cone theory. Tests with this cone before blunting gave surface pressures which averaged to within about 1 per cent of the value given by cone theory.

The present surface data are not believed to be affected to any considerable extent by viscous effects since data were obtained at values of R_D as low as 0.50×10^4 and as high as 5.4×10^4 and did not show a deviation which could be ascribed to Reynolds Number effects. The data presented are for the pressure levels at which the most accurate measurements can be made in the tunnel.

The general appearance of the curve of surface-pressure coefficient with distance in Fig. 5 is similar to that obtained by Oliver[4] in his tests at $M_\infty = 5.8$ of a 40° half-angle cone with a tangent sphere forming the nose. In these $M = 5.8$ tests, essentially cone static pressure was attained in about 1.5 tip diameters (measured along the surface). The overexpansion immediately following the nose of Oliver's test configuration was not nearly so pronounced as that exhibited by the test data shown in Fig. 5. It is probable that, had Oliver situated orifices between the ones that were adjacent to the sphere-cone tangent point, a more abrupt and slightly lower dip would have manifested itself than is indicated by his fairing of his data.

For the flat plate, the effect of leading-edge blunting in increasing the Reynolds Number for transition[3] is now rather widely known—at least for the relatively thin leading edges for which significant data have been obtained. The extrapolation of such results to the blunted cone—at any rate for the large bluntings investigated here—does not appear to be obvious. At the nose there is a normal shock with its associated losses; to about 7 diameters from the nose there is a strong negative pressure gradient, at the surface; from about 7 to 30 diameters from the nose there is a weaker positive pressure gradient at the surface, and the surface Mach Number is approximately 2.5. Qualitatively, the effect of the losses through the normal shock combined with the resulting Mach Number and the pressure gradient on the boundary-layer thickness can be seen in the schlieren photographs, Figs. 1 and 2, where a considerable increase in boundary-layer thickness at the base is readily discernible for the cone in the blunted condition.

Some indication of the relative effects of leading-edge (tip) blunting on a flat plate and a cone may be offered by the results obtained at $M = 3.05$ by a group at the University of Minnesota.[5, 6] From these tests, apparently because of the three-dimensional nature of the flow on the cone, the change in the momentum thickness from the theoretical value was an order of magnitude reduced from the change obtained on a flat plate with a comparable blunting. Also, there was an indication that blunting decreased the shear stress on both the cone and the flat plate, although the percentage reduction in shear stress in the case of the cone was half that obtained for the flat plate. For the flat plate, however, the closest that the leading edge was approached was about 140 leading-edge thicknesses while, for the cone, the closest approach to the tip was about 730 tip diameters.

It appears that measurements of the effects of tip blunting on boundary-layer transition, heat transfer, and skin friction in the regions of cones in proximity to the tip would be of considerable interest, warranting further investigation. In the present case, proximity to the nose would be considered to extend up to 30 or 40 diameters from the nose.

References

[1] Sommer, S. C., and Stark, J. A., *The Effect of Bluntness on the Drag of Spherical-Tipped Truncated Cones of Fineness Ratio 3 at Mach Numbers 1.2 to 7.4*, NACA RM A52B13, April, 1952.

[2] Bertram, M. H., *Viscous and Leading-Edge Thickness Effects on the Pressures on the Surface of a Flat Plate in Hypersonic Flow*, Journal of the Aeronautical Sciences, Readers' Forum, Vol. 21, No. 6, pp. 430–431, June, 1954.

[3] Bertram, M. H., *Exploratory Investigation of Boundary-Layer Transition on a Hollow Cylinder at a Mach Number of 6.9*, NACA TN 3546, 1956.

[4] Oliver, R. E., *An Experimental Investigation of Flow Over Simple Blunt Bodies at a Nominal Mach Number of 5.8*, GALCIT Hypersonic Wind Tunnel Memorandum No. 26, June 1, 1955. Also Journal of the Aeronautical Sciences, Readers' Forum, Vol. 23, No. 2, pp. 177–179, February, 1956.

[5] Blumer, C. B., Bradfield, W. S., and Scott, C. J., *The Effect of Cone Tip Blunting on the Supersonic Conical Laminar Boundary Layer*, Univ. of Minnesota, Aeronautical Engineering Dept., EM No. 29, March, 1954.

[6] Bradfield, W. S., DeCoursin, D. G., and Blumer, C. B., *The Effect of Leading Edge Bluntness on a Laminar Supersonic Boundary Layer*, Journal of the Aeronautical Sciences, Vol. 21, No. 6, pp. 373–382, 398, June, 1954.

The Journal of Fluid Mechanics

The *Journal of Fluid Mechanics*, the first issue of which appeared in May, 1956, exists for the publication of theoretical and experimental investigations of all aspects of the mechanics of fluids and is issued in six parts per volume.

Authors wishing to have papers published should communicate them to any one of the persons below, choosing one in their own country where possible.

Editor: Dr. G. K. Batchelor, Cavendish Laboratory, University of Cambridge, Cambridge, England. Assistant Editors: Dr. T. B. Benjamin and Dr. I. Proudman. Associate Editors: Prof. G. F. Carrier, Pierce Hall, Harvard University, Cambridge 38, Mass. Prof. W. C. Griffith, Palmer Physical Laboratory, Princeton University, Princeton, N.J. Prof. M. J. Lighthill, Department of Mathematics, The University, Manchester, England.

Price, £1 ($3.00) per part. *Subscription price*, £5 10*s*. per volume of six parts, post free ($16.50 in U.S.A. and Canada). *Agents for U.S.A. and Canada:* Academic Press Inc., 125 East 23rd St., New York 10, N.Y.